Photonic crystals for light trapping in solar cells

by

Jo Gjessing

Thesis submitted for the degree of
Philosophiae Doctor

Department of Physics
University of Oslo

October 2011

Abstract

Solar energy is an abundant and non-polluting source of energy. Nevertheless, the installation of solar cells for energy production is still dependent on subsidies in most parts of the world. One way of reducing the costs of solar cells is to decrease their thickness. This will reduce material consumption and, at the same time, unlock the possibility of using cheaper lower quality solar cell material. However, a thinner solar cell will have a higher optical loss due to insufficient absorption of long wavelength light. Therefore, light-trapping must be improved in order to make thin solar cells economically viable.

In this thesis I investigate the potential for light-trapping in thin silicon solar cells by the use of various photonic crystal back-side structures. The first structure I study consists of a periodic array of cylinders in a configuration with a layer of silicon oxide separating the periodic structure from the rear metal reflector. This configuration reduces unwanted parasitic absorption in the reflector and the thickness of the oxide layer provides a new degree of freedom for improving light trapping from the structure. I use a large-period and a small-period approximation to analyze the cylinder structure and to identify criteria that contributes to successful light-trapping.

I explore the light-trapping potential of various periodic structures including dimples, inverted pyramids, and cones. The structures are compared in an optical model using a 20 µm thick Si slab. I find that the light trapping potential differs between the structures, that the unit cell dimensions for the given structure is more important for light trapping than the type of structure, and that the optimum lattice period does not differ significantly between the different structures.

The light-trapping effect of the structures is investigated as a function of incidence angle. The structures provide good light trapping also under angles of incidence up to 60 degrees. The behavior under oblique incidence angles can to a large degree be predicted by considering the number of escaping diffraction orders which may easily be found from the grating equation.

In addition to the well-known structures mentioned above I also introduce novel light-trapping structures. I use these structures to investigate what level of light trapping that may be achieved by freely selecting the unit cell geometry. The best light trapping is achieved for structures with low symmetry in their unit cells. The light confinement of one such structure even exceeds the Lambertian light trapping for normal incident light. Lambertian light trapping assumes total randomization of light inside the absorbing material. From geometric optics considerations such a structure will provide the maximum achievable light trapping within a dielectric slab. The Lambertian limit is independent of incidence angle and is therefore valid for isotropic illumination.

To experimentally study light trapping from periodic structures, and moreover to compare with our numerical simulations, we had periodic cylinder arrays fabricated by pho-

tolithography. The samples were divided into small blocks of cylinder arrays where lattice geometries and lattice periods varied between the blocks. The measured reflectances from the different blocks are in qualitative agreement with the numerical simulations. A quantitative comparison, on the other hand, is difficult due to the small size of the structured areas.

I have also been a part of a team at IFE investigating fabrication methods which may be better suited than photolithography for low-cost fabrication of photonic crystals for solar cells. These methods comprise nanoimprint lithography on very thin Si substrates and self-assembled structures using nanospheres. The work focused mainly on control and understanding of the fabrication methods. My contributions to this work were in transfer of the nanoimprinted structures from the resist to the substrate and the subsequent analysis, and in discussions and optical measurements of the self-assembled structures.

Acknowledgments

After my masters I felt tired of studying and considered to get a "real job", but after a visit at IFE the activity there seemed so interesting that they were able to pull me back in. And, in fact, I feel pleased with my decision. My timing could of course have been better than to deliver two days after the largest Norwegian solar cell company closes down their domestic factories. But, to look on the bright side, I have learned a lot of interesting stuff. I still think that the field of solar cells is extremely interesting. Imagine to work within a field that combines a fun and challenging subject with a dynamic industry that has a high priority on research and new ideas, and at the same time saving the world.

During parts of my PhD period I have functioned as the General Secretary of the Norwegian Solar Energy Society (NSES). This has been inspiring and brought context and real life to the PhD work, and it has provided me with a completely different set of challenges. It has also thought me the importance of concentrating one thing at the time, and as the extent of work increased I realized that I had to leave NSES to be able to finish my PhD in time. In hindsight I can say that this was a good decision.

My supervisor team during my four years at IFE has consisted of head supervisor Erik S. Marstein, an expert in solar cells, and co-supervisor Aasmund S. Sudbø, an expert in optics. Their complementary qualities, both professionally and personally, have been crucial for me as a PhD student and I owe them both great thanks.

My colleagues at the solar department deserve thanks for making IFE interesting. I have enjoyed our numerous conversations, both subject related and non-subject related. I have enjoyed the whole spectrum of cakes and buns we have shared. I have enjoyed your efforts in Holmenkollstafetten. I have enjoyed the social gatherings and your stamina at national and international conferences, and I have enjoyed some really good Soløl. Working with so many skilled and cheerful people has made my PhD period much easier.

I would also like to thank Obducat for nanoimprinted samples, Michal Mielnik at Sintef for RIE etching, the ePIXfab team at IMEC for sample fabrication, Lars Kirksæther for thinning my samples, Håvard Granlund and Einar Haugan for being such excellent master students, Hallvard Angelskår for valuable exchange of GD-Calc experience, Jon Erling Fonneløp for help with the AFM, and Annett Thøgersen for introducing me the to the Multiprep system at UiO.

Most important of all, I would like to thank Leonora for making me burst in laughter and Reniane for making me happy.

Contents

1. Introduction

1.1. Solar cells outlook

The world is screaming for energy. Today there are almost 1.5 billion people in the world that do not have access to electricity [1]. Enormous amounts of energy will be needed to meet the UN goal of reducing poverty for billions of people around the world. On top of this the world population is expected to increase from today's seven billion inhabitants to more than nine billion inhabitants within 2050 [2]. With this as a background it seems obvious that the energy demand will continue to rise in the decades to come. In fact, world energy consumption is predicted an increase by 50 % in the period 2008-2035, mainly driven by the growth in developing countries [3].

The great paradox is the fact that the expected increase in energy consumption must be accompanied by a significant reduction in CO_2 emissions to meet the two-degree target predicated by the international community [4]. This is a tremendous task, considering the fact that fossil fuels are expected to cover most of the increasing demand in the coming years. The reduced esteem for the largest CO_2 free energy source today, nuclear power, after the earthquake in Japan in 2011 does not make the situation any easier. The debate over how the two-degree target can be met has been a source of dispute between developing and industrialized countries and has even contributed to the formation of new power alliances [5].

Solar energy is one of the most promising candidates to replace fossil fuels. Solar energy is pollution free, and also the most abundant energy source available, with an energy flux at the earth's surface of several thousand times the worldwide power consumption. Solar power can be utilized in a number of ways where the most important technologies today are direct heating using solar collectors, electricity production from heat generated with concentrated solar power, and direct conversion of solar energy to electricity using solar cells. Solar cells, also known as photovoltaic (PV) cells, will be the focus of this thesis. A number of different PV technologies exist with the largest being solar cells made of silicon wafers, with a market share of 85 % in 2010, and thin-film solar cells which made up the remaining 15 % in 2010.

The PV industry is experiencing an unprecedented growth, with yearly growth rates of 45 % for the last 15 years [7]. Figure 1.1.1 shows the yearly installed capacity in MW_p[1]. New technologies and economies of scale are continuously reducing the cost of solar cells at approximately 20 % for each doubling of cumulative installed capacity [7]. This learning rate is significantly higher than what is found for other energy technologies.

[1] W_p (watt-peak) denotes the solar modules output at standard test conditions with a solar irradiance of 1000 W/m^2.

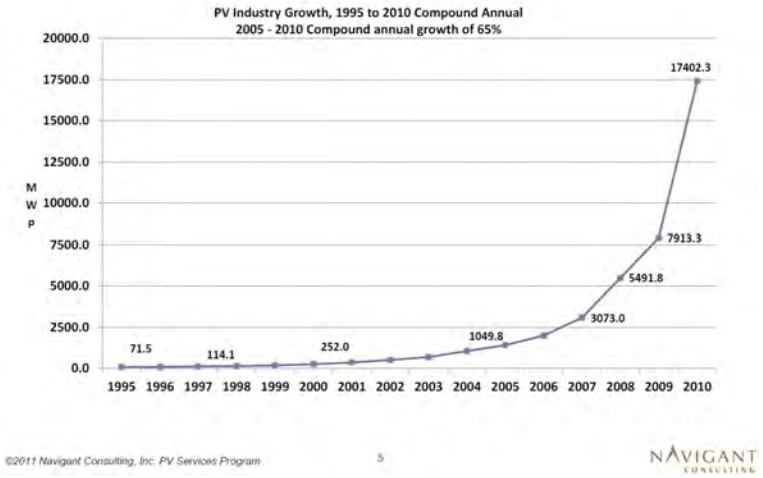

Figure 1.1.1.: Installed PV capacity from 1995 to 2010 [6].

Despite high growth rates and lower prices, PV is still dependent on subsidies in most major markets of the world. This makes the industry vulnerable to changes in government policies, and subsidies cannot be a solution in the longer run. The short term goal of the PV-sector is therefore to reach grid-parity, i.e. to become cheaper than the peak prices of grid electricity.

Spot prices for solar modules at the time of writing (August 2011) range from 0.85-1.39 €/W_p (1.17-1.92 \$/W_p) [8]. To reach sustainable prices of 1 \$/W_p has for a long time been an aim for the PV industry as one expects this to allow entrance to large markets without the need for subsidies. Due to a remarkable drop in prices since 2009 this goal seems to be within range earlier than expected. A long term goal is to reach a total system price of 1 \$/W_p, which would probably require a module cost close to 0.5 \$/W_p. At this cost PV is expected to be compatible in most of the world energy markets.

To reach these ambitious cost targets production costs need to be reduced and conversion efficiency must be improved. The conversion efficiency is particularly important as it also affects the balance of system costs. A higher efficiency means that fewer modules must be installed to reach a given output capacity, thus reducing the labor costs and hardware related costs like installation racks and wiring. The advantage of high efficiency is directly reflected in the spot prices where the high price range corresponds to high-efficiency crystalline silicon (Si) modules, while the lowest prices correspond to the less efficient thin-film and particularly a-Si thin film modules.

An important road for improving the economics of wafer based Si solar cells is to reduce their thickness. This has two main motivations. Firstly, a thinner wafer means less demand for expensive high-purity Si material, and secondly, it is advantageous with respect to efficiency. In a thinner solar cell the exited charge carriers will have to travel a shorter distance, and consequently, recombination losses are reduced. The same mechanism also allows the use of lower quality material without reducing the efficiency. This may sound too good to be true, but there is one important catch. The increase in optical

losses for the thin solar cell must be kept small, or the cost reduction will be offset by a reduction in solar cell efficiency.

1.2. Light trapping in solar cells

Optical losses may be divided in reflection from the front surface, preventing light from entering the solar cell, and poor absorption of infrared light. Silicon (Si) has many advantages as a solar cell material, but the optical properties are not among them. Near infrared light is difficult to absorb in Si due to long absorption length. The light which is not absorbed is either lost by escaping through the front side or it is absorbed in non-photo active materials in the solar cell such as the rear reflector. The main focus has traditionally been to reduce the front-surface reflectance because the solar cells have been sufficiently thick to absorb most of the light. However, as solar cells are made increasingly thinner, the optical losses due to poor light absorption becomes more and more important.

Light trapping aims at improving light absorption by designing the solar cell in such a way that the path length of light inside the photo active material is as long as possible. In wafer-based Si solar cells today this is achieved by texturing the surface with a random pattern of pyramids with a typical structure size that are several times the size of the wavelength of light. These structures are mainly applied to get light into the solar cell, but they also serve the purpose of scattering and thereby increasing the path length and thus absorption of light within the cells. These structures have proven to be very efficient and are used when possible. Unfortunately, this type of texture is not applicable to for instance multicrystalline solar cells, which has a larger market share than monocrystalline solar cells. Also, due to their size, these structures remove a large part of the material and may not be applicable to very thin cells. Additionally, new fabrication techniques for fabrication of very thin Si wafers that involve cleaving produces wafers with crystal orientation which does not allow the conventional texturing methods. Therefore, new light trapping methods are being investigated.

Thin-film solar cells need a different type of texture as their thickness typically is in the order of a micron. These cells commonly use a textured glass substrate for anti-reflection and light trapping. The feature sizes of the textured glass are a few hundred nanometers, i.e. much smaller than the textures on wafer-based solar cells. In thin-film solar cells the light trapping ability is typically given more attention than for the much thicker wafer-based solar cells. Nevertheless, the light trapping in thin-film solar cells still have more to gain by improving the textures and new texture types are therefore being investigated.

1.2.1. Light trapping with photonic crystals

Periodic structures with lattice periods similar to the wavelength of light are known as photonic crystals [9]. Light interaction with such structures may yield phenomenon such as diffraction and optical band gaps which are caused by the wave nature of light. Utilizing these phenomenons may provide light trapping effects that are not achievable

with conventional textures. An important property of these structures is the fact that their response may be tailored to fit the part of the solar spectrum of interest simply by tuning the size of the lattice period. The size of these structures, which are typically comparable to the wavelength of light, makes them compatible also with thin solar cells.

Any type of process used to make solar cells must have the potential of high throughput and low cost. Consequently, if photonic crystals are to be used in solar cells, a fabrication method is required that can make such structures on a large area at an affordable price. The semiconductor industry mainly uses photolithography to make this type of small, well-defined structures. This is considered to be too expensive for large scale production of solar cells. However, other promising fabrication methods exist such as nanoimprint lithography, or hot embossing, and interference lithography. Yet another interesting method is structures made by self-assembly. One such example, which I will discuss in more detail later in the thesis, is the use of self-assembled colloidal templates to fabricate 2D or 3D photonic crystals.

1.3. What is our contribution?

In this thesis I investigate photonic crystal structures for light trapping in solar cells. By utilizing the diffraction properties of the photonic crystal surface, light may be coupled into diffraction orders that will increase the path length of light inside the absorbing material. I focus my attention on photonic crystals applied to the back side of solar cells. Here the spectrum of wavelengths that reach the photonic crystal is much narrower than the full solar spectrum incident at the front side. The inherent wavelength dependent optical properties of periodic structures make them particularly suited when targeting a narrow wavelength range.

The first structure we investigate is a bi-periodic array of cylinders. Numerical simulation of such a two-level, or binary, structure requires less computational power than more complex structures, and additionally, the structure may be fabricated using standard photolithography processes. We analyze the light-trapping properties of the cylinder structure using a metamaterial approximation in the limiting case of small lattice periods and by using a phase difference condition for the limiting case of large lattice periods. We use these models to improve our understanding of the mechanisms of light trapping and to predict favorable dimensions for cylinder height, cylinder fill factor, and also the thickness of the back-side oxide layer. The oxide layer mainly serves to reduce unwanted absorption of light in the rear metal reflector. This is a problem in solar cells today, and will become an even greater problem for thin solar cells with a periodically structured metallic mirror. In rigorous numerical simulation of the structure we focus on reducing this parasitic absorption at the same time as we achieve a high light-trapping efficiency.

From the cylinder array we move on to investigate periodic structures with other unit cell geometries such as an inverted pyramid, dimple, and cone structure. In addition we introduce two novel structures which exhibit a lower symmetry in their unit cell geometry. We investigate the light-trapping potential of all these structures and show that the structures with the lowest symmetry have the highest light-trapping potential. The light

trapping from the best low-symmetry structure even exceeds that of Lambertian light trapping at normal incidence. Lambertian light trapping assumes total randomization of light inside the absorbing material. Lambertian light trapping is known to give the highest achievable light trapping under isotropic illumination for any structure in the geometrical optics description of light. The performance of our low symmetry structure fall below the Lambertian limit at higher angles of incidence.

We also compare light trapping from periodic structures with that of a front-side and a double-sided random pyramidal texture, textures which are commonly used in monocrystalline solar cells today. As expected, a front side textured with pyramids provides a much lower front-side reflection than the configurations with planar front sides and rear-side periodic structures. The disadvantage of a higher front-side reflection of planar surfaces is significantly reduced for multilayer anti-reflection coatings (ARCs) and for encapsulated solar cells. Yet the best double-sided pyramidal texture did slightly exceed the best periodic structure, even with a double layer ARC covering the planar front side of the periodic structure. The fact that pyramidal structures may yield this level of light trapping will probably limit the use of periodic structures to solar cells where this type of texturing is not possible, such as multicrystalline Si, crystalline Si with other crystal orientations than the standard [100] orientation, and very thin solar cells where the pyramids, with their typical size of several microns, may not be applicable.

To compare with our simulation results we had small area samples produced by state-of-the-art photolithography at IMEC in Belgium. We thinned the samples by mechanical lapping to a thickness of approximately 20 µm so that their optical properties could be characterized at the desired wavelength range. The measured reflectance agreed qualitatively with what we had found from simulations. The reflectance was substantially reduced compared to a planar reference and the samples with the optimal grating dimensions and lattice structure also exhibited the lowest reflectance. The small size of the samples limited the accuracy of the optical measurements, and a quantitative comparison with the simulation results was difficult. In addition to the lithography, we also investigated possible methods for large scale fabrication such as nanoimprint lithography and self-assembled structures. Most of the experimental work here was performed by colleagues and collaborators. My contribution consisted in pattern transfer and analysis of the nanoimprinted pattern and supervision and measurements for the self-assembled structures.

1.4. Structure of the thesis

This thesis is written as a collection of papers where the purpose of the text is to link the papers together and to put the work into a broader context. The content of the papers will not be explicitly repeated, but a short summary of all papers is given in section 1.5. The papers themselves are attached at the end of the thesis in chronological order.

The main section of this thesis is divided into eight chapters including the introduction. The content of chapters II-IV contains supporting information for understanding and motivation for the papers. The principles of, and motivation for, light trapping in

solar cells are explained in chapter II, succeeded by an overview of existing literature on periodic light-trapping structures. Chapter III deals with the optical theory describing light propagation in periodic structures. Here I also introduce the theory behind the simulation tools that we have employed. Chapter IV is closely linked to Chapter III and provides a more detailed overview of the actual modeling tools and methodology. I discuss the strength and weaknesses of the individual methods, why we have chosen them, and the validity of the results that accompany the method.

Chapter V deals with the experimental part of the thesis. Here the characterization and processing tools are described followed by a summary of the results that were obtained. This part of the thesis is not described in any of the papers, except for the part concerning self-assembled structures.

In chapter VI I discuss the main results from our papers and their relevance for the field of PV today. Here I also discuss the potential for large scale fabrication.

The last two chapters of the main section, chapter VII and chapter VIII contain conclusion and suggestions for further work.

The appendix contains mathematical details from the calculation of effective medium in the cylinder array.

1.5. Summary of papers

Here I will give a short summary of each of the papers and proceedings that are a part of this thesis. The papers and proceedings, from now on referred to as the papers, are attached in their entirety in chronological order at the end of the thesis. With the exception of **Paper VI**, where I am co-author, I have written and performed most of the work in all papers, with input from discussions with my supervisors. My contribution to **Paper VI**, which discusses experimental methods for synthesizing self-organized photonic crystals, relies mostly in discussions and input regarding how the photonic crystals should be designed to achieve attractive light-trapping properties.

Paper I *J. Gjessing, E.S. Marstein, A. Sudbø, "Modeling of light trapping in thin silicon solar cells with back side dielectric diffraction grating", presented at the 24th EU PVSEC, Hamburg, Germany, 21-25 Sept., pp. 2604-2607, 2009.*

In this paper we investigate a light trapping stack consisting of a bi-periodic cylinder structure separated from an Al reflector with a planar layer of silicon oxide. We study the effect of the thickness of the oxide layer on Si absorption and we show the influence of cell thickness on the maximum achievable light-trapping. We find for a 20 µm thick cell a potential improvement in total sunlight absorption of 15 % compared to a planar reference cell with similar anti-reflection coating and a rear Al reflector. This work was presented as a poster at the conference.

Paper II *J. Gjessing, E.S. Marstein, A. Sudbø, "2D back-side diffraction grating for improved light trapping in thin silicon solar cells", Optics Express, Vol. 18, Issue 6, pp. 5481-5495 (2010).*

In this paper we go further in the analysis of the cylinder array. We analyze the influence of grating thickness and oxide thickness on light trapping and explain the results using an effective medium approach for small lattice periods and a multilayer slab structure for large periods. The effect of lattice period and cylinder fill factor is calculated using rigorous numerical simulations and optimal grating dimensions are found. The effect of the oxide thickness on Si absorption and Al parasitic absorption is calculated, revealing an oscillating behavior for the Si absorption, but not in the Al absorption. Finally we study the behavior of the optimized grating structure under oblique incidence for both s and p-polarization.

Paper III *J. Gjessing, A. Sudbø, E.S. Marstein, "2D blazed grating for light trapping in thin silicon solar cells", oral presentation at the Optics for Solar Energy (SOLAR), Tucson Arizona, USA, 7-9. June 2010.*

In this paper we present one of our low-symmetry structures which we here called the 2D blazed structure (later named the rose structure). This structure showed significant improvement in light trapping compared to the cylinder structure we had described in earlier works. We showed that the light trapping from the 2D blazed structure corresponded to the light trapping in an eight times thicker planar Si wafer with an equivalent anti-reflection coating and rear metal reflector. The work was given as an oral presentation at the conference.

Paper IV *J. Gjessing, A. S. Sudbø, and E. S. Marstein, "A novel broad-band back-side reflector for thin silicon solar cells", EOS Annual Meeting, 26-28. Oct., Paris, France (2010).*

In this paper we present the initial results for the zigzag structure which shows light trapping exceeding Lambertian light confinement at normal incidence. We compare light trapping in the case of both an Al and Ag reflector. This work was given as an oral presentation at the EOSAM conference and a follow-up paper was published in J. Europ. Opt. Soc. Rap. Public. with a more comprehensive analysis of the structure.

Paper V *J. Gjessing, A. S. Sudbø, E. S. Marstein, "A novel back-side light-trapping structure for thin silicon solar cells", J. Europ. Opt. Soc. Rap. Public. 11020 Vol. 6 (2011).*

In this paper we analyze the zigzag structure in **Paper IV** in more detail. We explain the successful light trapping by the low symmetry of the structure and show that the lack of symmetry may be seen from its diffraction orders. Moreover, we analyze the light trapping at oblique incidence for both s and p-polarization at four different azimuth angles which corresponds to the different symmetry directions of the Brillouin zone.

Paper VI *E. Haugan, H. Granlund, J. Gjessing, E. S. Marstein, "Colloidal crystals as templates for light harvesting structures in solar cells", presented at E-MRS Strasbourg, symposium R, 2011.*

This paper addresses fabrication of 2D and 3D photonic crystals by self-organization of polystyrene and silica beads. The 2D photonic crystals were made by spin coating a colloidal solution onto a substrate while the 3D crystals were synthesized by evaporation of a colloidal solution. The 2D crystals were used as a mask for subsequent silicon nitride or Ag deposition. The nitride served as an etch mask while the Ag was used as a catalyst for etching vertical walls. The 3D crystals were infiltrated with titania and the polystyrene beads were removed by calcination. The 3D crystal exhibited reflection peaks that were blue shifted by the calcination step. My part in this paper was in discussions, in identifying suitable structure types, and in analysis of the measured reflectance spectra.

Paper VII *J. Gjessing, A. S. Sudbø, E. S. Marstein, "Comparison of periodic light-trapping structures in thin crystalline silicon solar cells", J. Appl. Phys. Vol. 110, 033104 (2011).*

In this paper we compare the light-trapping properties of bi-periodic structures consisting of cylinders, cones, dimples, and inverted pyramids together with three more complex structures with planes sloping in different directions. We compare the diffraction pattern of all structures and their calculated increase in optical thickness. The best structures are shown to be the ones with lowest symmetry, while the light-trapping behavior of the rest of the structures is quite insensitive to the shape of the unit cell. The structures are also compared at oblique angles of incidence, and their behavior is in part explained from the 2D grating equation which determines the number of propagating modes in Si and in the ambient at a given lattice period and incidence angle.

Paper VIII *J. Gjessing, A. S. Sudbø, E. S. Marstein, "Comparison of light trapping in diffractive and random pyramidal structures", presented at the 26th EU PVSEC, Hamburg, Germany, 5-9 Sept., section 3AV.3.3, 2011.*

In this paper we investigate by ray tracing light absorption in random pyramidal structures with different rear side reflector configurations. The rear side consists of a metal reflector made of either Al or Ag which may or may not be separated from the Si by a thin layer of silicon oxide. We compare light trapping from random pyramidal structures with light trapping from periodic structures in a 20 µm thick Si cell. We find that the best configuration of a double-sided random pyramidal structure exceed the best periodic structure. The difference is, however, only 0.3 mA/cm^2 and is due to the lower front surface reflectance of the pyramidal structure.

2. Solar cells and light trapping

In this chapter I will discuss light trapping in greater detail and give an updated summary of existing literature on periodic light trapping structures. First I will give a quick introduction to the operating principles of a solar cell.

2.1. The operating principle of a solar cell

A solar cell converts the energy of the solar irradiation directly to electricity using the photovoltaic effect. A sketch of a typical silicon solar cell is shown in Figure 2.1.1. An incident photon with sufficient energy may transfer enough energy to a bound electron so that it breaks free from the silicon lattice. The exited electron will leave an open position in the Si lattice, a hole, which may also move around in the lattice. The excitation process is known as creation of an electron-hole pair. The electron-hole pair will typically recombine within a time frame of microseconds to milliseconds, depending on material quality, unless the electrons and holes are extracted as current within this time. To aid this process the electron-hole pair is separated by a so called pn-junction which is usually situated close to the front side of the solar cell. The pn-junction is created by the controlled addition of small amounts of impurities, called doping, of boron and phosphorous. The boron doped part creates an excess of free holes and is called the p-type region, while the phosphorous doping creates an excess of free electrons and is called the n-type region. When incident photons create new electron-hole pairs, the electrons will diffuse toward the n-region while the holes will diffuse toward the p-region. This creates a voltage between the contacts at the front and the rear side of the solar cell which can be used for electric power production, as illustrated in Figure 2.1.1.

The solar spectrum contains a continuum of photon energies with a typical energy distribution as shown in Figure 2.1.2. Photons with an energy below the band gap energy, E_g, of the solar cell material, corresponding to longer wavelengths, does not have enough energy to excite electron-hole pairs. The absorbing material is actually transparent to these sub-band gap photons and their energy is not utilized. Photons with energy above the band gap, $E_{ph} > E_g$, may excite electron-hole pairs. However, any excess energy above the band gap, $E_{ph} - E_g$, will be lost as heat in the solar cell. Consequently, the energetic photons with short wavelengths are not fully utilized since only a given amount of the energy may be utilized. This is called thermalization loss. Figure 2.1.2 illustrates what part of the solar spectrum that may actually be utilized by a silicon solar cell.

The maximum conversion efficiency that can be achieved with a solar cell have been found by Shockley and Queisser [10] to be around 30 % for a solar cell with an ideal band gap energy under one sun illumination. The efficiency limit for Si solar cells is slightly below 30 % because Si has band gap energy lower than the ideal band gap energy and due

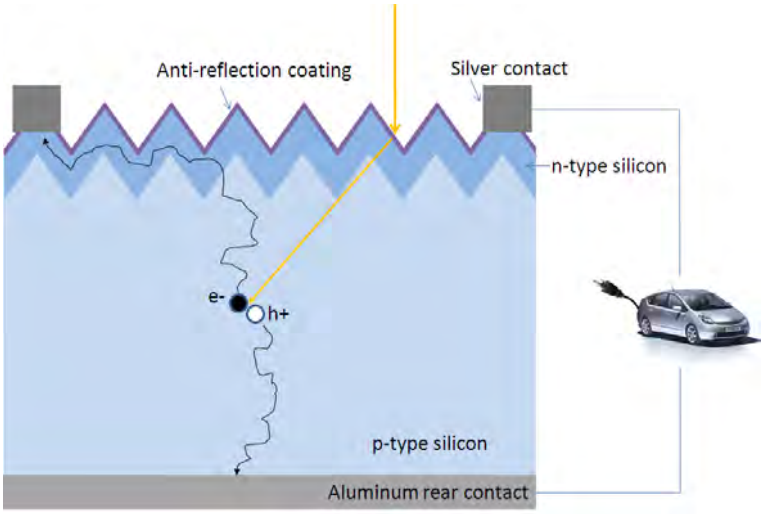

Figure 2.1.1.: A schematic picture of a typical silicon solar cell. Incident light creates an electron-hole pair named e- and h+, respectively. The electron diffuses towards the n-type region and to the front contacts while the hole diffuses towards the rear contact. The voltage between the two terminals may be used to drive a current through an external load.

to fundamental limitations in Si with inherent auger recombination. The best Si solar cell to date is a lab cell known as the PERL (passivated emitter, rear locally-diffused) cell with an efficiency of 24.7 % [11]. The highest efficiency for a multicrystalline cell is 20.4 % [12]. For solar modules, where multiple solar cells are connected and encapsulated, the efficiency record is 21.4 % for a commercial monocrystalline module and 17.8 % for a commercial multicrystalline module [12]. Typical efficiencies of standard commercial products are several percentage points below these records.

The Shockley-Queisser limit is a fundamental limitation for all solar cells composed of a single band gap material. Various concepts have been explored to exceed the Shockley-Queisser limit [14] and such concepts have been given the attractive name of third generation solar cells. The only successful third generation concept so far is the tandem cell which was discovered in the seventies. The tandem cell makes use of multiple solar cells with different band gaps stacked on top of each other. Due to the high cost of tandem cells they are usually operated under highly concentrated sunlight. They are therefore mounted on a double axis solar tracker and commonly need active cooling. Tandem cells have yielded efficiencies of up to 43.5 % [12] under high concentration. Despite continuously improved efficiency records for tandem cells lately, they still have an insignificant market share. Nevertheless, they are regarded to have a promising future and they remain an active area of research.

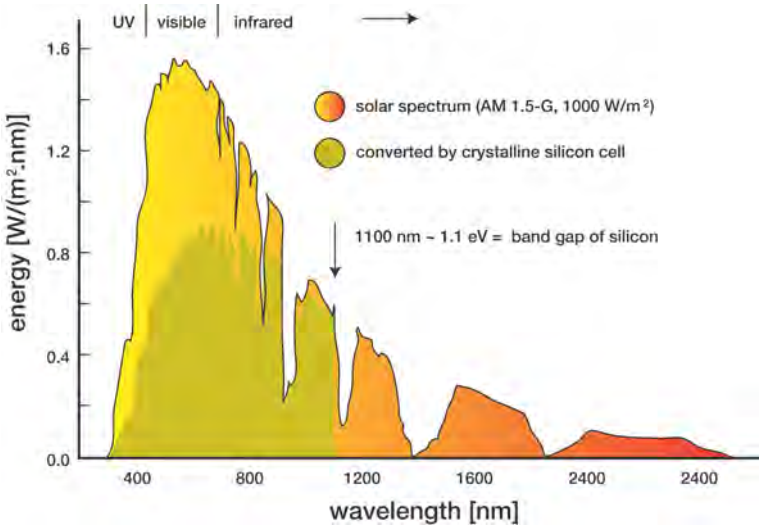

Figure 2.1.2.: The figure shows the AM1 1.5 solar spectrum together with the part the solar spectrum that may ideally be utilized by a silicon solar cell [13]. Long wavelength light does not have sufficient energy to excite an electron-hole pair and for short-wavelength light only a given amount of energy may be utilized.

2.1.1. Solar spectrum, short circuit current, and efficiency

The ultimate performance indicator of a solar cell is its efficiency, η. However, η does not reveal the specific strengths and weaknesses of the solar cell. The following parameters are therefore usually supplied in addition to the efficiency in a characterization of a solar cell:

- J_{sc}: short-circuit current density is the maximum current per unit area supplied by a solar cell with the terminals short circuited. Typical values for wafer-based silicon solar cells are 30-40 mA/cm^2. A high J_{sc} indicates good light absorption and low recombination.

- V_{oc}: open-circuit voltage is the maximum voltage over the terminals when no current is going through the external circuit. Typical V_{oc} values of a silicon solar cell are 600-700 mV. Low recombination, low series resistance, and high shunt resistance are among the factors that contribute to a high V_{oc}. In addition, V_{oc} scales with the logarithm of J_{sc}.

- ff: fill factor is the ratio of the current times voltage when the solar cell is working at its maximum power output to the product of J_{sc} times V_{oc}. A high ff indicates low series resistance and high shunt resistance and is a prerequisite for high efficiency solar cells.

The efficiency, η, is the product of these factors, as shown in Eq. 2.1.1:

$$\eta = J_{sc} V_{oc} ff \tag{2.1.1}$$

Standardized testing conditions require that the above values are measured with a power flux of 1000 W/m^2 and the AM 1.5 solar spectrum [15], which is shown in Figure 2.1.2.

J_{sc} can be calculated from Eq. 2.1.2:

$$J_{sc} = q \int_0^\infty \eta_c(\lambda) \Phi(\lambda) A(\lambda) d\lambda \tag{2.1.2}$$

Here q is the elementary charge, $\Phi(\lambda)$ is the spectral photon flux from the AM1.5 spectrum, $\eta_c(\lambda)$ is the collection efficiency, i.e. the probability that a generated electron-hole pair reaches its respective contacts, and $A(\lambda)$ is the spectral absorptance, i.e. the fraction of absorbed photons in the Si to the photons incident at the front side of the solar cell at a given wavelength. Note that Eq. 2.1.2 does not contain a term for reflection loss because this is already included in the definition of the spectral absorptance.

Because the optical properties are of primary interest in this thesis, I have set η_c equal to unity for all wavelengths. This reveals the maximum potential J_{sc} without making any assumptions about the electronic properties of the solar cell. The maximum potential J_{sc} therefore corresponds to the photo-generated current density J_{ph}. This is in line with the literature which commonly uses J_{sc} or J_{ph} for benchmarking of light-trapping structures.

The integration of Eq. 2.1.2 comprise all photon wavelengths, but in reality the integral is performed from 300 nm to around 1200 nm. The absorption above 1200 is negligible while the irradiance is too low below 300 nm to make a significant contribution to J_{sc}. The potential J_{ph} for a 400 µm thick Si slab is 44.7 mA/cm^2 assuming zero front-side reflectance and perfect Lambertian light trapping, which will be explained in more detail in section 2.2.1. For a 20 µm thick slab the potential J_{ph} is 41.3 mA/cm^2. For comparison the J_{sc} of a 24.7 % efficient PERL cell with a thickness of 400 µm has been measured to 42.2 mA/cm^2 [11].

In reality, several loss mechanisms will contribute to reduce J_{sc} below J_{ph}. Some of the most important ones are shadowing, free carrier absorption (FCA), and recombination as illustrated in Figure 2.1.3:

- Shadowing is caused by the front contacts that cover about 7-8 % of the solar cell surface of a typical wafer based Si solar cell. The loss due to shadowing may be reduced e.g. by using buried contacts, metal wrap through, or back-side contacted cells [16].

- FCA is the absorption of light by an already excited electron or hole. The energy of this absorption process will be dissipated as heat in the solar cell. FCA is dependent on the number of excited electrons and holes which again is determined by the doping levels and therefore varies with cell configuration. FCA is wavelength dependent and may be calculated with simple empirical formulas for moderately doped Si [17] or from first principles for heavily doped Si [18].

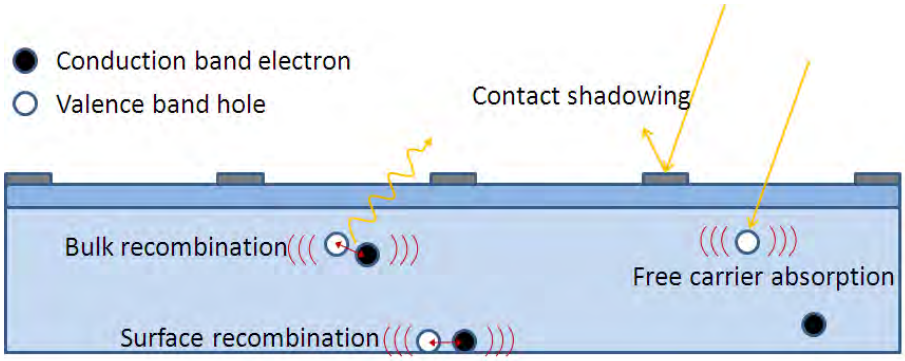

Figure 2.1.3.: The figure illustrates shadowing, free carrier absorption (FCA), and recombination, all mechanisms inherent in a real solar cell that will reduce the J_{sc} below its maximum potential. Energy lost in FCA or recombination is transformed to heat in the solar cell. Bulk recombination may either be in the form of a photon emitted through radiative recombination or in the form of heat through auger or Shockley-Read-Hall (SRH) recombination. Surface recombination is of the SRH-type.

- Recombination within the solar cell, or at the front-side or back-side surface inhibits the electron-hole pairs from reaching their respective contacts. This results in a collection efficiency, η_c, below unity. In a thin solar cell the electron-hole pairs will have a short distance to their respective contacts and the bulk recombination loss will be lower than in a thicker solar cell. However, back-side passivation is much more important in thin solar cells because the light will be absorbed closer to the back side.

2.2. Light trapping

Solar cells are made continuously thinner to reduce material consumption and thereby lower the cost of PV. Silicon solar cells today have a thickness of around 160-200 µm. At least another 100 µm of Si material is lost in the process of sawing the wafers out of a block, so called kerf loss. A reduction of thickness may actually also be advantageous with regards to efficiency. Thin solar cells have the advantage of a lower demand on material quality. On the other hand, they also have a more severe demand on surface passivation. Maximum theoretical efficiency is achieved at 80 µm for a solar cell with Lambertian light trapping and zero surface passivation, but conversion efficiencies well above 20 % is still possible down to a thickness of 1 µm [19].

Reducing wafer thickness and kerf loss from sawing is an ongoing research area and the PV industry's road map has a target wafer thickness of 100 µm by 2020 [20]. On the other hand several alternative routes have been suggested to fabricate very thin layers of

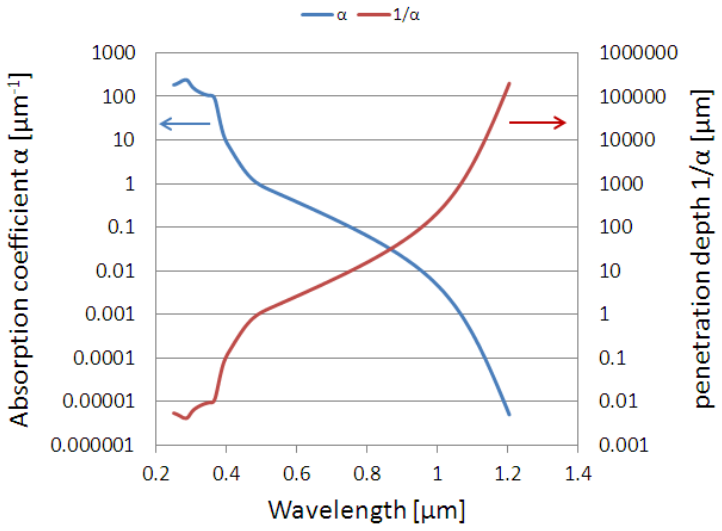

(a)

Figure 2.2.1.: Absorption coefficient α and penetration length $1/\alpha$ for silicon with data from [28].

Si. These includes deposition by CVD and LPCVD [21], porous silicon cleaving [22, 23], exfoliation of thin Si films from thicker wafers [24], and cleaving by ion implantation, also known as the proton knife [25, 26, 27]. These techniques have been demonstrated to produce Si thicknesses down to and below 20 µm, and at the same time they do not have the kerf loss associated with the sawing process.

Light trapping is essential to realize the potential of thin Si cells with a high efficiency. The need for light trapping is easily understood by considering the absorption coefficient, α, of silicon (Si) shown in Figure 2.2.1. Since Si is an indirect band-gap semiconductor, the absorption of a photon near the band edge requires a simultaneous creation or annihilation of one or several phonons. This requirement reduces the probability of an absorption event and makes Si a poor absorber compared to the direct band-gap absorbers commonly used for thin-film solar cells. The absorption of light near the band edge is very low and at 1.1 µm the penetration depth, $1/\alpha$, is several millimeters, a factor 10 above the typical cell thickness used today.

The relation between the absorption coefficient, α, and the imaginary part of the refractive index, k, also known as the extinction coefficient, is shown in Eq. 2.2.1:

$$\alpha = \frac{4\pi k}{\lambda} \tag{2.2.1}$$

The light intensity, I, decays exponentially with propagation length, t, in a linear absorbing material. This is known as the Beer-Lambert law:

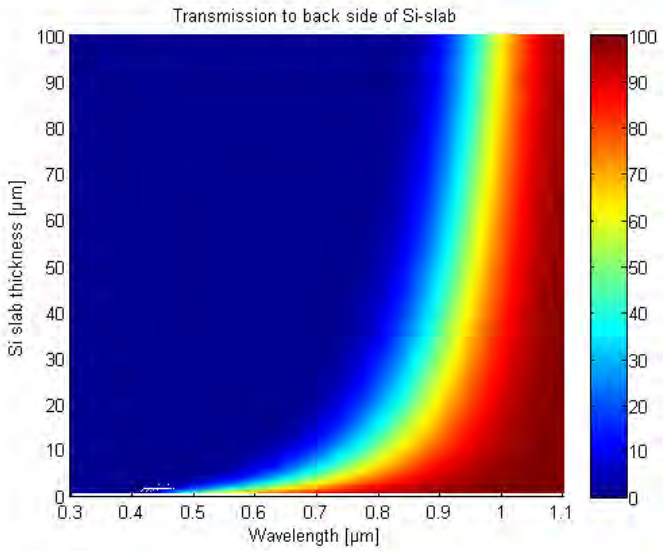

(a)

Figure 2.2.2.: Transmission of light through a silicon slab as a function of wavelength and silicon thickness. The color bar indicates the percentage of light that is transmitted through a given thickness.

$$I(x) = I_0 e^{-\alpha(\lambda)x} \tag{2.2.2}$$

Here I_0 is the intensity at $x = 0$. The surface plot in Figure 2.2.2 shows transmission, i.e. I/I_0, of light through Si as a function of wavelength, λ, and Si, x, thickness according to Eq. 2.2.2. The color bar indicates the percentage of light that reaches a certain thickness at a given wavelength. The Si slab functions as a spectral filter so that the wavelength spectrum at the rear side will be significantly reduced compared to the front side. A back-side light-trapping structure will therefore only need to be designed for the wavelengths that are transmitted through the Si slab.

A planar Si slab is a poor light absorber. The planar Si surface will reflect more than 30 % of the incident light, which comes in addition to poor absorption in the infrared part of the spectrum. Textures and anti-reflection coatings (ARCs) are usually applied to the Si slab to increase absorption. The textures and the ARC will reduce front-side reflectance. In addition, the textures scatter light and increase the path length inside the Si and thereby improve light absorption.

An unfortunate side effect of texturization is the resulting increase in surface area which leads to an increase in surface recombination. The surface area of the commonly used pyramid texture is about 1.7 times larger than for a planar surface and a similar increase in surface recombination could be expected. However, the presence of a surface texture exposes various crystal planes and sharp edges. This makes surface passivation more difficult and the increase in surface recombination from a textured surface is usually

higher than just the increase in surface area [29]. A reduction of the solar cell thickness will result in a higher generation rate of electron-hole pairs close to the back side. Consequently, the passivation of the back side will become more important the thinner the solar cell. A light-trapping configuration designed for a thin solar cell should therefore incorporate a proper surface passivation.

Most solar cells are expected to last for at least 25 years in the field and to achieve this they are encapsulated in a solar module with a protective glass on the front side. The glass is usually optically coupled to the solar cell with a lamination material with a refractive index similar to that of glass, e.g. the polymer material ethylene-vinyl acetate (EVA). The transition in refractive index from Si, n_{Si}, to glass, n_{glass}, is less than that from Si to air and the ARC must be optimized for the new interface. The ARC in a solar module should ideally have a refractive index $n_{arc} = \sqrt{n_{glass} n_{Si}}$ [14], and an optical thickness of a quarter of the target wavelength. Reflection from the solar cell surface will in general be lower when the solar cell is encapsulated than for an unencapsulated solar cell due to the reduced step in refractive index. However, the interface between air and glass has a reflection of about 4 % which comes in addition to the light reflected from the solar cell surface. The combined reflection from a solar module is therefore usually higher than for an unencapsulated solar cell unless the glass is textured or coated with an ARC.

2.2.1. Lambertian light trapping

Surfaces that randomize light are known to be well suited for light trapping [30, 31]. In fact, Yablonovitch [32] showed that an ideal Lambertian surface will provide the best light trapping possible in a slab type geometry using geometrical optics considerations. A Lambertian surface has the property of looking equally bright at all view angles, i.e. it has a constant radiance, independent of the position of the illumination source.

A Lambertian light trapping scheme has been shown to yield a path length of $4n^2W$ inside a slab of thickness W and refractive index n in the limit of weak absorption, i.e. for $\alpha W << 1$. For Si this translates to a path length enhancement of about 50 times the actual thickness of the solar cell. Due to the isotropic response of the Lambertian surface this path length enhancement is independent of incidence angle and therefore also holds for isotropic illumination. It should be noted that light-trapping may in theory even exceed the Lambertian limit for other types of structures by limiting the angle of incidence [32]. The Lambertian limit is commonly referred to as the Yablonovitch limit, $4n^2$ limit, or ergodic limit.

The excellent light trapping displayed by a Lambertian surface in a Si slab is attributed to the narrow escape cone of Si. Only light which is not totally internally reflected may escape from the Si to air. This is demonstrated in Figure 2.2.3 for a rear side Lambertian reflector and a planar front side. The escape cone has a half angle, θ_c, which can be determined from the critical angle of internal reflection given by Snell's law of refraction:

$$n_i sin(\theta_i) = n_o sin(\theta_o) \tag{2.2.3}$$

Here θ_i is the angle between the incident light and the surface normal while θ_o is the

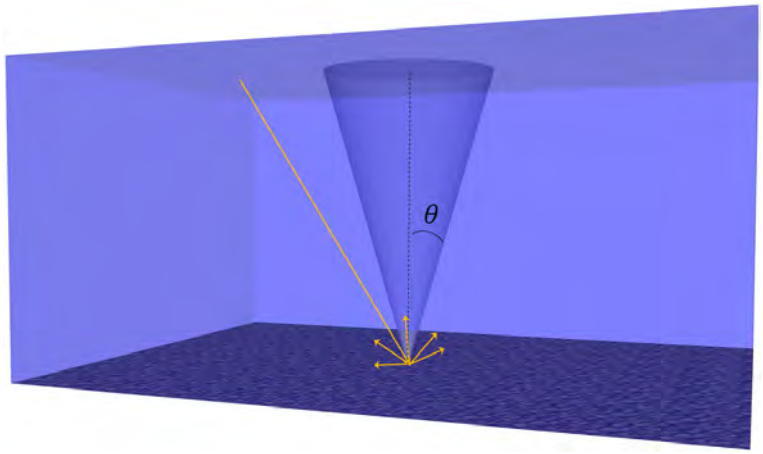

Figure 2.2.3.: Light incident on a textured rear surface after a total internal reflection at the front surface. Only light scattered within a narrow escape cone may leave the Si when reaching the front side. The half angle of the escape cone is about 16 degrees for Si.

corresponding angle of the outgoing light. The refractive index where the light propagates is denoted n_i for incident light and n_o for outgoing light. For reflected light $n_i = n_o$ and $\theta_i = \theta_o$. From Eq. 2.2.3 one can find that Si, with $n = 3.6$, will have a critical angle of internal reflection from Si to air of $\theta_c = sin^{-1}(1/3.6) \sim 16$ degrees. An integration over the escape cone reveals that a Lambertian surface will scatter only a fraction of $1/n^2$ into the escape cone. This implies that only a small part of the light will escape through the front surface for each reflection. In fact, the escape probability is the same also for a textured surface as it is related to difference in phase space inside and outside the material [32]. A series expansion using this escape probability results in a path length enhancement close to $4n^2$.

Even though materials with properties close to that of ideal Lambertian surfaces are used as reflection standards in most optical characterization labs, such a reflector has not yet been demonstrated in Si, although several attempts have been made [33, 34]. Some of the challenges in making such a randomizing structure are the wide spectral range that must be covered and that the available thickness of the Lambertian layer is often limited in a solar cell. An inviting option would be to place a standard Lambertian reflector on the rear side of the solar cell. Unfortunately, as long as the reflector is not optically coupled to the Si material such a scheme would result in a focusing of the Lambertian distribution upon entering the solar cell, as follows from Eq. 2.2.3. It has been shown that even a slight focusing of the Lambertian distribution will result in light trapping significantly below the Lambertian limit [35].

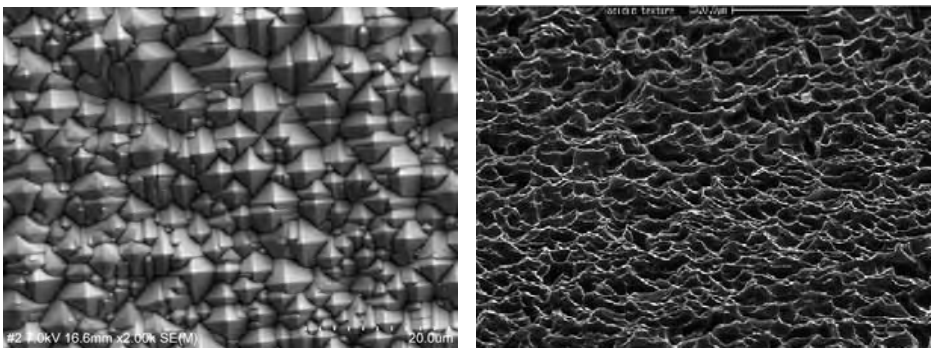

(a) (b)

Figure 2.2.4.: Scanning electron microscope image of the surface texture of a monocrystalline Si wafer after KOH etching at IFE (left). The surface consists of a random pattern of pyramids with well-defined facet angles. The texture of multicrystalline Si after isotropic etching consists of a random dimple-like structure (right) [37].

2.2.2. Conventional light-trapping structures

Light trapping in wafer-based Si solar cells today is achieved by front of double-sided texturing of the wafer. The type of texture usually depends on whether the Si material is monocrystalline or multicrystalline.

The texturing of a monocrystalline Si wafer is performed with an anisotropic alkaline etch, typically KOH [36]. Since the {111} planes etch much slower than the rest of the atomic planes, the result is a random pattern of pyramids where the {111} planes constitute the pyramid walls. Figure 2.2.4 (left) shows a scanning electron microscope (SEM) image of such a pattern of random pyramids. The angle of the pyramid facets are well defined with an angle of 54.7 degrees, determined by the crystal structure of Si. It must be emphasized that such structures are only possible for [100] oriented wafers. Technologies based on cleaving, which may provide very thin Si wafers [25], do not result in [100] oriented wafers and consequently a different type of texture is necessary for such wafers.

The typical size of the pyramids resulting from the alkaline etching is in the range of 1-10 µm, depending on etching time and concentration. The pyramid structure is well suited for reducing front-side reflectance because the light reflected at the first bounce will always get a second chance of entry as it hits the pyramid wall on the opposite side, as shown in Figure 2.2.5. Actually, inverted pyramids provide even lower reflectance because a larger fraction of the light will also experience triple bounces [38, 39]. The world record cell, PERL, used inverted pyramids on the front side to keep reflection losses at a minimum [11]. Inverted pyramids are, however, expensive to make as they currently are made using photolithography.

Multicrystalline Si has randomly oriented grains and an alkaline etch will therefore create pyramids with a random orientation. Several pyramid orientations will not yield

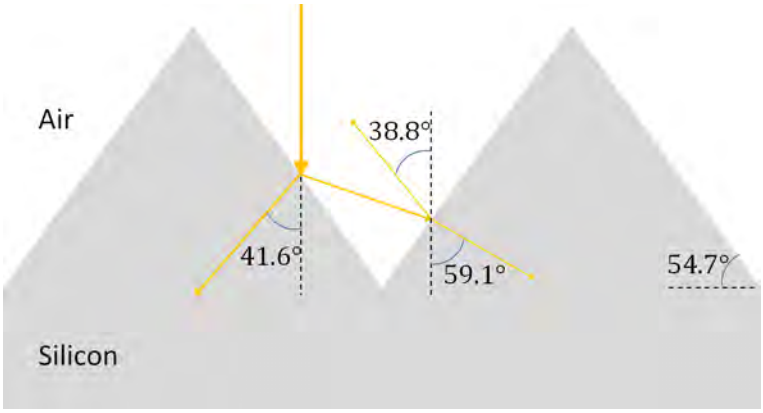

Figure 2.2.5.: Light incident on a pyramidal structure will have at least two chances of transmission into the Si. In combination with an anti-reflection coating this structure may yield a very low front-side reflection.

the double bouncing shown in Figure 2.2.5 and reflection from these areas will be close to the reflection from a planar surface [40]. Additionally, the different grains will have uneven etch rates resulting in steps between the grains that may complicate further processing. Isotropic acidic etching is therefore more commonly used for texturing of multicrystalline Si. Isotropic etching results in a lower reflection than alkaline etching of a multicrystalline wafer [37], but still significantly higher than for a monocrystalline wafer textured with pyramids. The isotropic etching makes use of the saw damage from the wafering process as a seed for the etching.

Texturization is primarily performed to reduce the front-side reflectance of the Si wafers, and secondary to increase light trapping by scattering the light into oblique paths. The light-trapping properties, however, could be even better. Therefore, several authors have investigated more advanced geometric light-trapping structures. These structures include bi-pyramids, perpendicular slats, patch pattern [41], and various types of prisms [42, 43]. Common for these structures are that they may exhibit better light confinement than the random pyramids, but naturally, fabrication is more complex.

Thin-film solar cells are made by depositing the active solar cell material on to a substrate or superstrate. Thin-film solar cells are usually made from direct band-gap materials which imply that their absorption is much better than for crystalline Si. The electronic quality of such films is usually much lower than for crystalline Si, and consequently, a thin layer is necessary to avoid high recombination losses. The thickness of a thin-film solar cell may range from less than 500 nm to several microns depending on the material. Due to the small thickness of these solar cells, light trapping is important in several types of thin-film solar cells despite their direct band gap.

Texturing of thin-film solar cells is most often performed by texturing the superstrate or substrate prior to deposition. One commonly used procedure is to deposit a transparent conducting oxide (TCO) on the front glass and to create a sub-micron random surface texture in the TCO [44, 45]. A challenge for such small structures is that they need to

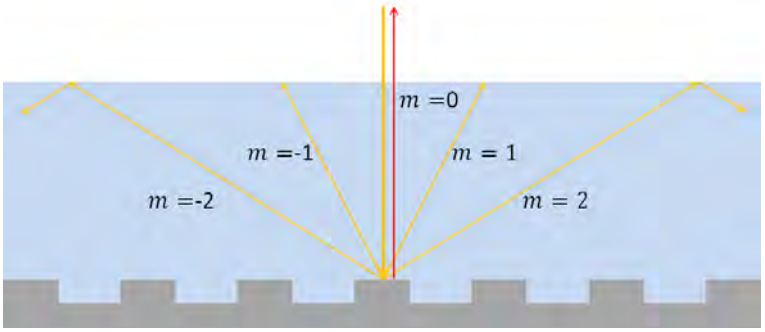

Figure 2.2.6.: Light diffracted by a periodic structure increases the path length inside the absorbing solar cell material. Total internal reflection at the front surface will further increase the path length.

have a low front-surface reflection for all wavelengths and at the same time scatter long wavelengths effectively to improve the light trapping.

2.2.3. Periodic light-trapping structures

Periodic structures with lattice periods comparable to the wavelength of light do not obey the laws of geometrical optics. Such periodic structures, also known as photonic crystals, are described using the wave nature of light which yields many interesting properties that are not encountered in geometrical optics. The photonic crystal may have one, two or three dimensional periodicity and serve different purposes in a solar cell. One type of application is the use of a periodic structure along the surface of a solar cell, as shown in Figure 2.2.6. The surface structure will diffract light and the angles of the diffracted light may be tuned by adjusting the lattice period. This improves light absorption by increasing the path length of light inside the absorbing material. The gratings may be periodic in either one dimension (uniperiodic or 1D) or two dimensions (bi-periodic or 2D). Such periodic structures are often referred to as gratings or diffractive structures.

The use of periodic structures to improve light trapping in solar cells was suggested already in 1983 by Sheng et al. [46]. They showed a potential gain in light trapping from a periodic structure compared to both a planar surface and a randomizing surface. Heine et al. [47] later showed through numerical simulations that the use of a blazed grating, shown in Figure 2.2.7 (bottom left), could improve the light-trapping efficiency compared to a symmetric binary grating, shown in Figure 2.2.6. They attributed the improved light trapping to a reduction in out-coupling of light due to the asymmetry of the blazed grating. Out-coupling is the process where propagating modes inside a material couples to propagating modes in the ambient.

Periodic structures that aim to diffract light and increase the path length inside an absorbing material may be applied to the back side [46, 47, 48, 49, 50, 51, 52, 53, 54, 55, 56], to the front side [47, 57, 58, 59, 60], and to both sides [61, 62, 63, 51, 64, 65], as illustrated in Figure 2.2.7. In fact, some designs even feature periodic structures all the way through the absorbing material [66, 60]. The advantage of a front-side structure

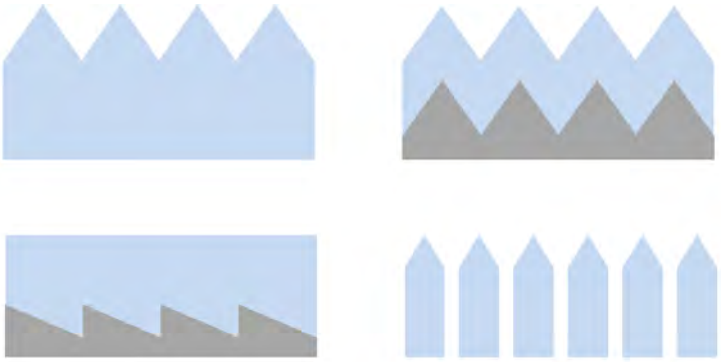

(a)

Figure 2.2.7.: Different approaches to placement of light trapping structures. The periodic structures may be applied to the front side (top left), both sides (top right), rear side (bottom left), and they may even penetrate all the way through the absorbing material (bottom right). The back side structure is here shown using a blazed grating.

is that both anti-reflective properties and light trapping may be achieved with the same structure. Back-side structures on the other hand need only to be optimized for light trapping and not for anti-reflection, and more importantly, back-side structures may be optimized for a more narrow spectral range. The width of the spectral range is determined by the thickness and spectral absorption of the solar cell which acts as a short wavelength filter (see Figure 2.2.2). A 20 µm thick Si slab will absorb most of the light below 800 nm before it reaches the back side. Therefore, the back-side periodic structure needs only to be optimized for the wavelength range from 800-1100 nm, which corresponds to a bandwidth $\triangle\lambda/\lambda$ of about 30 % .

A particular challenge for periodic back-side structures is the induction of parasitic absorption in the rear-side metal contact, which also serves as a reflector. In conventional low-cost industrial solar cells today, the back-side contact is produced by screen printing aluminum (Al) on the back side of the Si. The absorption of such a Si-Al boundary may be several tens of percent even for a planer boundary. Periodic structures in the rear metal reflector may induce surface plasmons in the metal leading to a significant increase in parasitic metal absorption [67]. Parasitic absorption is also a problem if silver is used as a reflector material [68], even though silver has a much higher reflectance than Al. To avoid parasitic absorption all together, diffraction gratings have been combined with dielectric reflectors in the form of Bragg stacks [48, 51, 50]. Yet another approach, which we apply in this work, is to separate the grating from the metallic rear reflector by a dielectric layer with a low refractive index. This layer needs to be sufficiently thick, typically more than 100 nm, so that evanescent waves from the grating do not couple to the metal. By choosing the thickness of this layer properly, it may act together with the grating to enhance coupling of light to obliquely propagating modes inside the absorbing material as we discuss in **Paper II**.

Combined front-side and back-side gratings are commonly found in thin-film solar cells where the absorbing material is deposited onto a patterned substrate [61, 64, 69]. Due to the small thickness of the thin-film solar cells the pattern will also be visible on the surface of the deposited materials. The quality of the grating, however, will be reduced with the number and thicknesses of the deposited layers [64]. The use of front-side and back-side structures with different lattice period and lattice geometry gives additional degrees of freedom [51], although at the cost of increased complexity.

Studies of periodic structures include both 1D [46, 47, 51, 65, 52, 70] and 2D [48, 50, 60, 59, 71] periodic structures. 1D gratings have the advantage that they are less complex and therefore potentially easier to fabricate. 2D gratings, on the other hand, have the advantage of targeting both s and p-polarized light, in contrast to 1D gratings which usually have a higher efficiency for one polarization. Moreover, 2D gratings allow coupling to more diffraction orders which have recently been shown to result in a higher theoretical potential for light trapping [72, 59]. This was already suggested by Sheng et al. [46] in 1983.

The theoretical potential for light trapping in periodic structure is an important discussion. Earlier work has suggested that light trapping with periodic structures may exceed the Lambertian limit for a limited spectral region [46, 73]. However, as the solar spectrum is a broad-banded source, it is unclear whether periodic structures have the potential of exceeding the Lambertian limit over a wider wavelength range. It has been shown that an improvement over that of the Lambertian limit may be obtained for very thin cells, i.e. tens of nanometers, over the whole solar spectrum [74]. However, due to the small thickness, the overall absorption in such a slab is still very low. Ref. [72] discussed the case of a periodic structure by considering only the power inherent in each diffraction order, neglecting other resonances within the slab. They found that for a periodic structure the path length could be increased beyond that of the Lambertian limit, but only for a narrow angle of incidence and wavelength range. They concluded that the Lambertian limit was still valid for isotropically incident light. Ref. [59], on the other hand, found that the Lambertian limit no longer holds for absorbing materials with a thickness comparable to the wavelength of light, or for periodic structures with lattice period comparable to the wavelength of light and a thickness of a few microns. They showed in numerical examples that the Lambertian limit could be exceeded, but with a significant angular dependency.

Recent numerical results have shown periodic structures exceeding Lambertian light trapping at near normal incidence ([59, 60] and **Paper V**). The key for these structures has been the use of low symmetry structures with a lattice period slightly lower than the target wavelength. This lattice period allows several discrete modes inside the Si-slab without any escaping modes except for the zero order. The low symmetry of the grating allows coupling also to non-symmetric modes [75] and reduces the probability of out coupling.

Experimental results for light trapping using periodic structures are also reported in the literature. Both thin-film Si solar cells [61, 64, 49, 76, 77] and thin film organic solar cells [69, 78] have been fabricated with periodic structures. Direct comparison between experimental results and simulation results has been shown for a 2 µm thick crystalline

Si solar cell [52]. The experimental results were lower than expected, but followed the trends of the numerical results [52]. The same observation was also reported elsewhere [79] for a proof-of-concept structure. Recently a periodic plasmon structure has been shown to exceed the light trapping of an Asahi U-type structure [76], which is the thin-film industry standard. Another group arrived at a similar result with a periodical dimple structure with a hexagonal pattern made by anodic oxidation [49, 71].

Periodic light-trapping structures have also been shown to improve light trapping when applied to the back side of a wafer based Si solar cell [55, 56]. The periodic structure provided a slight improved in light trapping when applied to the back side of solar cell with a random pyramid texture on the front side. A periodic structure with light trapping exceeding the Lambertian limit over an extended wavelength range has not been experimentally demonstrated yet.

2.2.3.1. Fabrication

New light-trapping structures provide new challenges and possibilities with respect to fabrication. Most light-trapping structures today are made with a large-area wet-etch approach requiring no spatial alignment. The record PERL cell [80] was made using inverted pyramids on the front side defined with photolithography. Photolithography, however, is regarded to be too expensive to be used in solar cell production. Concentrator solar cells and solar cells for space applications, where cost per area is less critical, might be an exception.

No methods are in use today to make periodically patterned solar cells for commercial purposes. However, several potential fabrication methods exist and are being investigated for this purpose. Some of these include nanoimprint lithography (NIL) or hot embossing [57, 64, 81, 69] and interference (holographic) lithography [57, 82, 61]. The same technology used for patterning Blu-ray discs has also been investigated as a means of creating periodically textured structures [64]. Self-assembled structures are another interesting approach to fabrication. Self-assembly describes structures that are fabricated without the need for controlling the individual structural components. Examples of such fabrication methods are the use of monodispersive spheres as a mask for etching or deposition as in Refs. [83, 55] and **Paper VI**, and anodic etching resulting in a self-assembled dimple pattern [49].

If new light-trapping structures are to become commercially acceptable, the improvement in efficiency must outweigh a potential increase in cost. The solar cell process step accounts for about 1/3 of the total cost of a solar module, which again accounts for a bit more than half the cost of a fully installed solar energy system. Increased costs of the solar cell processing step may therefore be acceptable as long as it results in an increase in efficiency or a reduced cost of the other processing steps.

3. Theory

This chapter deals with the optical theory describing light propagation in a material with a periodic variation in permittivity. I also describe the fundamental theory behind the simulation tools and models that I have used in my thesis.

3.1. Photonic crystals

Photonic crystals are materials that exhibit a periodic variation in the permittivity with a lattice period in the same order of magnitude as the wavelength of light. The material can be periodic in one, two, or three dimensions. Such structures may exhibit photonic band gaps, i.e. directions where light in a given frequency interval is not allowed to propagate. The most familiar one dimensional photonic crystal is the Bragg-stack. Alternating layers of high and low refractive index materials, where each layer has an optical thickness of a quarter of a wavelength, creates a photonic band gap. A larger contrast in refractive index leads to a wider band gap. This is commonly used to make dielectric mirrors with a reflection coefficient close to unity. A photonic crystal which is periodic in three dimensions may exhibit a band gap in all directions for a certain frequency interval. This is known as a full photonic band gap [84].

The concept of photonic crystals was introduced in 1987 independently by Yablonovitch and by John [9, 85] although photonic crystals in the form of Bragg mirrors have been known for the last century. The field of photonic crystals has since seen numerous applications which include resonators, waveguides, highly dispersive materials, nonlinear effects, controlling spontaneous emission, and negative index materials [84].

From the Maxwell equations for a linear isotropic loss-less nonmagnetic material the governing equation of photonic crystals may be derived by decoupling the Maxwell equations into the electric field, $\mathbf{E}$, and the magnetic field, $\mathbf{H}$ [84]:

$$\nabla \times \left(\frac{1}{\epsilon_r(\mathbf{r})} \nabla \times \mathbf{H}(\mathbf{r}) \right) = \left(\frac{\omega}{c} \right)^2 \mathbf{H}(\mathbf{r}) \tag{3.1.1}$$

Here c is the speed of light in free space, ω is the angular frequency of light, $\mathbf{r}$ is the position, and $\epsilon_r(\mathbf{r})$ is the position dependent relative permittivity. The electric field, $\mathbf{E}$, can be found from $\mathbf{H}$ through their coupling in the Maxwell equations. Eq. 3.1.1 is a Hermittian eigenvalue problem, implying that the eigenmodes of this equation forms a complete basis of solutions. An important property of Eq. 3.1.1 is that it is scale invariant. In other words, the eigenmodes and eigenfrequencies, and thereby also any band gap, may be tuned by changing the periodicity of ϵ_r.

It can be shown that [84] solutions to Eq. 3.1.1 may be written as Bloch states, $\mathbf{H}_\mathbf{k}$:

$$\mathbf{H_k}(\mathbf{r}) = e^{i\mathbf{k}\cdot\mathbf{r}}\mathbf{u_k}(\mathbf{r}) \tag{3.1.2}$$

The Bloch wave, $\mathbf{u_k}$, is periodic, i.e. $\mathbf{u_k}(\mathbf{r}) = \mathbf{u_k}(\mathbf{r}+\mathbf{R})$ where $\mathbf{R}$ is the fundamental lattice vector. Since there are no points of special significance in the infinitely repeating lattice of the photonic crystal, the electromagnetic field must also be periodic. Eq. 3.1.2 may be interpreted as a plane wave modulated by a periodic function with a period equal to that of the permittivity, $\epsilon_r(\mathbf{r})$. For a given Bloch vector, $\mathbf{k}$, there is a complete basis of Bloch states, each state with its own frequency. The complete basis describes the field inside one unit cell of the photonic crystal.

Eq. 3.1.1 may be solved by inserting the Bloch states and a Fourier expansion of $1/\epsilon_r$ into Eq. 3.1.1, and applying the appropriate boundary conditions. The procedure is explained in more detail in [84]. This may be used to calculate the band diagram, i.e. the dispersion relation, of the photonic crystal. The band diagrams reveal many of the interesting properties of the photonic crystal. Furthermore, the electromagnetic field patterns inside the photonic crystal may also be calculated in this way. I will return to some commonly used computation methods later in this chapter.

The equations that are used for calculating the optical properties of a photonic crystal usually rely on the assumption of infinite spatial extension of the photonic crystal. Defects, such as a surface, will break the periodicity of the crystal and may induce new modes close to the defect. Such modes will be spatially confined to the defect and decay exponentially when moving away from the defect. These modes are known as evanescent modes. In most cases the results obtained for idealized crystals may be used to predict the properties also for finite photonic crystals.

3.2. The grating equation

It is well known that monochromatic light incident on a material with a periodic modulation in refractive index will be diffracted into a finite number of directions, called diffraction orders. The directions of the diffracted orders are independent of the geometry of the modulation and depend only on the ratio of the lattice period to the wavelength of light. This property is commonly used in spectroscopy to separate light into its spectral components. Diffraction from a 1D diffraction grating is illustrated in Figure 3.2.1.

The directions of the diffraction orders are determined by the allowed momentum changes for the incident light, which again are determined by the reciprocal lattice vector. Consider a plane wave with wave vector $\mathbf{k}_\mathrm{i}$ incident on a diffraction grating with lattice period Λ. The incident wave vector, with a polar angle θ_i and azimuth angle ϕ_i, as defined in Figure 3.2.2, can be written in the following way:

$$\mathbf{k}_i = \frac{2\pi n_i}{\lambda}\left\{sin(\theta_i)cos(\phi_i)\underline{\hat{\mathbf{x}}} + sin(\theta_i)sin(\phi_i)\underline{\hat{\mathbf{y}}} + cos(\theta_i)\underline{\hat{\mathbf{z}}}\right\} \tag{3.2.1}$$

Here λ is the free-space wavelength, n_i is the refractive index of the incident medium, and $\underline{\hat{\mathbf{x}}}$, $\underline{\hat{\mathbf{y}}}$, and $\underline{\hat{\mathbf{z}}}$ are orthogonal unit vectors in the Cartesian coordinate system.

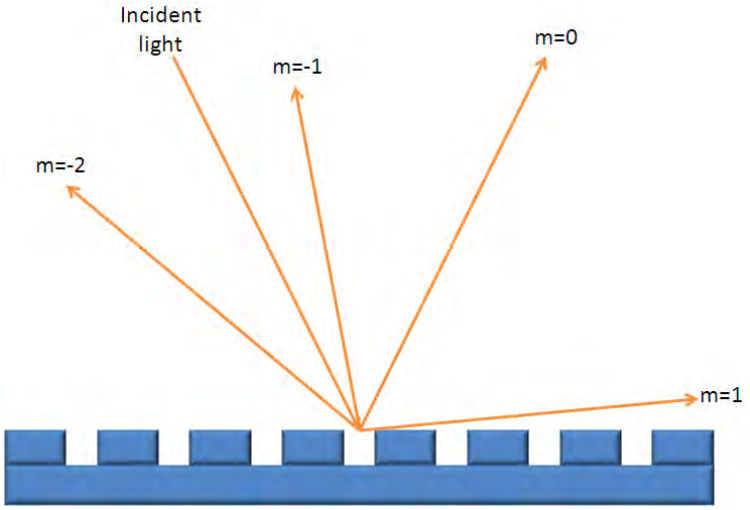

(a)

Figure 3.2.1.: Diffraction from a 1D periodic structure. Incident light is diffracted into a finite number of well defined directions depending on the ratio of the lattice period to the wavelength. The zero diffraction order ($m = 0$) corresponds to specular reflection.

According to Bloch's theorem, interaction with the grating will allow the wave vector to change by an integer value, m, of the reciprocal lattice vector $2\pi/\Lambda$, in the direction of periodicity. Here I limit the discussion to the case of a bi-periodic grating with orthogonal lattice periods. A discussion of a bi-periodic grating with non-orthogonal periodicity may be found in [86]. The outgoing wave vector, $\mathbf{k}_o$, may be diffracted in either the x or the y direction according to the following equation:

$$\mathbf{k}_o = \frac{2\pi n_o}{\lambda}\left\{\left(\frac{n_i}{n_o}sin(\theta_i)cos(\phi_i) + \frac{m_x\lambda}{n_o\Lambda_x}\right)\underline{\hat{\mathbf{x}}} + \left(\frac{n_i}{n_o}sin(\theta_i)sin(\phi_i) + \frac{m_y\lambda}{n_o\Lambda_y}\right)\underline{\hat{\mathbf{y}}} + cos(\theta_o)\underline{\hat{\mathbf{z}}}\right\} \tag{3.2.2}$$

The subscripts i and o denotes incidence and outgoing respectively, and m_x and m_y are integers denoting the diffraction order in the x and y direction. For reflection gratings $n_i = n_o$ so the factor $\frac{n_i}{n_o}$, from Snell's law of refraction, can be ignored for reflection gratings and for transmission gratings if the incident medium has the same refractive index as the outgoing medium. If the size of the x and y components of $\mathbf{k}_o$ exceeds $|\mathbf{k}_o|$, the corresponding diffraction order will be a non-propagating evanescent wave. The following inequality therefore determines the allowed number of propagating diffraction orders:

$$\left(\frac{n_i}{n_o}sin(\theta_i)cos(\phi_i) + \frac{m_x\lambda}{n_o\Lambda_x}\right)^2 + \left(\frac{n_i}{n_o}sin(\theta_i)sin(\phi_i) + \frac{m_y\lambda}{n_o\Lambda_y}\right)^2 \leq 1 \tag{3.2.3}$$

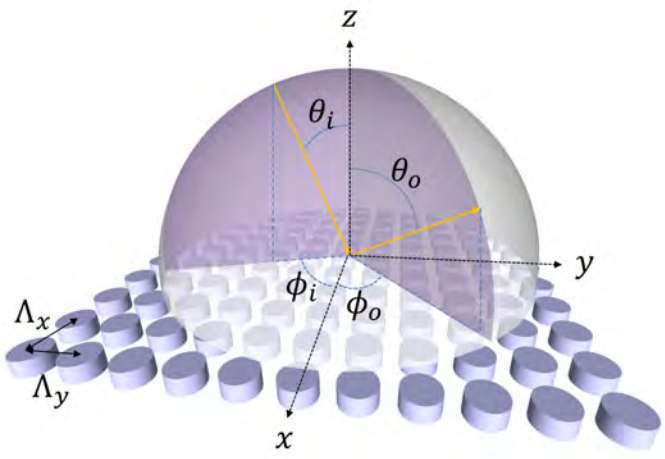

(a)

Figure 3.2.2.: The figure illustrates the angles involved in diffraction from a bi-periodic grating. The grating allows a change in momentum for the incident wave vector equal to a multiple of the reciprocal lattice vector. The fact that the magnitude of the wave vector must be constant, i.e. the energy is conserved, limits the number of allowed diffraction orders. The constant magnitude of the wave vector is illustrated in the figure as a sphere where the radius corresponds to the magnitude of the wave vectors.

The z component of $\mathbf{k}_o$ is determined from $k_x^2 + k_y^2 + k_z^2 = k_o^2$. Inserting $\mathbf{k}_o$ into this expression and rearranging the terms gives the following expression for the polar angle of the outgoing wave, θ_o:

$$sin^2(\theta_o) = \left(\frac{n_i}{n_o} sin(\theta_i) cos(\phi_i) + \frac{m_x \lambda}{n_o \Lambda_x}\right)^2 + \left(\frac{n_i}{n_o} sin(\theta_i) sin(\phi_i) + \frac{m_y \lambda}{n_o \Lambda_y}\right)^2 \tag{3.2.4}$$

The azimuth angle ϕ_o of the outgoing wave can be found by taking the tangent of the y and x component of $\mathbf{k}_o$. The sign of the x and y component determines the quadrant in which ϕ_o is found.

$$tan(\phi_o) = \frac{\frac{n_i}{n_o} sin(\theta_i) sin(\phi_i) + \frac{m_y \lambda}{n_o \Lambda_y}}{\frac{n_i}{n_o} sin(\theta_i) cos(\phi_i) + \frac{m_x \lambda}{n_o \Lambda_x}} \tag{3.2.5}$$

For a uniperiodic reflection grating with periodicity in the x direction and incidence in the plane of periodicity, also called the classical mount, Equation 3.2.4 simplifies to the well-known grating equation for uniperiodic gratings:

$$sin(\theta_o) = sin(\theta_i) + \frac{m_x \lambda}{n_o \Lambda_x} \tag{3.2.6}$$

The reciprocal grating shown in Figure 3.2.3 is a useful visualization of the allowed diffraction orders of a bi-periodic grating. Each point in the reciprocal lattice represents a diffraction order. The zero order is at the center of the coordinate system. The propagating diffraction orders must satisfy the inequality of Eq. 3.2.3. This is illustrated in Figure 3.2.3 with a black circle for propagation in Si ($n = 3.6$) and with a red circle for propagation in air. In this example I have chosen the lattice period $\Lambda = \lambda_x = \Lambda_y$ to be slightly smaller than the wavelength in air. Consequently, normal incident light will only support zero order diffraction in air, illustrated in the top left of Figure 3.2.3 with a red circle that contains only one diffraction order. The black circle that illustrates Si supports several diffraction orders.

Increasing the incidence angle θ_i along the x axis moves the center of the circles a distance $k_{x,i} = k_i sin(\theta_i)$ (assuming incidence from air). As a result, the set of propagating diffraction orders changes as depicted in Figure 3.2.3 (top right). In this case two diffraction orders may propagate in air, the zero order and the (-1,0) order. Figure 3.2.3 (bottom) shows that for incidence along the $\phi = 45°$ plane up to four diffraction orders (zero order plus three higher orders) are allowed in air.

3.3. Rigorously coupled wave analysis (RCWA)

Diffraction angles for light incident on a periodic structure may be calculated by Eq. 3.2.4, but the power distributed into each of the diffracted waves, i.e. the diffraction efficiency, must be found by other means. Several scalar approaches exist for calculating diffraction efficiency and field distributions from a grating [87], yet their range of validity

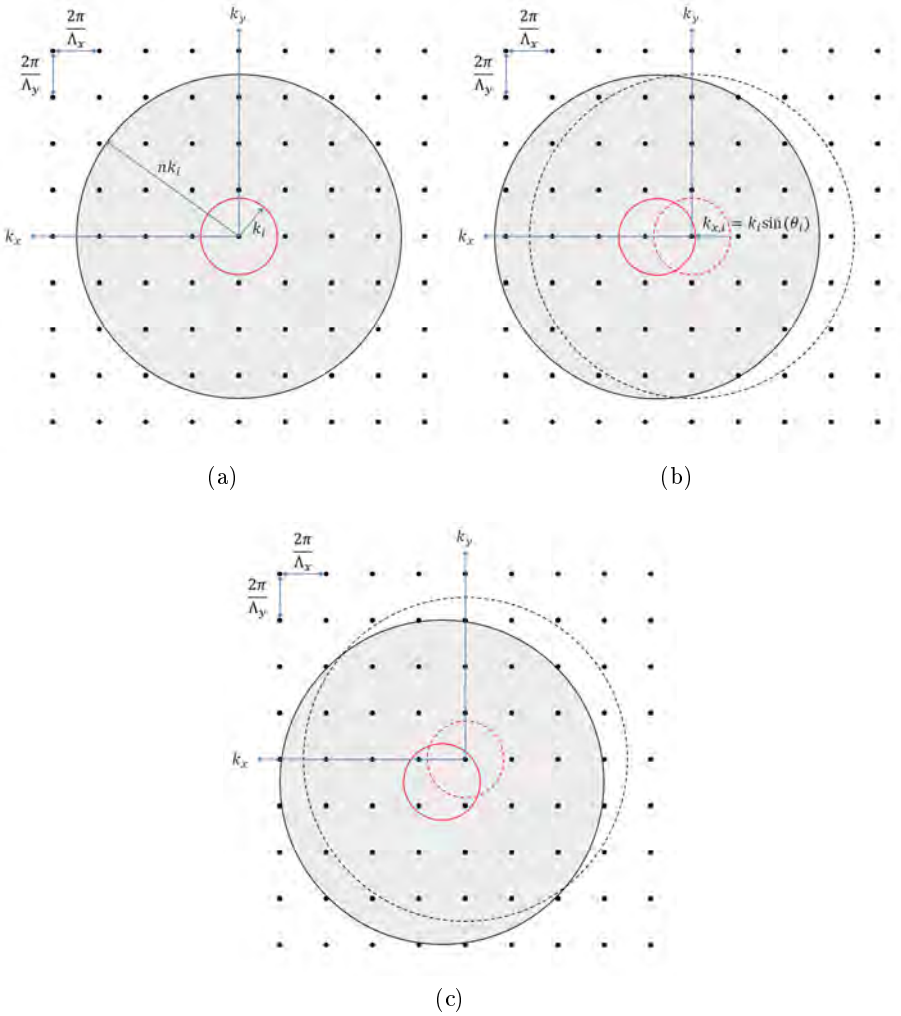

Figure 3.2.3.: The circle of diffraction is a useful visualization of the allowed diffraction orders from a bi-periodic grating. The figure shows the reciprocal lattice for the case where $\Lambda_x = \Lambda_y$. Each point in the reciprocal lattice represents a diffraction order with the zero order in the center. The gray area encircled by the black line shows propagating diffraction orders in Si ($n = 3.6$) while the red circle shows propagating diffraction orders in air. The example in this figure illustrates the case where the incident wavevector k_i is slightly smaller than the reciprocal lattice vector, $2\pi/\Lambda$, so that only the zero diffraction order may propagate in air at normal incidence. Each figure represents a different incidence angle. The figures represents normal incidence (top left), incidence along the x direction (top right), and incidence along the $\phi = 45°$ plane (bottom). The dashed circle shows the diffraction orders at normal incidence.

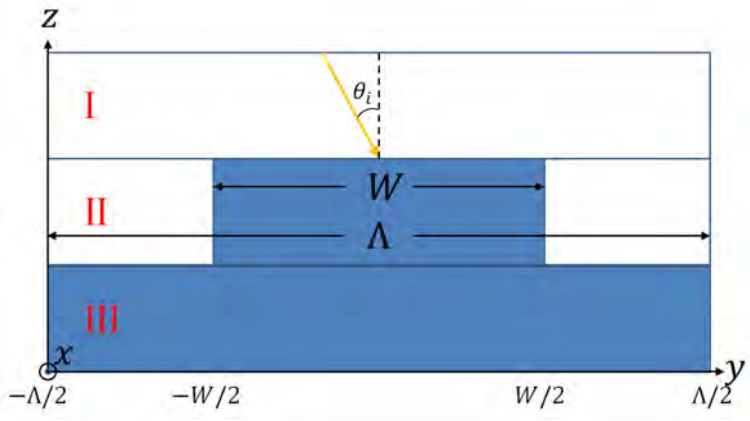

(a)

Figure 3.3.1.: To solve a diffraction problem using rigorously coupled wave analysis the structure is divided into strata so that each stratum is homogeneous in the z direction. The figure shows the computational regions for a 1D periodic diffraction problem.

are limited to the case of small diffraction angles. If the lattice period of the structure is comparable to the wavelength of light then the Maxwell equations in vectorial form need to be solved.

Rigorously coupled wave analysis (RCWA or RCW) is a well-known method to calculate the diffraction efficiencies from a periodic structure [88, 89, 90, 87]. RCWA is also known as the Fourier modal method (FMM) [90]. The method of RCWA in its basic form aims at solving the equations of light propagation from a homogeneous superstrate through a periodic medium to a homogeneous substrate as illustrated in Figure 3.3.1. RCWA requires that region II in Figure 3.3.1 is homogeneous in the z-direction. To calculate arbitrary periodic structures where the periodic structure itself is not homogeneous in the z direction, the structure may be divided into several strata where each stratum is homogeneous in the z direction, as shown in Figure 3.3.2. The materials are assumed to be linear, homogeneous, isotropic, and nonmagnetic. This is a good assumption for most dielectrics under solar illumination.

Here I will briefly explain the procedure commonly used in RCWA for the case of a 1D periodic structure with incidence in the plane of periodicity, as shown in Figure 3.3.1. The procedure may be generalized to the case of a bi-periodic structure, but the formalism for a 1D periodic structure is more transparent. The procedure shown below builds on Ref. [91] and is explained in further detail there. A more thorough discussion may also be found elsewhere [87].

The TE and TM polarization need to be separated because different boundary conditions are applied for the two polarizations and it is easier to solve the propagation problem for the transverse polarization. The equations may then be solved for the transverse field alone and the other field components may be found from the coupling of the

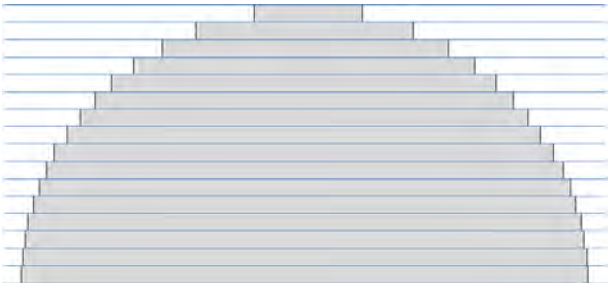

Figure 3.3.2.: An arbitrary shape may be computed with rigorously coupled wave analysis by constructing the unit cell out of several strata where each stratum is homogeneous in the z direction.

E and **H** field in the Maxwell equations. Here I use TE polarization as a case. The procedure for the TM polarization is similar except for the form of the wave equation and a different set of boundary conditions.

The equation that we need to solve is the wave equation, also known as the Helmholtz equation, which is derived directly from the Maxwell equations. The wave equation may take several forms, one of which is shown in Eq. 3.1.1. For the situation depicted in Figure 3.3.1 with incidence in the plane of periodicity and TE polarized light, the wave equation becomes:

$$\left(\frac{d^2}{dy^2} + \frac{d^2}{dz^2}\right) E_x(y,z) + k^2 \epsilon_r(y,z) E_x(y,z) = 0 \tag{3.3.1}$$

Here E_x is the only nonzero electric field component, k is the wavevector, and ϵ_r is the relative permittivity. The relative permittivity, ϵ_r, is periodic in the y direction so that $\epsilon_r(y+\Lambda, z) = \epsilon_r(y,z)$. The Bloch-Floquet theorem [84] states that the electric field in such a structure will be a pseudo periodic wave known as a Bloch wave. Since it is a periodic function in the y direction we expand the E_x field in a Fourier series:

$$E_x(y,z) = \sum_{m=-\infty}^{m=\infty} E_m(z) exp^{i(\alpha_0 + mG)y} \tag{3.3.2}$$

Here $\alpha_0 = k_i sin(\theta_i)$ is the incoming wave vector in the y direction and $G = 2\pi/\Lambda_y$ is the reciprocal lattice vector.

In region I and III of Figure 3.3.1 the permittivity is a constant and the wave equation simplifies to the homogeneous Helmholtz equation. Inserting Eq. 3.3.2 into Eq. 3.3.1 gives the following expression:

$$\sum_{m=-\infty}^{m=\infty} \left(\frac{d^2}{dz^2} + k^2 \epsilon_r - (\alpha_0 + mG)^2\right) E_m(z) exp^{i(\alpha_0 + mG)y} = 0 \tag{3.3.3}$$

For Eq. 3.3.3 to be satisfied each term in the sum must equal zero, i.e.:

$$\left(\frac{d^2}{dz^2} + k^2\epsilon_r - (\alpha_0 + mG)^2\right) E_m(z) = 0 \tag{3.3.4}$$

To simplify this equation we define:

$$\alpha_m = \alpha_0 + mG \tag{3.3.5}$$

$$\gamma_m = \sqrt{k^2\epsilon_r - \alpha_m^2} \tag{3.3.6}$$

Eq. 3.3.4 is easy to solve and yields the following expression for $E_m(z)$:

$$E_m(z) = A_m exp(i\gamma_m z) + B_m exp(-i\gamma_m z) \tag{3.3.7}$$

Here A_m and B_m are unknown coefficients. Inserting Eq. 3.3.7 into Eq. 3.3.2 gives the general solution for the electric field in region I and region III:

$$E_x(y,z) = \sum_{m=-\infty}^{m=\infty} A_m exp[i(\alpha_m y + \gamma_m z)] + \sum_{m=-\infty}^{m=\infty} B_m exp[i(\alpha_m y - \gamma_m z)] \tag{3.3.8}$$

Eq. 3.3.8 can be interpreted as a sum of outgoing ($+\gamma_m$) and incoming ($-\gamma_m$) plane waves. From Eq. 3.3.6 we see that γ_m will become imaginary if $\alpha_m > k^2\epsilon_r$. Consequently, these waves will have exponentially decaying or increasing amplitude when moving away from the grating. The waves with exponentially decaying amplitudes are called evanescent waves. The fields where the amplitudes diverge are discarded since they are clearly nonphysical. For region I this results in the following solution for the electric field $E_x^I(y,z)$:

$$E_x^I(y,z) = \sum_{m=-\infty}^{m=\infty} A_m exp[i(\alpha_m y + \gamma_m z)] + B_0 exp[i(\alpha_0 y - \gamma_0 z)] \tag{3.3.9}$$

This is called the Rayleigh expansion [92]. Eq. 3.3.9 shows an incoming field with amplitude B_0 and a sum of outgoing propagating and evanescent waves. Even though the evanescent waves will have zero amplitude at large distances from the grating, they may still carry energy over shorter distances. A similar approach is applied in region III. Here the Rayleigh expansion consists of only outgoing (transmitted) plane and evanescent waves.

In region II the permittivity is a periodic function of y and Eq. 3.3.1 do not simplify to the homogeneous Helmholtz equation. However, since the permittivity is periodic, it may be expanded into a Fourier series. The Fourier expanded permittivity, ϵ_r, and the E_x field is then inserted into Eq. 3.3.1. The coefficients of the following second order differential equation are solved as a matrix eigenvalue problem. This is the most computational intensive part of the RCWA method.

The final step of the RCWA procedure is to match the field solutions in region I, II and III at the boundaries by requiring continuity of the tangential E field, i.e. E_x.

The diffraction efficiencies of the reflected and transmitted diffraction orders may now be extracted from the amplitudes of the Rayleigh expansion in regions I and III respectively.

RCWA is rigorous in the way that the accuracy of the solution improves with increasing number of terms of the Fourier expansion. However, a numerical implementation of RCWA requires the Fourier expansion above to be limited to a finite number of terms. This is commonly achieved by truncating the Fourier expansion after a certain number of terms, m_{max}. The computational time for RCWA scales with m_{max}^3 for a uniperiodic grating. For a bi-periodic grating, where the number of diffraction orders scales as m_{max}^2, the computational time scales as m_{max}^6. Consequently, there is always a compromise between computational time and the required accuracy. It is not sufficient to perform the calculation only with the propagating diffraction orders as evanescent waves may also carry energy over shorter distances. The exponential nature of the evanescent waves may also induce numerical instability in RCWA due to round-off errors when using thick layers.

For TM polarization the E field diverges with decreasing distance to the 90 degree edges, i.e. at $-W/2$ and $W/2$ in Figure 3.3.1 [93]. This divergence is intrinsic to the model due to the perfect 90 degree edges, and it is not a numerical artifact. Consequently, the field will converge more slowly for TM polarization than for TE polarization. The use of 90 degree corners is an inherent problem of RCWA when using for instance stair case approximation since all objects are made out of rectangular blocks. The problem is particularly challenging for deep metallic gratings.

I used RCWA to calculate photo absorption, diffraction efficiencies, and field distributions for bi-periodic dielectric gratings. I will go more into detail about this in Section 4.3.

3.4. Finite difference time domain (FDTD)

Finite difference time domain (FDTD) [94] is a numerical method where the Maxwell equations are solved by discretizing time and space. The spatial discretization utilizes a Yee lattice where the E and H field are stored at intermediate positions to reduce the memory consumption. The E and H field are then solved in discrete time intervals within the Yee lattice using the Maxwell equations in partial differential form. The time resolution is usually directly related to the spatial resolution. FDTD does not require the structure to be periodic, but periodic, or Bloch wave, boundary conditions may be applied for simulations of waves in periodic media.

The source in an FDTD simulation is an electromagnetic pulse with a given frequency and duration. The FDTD software computes the E and H field at every time step until the magnitude of a chosen field component at a given detector position reaches a certain threshold value. A short pulse length in the temporal domain will result in a broadening of the frequency spectrum, i.e. one pulse consists of an extended range of frequencies centered on a mean frequency. The response at the detectors may be Fourier transformed to get spectrally resolved reflection and transmission. In other words, the response at all frequencies may be computed in only one run.

I used FDTD to calculate reflection and transmission from pure dielectric grating structures. I return to this in Section 4.4.

3.5. Ray tracing

Ray tracing is a geometrical optics approximation for absorption, reflection and transmission, where the wave nature of light is ignored and rays travel in straight paths between interfaces. At interfaces the rays may be chosen to be partially reflected or transmitted according to the Fresnel equations, but it is also possible to incorporate other effects such as for instance any type of scattering. Interference effects are ignored in such an approximation, but most ray tracing software still allow thin-film interference effects by applying this as surface properties to interfaces.

In this thesis I have used ray tracing to calculate reflectance and absorptance of Si textured with random pyramids (see Section 4.5). Since the dimensions of the pyramids are much larger than the wavelength of the sunlight, ray tracing may be applied for such simulations. Several authors have commented on the accuracy of this approximation [92, 40, 95, 96].

4. Numerical simulation tools and methodology

In Chapter 3 I introduced the theory behind the simulation tools that we have applied in this thesis. This chapter will focus on the simulation tools, how they have been employed, and important limitations and approximations. Computations have been performed either on an ordinary desktop computer or on a dedicated server. The more heavy numerical simulations have been performed on the Titan Cluster at the University of Oslo [97].

First I will go through the methodology that we employed to analyze bi-periodic cylinder arrays using a low-frequency and high-frequency approximation. To obtain good light trapping with a periodic structure it is important to have efficient coupling to higher diffraction orders. This is equivalent to reducing the specular, or zero order, reflection. Specular reflection may be reduced, and even totally extinguished, if it experiences destructive interference from the grating layer. Below we apply this idea to both the low-frequency and the high-frequency approximation and find which conditions that satisfy the criteria of low zero order reflection.

4.1. Low-frequency approximation

The effective medium model is a good approximation for light propagation in a periodic medium where the lattice period is much smaller than the wavelength of light, as shown in Figure 4.1.1 (left). In this model the periodic structure behaves like a homogeneous material with an effective relative permittivity ϵ_m. The permittivity ϵ will in general be a tensor, and the electric displacement field in the direction i, D_i, is the sum over the contributions from each electric field component:

$$D_i = \Sigma_k \epsilon_{ik} E_k \tag{4.1.1}$$

We can always find three linearly independent low-frequency solutions for the electric field, and for cylinders in a square lattice, we may choose them to be polarized mainly in either one of the three directions x, y, and z. We define the average polarization of a field component in a unit cell, uc, as follows:

$$< E_i >= \int_{uc} E_i(\mathbf{r}) dV \tag{4.1.2}$$

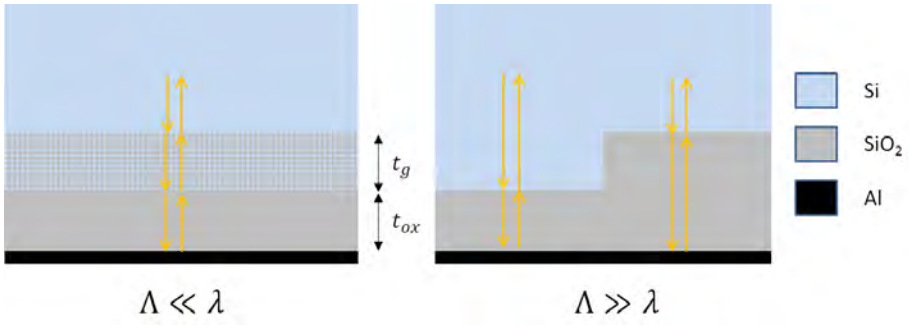

Figure 4.1.1.: The low-frequency, or small-period approximation (left), and the high-frequency, or large-period approximation (right). In the small-period approximation the grating layer can be compared to a homogeneous layer with an effective refractive index. In this case extinction of specular reflection is achieved when light reflected from the top of this layer interferes destructively with the light reflected from the layer below. In the large-period approximation extinction of zero order reflection is achieved when light reflected from the tops and valleys of the grating structure interfere destructively.

Here the subscript i denotes the original orientation of the E field, i.e. in the x, y, or z direction. In the low-frequency approximation $< E_i >$ is independent of where we center the unit cell.

Now the effective relative permittivity along the axes i, $\epsilon_{m,i}$, may be defined as follows:

$$\epsilon_{m,i} = \frac{\int_{uc} \epsilon_r(\mathbf{r}) E_i(\mathbf{r}) dV}{< E_i >} \tag{4.1.3}$$

In Eq. 4.1.3 the relative permittivity, ϵ_r, is weighted against the electric field with the desired orientation. We now choose the coordinate system so that the z direction is along the axis of the cylinders, while the x and the y axes are along the directions of periodicity. For a field oriented in the z direction, i.e. TM polarization, the E_x and E_y components will be zero everywhere. For a field originally oriented in the x direction, on the other hand, the E_y field will not be zero throughout the unit cell. However, the average of E_y over one unit cell will add up to zero, and for a square array of cylinders with isotropic materials, the average of the product $\epsilon_r(\mathbf{r})E_y(\mathbf{r})$ will also add up to zero. In this case the effective medium tensor will be given as follows:

$$\epsilon_m = \begin{pmatrix} \epsilon_{TE} & 0 & 0 \\ 0 & \epsilon_{TE} & 0 \\ 0 & 0 & \epsilon_{TM} \end{pmatrix} \tag{4.1.4}$$

Here ϵ_{TE} and ϵ_{TM} denotes the effective relative permittivity for TE and for TM polarized light, respectively. The effective medium is anisotropic even though the materials

in the cylinder array have isotropic permittivities. The anisotropy originates from the anisotropic distribution of dielectric material within the unit cell of the photonic crystal. We can easily remove the equivalence between the two possible TE polarizations, for example by having a rectangular unit cell instead of a square unit cell. This would result in different effective permittivities for the two TE polarizations. In the TM case the electric field points along the cylinder axes and have equal strength in the cylinders and the matrix surrounding the cylinders due to the continuity of the tangential electric field. Consequently, ϵ_{TM} may be calculated simply as the weighted sum of the permittivities of the two materials ϵ_1 and ϵ_2, where the geometric fraction of each material, f_1 and f_2, constitutes the weights:

$$\epsilon_{TM} = \epsilon_1 f_1 + \epsilon_2 f_2 \tag{4.1.5}$$

For light normally incident on the plane of cylinders the electric field orientation will be normal to the cylinder axis, corresponding to TE polarization. In this case the electric field tends to concentrate in the dielectric with the highest refractive index. We calculated the field distribution for TE polarization in a cylinder structure in the electrostatic case using a series expansion of the electric potential in cylindrical coordinates. The coefficients for the series expansion are found by employing the Maxwell boundary conditions at the cylinder interface and imposing periodic boundary conditions at the unit cell interface. This procedure is described in further detail in Appendix A.

In the small-period approximation the grating layer will, together with the oxide layer on the back side, behave like a homogeneous thin-film stack. Specular reflection from this stack can be minimized when reflection from the top of the effective medium layer interferes destructively with reflection from the layers below, as shown in Figure 4.1.1 (left). Specular reflection will of course only be suppressed if higher diffraction orders may propagate in the Si superstrate. This implies that the lattice period needs to be at least $\Lambda > \lambda/n_{Si}$ to allow propagating orders in the Si. We showed in **Paper II** that the small-period approximation may be used to predict the light-trapping behavior of the grating even for this case where the lattice period is large enough to allow diffraction orders.

4.2. High-frequency approximation

The effective medium approximation is no longer valid when the lattice period is much larger than the wavelength of light. In this case reflection may instead be assumed to occur independently from the tops and the valleys of the cylinder structure, as shown in Figure 4.1.1 (right). Specular reflection can in this case be reduced if the light reflected from the tops and the valleys has a phase difference of π, i.e. a destructive interference. In a simple metallic grating, a complete extinction of specular reflection is obtained if the thickness of the grating, t_g, fulfills the following equation:

$$t_g = \frac{\lambda}{4n}(1 + 2m) \tag{4.2.1}$$

Here λ is the wavelength of light in vacuum, n is the refractive index of the grating material, and m is zero or any positive integer. The cylinder structure we investigated is more complex as it exhibits a pure dielectric grating on top of a planar layer of oxide and with a metallic rear reflector, as shown in Figure 4.1.1 (right). In this case interference effects may occur within the various layers and the equation for extinction of zero order reflection is not as straight forward. To find the oxide and grating thickness that provides extinction of specular reflection we used the transfer matrix method [98]. We compared the phase difference between the light reflected from the tops of the grating and the light reflected from the valleys. Specular reflection was suppressed for the combinations of grating thickness and oxide thickness that provided a phase difference of π.

In a grating structure where the lattice period is close to the wavelength of light, higher diffraction orders may also contribute to interference within the layers, and the approximations above are no longer valid. To find exact locations and values for zero order extinction for such lattice periods, full vectorial computations are necessary. Below, two different methods for such computations are presented. However, we found in **Paper II** that for lattice periods between the two extremes the grating behavior resembles both the approximations.

4.3. GD-Calc

Computation of the optical properties of structures with feature size similar to the wavelength of light requires the use of rigorous modeling tools. Rigorously coupled wave analysis (RCWA) (see section 3.3) is particularly well suited for periodic structures, and a RCWA-based software package called GD-Calc [99] has therefore been the main modeling tool in this thesis. GD-Calc is a commercial software package which is integrated in Matlab [100].

GD-Calc computes the transmitted, reflected, and diffracted plane waves from 1D or 2D periodic structures. GD-Calc computes the diffraction efficiencies simultaneously for any input polarization. A summation of the power density in all diffraction orders provides the reflection, R, and similarly the transmission, T, of the structure. Absorption is calculated as $A = 1 - R - T$. The field distribution inside the structure may be calculated with a supplementary full field package. GD-Calc uses RCWA together with the S-matrix formalism [89] to couple together multiple homogeneous or periodic strata. The S-matrix algorithm reduces numerical instabilities which may arise in computations of deep gratings or thick layers [87].

The unit cell geometry in GD-Calc is made out of rectangular bricks arranged in the hierarchy of strata which are divided into lateral stripes and subdivided into blocks, as shown in 4.3.1. Consequently, oblique geometries in GD-Calc must be constructed from several discrete strata, a method known as the stair-case approximation. A similar approach is used to make non-rectangular shapes in the xy plane, e.g. a cylinder.

The number of bricks used to approximate the unit cell may affect the accuracy of the simulations. The resolution that is needed in the z direction may differ from the resolution needed in the xy plane. A thorough discussion on this topic may be found

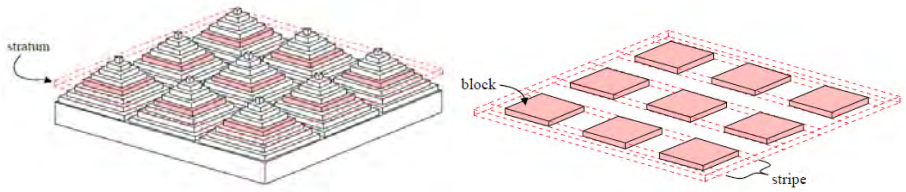

Figure 4.3.1.: Arbitrary periodic structures may be created by dividing the unit cell into lateral strata and in-plane stripes and blocks. The figures shown here represent a pattern of pyramids [103].

elsewhere [86, 101]. We have used a number of strata in the z direction so that the optical thickness of each stratum was less than $1/30$ of the wavelength of light inside the material, as suggested in Ref. [102]. Consequently, the number of strata N_{tr} is chosen so that $N_{tr} > 30 n_s t_g/\lambda$, where t_g is the grating thickness and n_s the refractive index of Si.

The parameter with the most profound influence on the accuracy of the simulations is the Fourier-series truncation limit, m_{max}. This parameter determines the number of terms in the Fourier expansion of the field (see Eq. 3.3.2), and consequently what level of detail that can be resolved in the electric and magnetic fields. As the periodicity in the x and y direction was identical in most simulations, we used the same truncation parameter for both directions of periodicity. The selection of orders could be performed using the quadratic truncation where all orders satisfying $|m_x| \leq m_{max}$ and $|m_y| \leq m_{max}$ are included in the computation. Alternatively, the diagonal truncation could be used where only the orders satisfying $|m_x| + |m_y| \leq m_{max}$ are included. These truncation limits are illustrated in Figure 4.3.2.

The number of diffraction orders, m_{tot}, resulting from the quadratic truncation is given by $m_{tot} = (2m_{max} + 1)^2$, as can be seen from Figure 4.3.2. The computational time proportional to m_{tot}^3, and consequently, for a 2D grating it is proportional to m_{max}^6. The quadratic truncation yields about twice the number of discrete Fourier orders as the diagonal truncation, resulting in an eight fold increase in computational time. Both truncation types converge towards the same result, but the triangular truncation may in some cases yield a faster convergence. I have used both truncations in my simulations.

The number of diffraction orders needed in the simulation depends on the particular structure. If the wavelength is small compared to the lattice period, a larger number of propagating diffraction orders will exist and a higher truncation limit will be needed. A rule of thumb is to use a truncation limit, m_{max}, that is twice as large as the highest propagating order [102]. I typically used a truncation limit of 6-10 for my simulations. For more complex systems the number of diffraction orders should be increased. In structures where the field is expected to change rapidly, as for instance around the corners of metal gratings, a high truncation limit is required to resolve the rapid field changes. The divergent behavior of the electric field in TM polarization close to these edges also poses a challenge with convergence [93].

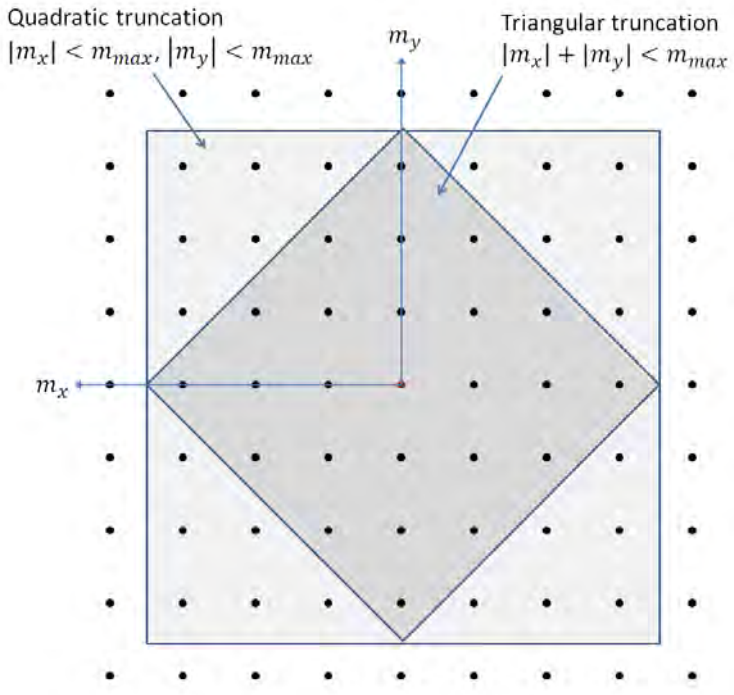

(a)

Figure 4.3.2.: Two different ways of truncating the Fourier expansion called the quadratic and the triangular truncation. The number of points inside the squares determines the number of Fourier orders that are used in the computation. Here we use a truncation limit $m_{max} = 3$ for illustration purposes. Most simulations were performed with a truncation limit between 6 and 10.

For the zigzag and roof-mosaic structure from **Paper VII** the computational unit cell was chosen to be twice the size of the primitive unit cell because it was easier to implement in GD-Calc. In this case half of the diffraction orders will hold zero power and the computational time will increase eightfold compared to simulation of the primitive unit cell. The GD-Calc software allowed us to discard the zero-power half of the diffraction orders in the simulations so that we could obtain the same resolution with the same computational time as one would expect for the primitive unit cell.

4.3.1. Full field calculations

A full-field extension of the ordinary GD-Calc software made it possible to extract the Fourier coefficients at the interface between each stratum. The spatial distribution of the electric and magnetic field inside the structure may then be obtained by a Fourier transform. The resolution in the z direction is determined by the number of strata, while the resolution in the xy plane is determined by the sampling of the Fourier transform.

The full field data allowed the extraction of absorption within a given stratum of the structure. We used this to separate parasitic absorption in the metal from absorption within the photo active Si material. The absorptance in stratum i was calculated as the change in power flux over the given stratum, i.e. the change in Poynting vector, $\mathbf{S}$, in the z direction, $\triangle \mathbf{S}^i \cdot \hat{\mathbf{z}}$. Since the Fourier orders are orthogonal, the Poynting vector could be calculated by summing up the contribution from each Fourier order independently:

$$S_z^i = \frac{1}{2} \sum_{l=-M}^{M} \sum_{j=-M}^{M} \mathbf{e}_{l,j}^i \times conj(\mathbf{h}_{l,j}^i)\hat{\mathbf{z}} \tag{4.3.1}$$

Here $\mathbf{e}^i$ and $\mathbf{h}^i$ is the electric and magnetic field at the interface of stratum i in Fourier space, i.e. as a function of spatial frequency. The summation indexes l and j represents summation over the diffraction orders m_x and m_y while M represents the truncation limit m_{max}. The summation in Eq. 4.3.1 represents the quadratic truncation (see Figure 4.3.2). The summation will be somewhat different for the triangular truncation as fewer terms are needed to cover all combinations of m_x and m_y.

In some structures parasitic and photo-active absorption may occur within the same stratum. For example will a grating consisting of Al and Si have absorption in both materials, whereas only the Si absorption will contribute to generation of electron-hole pairs. To extract the photo active absorption we first need to calculate the spatial distribution of the electromagnetic fields. The absorption within an infinitesimal volume may then be calculated either as the rate of change of the Poynting vector in the same volume, i.e. the divergence of the Poynting vector $\nabla \cdot \mathbf{S}$, or directly from the electric field distribution, $E(x, y, z)$, as:

$$A(x, y, z) = -\frac{\omega \epsilon''}{2} \cdot |E(x, y, z)|^2 \tag{4.3.2}$$

Here $A(x, y, z)$ is the spatial absorption profile,ϵ'' is the imaginary part of the relative permittivity, and ω is the angular frequency of light.

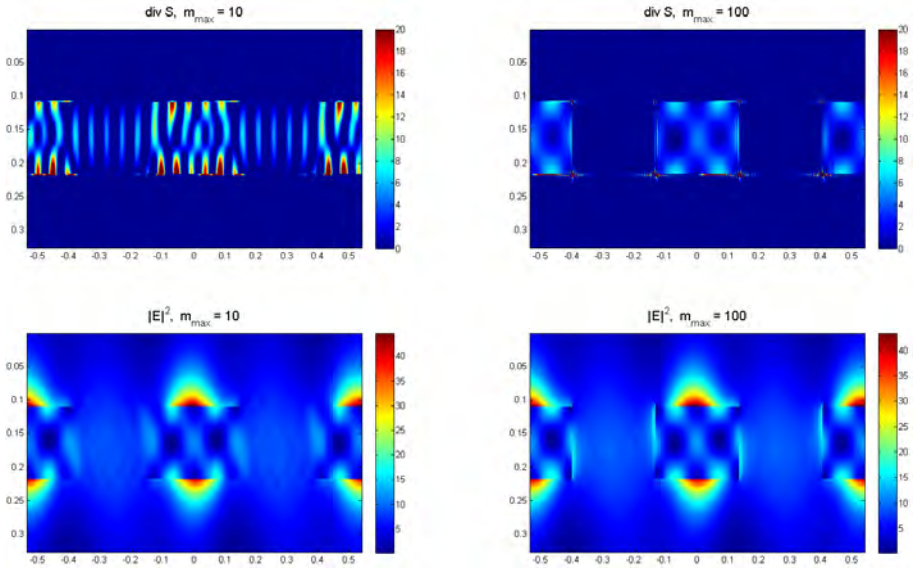

(a)

Figure 4.3.3.: Absorption in a uniperiodic grating consisting of Si and air calculated as the divergence of the Poynting vector with a truncation limit of $m_{max} = 10$ (top left) and $m_{max} = 100$ (top right). The field intensity $|E|^2$ calculated with a truncation limit of $m_{max} = 10$ (bottom left) and $m_{max} = 100$ (bottom right).

Figure 4.3.3 compares maps of $\nabla \cdot \mathbf{S}$ and the field intensity $|E(x,y,z)|^2$ calculated using truncation limits of $m_{max} = 10$ and $m_{max} = 100$. We see a large change when going from a truncation limit of 10 to 100 in the figures displaying $\nabla \cdot \mathbf{S}$, while a similar change is not observed for the field intensity maps. We believe the oscillations in the $\nabla \cdot \mathbf{S}$ maps are due to the use of the divergence operator on a field which has oscillations resulting from the Fourier expansion. This problem is not encountered when using Eq. 4.3.2.

4.3.2. Optical constants and wavelength sampling

The optical properties of a material are determined by its complex refractive index $\tilde{n}(\lambda) = n(\lambda) - ik(\lambda)$ which in the case of an isotropic material is a scalar value. The imaginary part of the refractive index is directly related to the absorption of the material through Eq. 2.2.1, while the real part n is related to the optical density of the material. The complex refractive index is related to the complex relative permittivity as $\tilde{n} = \sqrt{\tilde{\epsilon_r}}$.

In RCWA the computations at each wavelength are independent from each other and tabulated data for the optical constants are easy to implement. We have used wavelength dependent optical data for Al and Ag [105], but for silicon oxide and silicon nitride we used a constant refractive index of 1.5 and 1.95 respectively. This was a choice of convenience as a number of different types of silicon oxides and silicon nitrides exist. The assumption neglects the UV-absorption of a real silicon nitride layer, but the influence is negligible in the wavelength range where light trapping is important.

Throughout this work I have mostly used the Si data denoted Si_jaw in Figure 4.3.4 (top). These data are determined by ellipsometry [28] and have been used in literature on light trapping in solar cells [48]. Figure 4.3.4 (top) also shows another set of optical data denoted Si_green. These data are determined by transmission measurements [104] while the absorption coefficient close to the band gap is determined from the response of a high-quality solar cell. In Figure 4.3.4 I compare the calculated absorptance for these two sets of optical data with the measured absorptance (actually the measured quantity is the transflectance which is a simultaneous measurement of R and T) for the case of a 50 µm thick double-sided polished Si wafer.

Figure 4.3.4 indicates that the optical data from Ref. [104] corresponds better with our measurements than the optical data that we used in our simulations. I did simulations for both sets of optical data and found that a planar 20 µm thick wafer with an Al mirror will have a $J_{ph} = 31.9$ mA/cm^2 using Si_green compared to 30.7 mA/cm^2 using Si_jaw. For the optimized cylinder structure in **Paper II**, the use of Si_green yields $J_{ph} = 36.1$ mA/cm^2 compared to 35.6 mA/cm^2 using Si_jaw. The difference between Si_green and Si_jaw for Lambertian light trapping is only 0.15 mA/cm^2. Good light trapping corresponds to a long path length inside the absorbing material. Due to the exponential nature of the absorption (recall the Beer-Lambert law Eq. 2.2.2) the deviation between the two set of optical data is reduced with improved light trapping. Even though the choice of optical data affects the absolute value of the calculated J_{ph} to a certain degree, the relative comparison of different structures is not affected as long as one is consistent in the use of one set of optical data.

To perform the calculations of photogenerated current density requires a fine wave-

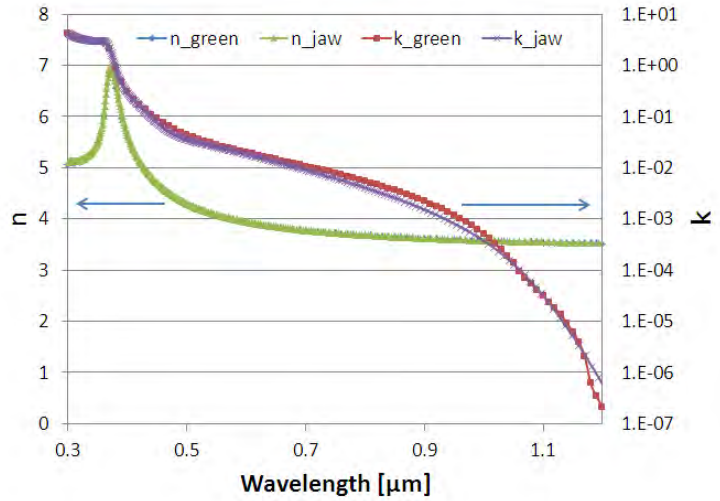

(a)

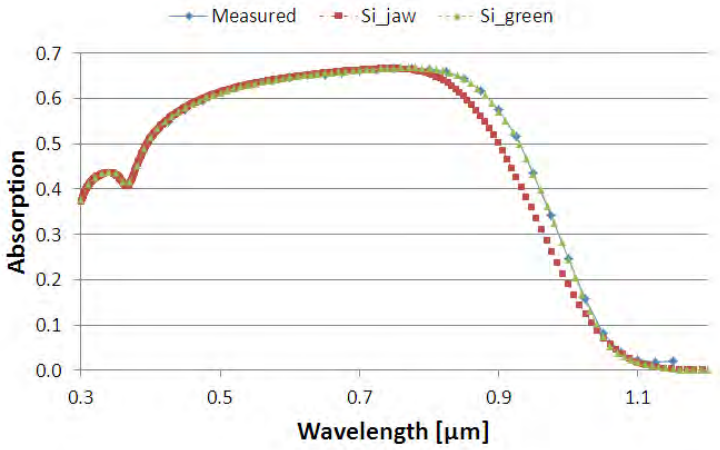

(b)

Figure 4.3.4.: The top figure shows the real and imaginary part of refractive index of Si from two different sources [104, 28]. The real part of the refractive index is in good agreement, and the two curves are difficult to separate. The imaginary part is plotted using an logarithmic scale, and a discrepancy between the curves can be seen. The figure below shows a comparison between measured and calculated absorptance of a 50 µm thick double-sided polished Si wafer. Calculations are performed using the two sets of optical data from the figure above.

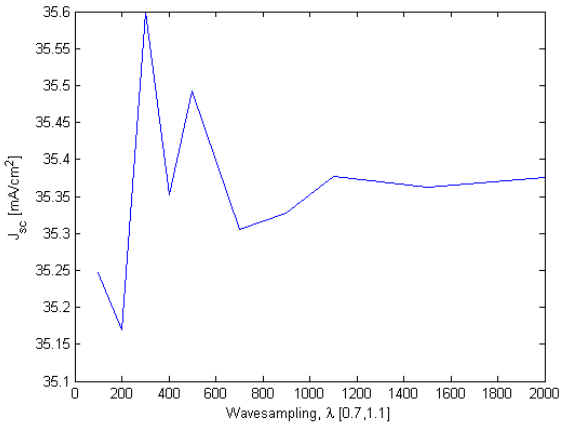

(a)

Figure 4.3.5.: Calculated photogenerated current for a cylinder structure on the rear side of a 20 µm thick Si slab as a function of the number of wavelengths used in the computations.

length sampling to be able to spectrally resolve the fringes resulting from interference in the 20 µm thick Si slab. Since wavelengths below 700 nm is absorbed before they reach the back side I only needed to perform the computations for wavelengths from 700 nm to the band gap at about 1100 nm. Figure 4.3.5 shows the variation in the calculated J_{ph} as a function of the number of wavelengths used in this interval. I typically used a wavelength sampling of 1000 wavelengths for computations of J_{ph}.

4.4. Meep

In addition to GD-Calc I have used the freely available software package Meep [106] to perform full vectorial electromagnetic field computations on bi-periodic structures. Meep, which is a freeware developed at Massachusetts Institute for Technology (MIT), is based on finite difference time domain (FDTD) (see section 3.4). In an early phase of the work Meep was used to investigate the possibility of making a broad-band mirror from a cylinder array. Later I used Meep as a comparison to check the validity of the results from GD-Calc for non-absorbing materials. I found a good agreement between results from Meep and GD-Calc for a cylinder structure and for a cone structure using the stair-case approximation with a ten-step stair case, as shown in Figure 4.4.1. The cone structure in Figure 4.4.1 (top left) consisted of cones pointing into the Si ($n = 3.6$) and filled with silicon oxide ($n = 1.5$), with light incident from a Si superstrate and transmitted to a silicon oxide substrate. The cones had a lattice period of 1 µm, a base radius of 500 nm, and a thickness of 550 nm. The cylinder structure in Figure 4.4.1 (top right) consists of silicon oxide cylinders in a Si matrix with a lattice period of 700 nm, a fill factor of 0.6 and a cylinder height of 230 nm. The cylinder structure in Figure

4.4.1 (bottom) shows an example of a broad banded reflection properties achieved with an oxide layer placed between the Si superstrate and the grating layer.

The advantage of Meep over that of GD-Calc is that structures in Meep are not necessarily constructed from rectangular bricks, a property which makes the stair-case approximation redundant. Additionally, with Meep all wavelengths are calculated in one run. The implementation of wavelength dependent refractive indices, on the other hand, is less convenient with Meep and FDTD in general. The optical constants must be fitted to a semi analytical formula and tabulated data cannot be used directly for computations where several wavelengths are computed in the same run. Meep does not offer the possibility of using a variable mesh size. Consequently, thick layers are not very convenient to model because the area with the highest requirement on resolution will determine the resolution for the whole computational area. Oblique incident angles were also easier to implement with GD-Calc. Perhaps the most important advantages of GD-Calc over Meep for our purpose was the fact that diffraction efficiencies were obtained without the need for post processing, and the fact that the speed of RCWA was superior to that of Meep for the computations we performed since many calculations were of the system response at a single frequency.

4.5. Tracepro

Ray-tracing on pyramidal surfaces has been extensively studied in the past [107, 95, 42, 108] for both regular and random upright pyramids. We used ray-tracing to compare the results from GD-calc on periodic back-side structures with the best light-trapping structures in use today, i.e. random upright pyramids. In **Paper VIII** we investigate the light trapping of both front-side and double-sided random pyramids with different rear reflector material and compare this with the light trapping that may be achieved by rear-side periodic structures with the same Si thickness. The commercial software Tracepro [109] was used for ray tracing.

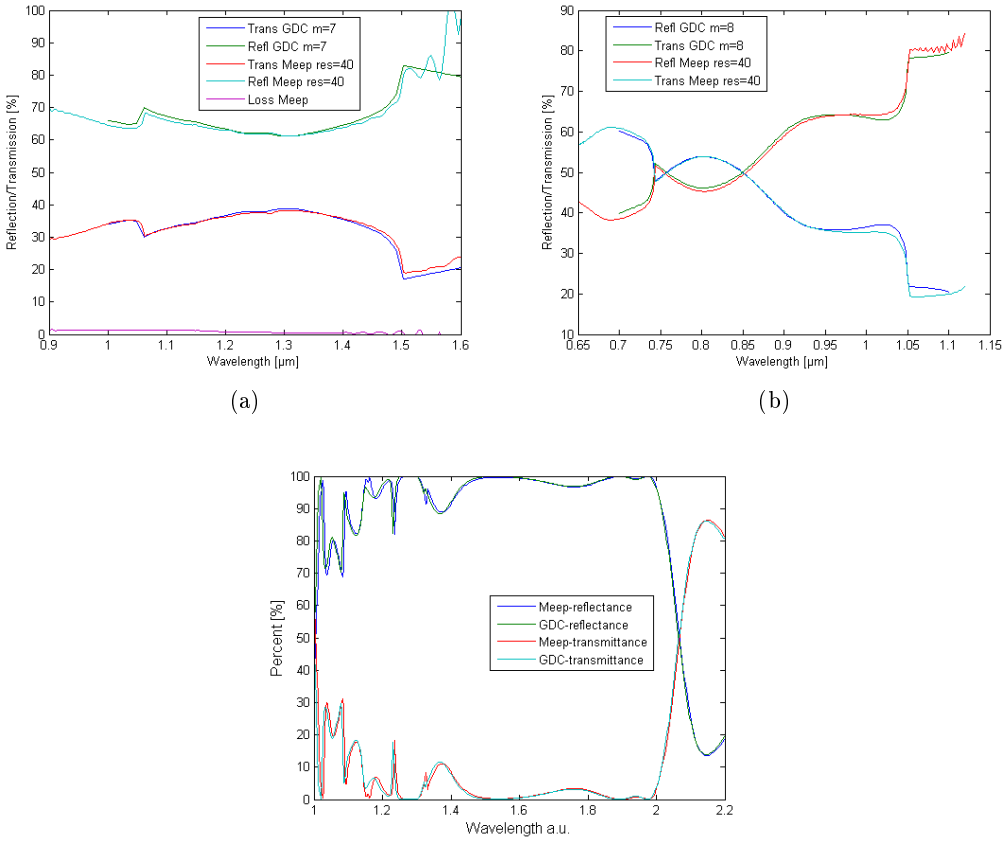

Figure 4.4.1.: Comparison of calculations performed with finite difference time domain (using Meep) and rigorously coupled wave analysis (using GD-Calc) using non-absorbing materials. The top left figure shows reflection and transmission from a grating layer consisting of cones with a lattice period of 1 µm, base radius of 500 nm, and a thickness of 550 nm made using a ten-step stair case. The top right figure shows reflection and transmission from a cylinder structure with a period of 0.7 µm. The bottom figure shows a broad banded reflection behavior of a cylinder grating in arbitrary wavelength units.

5. Experimental methods and results

This chapter is divided into three parts: The first part introduces processing equipment, the second introduces characterization equipment while the third part focuses on the fabrication of photonic crystals. The last part shows three different approaches to fabrication: photolithography for proof-of-concept, nanoimprint lithography, and finally self-assembly in the form of nanosphere lithography.

5.1. Processing tools

5.1.1. Lithography

Photolithography (PL)

Photolithography, or optical lithography, is a method where a thin film of photosensitive material, a photoresist, is exposed by light through a photo mask with a predefined pattern. The illuminated region may be opened for subsequent processing steps by removing the exposed photoresist. Photolithography is a well-suited tool to mass-produce reproducible, small structures with dimensions down to and even below 100 nm. This tool is one of the foundations of the modern semiconductor industry.

The photo mask is commonly fabricated using e-beam lithography, which is an expensive and low-throughput tool. Once the photo mask is made, it may be reused a large number of times. The photoresist is spin-coated on the surface of a substrate and exposed to light through the photo mask. Figure 5.1.1 shows a simplified version of the process flow for patterning a substrate using photolithography. The structure may be transferred to the substrate by various methods, for instance through plasma etching (see section 5.1.2) such as reactive ion etching (RIE). More information about the physics and chemistry of photolithography is found in standard textbooks on semiconductor processing [110]. A review of state-of-the art photolithography methods and resolution limits is given in Ref. [111].

The silicon photonics platform ePIXfab [112] offers multi-project wafer (MPW) shuttle runs where members may send in designs which are fabricated at either IMEC in Belgium or LETI in France. In such a MPW run several participants share the cost of a photo mask which is patterned by e-beam lithography. The mask is divided into small parts with typical block size below 1 cm^2. The block is replicated to cover a full 200 mm wafer. We used a MPW run at IMEC to make a prototype of a light-trapping structure consisting of an array of cylindrical holes etched into Si. The photolithography machine at IMEC is a ASML PAS5500/1100 stepper, which uses a laser source with a wavelength of 193 nm, provides critical dimensions down to around 100 nm.

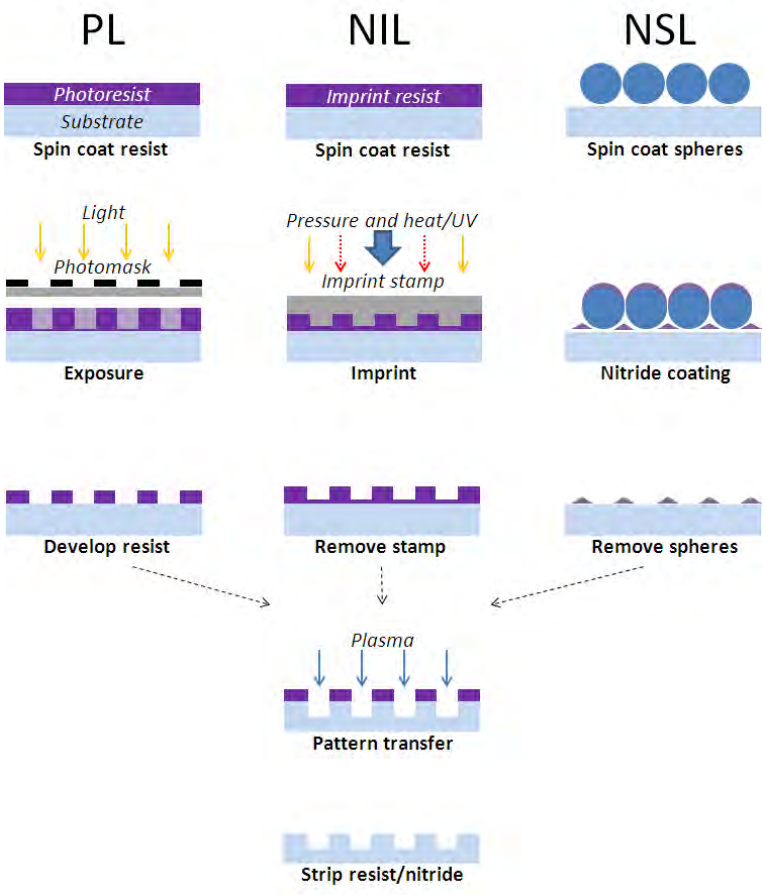

Figure 5.1.1.: Simplified process flow for patterning of a substrate using photolithography (PL), nanoimprint lithography (NIL), and nanosphere lithography (NSL). PL and NIL require a photo mask and a working stamp, respectively. These are usually fabricated using e-beam lithography.

Nanoimprint lithography (NIL)

Nanoimprint lithography is a method for fabrication of nano scale structures by imprinting. A thin layer of imprint resist is spin coated onto a sample and the sample is pressed together with a mold. The imprint resist is cured using heat, UV-light or both, so that the resist maintains the structure of the mold after it is removed. The process flow of sample patterning using NIL is shown in Figure 5.1.1. NIL was invented by Stephen Chou in the mid-nineties [113].

Analogue to optical lithography, NIL also requires the initial production of a master template. The master stamp used in NIL is commonly made by e-beam lithography. The master stamp may then be copied into several working stamps each of which may be used several thousand times. An advantage of NIL compared to optical lithography is that it is not limited by diffraction and is therefore capable of producing very small structures.

Nanosphere lithography (NSL)

In nanosphere lithography a layer of monodispersive spheres is used as a mask for etching or deposition [83]. The monodispersive spheres will under certain conditions self-assemble in a hexagonal, close-packed periodic pattern. One method for monolayer fabrication is to spin coat a droplet of the colloidal solution on to a sample using appropriate sphere concentration and spinning speed [114]. Multilayer structures may also be fabricated, for instance by pulling a sample slowly out of a colloidal solution so that the spheres have time to deposit in a crystal lattice. An example of the process flow for patterning a substrate using nanosphere lithography is shown in Figure 5.1.1.

An advantage of nanosphere lithography is that a predefined template is not required since the spheres organize by self-assembly. The method may be applied to full size wafers and is therefore an interesting alternative for the low-cost high-throughput fabrication needed in the PV industry. One important challenge with this fabrication method is to get the required long range crystal quality. The colloids have a tendency to form several islands of small domains free of defects. The size of these domains is typical measure of the crystal quality.

5.1.2. Plasma etching

Plasma etching is a dry etching method that is commonly used to transfer a structure from a photoresist to the underlying substrate. The different regimes of plasma etching span from ion milling to pure chemical etching. Ion milling is a pure physical process where ions in the plasma knock out atoms in the substrate material. In the other part of the spectrum is the chemical plasma etching where radicals in the plasma react with the substrate material without any ion bombardment. Reactive ion etching (RIE) is somewhere in between these two extremes and uses the damage from the ion bombardment to enhance the chemical reactions at the surface. Different forms of plasma etches can be used to obtain various degrees of selectivity and directionality. A physical process like ion milling will in general be highly directional, with straight walls and little undercutting, while a

chemical process will provide a better selectivity. More information about plasma etches can be found in standard semiconductor textbooks [110].

We used plasma etching to transfer patterns made with NIL to the underlying Si substrate. This is explained in greater detail below in section 5.3.2. An Alcatel AMS 200 I-Speeder machine was used for plasma etching. The etching was performed by an experienced operator at Sintef in Oslo.

5.1.3. Plasma enhanced chemical vapor deposition (PECVD)

Plasma enhanced chemical vapor deposition (PECVD) is commonly used in the PV industry to deposit anti-reflection coatings and surface passivation layers. The PECVD unit uses a strong electric field to ionize gases and create a plasma. The ionized species react on the surfaces in the PECVD chamber to create an amorphous thin-film layer. The advantage of the PECVD process over ordinary chemical vapor deposition (CVD) is that it allows fast deposition and homogeneity at low temperatures. The interested reader can find more information regarding PECVD in standard textbooks on semiconductor processing technology [110]. We used an Oxford instruments plasmalab system 133 to deposit silicon nitride anti-reflection coatings and silicon oxide coatings.

5.1.4. Thermal evaporator

To make the rear metal reflector I used a thermal evaporator [110] to deposit a thin layer of silver (Ag) on a glass microscope slide. Ag with purity above 99.9 %, purchased from K. A. Rasmussen, was deposited using an Balzers BAE 250 coating system at the University of Oslo. An Ag layer with a thickness of 130 nm was deposited on several glass slides and the thickness was confirmed using a profileometer of type Alpha-Step 200. This thickness is sufficient to avoid any light transmission through the Ag layer. The reflectance of the Ag layer was measured to be above 98 % for wavelengths between 700 nm and 1100 nm. The photonic crystal samples were attached to the microscope slide with the patterned side facing the metal reflector.

5.1.5. Lapping and polishing

The samples with photonic crystals that we received from IMEC had a thickness of about 300 µm, but their light trapping properties were designed for light trapping in a 20 µm thick Si slab. To reduce the sample thickness we used mechanical lapping. The samples were attached to microscope slides, with the photonic crystal facing the microscope slide. We used either an epoxy (Huntsman Araldite 2020 A/B) or the thermoplastic wax crystalbond™ to attach the samples to the microscope slides.

The first samples were prepared by Lars Kirksæther at IFE. He used a Struers Discoplan-TS machine to grind the samples down to a thickness slightly above 20 µm. He then performed lapping by hand on a rotating steel plate with SiC and water, first using grit 800 and then grit 1200. Finally he did a polishing step with a polishing cloth using a diamond spray with 1 µm particles. The samples were cleaned in water and liquid soap.

I processed the rest of the samples using an Allied MultiPrep™ System at the University of Oslo. The MultiPrep system used abrasive papers of various degrees of coarseness with SiC particle size ranging from 15 µm down to 0.5 µm. Most of the material was removed using the courser abrasive paper. The thickness was controlled using a contact precision gauge. The lapping was performed with gradually finer abrasive papers so that the deeper lines of the last paper were completely removed before moving on to the next paper. Finally, the sample was polished using a 0.05 µm silica colloidal solution with a polishing cloth.

We experienced that the Si surface after lapping exhibited a reflectance several percent above that of a standard commercially polished Si wafer. The reason for this effect is not clear, but we believe it might be attributed to the remains of SiC particles from the lapping process. An ultrasonic cleaning process had no detectable effect on the reflectance, but a few tens of seconds in a CP5 etch (10:2:5, HNO3:HF:CH3COOH) reduced the reflectance so that it was closer to the reflectance of ordinary polished Si. I discovered that by increasing the time of the polishing step with the silica colloidal solution to more than 10 minutes, the measured reflectance was close to that of a standard polished Si wafer.

5.2. Characterization tools

5.2.1. Integrating sphere

An integrating sphere is an excellent tool for measuring total hemispherical reflection and transmission. An integrating sphere is coated on the inside with a highly reflective material with near Lambertian reflection properties. Light entering the sphere will therefore be isotropically distributed after only a few reflections inside the sphere. A certain fraction of the light will reach the photo detector on the wall of the sphere. Consequently, reflection, or transmission, is measured as the fraction between the detector signal when the sample is illuminated, S_s, and the detector signal when a known reference is illuminated, S_r. The reflectance of the sample, R_s, may be calculated from Eq. 5.2.1.

$$R_s(\lambda) = \frac{S_s(\lambda)}{S_r(\lambda)} R_r(\lambda) \tag{5.2.1}$$

Here R_r is the reflectance of the reference. Figure 5.2.1 shows a picture of an integrating sphere and a schematic drawing illustrating a reflectance measurement. Measurements are performed in comparison mode. This means that the reference measurement is performed with the reference in port A, which is illuminated, and the sample in port B. The sample measurement is performed with the sample in port A and the reference in port B. By keeping both the sample and the reference on the sphere wall at the same time, the sphere throughput remains constant and systematic measurement errors are reduced [115].

The measurement system consists of a 6 inch integrating sphere from Labsphere. The incident wavelength is controlled with a Digikröm DK240 monochromator from CVI

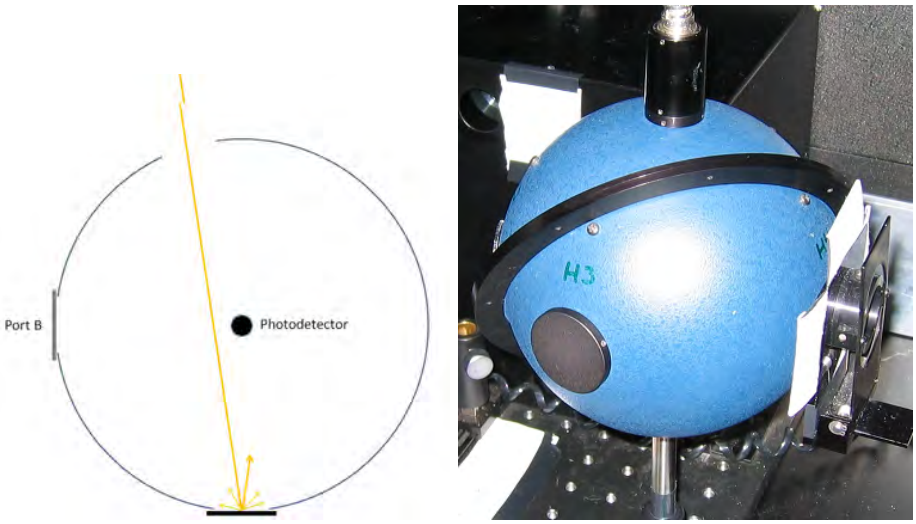

(a) (b)

Figure 5.2.1.: The figure shows a picture of an integrating sphere and a schematic cross section viewed from above. Measurements are performed in comparison mode where the sample and a reflectance reference is present in their respective sphere ports at the same time. A reference measurement is performed with the reference in port A and the sample in port B, while they are switched for the sample measurement. The photo detector is located at the north or south pole of the sphere.

Laser Corporation and a 30 W QTH light source. A chopper, preamplifier and a lock-in amplifier is used to improve the signal to noise ratio in the measurements.

I used this measurement setup to measure the reflectance of the Si samples after lapping and polishing, and to measure the reflectance of evaporated Ag. An integrating sphere with a center mount that allowed simultaneous measurement of reflectance and transmission was used to measure absorption in a 50 µm thick double-sided polished Si wafer. This measurement was performed to check the validity of our optical data (see section 4.3.2).

5.2.2. Ellipsometer

An ellipsometer is an excellent tool for characterizing thin-film properties such as thickness and refractive index [116]. The thin films or thin-film stacks are characterized by comparing the reflected amplitude and phase for incident light of different polarization. We have a variable angle spectroscopic Vase ellipsometer from J.A. Wollam in our lab.

My use of the ellipsometer was mainly to measure reflectance. Reflectance could be measured with a 200 µm diameter spot size by applying focusing probes. The small spot size was necessary to be able to perform measurements on our square millimeter sized photonic crystal samples. The xy stage of the ellipsometer also made alignment of the sample with the incident light much easier.

As the ellipsometer is not constructed for reflectance measurements there were a few challenges with this approach. Firstly, the minimum possible angle of incidence was 18 degrees. Secondly, measurements were slow and drift was a significant problem. The peaks in the spectrum from 800-1100 nm due to the Xenon light source were particularly prone to drift. Thirdly, realignment was required between the sample and reference measurement. This was time consuming and it increased the possibility of alignment errors. Finally, the ellipsometer only detects the specular reflectance so any scattered light is not detected. These obstacles made a quantifiable comparison with the simulation results difficult.

5.2.3. Semilab

I used a Semilab WT-2000 to do a reflectance mapping of the surface of our photonic crystal samples after the thinning process (see section 5.1.5). The semilab uses lasers to generate light with four distinct wavelengths; 406 nm, 853 nm, 952 nm, and 968 nm. Both specular and diffuse reflection can be measured. The specular reflection is measured at 0 degree incidence using a beam splitter to direct the reflected beam to a detector. The diffuse reflection is collected by a parabola and reflected onto the diffuse-light detector. Only light which is reflected with an angle to the surface normal below 60 degrees is collected by the diffuse-light detector.

The semilab can make a spatial reflectance map of the sample by scanning the light source and detector over the sample. The spatial resolution may be as low as 62.5 µm per pixel. The absolute reflectance measured with the semilab does not correlate very well with reflectance measured by more accurate tools such as the integrating sphere.

The reflectance maps were therefore used mainly as a relative comparison of reflection from different parts of a sample.

5.2.4. Microscopy

Scanning electron microscope (SEM)

A scanning electron microscope (SEM) images a sample surface by scanning the surface with a beam of electrons and detecting secondary electrons. To allow a sufficient mean free path length of the electrons the SEM is operated under vacuum. The resolution of the instrument depends on the type of material and the operator, but can in principle approach 1 nm. I used a SEM Hitachi S-480 to investigate the surfaces of our samples after lapping and polishing, to inspect the cylinder arrays made at IMEC before and after thin-film deposition, and to study samples after plasma etching.

Atomic force microscope (AFM)

An atomic force microscope (AFM) is used to measure surface structure on a nanometer scale. The surface is measured by scanning a mechanical probe over the surface. The probe may either be in direct contact with the surface, or it may only be brought close enough so that the forces between the surface and the probe tip is recorded. Due to the finite size of the probe tip vertical walls will appear to be gradually sloping in an AFM image. We used an AFM PicoStation from Surface Imaging System to measure the depth of the cylinder structures made at IMEC.

5.3. Photonic crystal fabrication

5.3.1. Fabrication by photolithography

To experimentally study light trapping from photonic crystals and at the same time to verify our numerical simulations we had samples manufactured by photolithography in a multi-project wafer (MPW) run [112] at IMEC. From the MPW run we received an 8 inch Si wafer diced into almost 200 samples.

We had to our disposal an active block area of 2.4 mm by 6 mm. To investigate the effect of the lattice period and lattice structure we divided the main block into eight sub blocks of 1 mm by 1.4 mm. The block division is shown in Figure 5.3.1. Four sub blocks was made with a square lattice of cylindrical holes and four with a hexagonal lattice of cylindrical holes. Each sub block had a different lattice period and hole diameter. Additionally, IMEC fabricated different sets of samples with different exposure times, resulting in different diameters, or fill factors, in the fabricated structures. As a result we received samples with diameters both smaller and larger than the ones shown in Figure 5.3.1.

Figure 5.3.2 shows a scanning electron microscope (SEM) image and an atomic force microscope (AFM) image of different sub blocks from one of the samples. The definition

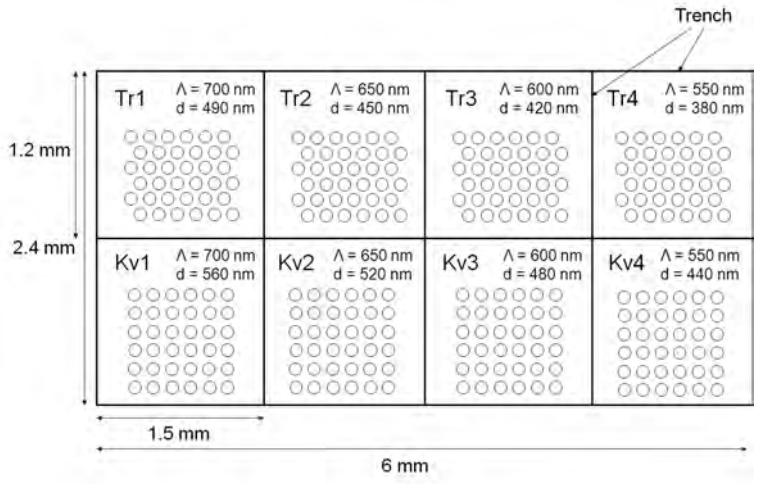

(a)

Figure 5.3.1.: The figure shows the block layout of the samples fabricated by photolithography at IMEC. The lattice period Λ and hole diameter d are shown for each sub-block.

of the cylinders in the array is very good. AFM pictures and SEM cross-sections (not shown) confirm that the depth of the cylinders is close to the target depth of 220 nm.

Sample processing

The samples we received from IMEC had a thickness of about 300 µm, while we had investigated the light-trapping properties of the structures in a 20 µm thick Si slab. Moreover, edge effects from laterally propagating light is much more pronounced in a sub block of 1 mm by 1.4 mm with a thickness of 300 µm than for a thickness of only 20 µm. We therefore decided to thin the samples down to a target thickness of 20 µm.

The process flow for thinning is illustrated in Figure 5.3.3. First a 130 nm thick Ag layer was deposited on a glass microscope slide using thermal evaporation. The patterned Si sample was then attached to the substrate with epoxy with the patterned side facing the Ag. Finally, the Si sample was mechanically lapped to a thickness of about 20 µm and subsequently polished.

The Ag layer plays the role of rear reflector while the oxide layer from the simulations is replaced by the transparent adhesive. In some cases we covered the cylinder array with a 200 nm thick layer of silicon oxide, deposited with PECVD, before we applied the adhesive. Since the refractive index of the adhesive layer is similar to that of silicon oxide, the optical effect of the oxide layer was similar to increasing the thickness of the adhesive layer by 200 nm. However, this effect was negligible since we had a very poor control of the adhesive layer thickness which could reach a thickness of several microns.

The intention of the oxide layer was to have control of the thickness of the low permittivity dielectric, and to subsequently evaporate Ag or Al on top of the oxide layer.

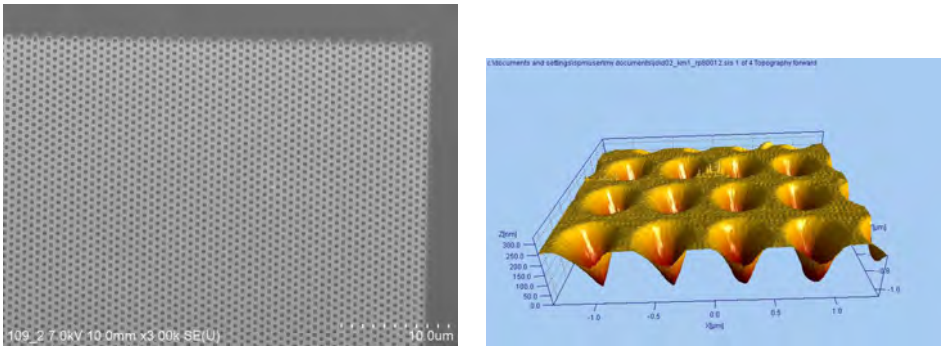

(a) (b)

Figure 5.3.2.: Scanning electron microscope image (left) of a hexagonal pattern of cylinders. An atomic force microscope (AFM) image of a cylinder array with a square lattice is shown to the right. The cylinder walls in the AFM picture are smeared out due to the finite thickness of the AFM-scanning probe. In reality, the walls are near vertical.

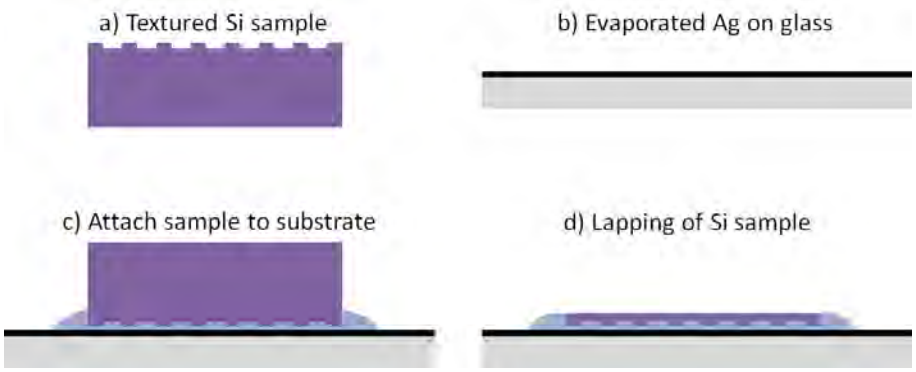

(a)

Figure 5.3.3.: Process flow for preparation of thin samples with back-side light-trapping structures. The patterned Si samples are attached to an Ag coated microscope slide by a thin layer of adhesive. The Si is mechanical lapped and subsequently polished.

However, the 200 nm thick oxide layer exhibited a similar periodic structure as patterned Si substrate, and a subsequent deposition of Ag would result in a textured Ag layer which is known to have significantly higher absorption than a planar Ag layer [117]. Because we could not distinguish between absorption occurring in the Si and in Ag in our optical measurements we wanted to keep the Ag absorption as low as possible. Therefore, we chose to put the Ag layer on the planar glass slab. As a consequence, we lost the possibility of controlling the separation distance between the grating and the reflector.

Optical characterization

We characterized the light-trapping properties of the samples from IMEC by measuring the amount of reflected near infrared light, i.e. 700-1150 nm. Figure 5.3.4 shows reflectance measured with an ellipsometer (see section 5.2.2) and a spatial reflectance map performed at a single wavelength using the semilab (see section 5.2.3).

The eight sub blocks from Figure 5.3.1 are easily distinguished in the reflectance map in Figure 5.3.4. Because the sample is face down, the sub blocks is mirrored around the horizontal axis compared to Figure 5.3.1 and the top left sub block is Kv1, with a square lattice, while the bottom left sub block is Tr1, with a hexagonal lattice. Oscillations with alternating high and low reflectance is easily visible in the reflectance map. We believe this is caused by interference in the Si sample resulting from a non-planar attachment of the sample to the underlying substrate. With a broad banded source such an interference pattern might not be visible, but with a coherent laser source, as is used in this case, the interference pattern will be visible even for a Si thickness of around 20 µm. Interference patterns were also observed for samples without a metal rear reflector. This indicates that the major contribution to the oscillations originates from oscillations within the Si slab and not in the adhesive.

Ellipsometer reflectance measurements were performed on four of the eight sub blocks, named Kv1, Kv3, Tr1 and Tr3. The names and corresponding dimensions are found in Figure 5.3.1. The square lattice Kv1 has the lowest reflectance and therefore best light trapping of the four sub blocks. Tr3 has the highest reflectance. This agrees well with the semilab reflectance map at 968 nm. The same trend is also found from the simulations, but here the reflectance values approach unity at 1150 nm as is expected when the absorption coefficient of Si approaches zero. As explained in section 5.2.2, the uncertainties in reflectance measurements from the ellipsometer are quite large, particularly since only the specular part of the reflectance is measured. We do not know the reason for the sudden shift in reflectance for sub block Tr3 at a wavelength above 1050 nm, but it might be due to an error in the measurement because it occurs at the same wavelength as the ellipsometer changes detector. To reduce the error, each measurement is repeated three times and the values shown in Figure 5.3.4 is an average over these measurements.

The sample (named D02_kp5_rp2) is prepared as shown in Figure 5.3.3, with an additional 200 nm layer of silicon oxide deposited by PECVD on the patterned Si surface prior to application of adhesive. As mentioned in section 5.3.1, this layer is expected to have a negligible effect on the optical measurements. The front surface was etched for 20 seconds in CP5 (5:1:2.5, HNO3:HF:CH3COOH) to remove any residual particles from

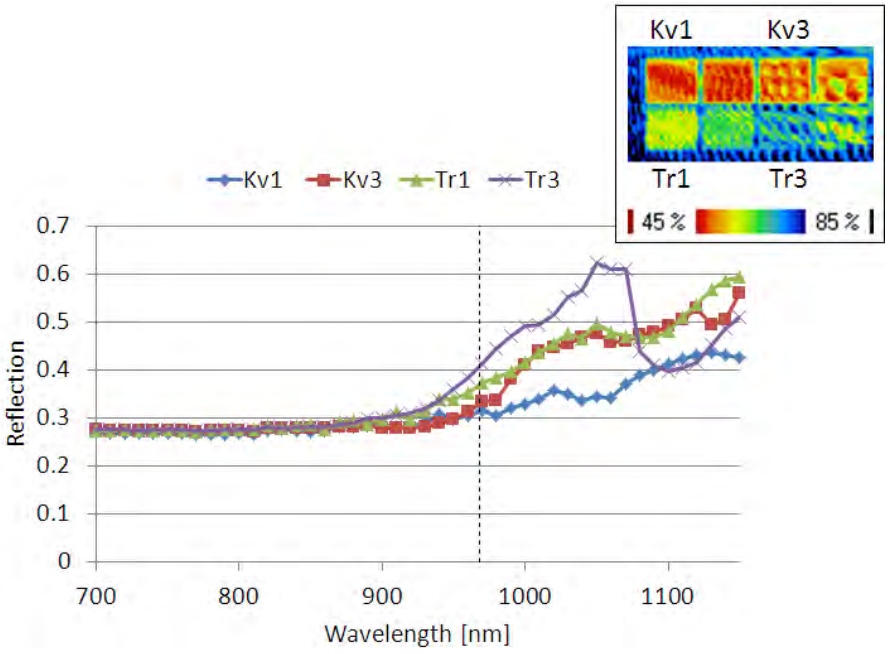

(a)

Figure 5.3.4.: Reflectance from p-polarized light measured with an ellipsometer at an incidence angle of 18 degrees. Kv1 and Kv3 are sub blocks with a quadratic lattice while Tr1 and Tr3 are sub blocks with a triangular lattice. The inset shows a reflectance map at normal incidence for a wavelength of 968 nm. This wavelength is also marked in the ellipsometer data with a dashed vertical line.

Figure 5.3.5.: A two inch Si wafer with a thickness of 50 µm is imprinted with a periodic structure using nanoimprint lithography. The wafer broke during demolding.

the lapping and polishing process. After etching the reflectance corresponded quite well with that of standard polished Si.

5.3.2. Fabrication by nanoimprint lithography

A straight-forward method for implementing periodic light-trapping structures in thin Si solar cells is to fabricate them directly on a thin wafer. In collaboration with Obducat [118] we performed some preliminary tests of imprinting periodic patterns on thin Si wafers. Obducat is a Swedish company which makes nanoimprint lithography (NIL) machines for research and commercial customers. NIL is an interesting tool as it may have the potential for large-scale high-throughput processing, which is crucial for the PV industry. We supplied Obducat with 50 µm and 25 µm thick Si wafers purchased from Universitywafers [119].

Obducat were successful in spin coating of the resist and imprinting the pattern in the resist. They used an existing mold with a periodic structure with a lattice period of 450 nm. However, the wafers broke during demolding, i.e. when removing the stamps. A picture of the broken wafer is shown in Figure 5.3.5. Obducat believe this may be avoided by using sample holders adapted to such thin wafers, for instance a proper vacuum chuck. The 25 µm wafers were also successfully imprinted, but the wafers broke into several more pieces than the 50 µm wafers.

To transfer the pattern from the resist to the Si substrate a plasma etch was performed with an Alcatel AMS 200 I-Speeder machine at Sintef in Oslo. As this was considered an initial investigation we tried two opposite extremes of plasma etching, physical ion milling and pure chemical etching. The result of the ion milling is shown in Figure 5.3.6 while the result of the chemical etching is shown in Figure 5.3.7. Both processes were

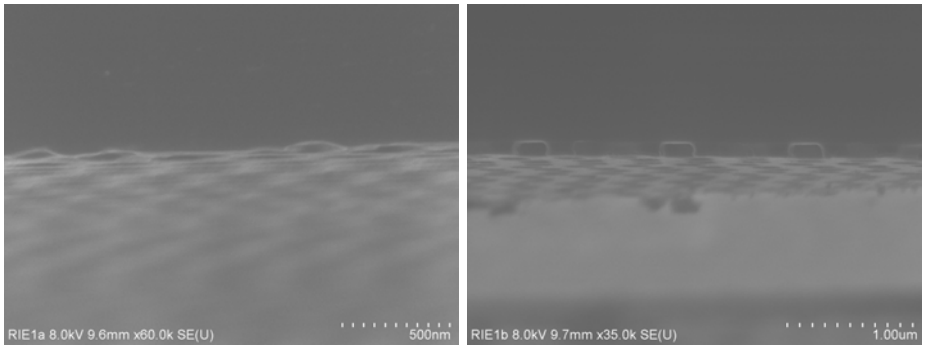

(a) (b)

Figure 5.3.6.: Scanning electron microscope images of a Si wafer covered by a resist pattern prepared by nanoimprint lithography, followed by a physical plasma etch process with C_4F_8 at 1500 W. Etch time on the left hand side is 20 seconds. This is too long and only small bumps with a depth of less than 50 nm remain of the structure. The etch time on the right hand side is 10 seconds. This results in well defined walls and a structure depth of about 110 nm.

performed with a long and a short etch time based on a best guess from operator of the machine.

Our aim was to transfer the pattern from the resist to the Si wafer, while conserving the well-defined structure with straight walls and a flat bottom. For this purpose the physical process with a short etch time was the best process. The limitation of this process is that it is difficult to achieve a greater depth than the thickness of the resist which in this case was slightly above 100 nm. By using a more selective process with alternating passivation and etching steps it should also be possible to achieve a greater structure depth. Figure 5.3.7 shows that the chemical process provides more rounded dimple-like structures. In **Paper VII** we show that such a structure may provide even better light trapping than for instance a cylinder structure. Consequently, chemical etching might therefore be a better alternative than physical etching for fabrication of light trapping structures.

5.3.3. Fabrication by nanosphere lithography

Any fabrication methods where the periodic structures are created by self-assembly are particularly interesting for solar cells due to the possibility low processing costs. One such method is nanosphere lithography. A single layer of monodispersive spheres, arranged in a hexagonal periodic pattern, are here used as a mask for subsequent processing. The mask may be used to transfer the pattern to the underlying substrate or it may be used as a deposition mask for creating a periodic structure.

The fabrication of the monolayers was performed by Einar Haugan [114], a master

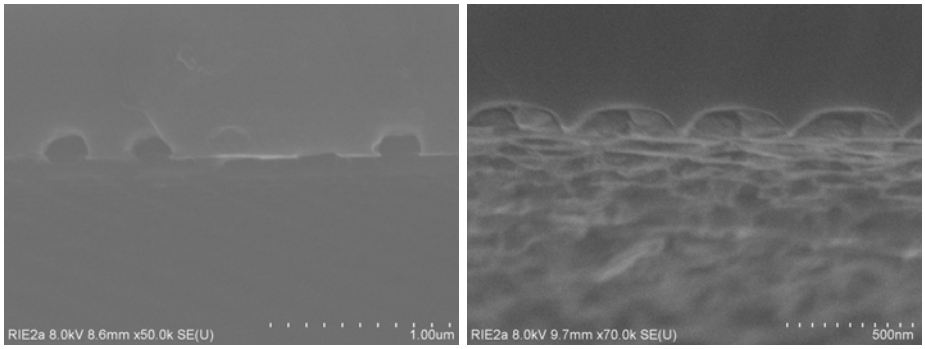

(a) (b)

Figure 5.3.7.: Scanning electron microscope images like in figure 5.3.6, with chemical plasma etch using SF_6. Etch time on the left hand side is 40 seconds, resulting in a structure depth between 125-150 nm and rounded walls. The etch time on the right hand side is 1 minute. This results in highly rounded structures with a depth of around 100 nm.

student in our group. He fabricated the monolayer by spin coating a droplet of monodispersive polystyrene spheres in a water solution onto a Si wafer. The surface of the wafer was pretreated to give it a hydrophilic surface so that the spin coated water based solution would stick to the surface. The focus was mainly on fabrication and process control. With this method it was possible to pattern a 50 µm thick Si wafer with a periodic structure. Figure 5.3.8 shows cylinders transferred to the substrate by this method using Ag catalyzed etching [120].

Multilayer periodic structures, i.e. 3D photonic crystals, were fabricated by two master students from our group, Einar Haugan [114] and Håvard Granlund [121]. The samples were placed in a solution of monodispersive spheres in water. When the water slowly evaporated a colloidal close packed crystal was formed at the surface of the sample. A dielectric was later deposited in the voids of the crystal and the polystyrene spheres were removed by calcination. The resulting structure was an inversion of the original crystal structure, known as an inverted opal structure. This structure may possess a complete photonic bandgap if the dielectric constant is sufficiently large [84].

The work of the two master students resulted in **Paper VI**. My contribution to this work consisted in discussions, particularly concerning structure type and dimensions suitable for light trapping, in optical measurements, and in analysis of the results.

5.4. Summary and status

In this chapter I describe three different roads to fabrication of periodic light-trapping structures; photolithography, nanoimprint lithography and nanosphere lithography.

I showed that periodic light-trapping textures fabricated by photolithography will improve light-trapping compared to a planar surface. More importantly, the light trapping

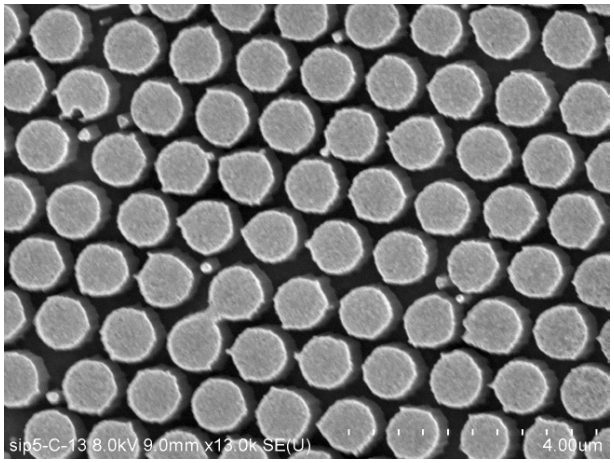

(a)

Figure 5.3.8.: Scanning electron microscope image of a periodic array of cylinders created by silver catalyzed etching at IFE. Picture from Ref. [114].

is observed to vary considerably with grating dimensions, and the variations that we see is also predicted by numerical simulations. Uncertainties must be reduced in the optical measurements to be able to quantify the light trapping and to perform a quantitative comparison with the numerical simulations. This may be achieved by increasing the sample size so that accurate reflection measurements may be performed using an integrating sphere.

Together with Obducat we have investigated the possibility of using nanoimprint lithography (NIL) to fabricate periodic structures on thin Si substrates with a thickness of 25 µm and 50 µm. Obducat imprinted the structures successfully on the thin wafers, but they broke during demolding. This problem may probably be avoided, at least for 50 µm thick wafers, by using sample holders specially designed for thin wafers. In the transfer of the structures to the Si wafer I had help from a skilled machine operator at Sintef and with his initial guess we were able to transfer the pattern to the Si substrate. With some additional optimization he expected that we would also be able to achieve a greater structure depth.

Finally, we showed that periodic structures may be fabricated by a self-assembly method using small monodispersive spheres. This work, performed by two master students in our group, resulted in fabrication of both 2D and 3D periodic structures. The quality of the crystals may be further improved and optical characterization remains for the 2D periodic structure. An interesting continuation of this work would be to deposit a high permittivity dielectric on a 2D periodic template of monodispersive spheres. This may allow a configuration with a planar Si surface covered by a thin optically inactive SiO_x layer and with the periodic structure on top of the SiO_x layer. Such a configuration may provide a very low back-surface recombination velocity, which is crucial for thin high-efficiency solar cells.

A challenge for all the above mentioned designs is how to avoid parasitic absorption

in the back-side mirror. A thin oxide layer deposited on top of a periodic structure will to a certain degree retain the periodic structure of the substrate and so will any subsequently deposited metal films. This may lead to a high parasitic absorption. The texture in the metal will be reduced if the thickness of the oxide layer is increased to several hundred nanometers. This will smooth out the periodic structure at the cost of increased fabrication time. Another option for reducing parasitic absorption is the use of a dielectric Bragg stack on the back side [48, 51, 50], but this will require deposition of multiple thin films.

Optical characterization has so far been limited to measurement of the sample reflectance, and we have assumed that the light not reflected is absorbed in the Si. If the metal back reflector is made of Al, or if it is textured, this assumption may no longer hold, and we need to separate Si absorption from parasitic metal absorption. Absorption in the metal film might be measured with a technique called photothermal deflection spectroscopy (PDS) [122]. Another alternative is to fabricate a complete solar cell and to extract Si absorption indirectly by measuring reflectance together with external quantum efficiency (EQE) [123]. Fabrication of a complete solar cell, however, requires optimization of several processing steps, in particular to control surface passivation and to make good electrical contacts. Additionally, if we want to investigate the effect in a thin solar cell, the handling challenge must also be resolved.

6. Discussion and future perspectives

In this chapter I discuss the results of our work and their relevance for future solar cells. The chapter is divided into three parts. In the first part I discuss our results, motivate the choices that have been made, and try to give some advice for the future based on our experience. In the second part of this chapter I relate our results to existing textures and discuss what implications front-side textures and encapsulation will have on a solar cell with a periodic light-trapping structure. The final part of this chapter concerns fabrication, and I discuss possible fabrication techniques and important factors for synthesizing periodic structures on a large scale.

6.1. Discussion of results

One of the most important challenges for future Si solar cells is to find good solutions for light trapping in thin Si wafers. The goal at the start of my thesis was to investigate the use of photonic crystals to improve light-trapping in solar cells. Literature studies indicated that periodic light-trapping structures might be a promising candidate for this purpose. The wavelength dependent nature of photonic crystals led us to investigate photonic crystals at the rear side of the solar cell where the spectral width of the solar spectrum is significantly narrower than at the front side due to the absorption of short wavelength light in the Si slab. We focused our attention on bi-periodic, or 2D periodic, structures instead of 1D periodic structures. Solar irradiance is unpolarized and 1D structures have a tendency to be most effective for only one polarization. Moreover, 1D structures were more frequently investigated in the literature even though 2D gratings had been suggested to hold a higher potential for light trapping [46].

I started with the investigation of a cylinder structure because fabrication of such a structure is an established process, and because a binary structure is simpler to analyze and requires less computational power than non-binary structures. In **Paper II** we analyze the cylinder structure in the case where the lattice period is either large or small compared to the wavelength of light. For small lattice periods one may apply the effective medium theory to predict grating dimensions for optimal light trapping, while for large lattice periods one may use the interference between tops and valleys of the cylinders to do the same. We used these models improve our understanding of the mechanisms of light trapping and to narrow the degrees of freedom in the search for optimal grating dimensions.

Unwanted absorption in the rear metal reflector was reported in the literature as a particular problem for periodic structures [67]. We aimed at reducing the parasitic absorption by separating the periodic structure from the rear reflector by a low permittivity dielectric. One of our first ideas was to make a combined broad mirror and light coupler

with by using an array of cylinders with a planar layer of silicon oxide on each side of the cylinder structure. We found that such a structure could provide a surprisingly high reflectance of more than 95 % over a wavelength range corresponding to a bandwidth of 30 % (see Figure 4.4.1, bottom). We did not report these results, however, because we quickly discovered that the dimensions that provided broad band reflectance also resulted in poor light coupling. In fact, the structure functioned mostly as a specular reflector. In **Paper I** and **Paper II** we show that the use of an oxide layer to separate the periodic structure from metal reflector significantly reduces parasitic metal absorption. Moreover, the thickness of the oxide layer provides another degree of freedom which may be used to increase the light trapping from the periodic structure.

The shape of the unit cell is likely to influence the light-trapping properties of a periodic structure. We studied the light-trapping potential for periodic structures with unit cells consisting of inverted pyramids, cones, and dimples. The choice of a periodic dimple structure was inspired by recent reports of self-assembled fabrication of such a structure [71]. These structures, which are all non-binary, or oblique, separated themselves from the binary cylinder structure in the fact that they exhibited broader areas of low zero order reflection. This corresponds well with several recent papers which report that oblique shapes are better for light coupling due to a smoother transition in refractive index [124, 59, 60].

In **Paper VII** we show that several different types of oblique structures are indeed capable of providing light trapping that exceeds the light trapping from a periodic cylinder structure. We also found that the optimal lattice period did not vary appreciable between the structures. This is interesting since the optimal lattice periods reported in the literature varies considerably. We achieved best light trapping for lattice periods that allowed many propagating diffraction orders inside the Si slab and only the zero order in the ambient. This is in good agreement with a design criterion recently described by Yu et al. [59].

The symmetry of the unit cell in a periodic structure has been reported to influence light trapping. A 1D blazed grating has been shown to improve light trapping over a symmetric binary grating [47], an effect that was attributed to reduced out-coupling. We extended this principle to a 2D periodic structure and constructed two novel structures without any mirror symmetry. The structures called zigzag (**Paper IV** and **Paper V**) and rose (**Paper III**) have unit cells consisting of planes sloping in two and four different directions. In Figure 6.1.1 we see that the light-trapping potential of these structures is superior to the rest of the structures that we investigated. In fact, in **Paper V** we show that the light-trapping potential of the zigzag structure with an Ag reflector slightly exceeds the Lambertian light-trapping limit at normal incidence when comparing both structures using the same ARC. The Lambertian limit holds for isotropic incident light, and may in principle be exceeded for a narrower set of incidence angles [32] . As expected, the light trapping from the zigzag structure was indeed reduced below the Lambertian limit at non-normal incidence.

Our results show that a one may achieve good light trapping with a wide variety of periodic structures as long as the grating dimensions are chosen correctly. Although a wide set of grating dimensions will result in good light trapping efficiency, a wide set

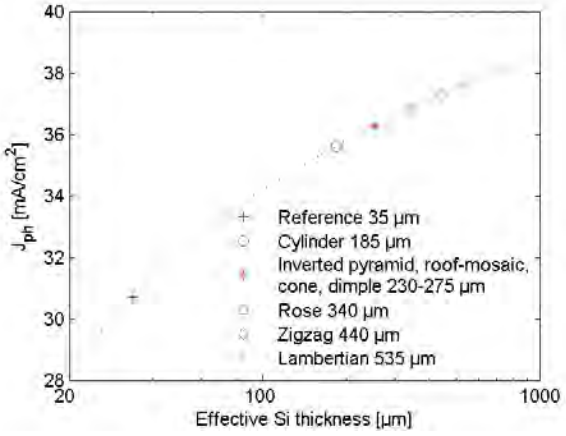

(a)

Figure 6.1.1.: Effective Si thickness of the various structures that we investigated applied to a 20 µm thick slab of Si. All structures have Al reflectors. Also shown is the effective thickness of a slab with an ideal Lambertian reflector and a front side equivalent to the rest of the structures, i.e. planar, with a single layer anti-reflection coating. The figure is published in **Paper VII**.

of grating dimensions will also result in poor light trapping efficiency. The best light trapping is obtained from periodic structures where the unit cells have low symmetry. Even though we have focused our investigation on a slab thickness of 20 µm, considerably thicker than the commonly used thickness of thin-film solar cells, the findings are still relevant also for thinner solar cells. The optimal grating dimensions will probably be different, but the methodology applied is equally relevant also for thin-film cells.

6.2. Comparison with conventional textures and implications of front side textures and encapsulation

Light absorption in a planar wafer is commonly reported in solar cell literature as a metric for evaluation of new light-trapping structures. This is a very simple and easily implemented standard both in simulations and for experimental work. However, this is not a very realistic standard because any texture will usually improve light trapping compared to a planar cell. In the opposite side of the scale is the Lambertian light-trapping limit which gives an upper limit on light trapping. Most light-trapping structures perform somewhere between these two extremes. The most interesting comparison is therefore the comparison with existing light trapping structures.

The common choice of texture for monocrystalline solar cells is random pyramids. These textures are typically found on wafers with a thickness of 150-200 µm and for that reason they are not easily compared with periodic light-trapping structures on much thinner substrates. To be able to compare these different types of structures we used

ray-tracing to investigate what level of light trapping that could be expected from front-side and double-sided pyramids if they were applied to a 20 µm thick wafer. In **Paper VIII** we show that the periodic light-trapping structures, particularly the low-symmetry zigzag structure, exhibit good light trapping at longer wavelengths compared to the pyramids. However, the pyramids provide very low front-side reflection compared to the planar front side used for the periodic back-side structures. The disadvantage of such a planar surface may be reduced with the use of multilayer ARCs and in encapsulated solar cells. Nevertheless, the best pyramidal structure did in fact exceed the zigzag structure with a double-layer anti-reflection coating, despite the fact that the zigzag structure had slightly better light confinement for longer wavelengths. In fact, a double sided random pyramidal structure with an ideal mirror will trap light as well as a Lambertian structure at normal incidence. It should be noted however that we have considered the effective Si thickness in these calculations. This approximation ignores the fact that some Si material will be lost in the process of etching the pyramids.

The possibility for high-quality light trapping with a structure that is as simple to fabricate as the random pyramids will probably limit the use of periodic structures to situations where random pyramidal textures are not applicable. The random pyramidal texture is applicable to monocrystalline wafers grown with a (100) orientation. However, promising ways of making thin solar cells, involving cleaving of Si [25], yields a crystal orientation that does not allow the conventional pyramidal texture. Moreover, the size of the pyramids may also prevent their use when the Si wafers get very thin. Fabrication of periodic structures is of course also difficult and possible fabrication methods will be addressed in the next section.

All solar cells will eventually end up in a solar module encapsulated with glass and a lamination polymer, typically EVA, which has a refractive index close to that of glass. This will change both the front-side reflectance and the critical angle of internal reflection in Si. Firstly, encapsulation will reduce the contrast in refractive index and therefore reduce reflection from the Si surface. This is particularly important if the cell suffers from a high front side reflection. Consequently, encapsulation will reduce reflection more for a planar surface than for a textured surface. Secondly, the presence of the encapsulant will change the critical angle of total internal reflection in Si from about 16 degrees up to about 24 degrees, which will more than double the size of the escape cone. However, light escaping the Si wafer with an angle between 16-24 degrees will still experience total internal reflection at the glass-air interface at the front-side of the solar module. Thus, the light trapping of the solar module should in principle not be affected. Real glass, however, will have non-zero absorption and several reflections within the glass layer will lead to additional optical losses.

What I have not addressed so far is the interaction between a periodically textured back side and a textured front side, which could be either a periodic texture or a conventional texture like the random pyramids. The configuration consisting of a periodic front and rear side is relevant for thin-film solar cells where the solar cell material is deposited on top of a textured substrate. The structure of the substrate will in this case be transferred to the subsequently deposited films [64]. This results in identical periodicity on the front and the rear side of the cell. Thus, this will not affect the number of allowed diffraction

orders, and should therefore not change the light trapping potential of the structure [59]. Such a structure could, however, make it easier to couple the light into the cell since both the front and the rear side will act as light couplers. Moreover, the textured front side would also provide a lower front side reflectance than a planar surface.

The configuration with a conventional pyramidal structure on the front side and a periodic structure on the rear side is a difficult modeling problem because the large front-side structures and the small back-side structures require different modeling tools [125]. It is reasonable to assume that the addition of a light-trapping structure to a solar cell will give a smaller contribution to light trapping if one of the surfaces is textured already. Experimental results have shown that a back-side periodic texture improves light trapping in a 250 µm thick cell with a front side textured with pyramids [56], however, the effect was found to be quite small.

In this thesis we have investigated a photonic crystal applied to the rear side of a solar cell. If we instead were to place the periodic structure on the front side of the cell one might achieve both low front-side reflection and light trapping with the same structure [58, 60]. Since the number of propagating orders in Si is independent of which side the grating is placed, a front-side grating could in principle have as good light trapping as a back-side grating [59]. A front-side grating would of course need to provide low reflection over the whole solar spectrum as well as good light trapping for long wavelengths. Nevertheless, this is achievable with oblique structures and such structures have been shown to hold great potential for light trapping [60].

6.3. Potential for fabrication

Any solar cell process needs to be able to fulfill the requirement of low cost and high throughput. Large scale fabrication of nano-structured surfaces is indeed a big challenge which so far has not been resolved. Photolithography, which is popular in the semiconductor industry, is considered to be too expensive for PV due to the requirement of a significantly lower cost per area. The fabrication methods that have been suggested to have the potential for large scale production of solar cells include nanoimprint lithography [81, 64] or hot embossing and interference (holographic) lithography[82, 61]. Other interesting possibilities include various types of self-assembled structures. One such fabrication method is the use of nanospheres to make 2D [83, 120, 55, 56] and 3D crystals[126, 127]. Another method is the use of anodic etching to produce a periodic dimple pattern [49, 71].

We have looked into both nanoimprint lithography and self-assembled structures (see **Paper VI**) in this thesis. Both methods seem to be achievable also on thinner substrates. The advantage of nanoimprint lithography is the high accuracy that may be achieved and also the fact that a form of nanoimprint lithography is already in use in mass production. Blu-ray discs are made with sub-micron structures using a type of NIL, and this technique has also been investigated to pattern the substrates of thin-film solar cells [64]. Fabrication by self-assembly, on the other hand, has the advantage that it requires no expensive master stamps of photo masks. Moreover, nanosphere lithography does not

put any great amount of stress on the wafer, which is important to avoid breakage of thin wafers. A limiting factor for nanosphere lithography is the quality of the periodic structure. Fabrication involving a nanosphere mask and deposition of a high permittivity dielectric seems to me to be a promising approach. This is demonstrated in Ref. [55] where the Si surface is first given a thermal oxide before silicon carbide is deposited on top of a mono layer of nanospheres. Such a fabrication method yields a planar rear side Si surface and could in principle result in a very good surface passivation.

In this work we have studied periodic structures consisting of Si and silicon oxide. These materials were chosen as they are likely candidates for fabrication and because they have a large contrast in refractive index. To fabricate such a structure one could pattern a resist, or deposit a layer of nanospheres, and transfer the pattern to Si by plasma or wet etching techniques. Another alternative would be to deposit Si on top of a patterned substrate. This method is typically encountered in thin-film photovoltaics and allows the use of cheap substrates that can be easily printed [69]. Unfortunately, deposited Si usually result in low crystalline quality.

A periodically structured metal reflector will induce large parasitic losses in the metal [56], and a planar rear reflector would be preferable. However, the implementation of a planar reflector on the back side of a periodic texture is not straight-forward. One approach could be to use a metal foil with a low permittivity dielectric that could be bonded by some means to a patterned Si wafer. If processing does not allow a planar metal reflector, the parasitic absorption will also be reduced by moving the metal reflector away from the grating using a separation layer of low refractive index. At the same time, the texture size is also expected to be reduced with increasing thickness of the separation layer. Yet another possibility to reduce parasitic absorption is to use a Bragg reflector [48, 51].

In **Paper VII** we show that low symmetry in periodic structures is favorable for light trapping. The complexity of the non-symmetric structures we propose, however, makes them difficult to fabricate. Luckily, there are simpler ways to break the symmetry than the structures that we have suggested. One such structure could be an off-centered pyramidal shape as proposed in [60]. Dry etching or sputtering at an angle to a nanosphere mask is an example of how such asymmetric structures could be achieved. Another interesting method of breaking symmetries is the use of many very fine binary structures within a single unit cell [59]. Variation in the pattern density would result in variation in the effective refractive index and arbitrary patterns could be achieved. However, this approach requires very small pattern definition.

Compared to the rest of the semiconductor industry, solar cell fabrication is more robust with respect to small defects and imperfections. If a small part of a surface texture is missing this will only reduce the light trapping in this particular area and not destroy the whole solar cell. This makes solar cells versatile when it comes to choice of fabrication technology. The accuracy that is actually needed in fabrication of periodic structures is not explored in this thesis. Results from **Paper II** show that a broad range of grating dimensions will provide good light trapping. This indicates that there should be a certain tolerance for fabrication inaccuracies.

7. Conclusion

In this thesis I have investigated potential for light trapping by the use of bi-periodic back-side photonic crystal structures. The aim has been to understand the mechanisms of light trapping in this type of photonic crystals, to identify structures that can provide good light trapping, and to investigate their light-trapping potential and possibility for fabrication.

The first structure we investigated was a cylinder array together with a planar oxide layer and a metal reflector. With this structure we found that we could predict which grating and oxide layer thicknesses that favored light trapping by using simplified models for the case of small and large lattice periods. For large lattice periods we used the phase difference between the light reflected from the cylinders and the from the area surrounding the cylinders, while for small lattice periods we found that the effective medium model was well suited to predict the light trapping properties. For lattice periods in between these two extremes, the light-trapping behavior was influenced by both models.

In addition to the cylinder structure we investigated various other types of structures such as dimples, cones, and inverted pyramids, and we found that the optimal lattice period did not vary appreciably between the structures. The general trend was that the best light trapping was achieved when the lattice periods were slightly smaller than the wavelength of light in air. This allows several diffraction orders to propagate in Si and only the zero order to propagate in air. In fact, this analysis also explained the behavior of the various structures under oblique angles of incidence. Incidence angles that allowed more diffraction orders to propagate in the ambient generally showed a reduction in light-trapping efficiency.

A class of structures that stood out from the rest was the structures that exhibited a lower symmetry in their unit cell. These structures, which we named the rose and the zigzag structure, consisted of planes sloping in two or four different directions. Although their optimal lattice period were similar to the rest of the structures, their light-trapping efficiency was considerably better. The diffraction pattern from these structures displayed a lower symmetry then the rest of the structures and it is this property that we believe reduces the rate of out-coupling and therefore leads to a longer dwell time for the light within the cell. This explanation is in agreement with what we have found reported in the literature.

We compared the light-trapping potential of the various structures in the same numerical model, consisting of a 20 µm thick slab of Si. The photogenerated current density J_{ph} of the different structures was calculated and their optical thickness was extracted by comparing to the propagation distance required in Si to provide the same J_{ph}. The cylinder structure show an increase in optical thickness of about 9, the dimples, cones and inverted pyramids range from optical thicknesses of 12 to 14, the rose structure has

an optical thickness of 17, while the zigzag structure exhibits an optical thickness of 22. Replacing the Al absorber with an Ag absorber increases optical thickness of the zigzag structure to between 28 and 29. As a comparison, an ideal randomizing Lambertian reflector with the same front side yields an optical thickness below 27. Lambertian light trapping has been shown to be the upper limit on light confinement under isotropic illumination, and is commonly used as a benchmark when assessing the potential of light-trapping structures.

To compare the light-trapping potential of photonic crystals with the light-trapping potential of random pyramidal structures, we used ray tracing to calculate the J_{ph} of different pyramidal structures. We found that a double-sided pyramidal structure with an ideal non-absorbing reflector obtained the same light-trapping potential as a structure with random pyramids at the front side and a Lambertian rear reflector. A double-sided pyramidal structure with a rear surface covered by an Al or Ag reflector separated from the bulk Si by a thin layer of oxide showed a potential J_{ph} slightly above the best of the periodic structures which consisted of the zigzag structure with a similar reflector and a double-layer anti-reflection coating. The success of the random pyramids originates in much lower front-side reflectance than the periodic structures with their planar front sides. This advantage is reduced for multilayer anti-reflection coatings and for encapsulated solar cells. The high-quality light trapping exhibited by the random pyramidal structures will most likely limit the use of photonic crystals to cases where random pyramidal structures may not be applied, such as very thin solar cells and Si substrates which have a different crystal orientation than [100].

I have described three different approaches to fabrication of periodic structures: photolithography, nanoimprint lithography, and nanosphere lithography. I found a qualitative agreement between optical measurements on samples prepared by photolithography and numerical simulations. A spatial reflectance mapping revealed large variations in light-trapping properties from various cylinder structures where the only difference between the structures was different choices of grating dimensions.

The key to utilize periodic structures in commercial solar cells will be to fabricate these structures at a low cost, something that might be possible using nanoimprint lithography or self-assembled structures. We investigated these methods on 50 µm thick Si wafers. Nanoimprint was performed by a company that makes machines for nanoimprint lithography. The wafer broke during the process due to the lack of a proper sample holder, but the imprinting step was successful and pattern could be transferred to the Si substrate on the broken pieces. The pattern was successfully transferred with a physical plasma etch. Self-assembled colloidal structures were explored by two master students in our group, who developed methods for fabrication of monolayer and multilayer photonic crystals. They used a monolayer as a deposition mask and were able to fabricate a periodic structure of cylinders and inverted pyramids with a sub-micron lattice period which was determined by the diameter of the colloids. With improved process control, this method could allow fabrication of periodic structures on large areas on very thin Si wafers with a thickness of less than 50 µm.

8. Further work

In the course of a PhD thesis a great number of ideas appear that one does not have the time to investigate any further. The ideas that are pursued usually result in even more questions and ideas, thus the number of loose ends tends to be growing with time. Here I list some points for future work that I have not had the time to follow. The list is prioritized after which points I believe deserves the most attention.

1. *Further investigation of fabrication of periodic structures*: A suitable method for fabrication of photonic crystals must be in place if such structures are to be realized in commercial solar cells. A further investigation of methods for low-cost high-throughput fabrication of photonic crystals is therefore needed. In particular I would like to explore the possibility of fabrication of photonic crystals with a low symmetry unit cell using some type of nano-imprint lithography and nanosphere lithography.

2. *Simulation and fabrication of a thin solar cell with a decoupled rear side photonic crystal*: To achieve as low surface recombination as possible it is very tempting to make a solar cell with a planar front and rear side. The light trapping properties can be taken care of by a photonic crystal which is separated from the active solar cell material with an optically thin dielectric layer. Fabrication of a complete solar cell would also make it possible to measure the parasitic absorption in the rear reflector and the back-side surface recombination velocity.

3. *Explore nonlinear effects in photonic crystals*: The field strength is enhanced at certain areas inside a photonic crystal. Is it possible to find a structure which combines a large field enhancement with good light trapping? Such a field enhancement could be used to improve up-conversion efficiencies. This will require numerical simulations, fabrication and characterization.

4. *Photonic crystals applied to the front side*: Is it possible to find a periodic structure that has good anti-reflection properties and low absorption for the whole solar spectrum at the same time as it serves the purpose of light trapping for the longer wavelengths?

5. *Combining ray-trace and RCWA*: The idea is to use RCWA to calculate the scattering function of the grating and to implement a surface with equivalent scattering properties in a ray-tracing program. This work was already started by Peters et al. [125] for uniperiodic gratings. Is it a viable approach also for bi-periodic gratings and can it be automated in a good way?

6. *Implications of imperfections in the photonic crystal*: Since all real crystals will have defects and small deviations from a perfect structure it is important to know how this will affect the light-trapping properties. The sensitivity of the structures to imperfections is a decisive factor when determining which fabrication methods that may be applied. Imperfections could be explored numerically by the use of super-cell methodology.

7. *Effects of encapsulation and front-side texture*: How will encapsulation and a front-side texture affect the light-trapping properties of a periodic rear-side structure?

Bibliography

[1] International Energy Agency (IEA). http://www.iea.org/weo/electricity.asp, 2011.

[2] United Nations. http://esa.un.org/wpp/unpp/panel_population.htm, 2011.

[3] U.S. Energy Information Administration. International energy outlook 2011, www.eia.gov/ieo/pdf/0484(2011).pdf.

[4] The Guardian. http://www.guardian.co.uk/environment/2009/dec/18/how-copenhagen-text-was-changed, 2009.

[5] The Economist. http://www.economist.com/node/15912964, 2010.

[6] Paula Mints. The history and future of incentives and the photovoltaic industry and how demand is driven. *Proc. 26th PVSEC, Hamburg, Germany*, pages 4420 – 4424, 2011.

[7] C. Breyer and A. Gerlach. Global overview on grid-parity event dynamics. *Proc. 25th PVSEC, Session 6CV.4.11, Valencia, Spain*, pages 5283 – 5304, 2010.

[8] PVX spot market price index SolarServer. http://www.solarserver.de/, 2011.

[9] Eli Yablonovitch. Inhibited Spontaneous Emission in Solid-State Physics and Electronics. *Phys. Rev. Lett.*, 58(20):2059–2062, May 1987.

[10] William Shockley and Hans J. Queisser. Detailed balance limit of efficiency of p-n junction solar cells. *J. Appl. Phys.*, 32(3):510–519, 1961.

[11] Jianhua Zhao, Aihua Wang, and Martin A. Green. 24.5% Efficiency silicon PERT cells on MCZ substrates and 24·7% efficiency PERL cells on FZ substrates. *Progress in Photovoltaics: Research and Applications*, 7(6):471–474, 1999.

[12] Martin A. Green, Keith Emery, Yoshihiro Hishikawa, Wilhelm Warta, and Ewan D. Dunlop. Solar cell efficiency tables (version 38). *Progress in Photovoltaics: Research and Applications*, 19(5):565–572, 2011.

[13] From http://www.zianet.com/daystar/Spectrum.html, 2011.

[14] Jenny Nelson. *The Physics of Solar Cells*. World Scientific Publishing, first edition, 2003.

[15] American Society for Testing and spectrum G173-03 Materials (ASTM). http://rredc.nrel.gov/solar/spectra/am1.5/.

[16] Emmanuel Van Kerschaver and Guy Beaucarne. Back-contact solar cells: a review. *Progress in Photovoltaics: Research and Applications*, 14(2):107–123, 2006.

[17] M. A. Green and University of New South Wales. *Silicon solar cells: advanced principles & practice; p. 46*. Centre for Photovoltaic Devices and Systems, University of New South Wales, Kensington, 1995.

[18] Joerg Isenberg and Wilhelm Warta. Free carrier absorption in heavily doped silicon layers. *Appl. Phys. Lett.*, 84(13):2265–2267, 2004.

[19] M. A. Green. *Crystalline Silicon Solar Cells. In Clean Electricity from Photo-Voltaics; Chapter 4*. Archer, M. D., Hill, R., Eds.; Imperial College Press: London, 2001.

[20] International technology roadmap for photovoltaics (itrpv.net), second edition, March 2011.

[21] A. W. Blakers, K. J. Weber, M. F. Stuckings, S. Armand, G. Matlakowski, A. J. Carr, M. J. Stocks, A. Cuevas, and T. Brammer. 17 % efficient thin-film silicon solar cell by liquid-phase epitaxy. *Progress in Photovoltaics: Research and Applications*, 3:193–195, 1995.

[22] Karlheinz Feldrapp, Renate Horbelt, Richard Auer, and Rolf Brendel. Thin-film (25.5 μm) solar cells from layer transfer using porous silicon with 32.7 mA/cm^2 short-circuit current density. *Progress in Photovoltaics: Research and Applications*, 11(2):105–112, 2003.

[23] M. Ernst and R. Brendel. Large area macroporous silicon layers for monocrystalline thin-film solar cells. In *Photovoltaic Specialists Conference (PVSC), 2010 35th IEEE*, pages 003122 – 003124, 2010.

[24] R. A. Rao, L. Mathew, S Saha, S Smith, D Sarkar, R. Garcia, R Stout, A. Gurmu, E. Onyegam, D. Ahn, D. Xu, D. Jawarani, J. Fossum, and S. Banerjee. A novel low-cost 25 μm thin exfoliated monocrystalline si solar cell technology. In *Photovoltaic Specialists Conference (PVSC), 2011 37th IEEE*, 2011.

[25] F. Henley, A. Lamm, S. Kang, Z. Liu, and L. Tian. Direct film transfer (DFT) technology for kerf-free silicon wafering. *Proc. 23rd PVSEC, Valencia, Spain*, pages 1090 – 1093, 2008.

[26] F. Henley, S. Kang, A. Brailove, and A. Fujisaka. Kerf-free wafering for high-volume, high-efficiency c-si cell. *Proc. 26th PVSEC, Hamburg, Germany*, pages 971 – 978, 2011.

[27] H. Glavish, G. Ryding, and T. H. Smick. Ion source assembly for ion implantation apparatus and a method of generating ions therein, 2011.

[28] C. M. Herzinger, B. Johs, W. A. McGahan, J. A. Woollam, and W. Paulson. Ellipsometric determination of optical constants for silicon and thermally grown silicon dioxide via a multi-sample, multi-wavelength, multi-angle investigation. *J. Appl. Phys.*, 83:3323–3336, 1998.

[29] Thomas Lauinger, Jan Schmidt, Armin G. Aberle, and Rudolf Hezel. Record low surface recombination velocities on 1 Ωcm p-silicon using remote plasma silicon nitride passivation. *Applied Physics Letters*, 68(9):1232–1234, 1996.

[30] A. Goetzberger. Optical confinement in thin si-solar cells by diffuse back reflectors. *In proceedings of the 15th IEEE Photovoltaic Specialists Conference*, pages 867–870, 1981.

[31] Eli Yablonovitch and George D. Cody. Intensity enhancement in textured optical sheets for solar cells. *IEEE Trans. Electron. Dev.*, 29:300–305, 1982.

[32] Eli Yablonovitch. Statistical ray optics. *J. Opt. Soc. Am.*, 72(7):899–907, 1982.

[33] H. W. Deckman, C. R. Wronski, H. Witzke, and E. Yablonovitch. Optically enhanced amorphous silicon solar cells. *Applied Physics Letters*, 42(11):968–970, 1983.

[34] T. Tiedje, B. Abeles, J. M. Cebulka, and J. Pelz. Photoconductivity enhancement by light trapping in rough amorphous silicon. *Applied Physics Letters*, 42(8):712–714, 1983.

[35] Jeffrey E. Cotter. Optical intensity of light in layers of silicon with rear diffuse reflectors. *Journal of Applied Physics*, 84(1):618–624, 1998.

[36] Antonio Luque and Steven Hegedus. *Handbook of Photovoltaic Science and Engineering*. John Wiley & Sons Ltd, 2003.

[37] D. H. Macdonald, A. Cuevas, M. J. Kerr, C. Samundsett, D. Ruby, S. Winderbaum, and A. Leo. Texturing industrial multicrystalline silicon solar cells. *Solar Energy*, 76:277–283, 2004.

[38] A. Wang, J. Zhao, and M. A. Green. 24% efficient silicon solar cells. *Applied Physics Letters*, 57(6):602 –604, 1990.

[39] A.W. Smith and A. Rohatgi. Ray tracing analysis of the inverted pyramid texturing geometry for high efficiency silicon solar cells. *Solar Energy Materials and Solar Cells*, 29(1):37 – 49, 1993.

[40] Jessica Davina Hylton. *Light coupling and light trapping in alkaline etched multicrystalline silicon wafers for solar cells*. PhD thesis, University of Utrecht and Energy research Center of Netherlands (ECN), 2006.

[41] Patrick Campbell and Martin A. Green. High performance light trapping textures for monocrystalline silicon solar cells. *Solar Energy Materials and Solar Cells*, 65(1-4):369 – 375, 2001.

[42] R. Brendel. Coupling of light into mechanically textured silicon solar cells: A ray tracing study. *Progress in Photovoltaics: Research and Applications*, 3(1):25–38, 1995.

[43] A.W. Smith and A. Rohatgi. A new texturing geometry for producing high efficiency solar cells with no antireflection coatings. *Solar Energy Materials and Solar Cells*, 29(1):51 – 65, 1993.

[44] C. Beneking, B. Rech, S. Wieder, O. Kluth, H. Wagner, W. Frammelsberger, R. Geyer, P. Lechner, H. Rübel, and H. Schade. Recent developments of silicon thin film solar cells on glass substrates. *Thin Solid Films*, 351(1-2):241 – 246, 1999.

[45] O. Kluth, B. Rech, L. Houben, S. Wieder, G. Schöpe, C. Beneking, H. Wagner, A. Löffl, and H. W. Schock. Texture etched ZnO:Al coated glass substrates for silicon based thin film solar cells. *Thin Solid Films*, 351(1-2):247 – 253, 1999.

[46] P. Sheng, A. N. Bloch, and R. S. Stepleman. Wavelength-selective absorption enhancement in thin-film solar cells. *Appl. Phys. Lett.*, 43(6):579–581, 1983.

[47] Claus Heine and Rudolf H. Morf. Submicrometer gratings for solar energy applications. *Applied Optics*, 34(14):2476–2482, May 1995.

[48] Peter Bermel, Chiyan Luo, and John D. Joannopoulos. Improving thin-film crystalline silicon solar cell efficiencies with photonic crystals. *Optics Express*, 15(25):16986–17000, 2007.

[49] H. Sai and M. Kondo. Effect of self-orderly textured back reflectors on light trapping in thin-film microcrystalline silicon solar cells. *J. Appl. Phys.*, 105:094511, 2009.

[50] D. Zhou and R. Biswas. Photonic crystal enhanced light-trapping in thin film solar cells. *J. Appl. Phys.*, 103:093102, 2008.

[51] James G. Mutitu, Shouyuan Shi, Caihua Chen, Timothy Creazzo, Allen Barnett, Christiana Honsberg, and Dennis W. Prather. Thin film silicon solar cell design based on photonic crystal and diffractive grating structures. *Optics Express*, 16(19):15238–15248, September 2008.

[52] L. Zeng, P. Bermel, Y. Yi, A. Alamariu, K. A. Broderick, J. Liu, C. Hong, X. Duan, J Joannopoulos, and L. C. Kimerling. Demonstration of enhanced absorption in thin film si solar cells with textured photonic crystal back reflector. *Applied Physics Letters*, 93:221105, 2008.

[53] A. Campa, J. Krc, F. Smole, and M. Topic. Potential of diffraction gratings for implementation as a metal back reflector in thin-film silicon solar cells. *Thin Solid Films*, 516:6963–6967, 2008.

[54] R. Biswas, D. Zhou, and L. Garcia. Simulation of plasmonic crystal enhancement of thin film solar cell absorption. *Mat. Res. Soc. Symp. Proc.*, 1153, 2009.

[55] S. Janz, P. Voisin, D. Suwito, M. Peters, M Hermle, and S. W. Glunz. Photonic crystals as rear-side diffusers and reflectors for high efficiency silicon solar cells. *Proc. 26th PVSEC, Hamburg, Germany*, pages 1529–1533, 2009.

[56] P. Berger, H. Hauser, D. Suwito, S. Janz, M. Peters, B. Bläsi, and M. Hermle. Realization and evaluation of diffractive systems on the back side of silicon solar cells. *Proc. of SPIE*, 7725:772504–1, 2010.

[57] A. Gombert, K. Rose, A. Heinzel, W. Horbelt, C. Zanke, B. Bläsi, and V. Wittwer. Antireflective submicrometer surface-relief gratings for solar applications. *Sol. Energy Mater. Sol. Cells*, 54:333–342, 1998.

[58] H. Sai, Y. Kanamori, K. Arafune, Y. Ohshita, and M. Yamaguchi. Light trapping effect of submicron surface textures in crystalline si solar cells. *Progress in Photovoltaics: Research and Applications*, 15:415–423, 2007.

[59] Zongfu Yu, Aaswath Raman, and Shanhui Fan. Fundamental limit of light trapping in grating structures. *Optics Express*, 18(103):366–380, 2010.

[60] Sang Eon Han and Gang Chen. Toward the lambertian limit of light trapping in thin nanostructured silicon solar cells. *Nano Lett.*, 10:4692–4696, 2010.

[61] C. Eisele, C. E. Nebel, and M. Stutzmann. Periodic light coupler gratings in amorphous thin film solar cells. *Journal of Applied Physics*, 89:7722–7726, 2001.

[62] H. Stiebig, N. Senoussaoui, C. Zahren, C. Haase, and J. Müller. Silicon thin-film solar cells with rectangular-shaped grating couplers. *Progress in Photovoltaics: Research and Applications*, 14(1):13–24, 2006.

[63] C. Haase and H. Stiebig. Thin-film silicon solar cells with efficient periodic light trapping texture. *Appl. Phys. Lett.*, 91:061116, 2007.

[64] O. Isabella, A. Campa, M. Heijna, W. J. Soppe, R. van Erven, R. H. Franken, H. Borg, and M. Zeman. Diffraction gratings for light trapping in thin-film silicon solar cells. *Proc. 23rd PVSEC, Valencia, Spain*, pages 2320 – 2324, 2008.

[65] Darin Madzharov, Rahul Dewan, and Dietmar Knipp. Influence of front and back grating on light trapping in microcrystalline thin-film silicon solar cells. *Optics Express*, 19:A95–A107, 2011.

[66] S. H. Zaidi, R. Marquadt, B. Minhas, and J. W. Tringe. Deeply etched grating structures for enhanced absorption in thin c-Si solar cells. In *Proc. Conf Photovoltaic Specialists Conf. Record of the Twenty-Ninth IEEE*, pages 1290–1293, 2002.

[67] M.T. Gale, B.J. Curtis, H Kiess, and R Morf. Design and fabrication of submicron structures for light trapping in silicon solar cells. *Proc. SPIE*, 1272:60–66, 1990.

[68] Andrej Campa, Janez Krc, and Marko Topic. Analysis and optimisation of microcrystalline silicon solar cells with periodic sinusoidal textured interfaces by two-dimensional optical simulations. *Journal of Applied Physics*, 105(8):83107, 2009.

[69] F.-J. Haug, T. Söderström, M. Python, V. Terrazzoni-Daudrix, X. Niquille, and C. Ballif. Development of micromorph tandem solar cells on flexible low-cost plastic substrates. *Solar Energy Materials and Solar Cells*, 93:884 – 887, 2009.

[70] Ning-Ning Feng, J. Michel, Lirong Zeng, Jifeng Liu, Ching-Yin Hong, L. C. Kimerling, and Xiaoman Duan. Design of highly efficient light-trapping structures for thin-film crystalline silicon solar cells. *IEEE transactions on electron devices*, 54(8):1926–1933, 2007.

[71] H. Sai and et al. Back surface reflectors with periodic textures fabricated by self-ordering process for light trapping in thin-film microcrystalline silicon solar cells. *Sol. Energy Mater. Sol. Cells*, 93:1087–1090, 2009.

[72] I. Tobías, A. Luque, and A. Martí. Light intensity enhancement by diffracting structures in solar cells. *J. Appl. Phys.*, 104:034502, 2008.

[73] J.M. Gee. Optically enhanced absorption in thin silicon layers using photonic crystals. In *Proc. Conf Photovoltaic Specialists Conf. Record of the Twenty-Ninth IEEE*, pages 150 – 153, 2002.

[74] Z. Yu, A. Raman, and S. Fan. Fundamental limit of nanophotonic light-trapping in solar cells. *In proceedings of Optics for Solar Energy, OSA Technical Digest (CD), paper PDSWB1*, 2010.

[75] Onur Kilic, Michel Digonnet, Gordon Kino, and Olav Solgaard. Controlling uncoupled resonances in photonic crystals through breaking the mirror symmetry. *Optics Express*, 16:13090–13103, 2008.

[76] Vivian E. Ferry, Marc A. Verschuuren, Hongbo B. T. Li, Ewold Verhagen, Robert J. Walters, Ruud E. I. Schropp, Harry A. Atwater, and Albert Polman. Light trapping in ultrathin plasmonic solar cells. *Optics Express*, 18(102):237–245, 2010.

[77] C. Haase and H. Stiebig. Optical properties of thin-film silicon solar cells with grating couplers. *Progress in Photovoltaics: Research and Applications*, 14:629–641, 2006.

[78] M. Niggemann, M. Glatthaar, A. Gombert, A. Hinsch, and V. Wittwer. Diffraction gratings and buried nano-electrodes - architectures for organic solar cells. *Thin Solid Films*, 451-452:619 – 623, 2004.

[79] Benjamin Curtin, Rana Biswas, and Vikram Dalal. Photonic crystal based back reflectors for light management and enhanced absorption in amorphous silicon solar cells. *Applied Physics Letters*, 95(23):231102, 2009.

[80] J. Zhao, A. Wang, P. P. Altermatt, S. R. Wenham, and M. A. Green. 24 % efficient perl silicon solar cell: Recent improvements in high efficiency silicon cell research. *Sol. Energy Mater. Sol. Cells*, 41/42:87–99, 1996.

[81] M. Heijna, J. Loffler, B. Van Aken, W. Soppe, H. Borg, and P. Peeters. Nanoimprint lithography of light trapping structures in sol-gel coatings for thin film silicon solar cells. *Mat. Res. Soc. Symp. Proc.*, 1101, 2008.

[82] S. H. Zaidi, J. M. Gee, and D.S. Ruby. Diffraction grating structures in solar cells. *28th IEEE photovoltaic specialists conference*, pages 395–398, 2000.

[83] H. W. Deckman and J. H. Dunsmuir. Natural lithography. *Applied Physics Letters*, 41(4):377 –379, 1982.

[84] D. Joannopoulos, John, Steven G. Johnson, Joshua N. Winn, and Robert D. Meade. *Photonic Crystals: Molding the Flow of Light.* Princeton University Press, 2. edition, 2008.

[85] Sajeev John. Strong localization of photons in certain disordered dielectric superlattices. *Phys. Rev. Lett.*, 58(23):2486–2489, 1987.

[86] Kenneth C. Johnson. *Grating Diffraction Calculator (GD-Calc) - Coupled-Wave Theory for Biperiodic Diffraction Gratings*, 2006.

[87] Michel Nevière and Evgeny Popov. *Light propagation in periodic media.* Marcel Dekker, Inc., 2003.

[88] M. G. Moharam and T. K. Gaylord. Rigorous coupled-wave analysis of planar-grating diffraction. *J. Opt. Soc. Am.*, 71:811–818, 1981.

[89] L. Li. Formulation and comparison of two recursive matrix algorithms for modeling layered diffraction gratings. *J. Opt. Soc. Amer. A*, 13:1024–1035, 1996.

[90] Lifeng Li. New formulation of the fourier modal method for crossed surface-relief gratings. *J. Opt. Soc. Am. A*, 14:2758–2767, 1987.

[91] Hallvard Angelskår. *Diffractive optical elements for spectroscopy.* PhD thesis, Faculty of Mathematics and Natural Sciences, University of Oslo, 2010.

[92] F. Llopis and I. Tobias. Influence of texture feature size on the optical performance of silicon solar cells. *Progress in Photovoltaics: Research and Applications*, 13:27–36, 2005.

[93] A. S. Sudbø. Why are accurate computations of mode fields in rectangular dielectric waveguides difficult? 10(4):418–419, 1992.

[94] A. Taflove and C. Hagness, S. *Computational Electrodynamics: The Finite-Difference Time-Domain Method.* Artech House Publishers, 3. edition, 2005.

[95] David Thorp and Stuart R. Wenham. Ray-tracing of arbitrary surface textures for light-trapping in thin silicon solar cells. *Solar Energy Materials and Solar Cells*, 48(1-4):295 – 301, 1997.

[96] A. A. Abouelsaood, M. Y. Ghannam, and A. S. Al Omar. Limitations of ray tracing techniques in optical modeling of silicon solar cells and photodiodes. *Journal of Applied Physics*, 84(10):5795–5801, 1998.

[97] TITAN computing facilities at UiO, hosted by USIT by the VD (Research Computing Services) group. http://www.usit.uio.no/suf/vd/.

[98] H. A. Macleod. *Thin-Film Optical Filters*. Taylor & Francis, 3. edition, 2001.

[99] Kenneth C. Johnson. Grating Diffraction Calculator (GD-Calc). http://software.kjinnovation.com/GD-Calc.html.

[100] MATLAB. http://www.mathworks.se/index.html.

[101] Kenneth C. Johnson. *Grating Diffraction Calculator (GD-Calc) - Demo and Tutorial Guide*.

[102] Ian Marius Peters. *Photonic concepts for solar cells*. PhD thesis, Albert Ludwig University of Freiburg, 2009.

[103] Kenneth C. Johnson. *Optical Simulation of Grating Diffraction in MATLAB*.

[104] M. A. Green and M. J. Keevers. Optical properties of intrinsic silicon at 300 K. *Progress in Photovoltaics: Research and Applications*, 3:189–192, 1995.

[105] Edward. D. Palik, editor. *Handbook of optical constant of solids*. Academic Press, 1985.

[106] Ardavan F. Oskooi, David Roundy, Mihai Ibanescu, Peter Bermel, J. D. Joannopoulos, and Steven G. Johnson. MEEP: A flexible free-software package for electromagnetic simulations by the FDTD method. *Computer Physics Communications*, 181:687–702, 2010.

[107] P. Campbell and M. A. Green. Light trapping properties of pyramidally textured surfaces. *J. Appl. Phys.*, 62:243–249, 1987.

[108] J. M. Rodríguez, I. Tobías, and A. Luque. Random pyramidal texture modelling. *Solar Energy Materials and Solar Cells*, 45(3):241 – 253, 1997.

[109] TracePro. http://www.lambdares.com/software_products/tracepro/.

[110] Stephen A. Campbell. *The science and engineering of microelectronic fabrication*. Oxford university press, 2001.

[111] Kurt Ronse. Optical lithography - a historical perspective. *Comptes Rendus Physique*, 7(8):844 – 857, 2006.

[112] ePIXfab - The silicon photonics platform. http://www.epixfab.eu/.

[113] Stephen Y. Chou, Peter R. Krauss, and Preston J. Renstrom. Imprint of sub-25 nm vias and trenches in polymers. *Applied Physics Letters*, 67(21):3114–3116, 1995.

[114] Einar Haugan. Colloidal crystals as templates for light harvesting structures in solar cells. Master's thesis, Norwegian University of Science and Technology, 2011.

[115] Leonard M. Hanssen and Keith A. Snail. *Integrating Spheres for Mid- and Near-infrared Reflection Spectroscopy. Handbook of Vibrational Spectroscopy.* 2006.

[116] J. A. Wollam and Co. *User manual: Guide to using Wvase32. A short course in ellipsometry*, 2001.

[117] J. Springer, A. Poruba, L. Mullerova, M. Vanecek, O. Kluth, and B. Rech. Absorption loss at nanorough silver back reflector of thin-film silicon solar cells. *Journal of Applied Physics*, 95(3):1427–1429, 2004.

[118] Obducat. www.obducat.com.

[119] UniversityWafer. www.universitywafer.com/.

[120] Z. Huang, H. Fang, and J. Zhu. Fabrication of silicon nanowire arrays with controlled diameter, length, and density. *Advanced Materials*, 19(5):744–748, 2007.

[121] Håvard Granlund. Fabrication of photonic crystal using self assembly. Master's thesis, Norwegian University of Science and Technology, 2009.

[122] W. B. Jackson, N. M. Amer, A. C. Boccara, and D. Fournier. Photothermal deflection spectroscopy and detection. *Applied Optics*, 20(8):1333–1344, 1981.

[123] Bernhard Fisher. *Loss analysis of crystalline silicon solar cells using photoconductance and quantum efficiency measurements.* PhD thesis, University of Konstanz, 2003.

[124] Alongkarn Chutinan, Nazir P. Kherani, and Stefan Zukotynski. High-efficiency photonic crystal solar cell architecture. *Optics Express*, 17(11):8871–8878, 2009.

[125] M. Peters, M. Rüdiger, D. Pelzer, H. Hauser, M. Hermle, and B. Bläsi. Electro-optical modelling of solar cells with photonic structures. *Proceedings of the 25th European Photovoltaic Solar Energy Conference, Valencia, Spain*, 2010.

[126] Yurii A. Vlasov, Xiang-Zheng Bo, James C. Sturm, and David J. Norris. On-chip natural assembly of silicon photonic bandgap crystals. *Nature*, 414(6861):289–293, 2001.

[127] Andreas Bielawny, Johannes Üpping, et al. 3D photonic crystal intermediate reflector for micromorph thin-film tandem solar cell. *physica status solidi (a)*, 205(12):2796–2810, 2008.

A. Effective medium approximation

In this section I derive the equations used to calculate the effective relative permittivity of a cylinder structure where the electric field is perpendicular to the cylinder axis, i.e. TE polarization. For the case where the electric field points along the cylinder axis, i.e. TM polarization, the effective medium can be calculated as a geometrical average of the two materials as in Eq. 4.1.5. The calculation in this section applies electrostatic equations and is therefore valid only in the low-frequency approximation, or equivalently for lattice periods much smaller than the wavelength of light, i.e. $\Lambda << \lambda$.

The electric potential V in cylindrical coordinates may be expanded in a power series as:

$$V^p(r,\phi) = \sum_{n=1}^{\infty}[A_n^p r^n + B_n^p r^{-n}][C_n^p cos(n\phi) + D_n^p sin(n\phi)] \tag{A.0.1}$$

The superscript p is either 1 or 2, corresponding to the potential within the cylinder with relative permittivity ϵ_1 or in the material surrounding the cylinder with relative permittivity ϵ_2. A_n^p, B_n^p, C_n^p, and D_n^p are unknown constants. The electric field E^p is given by the gradient of the electric potential which in cylindrical coordinates becomes:

$$E^p = -\nabla V^p = -\frac{\partial V^p}{\partial r}\hat{r} - \frac{1}{r}\frac{\partial V^p}{\partial \phi}\hat{\phi} \tag{A.0.2}$$

Inserting Eq. A.0.1 into Eq. A.0.2 gives:

$$\begin{aligned} E^p(r,\phi) = &\sum_{n=1}^{\infty}[A_n^p n r^{n-1} + B_n^p(-n)r^{-n-1}][C_n^p cos(n\phi) + D_n^p sin(n\phi)]\hat{r} \\ &+ \sum_{n=1}^{\infty}[A_n^p r^{n-1} + B_n^p r^{-n-1}][(-n)C_n^p sin(n\phi) + nD_n^p cos(n\phi)]\hat{\phi} \end{aligned} \tag{A.0.3}$$

For an E field pointing in the x direction in the center of the cylinder, symmetry requires that only the *cos* terms may be nonzero for the radial part of the field, and only the *sin* terms may be nonzero for the azimuthal part. Additionally, for the field inside the cylinders all B_n^1 needs to be zero to avoid a divergent field in the center as $r \to 0$. The field components may therefore be expressed as follows:

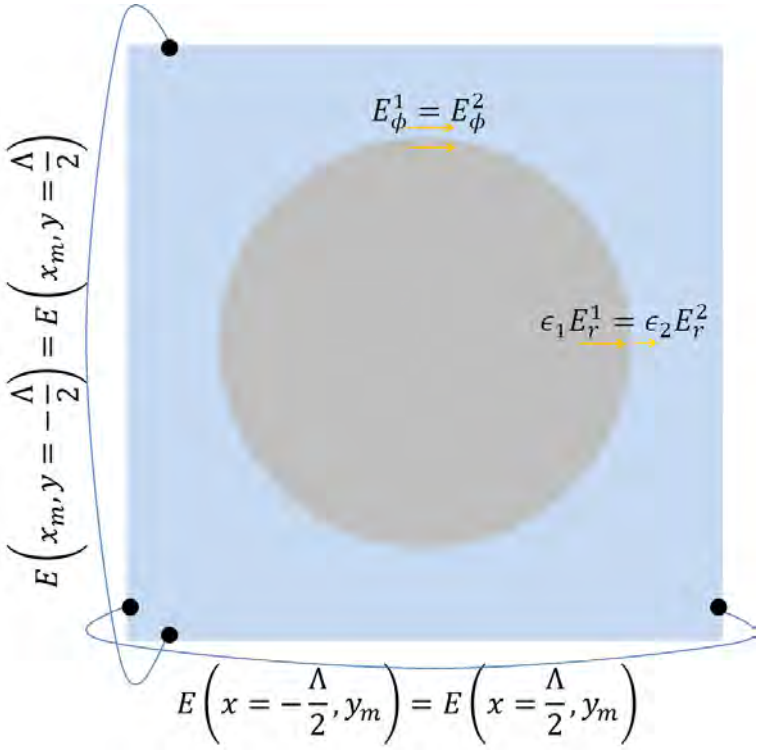

Figure A.0.1.: Boundary conditions for determining the effective permittivity of a cylinder array. Maxwell's boundary conditions are applied at the interface between the cylinder and the surrounding dielectric. Periodic boundary conditions are applied at the edges of the unit cell.

$$
\begin{aligned}
E_r^1 &= \sum_{n=1}^{\infty} A_n^1 C_n^1 n r^{n-1} cos(n\phi) \\
E_\phi^1 &= \sum_{n=1}^{\infty} A_n^1 C_n^1 (-n) r^{n-1} sin(n\phi) \\
E_r^2 &= \sum_{n=1}^{\infty} (A_n^2 C_n^2 n r^{n-1} - B_n^2 C_n^2 n r^{-n-1}) cos(n\phi) \\
E_\phi^1 &= \sum_{n=1}^{\infty} (A_n^2 C_n^2 n r^{n-1} + B_n^2 C_n^2 n r^{-n-1})(-sin(n\phi))
\end{aligned}
\tag{A.0.4}
$$

Maxwell's equations require that $\epsilon_1 E_r^1 = \epsilon_2 E_r^2$ and $E_\phi^1 = E_\phi^2$ at the boundary of the cylinder, i.e. for $r = a$ where a is the radius of the cylinder. This is illustrated in Figure A.0.1. The unknown coefficients outside the cylinder, $A_n^2 C_n^2$ and $B_n^2 C_n^2$, and inside the cylinder, $A_n^1 C_n^1$, may be related through the Maxwell boundary conditions. We now introduce the new coefficient $F_n = A_n^1 C_n^1 a^{n-1} n$. With the new coefficient, and after some algebra, the field components take the following form:

$$
\begin{aligned}
E_r^1 &= \sum_{n=1}^{\infty} F_n (\frac{r}{a})^{n-1} cos(n\phi) \\
E_\phi^1 &= \sum_{n=1}^{\infty} F_n (\frac{r}{a})^{n-1} (-sin(n\phi)) \\
E_r^2 &= \sum_{n=1}^{\infty} F_n \frac{\epsilon_2 + \epsilon_1}{2\epsilon_2} [(\frac{r}{a})^{n-1} - (\frac{a}{r})^{n+1}) \frac{\epsilon_2 - \epsilon_1}{\epsilon_2 + \epsilon_1}] cos(n\phi) \\
E_\phi^1 &= \sum_{n=1}^{\infty} F_n \frac{\epsilon_2 + \epsilon_1}{2\epsilon_2} [(\frac{r}{a})^{n-1} + (\frac{a}{r})^{n+1}) \frac{\epsilon_2 - \epsilon_1}{\epsilon_2 + \epsilon_1}] (-sin(n\phi))
\end{aligned}
\tag{A.0.5}
$$

To determine the unknown coefficients E_n we need to impose periodic boundary conditions to the x and y components of the electric field, E_x^2 and E_y^2. Therefore, we need to convert Eq. A.0.5 from cylindrical to Cartesian coordinates. After this transformation the field components in the Cartesian coordinates becomes:

$$
\begin{aligned}
E_x^1 &= \sum_{n=1}^{\infty} F_n (\frac{r}{a})^{n-1} [cos(n\phi)cos(\phi) + sin(n\phi)sin(\phi)] \\
E_y^1 &= \sum_{n=1}^{\infty} F_n (\frac{r}{a})^{n-1} [cos(n\phi)sin(\phi) - sin(n\phi)cos(\phi)] \\
E_x^2 &= \sum_{n=1}^{\infty} F_n \frac{\epsilon_2 + \epsilon_1}{2\epsilon_2} \{[(\frac{r}{a})^{n-1} - \frac{\epsilon_2 - \epsilon_1}{\epsilon_2 + \epsilon_1} (\frac{a}{r})^{n+1}] cos(n\phi)cos(\phi) \\
&\quad + [(\frac{r}{a})^{n-1} + \frac{\epsilon_2 - \epsilon_1}{\epsilon_2 + \epsilon_1} (\frac{a}{r})^{n+1}] sin(n\phi)sin(\phi)\} \\
E_y^2 &= \sum_{n=1}^{\infty} F_n \frac{\epsilon_2 + \epsilon_1}{2\epsilon_2} \{[(\frac{r}{a})^{n-1} - \frac{\epsilon_2 - \epsilon_1}{\epsilon_2 + \epsilon_1} (\frac{a}{r})^{n+1}] cos(n\phi)sin(\phi) \\
&\quad - [(\frac{r}{a})^{n-1} + \frac{\epsilon_2 - \epsilon_1}{\epsilon_2 + \epsilon_1} (\frac{a}{r})^{n+1}] sin(n\phi)cos(\phi)\}
\end{aligned}
\tag{A.0.6}
$$

Periodic boundary conditions require the field outside the cylinder, E_x^2 and E_y^2, to be identical for all points y_m at $x = \pm\Lambda/2$ and for all points x_m at $y = \pm\Lambda/2$. This is illustrated in Figure A.0.1. Hence both field components may be matched at the x and the y boundary. The point matching implies that $E_l^{2,+} = E_l^{2,-}$, where l is either x or y and the sign in the superscript denotes values the boundary $\pm\Lambda/2$ and may be either along the x or y boundary of the unit cell. We write the n-th term in the series expansion of Eq. A.0.6 as $E_{n,l}^{2,+}$. The point matching at one point takes the following form:

$$
E_{1,l}^{2,+} + E_{2,l}^{2,+} + E_{3,l}^{3,+} ... = E_{1,l}^{2,-} + E_{2,l}^{2,-} + E_{3,l}^{3,-} ... \tag{A.0.7}
$$

We gather all terms of Eq. A.0.7 on the left hand side and move the $n = 1$ term to the right hand side. We repeat the point matching at m different points along the edges of the unit cell. The resulting equations may then be written in one matrix equation:

$$\begin{pmatrix} a_{21} & a_{31} & . & . & a_{n1} \\ a_{22} & . & & & . \\ . & & . & & . \\ . & & & . & . \\ a_{2m} & . & . & . & a_{nm} \end{pmatrix} \begin{pmatrix} F_2 \\ F_3 \\ . \\ . \\ F_n \end{pmatrix} = -F_1 \begin{pmatrix} a_{11} \\ a_{12} \\ . \\ . \\ a_{1m} \end{pmatrix} \tag{A.0.8}$$

Here $a_{n,m} = E^{2,+}_{n,l}(l_m) - E^{2,-}_{n,l}(l_m)$ is the n-th component of the series expansion from Eq. A.0.6 at $r = l_m$, where l_m is the location of the m-th point that we match along the edge of the unit cell. We can now determine the field up to an arbitrary constant F_{ref}. By putting this point in the center of the cylinder we can see from Eq. A.0.6 that $F_1 = F_{ref}$ and the matrix equation may be solved. The number of terms in the series expansion N determines the minimum number of points that needs to be matched. We matched the field components E^2_x and E^2_y at both the x and y boundary at N points each. Thus, since $m > n$ in Eq. A.0.8, we end up with a system of linearly dependent equations. This did not affect the calculated values of the effective relative permittivity.

In Figure A.0.2 we show a picture of the calculated relative permittivity of SiO_2 ($\epsilon = 1.5^2$) cylinders in a Si ($\epsilon = 3.6^2$) matrix as a function of cylinder fill factor, i.e. the cylinder area to the area of the unit cell.

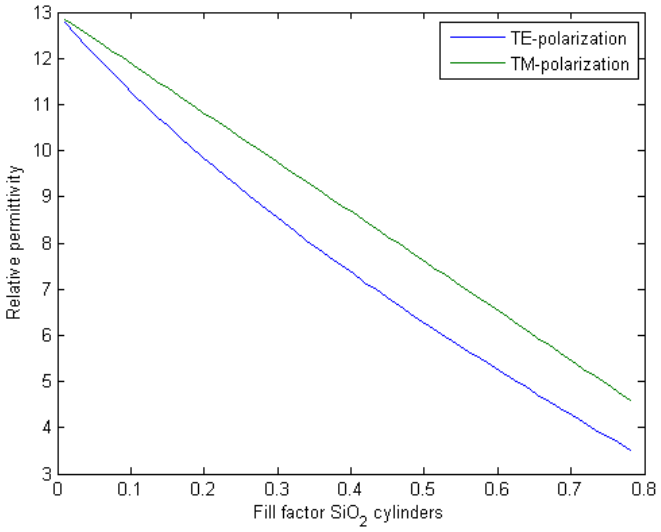

(a)

Figure A.0.2.: Calculated effective relative permittivity for a cylinder structure consisting of SiO_2 cylinders in a Si matrix as a function of cylinder fill factor, i.e. the cylinder area to the area of the unit cell. TM polarization represents the case where the electric field points along the cylinders and are calculated by Eq. 4.1.5. TE polarization represents the case of an electric field in the cylinder plane and is calculated for the electrostatic case using the method derived in this section.

MODELLING OF LIGHT TRAPPING IN THIN SILICON SOLAR CELLS WITH BACK-SIDE DIELECTRIC DIFFRACTION GRATING

J. Gjessing*[1,2,3], E. S. Marstein[1,4], A. Sudbø[4,2]

1. Institute for Energy Technology (IFE), Pb 40, N-2027 Kjeller, Norway
2. University Graduate Center at Kjeller (UNIK)
3. University of Oslo, Department of Physics
4. University of Oslo, Faculty of Mathematics and Science
*Corresponding author e-mail: jo.gjessing@ife.no

ABSTRACT: We have designed and investigated in numerical simulations a light-trapping structure in the form of a bi-periodic back-side diffraction grating. In addition to the grating, the light-trapping structure also includes an oxide (SiO_2) layer that separates the grating from the back-side aluminium (Al) mirror. This light-trapping structure is expected to give a potential short-circuit current density J_{sc} of 35.0 mA/cm^2 when put on the back side of a 20 µm thick Si solar cell with a single layer anti-reflection coating (ARC), assuming that all electron-hole pairs are collected at the contacts. This is an improvement of 15 % compared to a reference cell with the same thickness, a single layer ARC and a planar back-side Al mirror. The improvement is almost exclusively confined to the wavelength range from 800 nm to 1100 nm. We also investigate how the thickness of the Si substrate affects the light trapping efficiency.
Keywords: Light trapping, Optical properties, Modelling

1 INTRODUCTION

An effective way of reducing the cost of wafer based silicon (Si) solar cells is to make use of substantially thinner Si substrates than the wafers normally used today. This reduces both material consumption and the demand on material quality. However, a further reduction of substrate thickness will increase optical losses, thus reducing the solar cell efficiency. While state of the art solar cells today have Si substrate thicknesses down to around 160 µm, production of substrates with thickness down to 20 µm have recently been demonstrated [1]. The manufacture of efficient solar cells from such thin substrates requires the incorporation of a high performance light-trapping scheme into the solar cell structure.

To collect as much sunlight as possible within a thin Si-based solar cell, two types of light trapping structures are normally included. One is anti-reflective coatings (ARC). The other is surface textures. In mono crystalline Si solar cell technology, alkaline etching is frequently used to make inverted pyramids on the front side, while acidic texturing is becoming more important within multi crystalline Si solar cell technology. In both cases surface structures with sizes in the order of 2-10 µm are made.

Such large structures can be impractical for thin solar cells. Of higher importance is the fact that periodic structures have the potential of achieving better results than random structures when it comes to light trapping, at least for a limited spectral range [2]. They may also be made much smaller, thereby consuming less material than what is achieved in the alkaline or acidic etches used today. Finally, they can be compatible with surface passivating layers.

The use of sub-micron back-side structures for light trapping in solar cells has been addressed in earlier works [3], but also in several recent works [4, 5, 6, 7]. Most of these have focused on cells with a thickness below 5 µm, although [4] also has a brief comparison of the effect of the use of light trapping structures on thicker cells. In the present work we present the results from calculations of a specific light trapping structure applied to a cell with a thickness of 20µm.

2 MODEL AND MODELLING TOOLS

The light trapping structure investigated in this work is shown in Figure 1. The structure consists of a dielectric grating and an aluminium (Al) back reflector, separated by a layer of low permittivity dielectric (e.g. an oxide (SiO_x)). The light reflected from the grating is distributed into obliquely travelling modes that are totally internally reflected within the substrate. The separating layer reduces parasitic absorption in the metal, which is a common problem for grating-metal boundaries [8, 9].

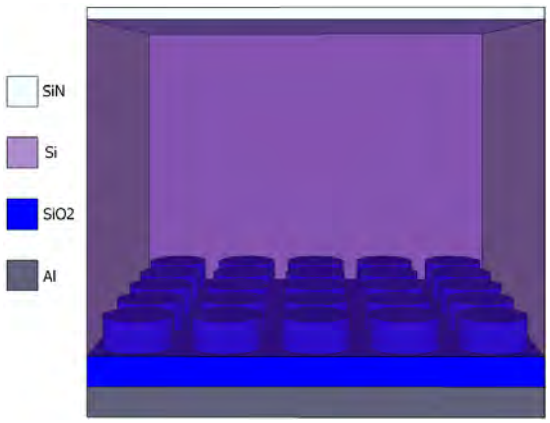

Figure 1: Solar cell model structure used in the computations (not to scale).

In order to assess the light trapping efficiency of the structure, simulations have been performed. The simulations have been performed with the software package Grating Diffraction Calculator (GD-Calc) [10]. GD-Calc uses rigorously coupled wave analysis (RCWA) [11], where the Maxwell equations are solved in the

Fourier space within each layer of a multilayer stack. The solutions from each layer are then matched with the solutions from the adjacent layers, imposing electromagnetic boundary conditions. RCWA is especially convenient when there are large variations in layer thicknesses in the stack. The power in each diffraction order is also easily extracted with RCWA. The software package Meep, which uses the method of finite difference time domain (FDTD) [12, 13, 14], has also been used to confirm the results from the RCWA computations. Whereas the RCWA easily handles dispersive and absorbing materials like the silicon and metal in a solar cell, this is not so straightforward with the FDTD method, so we have used a nonphysical nonabsorbing and nondispersive model of the light-trapping structure for the comparison. The simulated spectral reflectance obtained with the two methods then agrees very well, as shown in Figure 2.

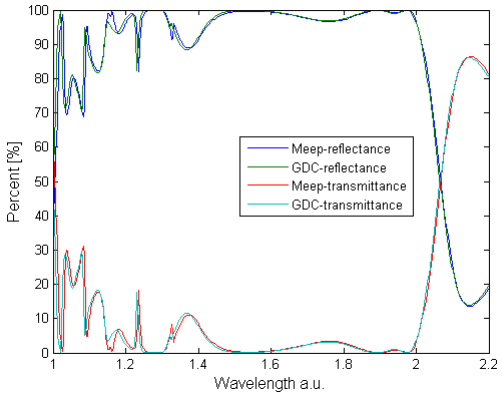

Figure 2: Comparison of reflection and transmission through a bi-periodic grating. The grating is similar in shape to the grating shown in Figure 1, but with a different set of parameters than what we present in this work.

The reference cell is similar to the cell shown in Figure 1, except that the grating layer and the oxide layer are removed, so that the Si is in direct contact with the planar back-side Al-layer. The short-circuit current density (J_{sc}) is used for quantitative comparison of the light-trapping effect for different configurations assuming a collection efficiency of 100 %. J_{sc} is found by weighting the spectral absorption against the AM 1.5 spectre [15] as shown in Equation (1).

$$J_{sc} = q\int_0^{\infty} A(\lambda)\Phi(\lambda)\mathrm{d}\lambda \qquad (1)$$

$A(\lambda)$ is the dimensionless spectral absorption factor calculated by GD-calc. $\Phi(\lambda)$ is the spectral density of the photon irradiance with dimension [$s^{-1}m^{-2}nm^{-1}$] from the AM1.5 spectrum, normalized so that the irradiance equals 1000 W/m^2. q is the elementary charge. The integration limits are 0 and ∞, but $\Phi(\lambda)$ is negligible below 300 nm and $A(\lambda)$ is negligible above 1100 nm. Thus in practice, an integration interval from 300 nm to 1100 nm is used in the calculations.

Wavelength dependent optical data have been used for Si [16] and for Al [17]. For simplicity, a constant refractive index for SiO_x (1.5) and Si_3N_4 (1.95) was used.

3 RESULTS

In Figure 1, several parameters that may be tuned to improve the light-trapping properties are indicated. The parameters include the grating period Λ, grating thickness t_g, oxide thickness t_{ox} and the fill factor. The fill factor is defined as the fraction of the oxide area to the total area of the grating.

The diffraction angles were calculated from the grating equation, where the grating period is a parameter. The diffraction angles should at least be larger than ~16º, which is the critical angle of total internal reflection from a Si-air interface. For maximum path length enhancement the diffraction angle should be close to 90º, i.e. parallel to the grating. However, for diffraction angles above 60º diffraction efficiencies has been shown to be poor [18]. The power fraction in each diffracted order is dependent on all the parameters mentioned above. RCWA simulations have been used to find the power fraction in each diffraction order. We found that a Λ of 0.65 µm, and a fill factor of 0.5 was favourable with respect to light-trapping.

The grating thickness should be chosen in such a way so that as much as possible of the incoming light is coupled to higher diffraction orders. This can be achieved with a grating thickness of $\lambda/(4n_{Si})$, where n_{Si} is the refractive index of silicon. The light reflected from the peaks and valleys of the grating will then be in opposite phase. For a fill factor of 0.5 their magnitudes will also be equal and cancellation of zero order reflection will occur, thus minimizing specular (i.e. zero order) reflection. Cancellation of zero order reflection could also be achieved through any odd multiple of the 'lambda-quarter' layer. We find that the diffraction efficiency is higher for a grating thickness of $3\lambda/(4n_{Si})$, which gives a grating thickness t_g of 0.21 µm.

Figure 3 shows the importance of the oxide layer that separates the grating from the back side aluminium. We have chosen a t_{ox} of 0.22 µm, corresponding to the first peak in Figure 3. A thicker layer would possibly give a minor improvement, but a thinner layer is advantageous from an industrial point of view.

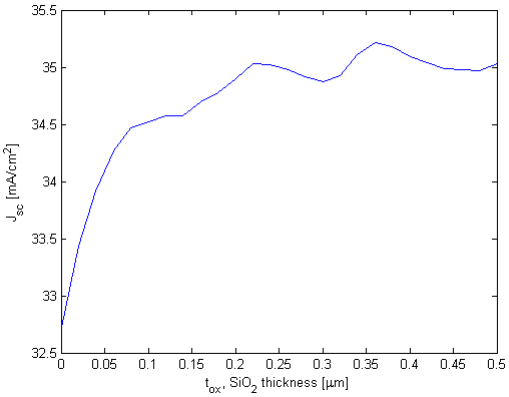

Figure 3: Influence of oxide thickness t_{ox} on J_{sc}. The rapid enhancement of J_{sc} up to a thickness of around 0.1 µm is corresponding to a reduction of parasitic absorption in the back-side aluminium.

The single layer ARC was optimized for a wavelength of around 600 nm.

Figure 4 shows the spectral contribution to the J_{sc} for a 20 µm thick cell with light-trapping, compared to other reference solar cell structures. The configuration with the 20 µm thick light-trapping cell performs significantly better than the reference cell of the same thickness. However, compared to the eight times thicker reference cell of 160 µm, the performance of the 20 µm thick light-trapping cell is slightly lower at most wavelengths. The topmost curve shows the theoretical potential given total absorption of the AM 1.5 spectrum from 300 nm to 1100 nm. The results from Figure 4 are summarized in Table I.

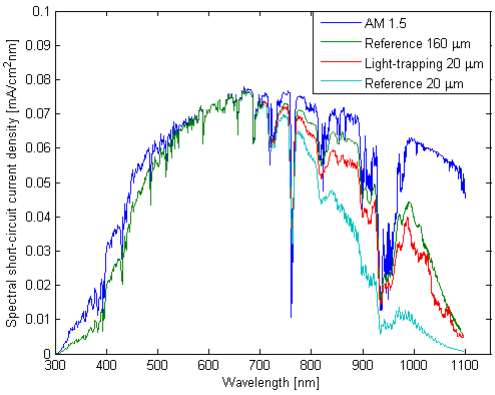

Figure 4: Simulation results for the spectral contributions to the short-circuit current density J_{sc} for different configurations. Digital low-pass filtering (a moving average) have been applied to the simulated spectra of both the reference cells and the light trapping cell to mask the rapid oscillations in the spectra resulting from Fabry-Perot interference in the Si slab.

Table I: Comparison of J_{sc} for the different models from Figure 4. Also shown is the single-layer ARC configuration which corresponds to total absorption in interval from 300 nm to 1100 nm, limited only by the front side reflection of a single layer planar ARC.

	J_{sc} [mA/cm^2]	Percent
AM1.5 spectrum	43.5	100 %
Single-layer ARC	39.8	91.5 %
Reference 160 µm	36.6	84.1 %
Light-trapping 20 µm	35.0	80.5 %
Reference 20 µm	30.4	69.9 %

Figure 5 shows the influence of the Si substrate thickness on light harvesting both for a reference solar cell with planar back side Al-mirror and for a cell with the back-side light-trapping structure. It is clear that the improvement in J_{sc} when using the light-trapping structure is more pronounced for thinner cells. Marked on the right axis in Figure 5 is also the potential J_{sc} for the AM1.5 spectre (from 300-1100 nm), the single layer ARC limited, and the J_{sc} for a 160 µm reference cell. These values are given in Table I.

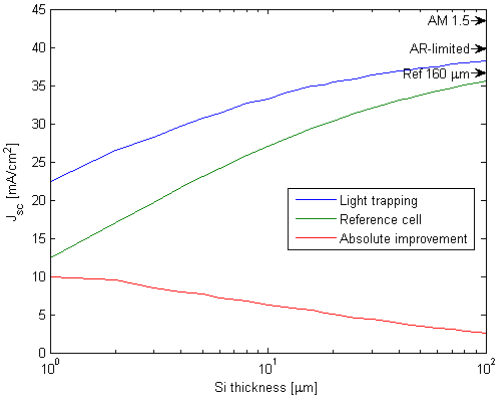

Figure 5: The figure shows the effect of thickness on the short-circuit current density J_{sc}. J_{sc} for the configurations in Table I are also marked with arrows on the right axis. Note the log scale on the x-axis.

4 DISCUSSION

We have observed that a bi-periodic back-side diffraction grating will significantly increase J_{sc} compared to a planar reference cell of the same thickness. This improvement is mainly due to the enhanced path length inside the Si, provided by coupling of light to oblique travelling totally internally reflected modes. Another contributing factor to the improved light harvesting is the reduction of parasitic absorption in the back-side Al mirror. Compared to a Si-Al boundary, the SiO_x layer decreases the impedance matching to the Al, and therefore also the parasitic absorption. In addition, the separation of the grating and the Al back-side mirror decreases the strength of the evanescent waves originating in the grating that reaches the Al surface. The fact that back side Al-mirror is planar helps to avoid excitation of surface plasmons which is a common cause of parasitic losses in metal gratings.

Figure 5 shows how the gain of adding a light-trapping device on the back side of the cell increases with decreasing thickness. However, J_{sc} is dropping steadily with decreased thickness both for the reference cell and for the cell with light-trapping. Therefore, the high-efficiency solar cell cannot be achieved with the proposed configuration for thin-film cells of only a few microns. It should be noted that a better ARC will increase J_{sc} further for all configurations.

For the light-trapping design shown in Figure 1 there is a need for electrical contacts from the Si back side to the Al. This can be achieved by replacing the SiO_x with a transparent dielectric material with low permittivity, such as transparent conductive oxide materials. Contacting could also be made through number of pattern defining processes, including a so-called laser process [19]. For an efficient Si solar cell, a major advantage of the presented structure with a back side SiO_x layer is the effective surface passivation supplied by this material. SiO_x is an excellent material for passivation of Si especially when combined with a thin layer of a-Si:H. This is an important feature for thin cells where more of the absorption will take place close to the back side.

5 CONCLUSION

We have shown the potential of a 2D back-side diffraction grating for light-trapping purposes. With a planar single layer ARC this design holds a potential J_{sc} of 35.0 mA/cm^2 for a 20 µm Si solar cell. This is an improvement of 4.6 mA/cm^2 or a 15 % increase compared to a reference cell with the same thickness, ARC and back-side Al mirror. The increase in J_{sc} is both due to enhanced path length inside the cell, and reduced parasitic absorption in the back-side Al mirror. In this work we also show the influence of Si thickness on the light harvesting. As expected, the gain from light trapping is most pronounced for the thinnest solar cells, but the gain is quite significant for cells as thick as 20 µm.

[1] F. Henley et al. (2008), *Direct film transfer (DFT) technology for kerf-free silicon wafering*. 23rd EU PVSEC, Valencia, Spain.

[2] J. M. Gee (2002), *Optically enhanced absorption in thin silicon layers using photonic crystals*, Twenty-Ninth IEEE Photovolt. Spec. Conf.

[3] C. Heine and R. H. Morf (1995), *Submicrometer gratings for solar energy applications.* Applied Optics, Vol.34

[4] Feng et al. (2007), *Design of Highly Efficient Light-Trapping Structures of Thin-Film Crystalline Silicon Solar Cells.* IEEE Transactions on Electron Devices Vol. 54, pp 1926-1933.

[5] Bermel et al. (2007), *Improving thin-film crystalline silicon solar cell efficiencies with photonic crystals.* Optics Express, Vol. 15.

[6] Zeng et al. (2008), *Demonstration of enhanced absorption in thin film Si solar cells with textured photonic crystal back reflector*. Applied Physics Letters, Vol. 93.

[7] D. Zhou and R. Biswas (2008), *Harvesting photons in thin film solar cells with photonic crystals.* Mater. Res. Soc. Symp. Proc., Vol. 1101

[8] M.T. Gale et al. (1990), *Design and fabrication of submicron structures for light trapping in silicon solar cells*, SPIE vol. 1272.

[9] A. Campa et al. (2008), *Potential of diffraction gratings for implementation as a metal back reflector in thin-film silicon solar cells*, Thin Solid Films, Vol. 516, pp 6963-6967.

[10] http://software.kjinnovation.com/GD-Calc.html

[11] L. Li (1996), *Formulation and comparison of two recursive matrix algorithms for modeling layered diffraction gratings.* J. Opt. Soc. Amer. A, vol. 13, pp. 1024-1035.

[12] http://ab-initio.mit.edu/meep/

[13] A. Taflove, S. C. Hagness (2005), *Computational Electrodynamics: The Finite-Difference Time-Domain Method.* Artech House Publishers, Third Edition.

[14] John D. Joannopoulos et al. (2008) *Photonic Crystals: Molding the Flow of Light.* Princeton University Press, Second Edition.

[15] http://rredc.nrel.gov/solar/spectra/am1.5/

[16] C.M. Herzinger et al. (1998), *Ellipsometric determination of optical constants for silicon and thermally grown silicon dioxide via a multi-sample, multi-wavelength, multi-angle investigation*, J. Appl. Phys., Vol. 83, pp 3323–3336.

[17] *Handbook of Optical Constants of Solids*, (1985) edited by E. D. Palik, Academic Press, Inc.

[18] S.H.Zaidi et al. (2000), *Diffraction grating structures in solar cells*, Twenty-Eighth IEEE Photovolt. Spec. Conf.

[19] E.Schneiderlöchner et al. (2002), *Laser-Fired Rear Contacts for Crystalline Silicon Solar Cells*, Prog. Photovolt. Res. Appl., Vol. 10, pp 29-34.

2D back-side diffraction grating for improved light trapping in thin silicon solar cells

Jo Gjessing,[1,2,3*] Erik Stensrud Marstein,[1,4] and Aasmund Sudbø[4,2]

[1] *Institute for Energy Technology, Pb 40, 2027 Kjeller, Norway*
[2] *University Graduate Center at Kjeller, Norway*
[3] *University of Oslo, Department of physics, Norway*
[4] *University of Oslo, Faculty of Mathematics and Sciences, Norway*
**jo.gjessing@ife.no*

Abstract: Light-trapping techniques can be used to improve the efficiency of thin silicon solar cells. We report on numerical investigation of a light trapping design consisting of a 2D back-side diffraction grating in combination with an aluminum mirror and a spacing layer of low permittivity to minimize parasitic absorption in the aluminum. The light-trapping design was compared to a planar reference design with antireflection coating and back-side aluminum mirror. Both normally and obliquely incident light was investigated. For normal incidence, the light trapping structure increases the short circuit current density with 17% from 30.4 mA/cm^2 to 35.5 mA/cm^2 for a 20 μm thick silicon solar cell. Our design also increases the current density in thinner cells, and yields higher current density than two recently published designs for cell thickness of 2 and 5 μm, respectively. The increase in current may be attributed to two factors; increased path length due to in-coupling of light, and decreased parasitic absorption in the aluminum due to the spacing layer.

OCIS codes: (050.1950) Diffraction gratings; (350.6050) Solar energy.

References and links

1. F. Henley, A. Lamm, S. Kang, and L. Tian, "Direct film transfer (DFT) technology for kerf-free silicon wafering," Proc. 23rd PVSEC, Valencia Spain, 1090–1093 (2008).
2. J. Nelson, *The Physics of Solar Cells*, (Imperial College Press, London, 2003).
3. E. Yablonovitch, "Statistical ray optics," J. Opt. Soc. Am. **72**(7), 899–907 (1982).
4. J. M. Gee, "Optically enhanced absorption in thin silicon layers using photonic crystals," Twenty-Ninth IEEE Photovolt. Spec. Conf., 150–153 (2002).
5. P. Sheng, A. N. Bloch, and R. S. Stepleman, "Wavelength-selective absorption enhancement in thin-film solar cells," Appl. Phys. Lett. **43**(6), 579–581 (1983).
6. C. Heine, and R. H. Morf, "Submicrometeer gratings for solar energy applications," Appl. Opt. **34**(14), 2476–2482 (1995).
7. M. T. Gale, B. Curtis, H. Kiess, and R. H. Morf, "Design and fabrication of submicron structures for light trapping in silicon solar cells," Proc. SPIE **1272**, 60–66 (1990).
8. H. Sai, H. Fujiwara, and M. Kondo, "Back surface reflectors with periodic textures fabricated by self-ordering process for light trapping in thin-film microcrystalline silicon solar cells," Sol. Energy Mater. Sol. Cells **93**(6-7), 1087–1090 (2009).
9. H. Sai, H. Fujiwara, M. Kondo, and Y. Kanamori, "Enhancement of light trapping in thin-film hydrogenated microcrystalline Si solar cells using back reflectors with self-ordered dimple pattern," Appl. Phys. Lett. **93**(14), 143501 (2008).
10. H. Sai, Y. Kanamori, K. Arafune, Y. Ohshita, and M. Yamaguchi, "Light trapping effect of submicron surface textures in crystalline Si solar cells," Prog. Photovoltaics **15**(5), 415–423 (2007).
11. R. Dewan, and D. Knipp, "Light-trapping in thin-film silicon solar cells with integrated diffraction grating," J. Appl. Phys. **106**(7), 074901 (2009).
12. A. Čampa, J. Krč, F. Smole, and M. Topič, "Potential of diffraction gratings for implementation as a metal back reflector in thin-film silicon solar cells," Thin Solid Films **516**(20), 6963–6967 (2008).
13. L. Zeng, Y. Yi, C. Hong, J. Liu, N. Feng, X. Duan, L. C. Kimerling, and B. A. Alamariu, "Efficiency enhancement in Si solar cells by textured photonic crystal back reflector," Appl. Phys. Lett. **89**(11), 111111 (2006).

#119649 - $15.00 USD Received 6 Nov 2009; revised 24 Feb 2010; accepted 24 Feb 2010; published 3 Mar 2010

14. N.-N. Feng, J. Michel, L. Zeng, J. Liu, C.-Y. Hong, L. C. Kimerling, and X. Duan, "Design of Highly Efficient Light-Trapping Structures of Thin-Film Crystalline Silicon Solar Cells," IEEE Trans. Electron. Dev. **54**(8), 1926–1933 (2007).
15. P. Bermel, C. Luo, L. Zeng, L. C. Kimerling, and J. D. Joannopoulos, "Improving thin-film crystalline silicon solar cell efficiencies with photonic crystals," Opt. Express **15**(25), 16986–17000 (2007).
16. D. Zhou and R. Biswas, "Harvesting photons in thin film solar cells with photonic crystals," Mater. Res. Soc. Symp. Proc. **1101**, (2008).
17. J. G. Mutitu, S. Shi, C. Chen, T. Creazzo, A. Barnett, C. Honsberg, and D. W. Prather, "Thin film solar cell design based on photonic crystal and diffractive grating structures," Opt. Express **16**(19), 15238–15248 (2008).
18. C. Haase, and H. Stiebig, "Optical Properties of Thin-film Silicon Solar Cells with Grating Couplers," Prog. Photovoltaics **14**(7), 629–641 (2006).
19. C. Haase, and H. Stiebig, "Thin-film silicon solar cells with efficient periodic light trapping texture," Appl. Phys. Lett. **91**(6), 061116 (2007).
20. F.-J. Haug, T. Söderström, M. Python, V. Terrazzoni-Daudrix, X. Niquille, and C. Ballif, "Development of micromorph tandem solar cells on flexible low-cost plastic substrates," Sol. Energy Mater. Sol. Cells **93**(6-7), 884–887 (2009).
21. J. Gjessing, E. S. Marstein, and A. Sudbø, "Modelling of light trapping in thin silicon solar cells with back side dielectric diffraction grating," Proc. 24th PVSEC, Hamburg Germany, 2604–2607 (2009).
22. http://software.kjinnovation.com/GD-Calc.html
23. L. Li, "Formulation and comparison of two recursive matrix algorithms for modeling layered diffraction gratings," J. Opt. Soc. Am. A **13**(5), 1024–1035 (1996).
24. http://ab-initio.mit.edu/meep/
25. A. Taflove, and S. C. Hagness, *Computational Electrodynamics: The Finite-Difference Time-Domain Method*, (Artech House Publishers, Norwood MA, 2005).
26. J. D. Joannopoulos, S. G. Johnson, J. N. Winn, and R. D. Meade, *Photonic Crystals: Molding the Flow of Light*, (Princeton University Press, New Jersey 2008).
27. C. M. Herzinger, B. Johs, W. McGahan, J. Woollam, and W. Paulson, "Ellipsometric determination of optical constants for silicon and thermally grown silicon dioxide via a multi-sample, multi-wavelength, multi-angle investigation," J. Appl. Phys. **83**(6), 3323–3336 (1998).
28. E. D. Palik ed., *Handbook of Optical Constants of Solids*, (Academic Press, San Diego, 1985).
29. http://rredc.nrel.gov/solar/spectra/am1.5/
30. M. A. Green, *Silicon Solar Cells – Advanced principles and practice*, (Centre for Photovoltaic Devices and Systems, Sydney, 1995).
31. H. A. Macleod, *Thin-Film Optical Filters*, (Institute of Physics Publishing, Bristol, 2001).
32. C. H. Henry, "Limiting efficiencies of ideal single and multiple energy gap terrestrial solar cells," J. Appl. Phys. **51**(8), 4494–4500 (1980).
33. E. Schneiderlöchner, R. Preu, R. Lüdemann, and S. W. Glunz, "Laser-Fired Rear Contacts for Crystalline Silicon Solar Cells," Prog. Photovoltacis **10**, 29–34 (2002).
34. http://www.mathworks.com/

1. Introduction

The cost per watt of solar cells needs to be reduced for solar electricity to become competitive with energy produced from fossil fuels. Thinner cells can reduce both the amount of material needed, and also demand on material quality, thereby reducing both production costs and energy consumption. Thin film technologies aim at reducing cost through decreased material consumption, but deposited thin film solar cells have inferior efficiency compared to the much thicker wafer based crystalline silicon (Si) cells. Recent discoveries have showed that it is also possible to make high quality crystalline Si substrates and solar cells with thickness down to 20 μm and below [1]. Although this approach holds much promise, one fundamental challenge must be overcome. Si exhibits an indirect band gap, and at this thickness a significant part of the light is lost due to insufficient absorption of the near infrared radiation. Thus, the decrease in cost obtained by using very thin Si substrates is offset by a decrease in efficiency. In order to avoid excessive optical losses, thin Si cells therefore need an efficient light-trapping scheme.

For monocrystalline Si the most common method in the industry today is alkaline anisotropic wet etching, which results in a random structure of pyramids [2]. This works well for [100] oriented wafers, but it is not as effective for the [111] orientation. This might pose a problem for wafers made by the technology used in [1] where wafers are [111] oriented. For multicrystalline Si, the use of isotropic acidic etches is more common. Especially the alkaline etching of monocrystalline Si has proved successful for front side light trapping. Both methods results in fairly large surface structures with sizes in the order of 2-10 μm. For deposited thin film Si cells, glass materials with textured transparent oxide coatings, are

#119649 - $15.00 USD Received 6 Nov 2009; revised 24 Feb 2010; accepted 24 Feb 2010; published 3 Mar 2010

popular substrates due to their potential for light trapping. These random structures have dimensions below 1 μm. Yablonovitch [3] showed that an ideal patterning with random total internal reflection, in the statistical limit would enhance absorption by $4n^2$, where n is the refractive index of the material ($4n^2$~50 for Si). However, it is not known whether nor how such ideal patterns can be fabricated.

Periodic structures have the potential of achieving better light trapping than random structures over a limited spectral range [4,5]. Periodic structures for light trapping in solar cells has been investigated earlier [5–7], and also in a number of recent works [8–19]. One type of such gratings is diffraction gratings made of metal. Such gratings are relative simple to fabricate. However, a problem with metal gratings is that they general suffer from strong narrowband absorption lines [7,12]. To overcome this problem, pure dielectric designs combining gratings and back reflectors made from Bragg stacks, have been proposed [13–17]. Zeng et al. [13] achieved good correspondence between the theoretical predictions and the measured short circuit current for a 5 μm thick c-Si solar cell. Low-cost fabrication of periodic structures has also been investigated. Haug et al. [20] made 2D structures on a low-cost substrate using hot embossing, while Sai et al. [8,9] has demonstrated a self ordered periodic structured back reflector with periods as small as 300 nm. With a period of 900 nm these structures showed better light-trapping properties than the Asahi U-type glass. The Asahi U-type glass is a state-of-the-art random texturing for thin-film solar cells. Most of the literature on the subject focuses on thin cells in the range of 0.5-5 μm. The effect of back-side light-trapping structures will in general be most prominent for such thin cells, due to low baseline absorption. Thicker cells on the other hand, will have the advantage that the solar spectrum that reaches the back side is more narrow-banded, which is an apparent advantage for periodic structures.

In [21] we presented a 2D-periodic back-side grating structure that combined a purely dielectric grating with a flat Al reflector, separated from the grating by a layer of SiO_2. The low refractive index of SiO_2 provides a large index contrast which gives the diffraction grating a spectrally broad response. Admittedly, air provides an even larger index contrast, but is impractical. In addition to reducing parasitic absorption in the Al, the oxide layer provides excellent surface passivation, a vital prerequisite for any highly efficient, thin, crystalline Si solar cell. High quality back-side surface passivation is especially important for thin cells where carrier excitation to a greater extent will occur close to the back side. In this paper we go into further details of the properties of the structure, and perform an optimization of the vital parameters grating period, fill factor, grating thickness and oxide thickness. We have also investigated how oblique incidence angle affects the light trapping properties. We focus in this work on a Si thickness of 20 μm, which is particularly relevant in the light of the recent findings of Henley et al. [1].

2. Numerical methods

To accurately predict the response of the back-side diffraction grating, rigorous electromagnetic modelling of the light is needed. Numerical modelling was performed with Grating Diffraction Calculator (GD-Calc) [22], a software package that uses rigorously coupled wave analysis (RCWA) [23]. GD-Calc is a fully vectorial solver and solves the Maxwell equations for a single frequency. The results from GD-Calc have been compared with results obtained with the software package Meep [24]. Meep uses the method of finite difference time domain (FDTD) [25,26] for solving the Maxwell equations numerically. Both methods (RCWA and FDTD) showed almost identical results for non-absorbing materials. However, with RCWA it is straightforward to analyze the strength of each diffraction order separately. This is imperative when analyzing the grating efficiency. Finally, RCWA is also better suited when the model structure contains layers with large differences in thickness.

There are at least two limiting cases that can be accurately described by simple scalar models for the propagation of light. These cases do not give us quantitative information about the light trapping design, but we have found the fast calculations allowed by the scalar models to be very useful in limiting the number of time-consuming RCWA simulations needed to do

#119649 - $15.00 USD Received 6 Nov 2009; revised 24 Feb 2010; accepted 24 Feb 2010; published 3 Mar 2010

the design. The fast calculations have allowed us to limit the size of the four-dimensional volume in parameter space that we had to map using RCWA simulations.

Figure 1 shows the structure that was modeled in GD-Calc. This structure has been compared with a reference model with equal thickness (e.g. 20 μm), single-layer AR coating, and a planar back-side Al mirror. Wavelength-dependent refractive index data (real and imaginary part) is used for absorbing materials (i.e. Si [27], Al and Ag [28]), while a refractive index of 1.5 and 1.95 is used for SiO_2 and Si_3N_4 respectively. The Si_3N_4 AR layer was designed to give a minimum reflectance at a wavelength just above 600 nm, which corresponds to a thickness of 78 nm.

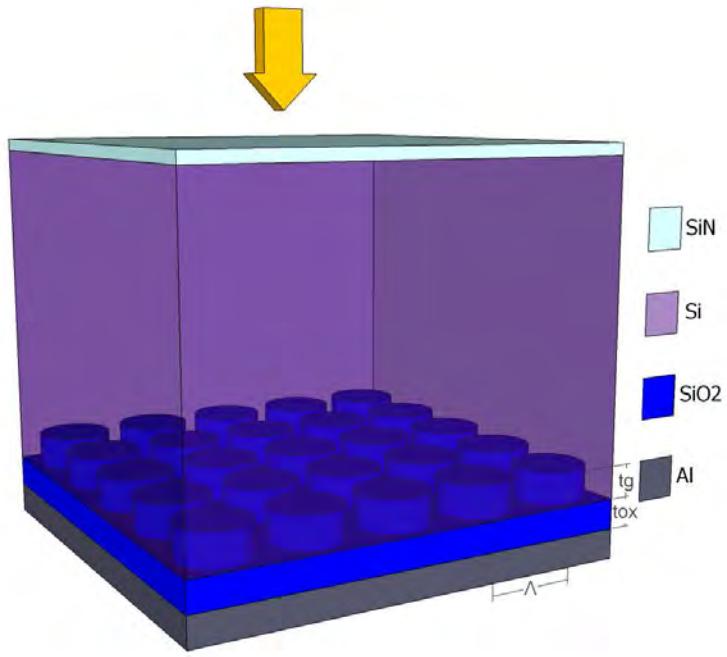

Fig. 1. Optical solar cell model structure used in the computations (not to scale). A single layer of Si_3N_4 is used as AR-coating. The reference structure is similar except that the SiO_2 and the grating layer are removed, and the Si is in direct contact with a planar Al-mirror.

A quantitative measure is needed for comparison of the different design parameters. The parameters as indicated in Fig. 1 are the grating period Λ, grating thickness t_g, thickness of the oxide layer t_{ox} and fill factor, here defined as the area covered by holes divided by the total area. A suitable measure of the performance of the structure is the short circuit current density (J_{sc}) excited by the AM 1.5 solar spectrum [29], which is calculated as shown in Eq. (1):

$$J_{sc} = q\int_0^\infty A(\lambda)\Phi(\lambda)\mathrm{d}\lambda \qquad (1)$$

Equation (1) provides a limit for the maximum J_{sc} that would be obtained if all the generated electron hole pairs reach the contacts. Here, λ is the wavelength in [nm], q the elementary charge in [C], $A(\lambda)$ the absorbance which is a dimensionless wavelength dependent factor between zero and one, calculated by GD-calc and $\Phi(\lambda)$ is the spectral density of the photon irradiance with dimension [$s^{-1}m^{-2}nm^{-1}$] from the AM1.5 spectrum normalized so that the irradiance equals 1000 W/m^2. The integration is performed from 0 to ∞ but $\Phi(\lambda)$ is negligible for λ<300 nm while $A(\lambda)$ is negligible for λ>1100 nm due to the bandgap of Si.

Absorption in the Al-mirror may be substantial, but does not contribute to J_{sc}. This parasitic absorption is therefore subtracted from the total absorption. The decoupling of parasitic absorption from the absorption in the rest of the cell is calculated in a straightforward

#119649 - $15.00 USD Received 6 Nov 2009; revised 24 Feb 2010; accepted 24 Feb 2010; published 3 Mar 2010

manner in GD-Calc. The absorption is calculated by taking the difference in Poynting vector going into and out of the given plane.

Free carrier absorption (fca) [30] is not considered in this model. As long as the Si is lightly doped, as is common in the bulk Si, fca will not make a big contribution for solar cell applications.

3. Grating analysis

3.1 Grating equation

The most important property of the grating is to increase the path length of light inside the Si by coupling the light into higher diffraction orders. The angles of the diffracted orders are given by the two-dimensional grating equation. We use the word grating in this article to describe our bi-periodic pattern of cylinders as shown in Fig. 1. The direction of the incident beam may be described by the polar angle θ, defined as the angle between the beam and the normal to the plane, and the azimuth angle φ, which determines the orientation in the plane. The outgoing beam may be diffracted in either direction of periodicity and will be characterized by two diffraction orders m_x and m_y. For each pair of diffraction orders (m_x, m_y), the corresponding beam angles θ, and φ for the diffracted beam are different.

For a one-dimensional (linear) grating and an angle of incidence in the plane of periodicity, the grating equation takes the form of Eq. (2). The two-dimensional grating equation is a straight forward extension of the one dimensional equation.

$$n_o \sin(\theta_m) = n_i \sin(\theta_i) + \frac{m\lambda}{\Lambda} \tag{2}$$

n is the refractive index, θ the angle between the beam and the normal to the plane in the direction of periodicity (classical mount), Λ the grating period, λ the free-space wavelength, and m the diffraction order. m is also the subscript of the angle θ_m of the diffracted wave corresponding to diffraction order m. The incident beam and material have the subscript i while the outgoing material has the subscript o. In this case we have diffraction in Si, so that $n_i = n_o \approx 3.6$. From Snell's low of refraction, the critical angle where total internal reflection will occur at a Si-air boundary is $\theta_c = \sin^{-1}(1/n_{Si})$ ~16 degrees. Light from the Si incident at the Si-air boundary at a larger angle will be totally internally reflected back into the Si. Adding layers of other materials between the Si and air does not change the critical angle for escape into the air.

From Eq. (2) we see that at normal incidence ($\theta_i = 0$) the angle of the diffracted beam is given by $\sin(\theta_m) = m\lambda/(n\Lambda)$. For small periods (i.e. $\Lambda<\lambda/n$) the equation has a real solution only for the zeroth order (m=0), i.e. specular reflectance. If the period is larger than the wavelength of light, the angle of the lower diffraction orders will become too small to efficiently increase the path length, and the lowest diffraction order will also lie in the escape cone of Si (~16 degrees). This limits the optimal grating period to the interval $\Lambda \in (\lambda / n_{Si}, \lambda)$.

Since the terrestrial solar spectrum contains a wide band of wavelengths we define a mean wavelength $\bar{\lambda}$ as shown in Eq. (3):

$$\bar{\lambda} = \frac{\int_0^\infty \lambda (A_{base}(\lambda) - A_{opt}(\lambda)) \Phi(\lambda) d\lambda}{\int_0^\infty (A_{base}(\lambda) - A_{opt}(\lambda)) \Phi(\lambda) d\lambda} \tag{3}$$

A_{base} is the absorbance of light through a slab of thickness L (i.e. [1-exp(−2α(λ)L]). The factor 2 in the exponential derives from assuming a perfect back-side reflector, which doubles the path length of the light. A_{opt} is the optimum absorbance given by the Yablonovitch limit [3] for the same thickness, so that the factor 2 is replaced by $4n_{Si}^2$. The light which is absorbed in an optimal cell, but is not absorbed in the baseline cell, is of most relevance when optimizing the periodic structure. Equation (3) gives a weighted distribution that goes to zero for both

#119649 - $15.00 USD Received 6 Nov 2009; revised 24 Feb 2010; accepted 24 Feb 2010; published 3 Mar 2010

short and long wavelengths, and with a $\bar{\lambda}$ of 0.98 μm for a 20 μm thick Si slab. For simplicity, an ideal AR-layer with zero reflectance is assumed in this calculation.

3.2 Diffraction efficiency

The diffraction angles may be found from the grating equation, but the power distributed in each diffraction order is a sensitive function of the grating thickness t_g. A convenient measure of the suitability of the grating for light trapping purposes is the power fraction diffracted into higher orders, D_{HO}, which is a dimensionless number between zero and one, defined in Eq. (4) in the same way as in [10]:

$$D_{HO} = \sum_{m_x=-\infty}^{m_x=\infty} \sum_{m_y=-\infty}^{m_y=\infty} D_{m_x m_y} - D_{00} \tag{4}$$

In order to calculate D_{HO}, a summation is done over all diffraction orders (m_x, m_y). Thereafter, the component in the zeroth order D_{00}, which represents specular reflection, is subtracted.

3.3 Large-period approximation

To maximize D_{HO}, the specular reflection power fraction D_{00} needs to be minimized. In the limit of a Λ much larger than λ, this is achieved by designing the grating thickness so that the reflection from the peaks and valleys of the grating interfere destructively. In a pure metal grating this is done by making the grooves $\lambda/4$ deep. In our design, however, the phase of the reflected light is dependent not only on the grating thickness t_g, but also upon the oxide thickness t_{ox}, which is the distance from the grating to the back-side Al-mirror. However, the principle of the $\lambda/4$ grating may be extended to the case of a multilayer structure by calculating the phase of the reflected wave from the peaks and valleys of the grating structure independently. The two phases can be calculated for two uniform multilayer slab structures, one representative for the peaks of the cylinders of Fig. 1, and the other representative of the space between the cylinders. For each slab structure, we used the method of transfer matrix [31] to calculate the phase of the reflected wave. This calculation is very much faster than an RCWA simulation.

3.4 Small-period (electrostatic) approximation

For small periods the light does not interact with the grating peaks and valleys independently. Instead, the EM-waves will behave as in a homogeneous material where the effective refractive index n_{eff} is determined by the distribution of the light between the low and the high dielectric. Thus, the phase of the light reflected from the grating structure behaves like the phase of the light reflected form a homogenous slab structure where the grating layer is replaced by a homogenous (so-called metamaterial) layer with an effective refractive index. Note that the grating structure will diffract light into higher orders as long as the period Λ is larger than λ/n_{Si}. Nevertheless we have found that we can use the small-period approximation to find the optimal grating thickness needed to minimize D_{00} also for Λ slightly larger than λ/n_{Si}. The thickness of the layers should be chosen so that the light reflected from the effective homogenous slab structure has a phase of π (or equivalently $-\pi$) relative to the top of the cylinders, referring to Fig. 1. With this condition satisfied D_{00} will be suppressed due to destructive interference. Again, the calculation of the effective refractive index of the metamaterials is much faster than an RCWA simulation.

4. Simulation results

4.1 Diffraction orders and phase plot

Figure 2 compares D_{HO} calculated with GD-Calc (a) as a function of t_g and t_{ox}, with the phase difference between grating peaks and valleys (b), as calculated for the large-period approximation explained above. The free space wavelength is 1 μm, while the period in the calculations with GD-Calc is 2 μm so it is closer to the large period regime than the small

#119649 - $15.00 USD Received 6 Nov 2009; revised 24 Feb 2010; accepted 24 Feb 2010; published 3 Mar 2010

period regime. The figure shows clear correlations between D_{HO}-maxima, and the parts of the phase plot where the phase difference is close to π (or equivalently -π). Increasing the period in GD-Calc to 5 μm gives an excellent correlation for the entire range of t_g, t_{ox} values shown in Fig. 2.

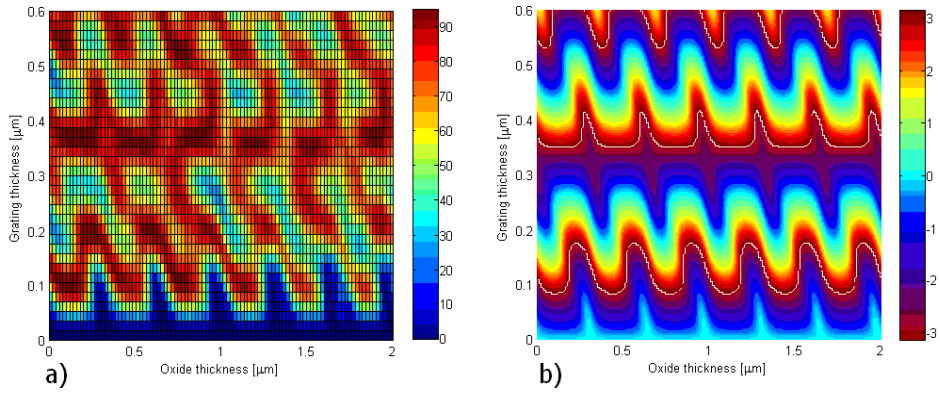

Fig. 2. Power fraction D_{HO} in higher-order diffracted beams (a), defined in Eq. (4) as a function of t_g and t_{ox} calculated with GD-calc using a period of 2 μm. (b) shows the phase difference between grating peaks and valleys calculated independently for the peaks and valleys by the transfer matrix method. A phase difference close to + π or -π indicates destructive interference at normal incidence, resulting in a corresponding maximum D_{HO}.

Figure 3 shows the small period case where the D_{HO} map (a) is calculated with a period of 0.3 μm (free-space wavelength of 1 μm), which is close to the minimum period that still allows higher diffraction orders to propagate in the Si superstrate. The phase map in Fig. 3(b) shows the reflected phase from a homogenous structure of layers where the grating layer is replaced by a slab of material with an effective refractive index n_{eff} of 3. We have written a Matlab [34] program to calculate the zero-frequency effective refractive index of a periodic pattern of parallel cylinders having the E-field perpendicular to the cylinder axes. We have used the standard angular harmonic solutions for Laplace's equation in cylindrical coordinates to set up a series expansion for the electric field, matched the electric field analytically at the surface of the cylinder, and imposed periodic boundary conditions by point matching of the electric field along the edges of a square unit cell. For this zero-frequency case we found a n_{eff} of 2.5 with a fill factor of 0.5. A general trend in the dispersion relation of the periodic structure is that the slope of the lowest band is reduced when the frequency increases. This corresponds to an increase in effective refractive index owing to accumulation of light in the dielectric with a high refractive index. Examples of such diagrams can be found in the book of Joannopoulos et a [26]. The discrepancy between the calculated value and the fitted value in Fig. 3(b) may be attributed to the fact that we are not comparing to a zero-frequency case. It is interesting to note that the grating structure has meta-material like properties also above the diffraction limit. For Λ between the two extreme cases, the D_{HO} map has features from both the small period phase map in Fig. 3 and the large period phase map in Fig. 2.

#119649 - $15.00 USD Received 6 Nov 2009; revised 24 Feb 2010; accepted 24 Feb 2010; published 3 Mar 2010

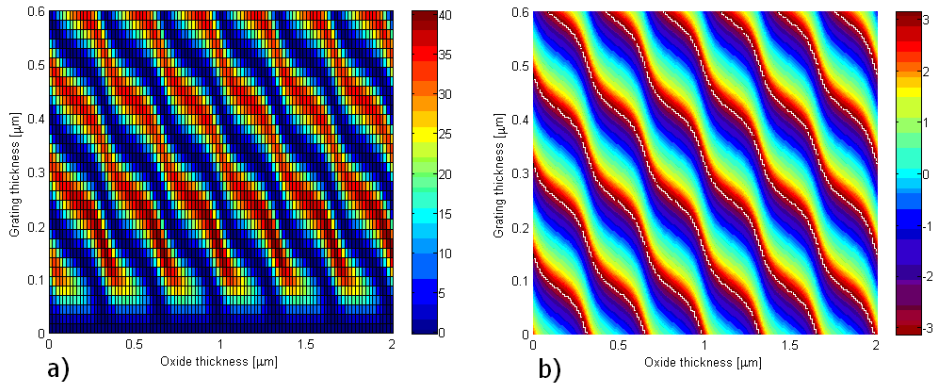

Fig. 3. (a) D_{HO} defined in Eq. (4) as a function of t_g and t_{ox} calculated with GD-calc using a period of 0.3 µm. Note that the magnitude of the higher order reflections is much lower than in figure Fig. 2(a). Figure 3(b) shows the phase plot of a reflected wave from a one dimensional stack of homogenous slabs where the grating layer have been substituted by a homogenous slab with an effective refractive index n_{eff} = 3. The calculation of phase is performed with the transfer matrix method.

The phase maps in Fig. 2(b) and Fig. 3(b) indicate the t_g and t_{ox} parameter space where we will expect to find D_{HO}-maxima. They also show us how the interactions between the layer thicknesses influence the positions of the maxima. However, the phase maps do not indicate the strength of the diffraction orders (as long as all phase maxima have the same phase e.g. ± π). In this case the analysis of the D_{HO} at the wavelength $\bar{\lambda}$ defined in Eq. (3) is a powerful tool. It provides the diffraction efficiency, and it can be performed without taking the 20 µm Si slab into account. The GD-calc simulations are faster without the slab on top. The presence of the slab with a thickness of many tens of wavelengths in the structure creates a need for a very fine wavelength sampling in every spectrum calculated, to be able to resolve the Fabry-Perot interference pattern from the 20-µm-thick Si slab. Correlation between the D_{HO}-map and absorption in the Si-slab is good, except that the D_{HO}-map seems to overestimate the light-trapping at shorter periods (not shown). To incorporate the effect of total internal reflections and secondary grating interactions simulations must be performed with the full model structure of Fig. 1.

4.2 Parasitic absorption

Al is the common choice as a back reflector for wafer based solar cells in industry today, mainly due to its low cost. However, Al reflectors suffer from a high absorption. Gratings may further enhance this problem by providing a means for coupling light to the reflector. To reduce parasitic absorption in the Al-mirror, we have placed a layer of SiO_2 between the grating and the Al mirror. Figure 4 shows the effect of t_{ox} on J_{sc} and parasitic J_{sc} (i.e. absorption current in the Al). We observe that the parasitic absorption in the Al, and therefore also the electric field strength in the Al, is only slightly effected by the thickness of the spacing layer for thicknesses above 0.2 µm. J_{sc} however continues to oscillate. This implies that it must be the *phase* of the light reflected from the Al that generates these oscillations. This is confirmed by seeing how the oscillations in J_{sc} match excellently with oscillations expected from Fabry-Perot interference in the oxide spacing layer. The same effect can also be seen in Fig. 2 and Fig. 3.

#119649 - $15.00 USD Received 6 Nov 2009; revised 24 Feb 2010; accepted 24 Feb 2010; published 3 Mar 2010

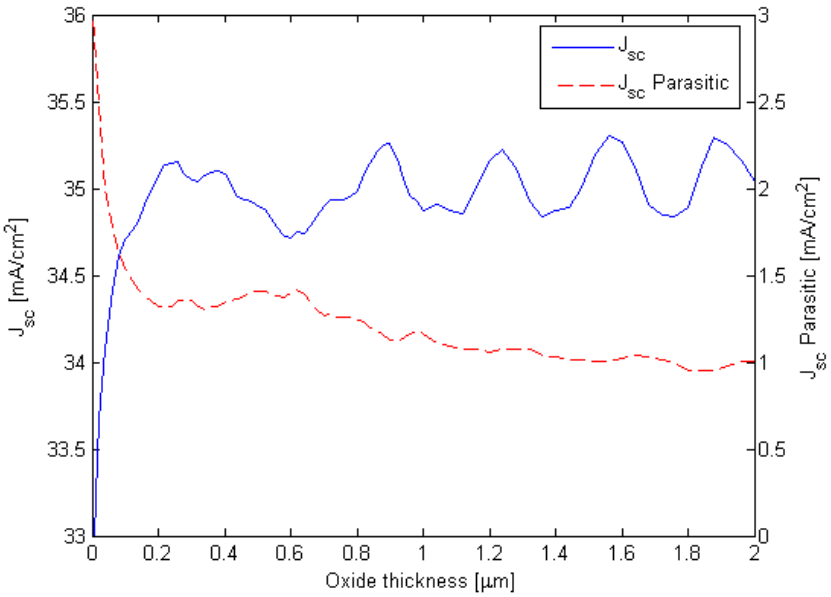

Fig. 4. The figure shows J_{sc} on the left axis, and parasitic absorption on the right axis as a function of thickness of the SiO_2 spacing layer t_{ox} between the grating and the Al mirror.

4.3 Short circuit current

Figure 5 displays a parameter scan over both Λ and fill factor for the full optical solar cell structure. A grating thickness t_g = 0.23 µm and spacing layer thickness t_{ox} = 0.2 µm was chosen on the basis of a D_{H0}–map similar to the ones shown in Fig. 2(a) and Fig. 3(a). We can see that highest values of J_{sc} are obtained over a broad parameter range with periods from 0.7 µm up to 1 µm. One should be aware that in general, for each t_g and t_{ox} we get a different version of Fig. 5, with different locations and values of the J_{sc} maxima. However, the highest J_{sc} values seem to be in the period range from around 0.6 µm to 1 µm also for other t_g and t_{ox} combinations (not shown). In addition, the trend that the ridges corresponding to high J_{sc} values moves towards higher period with increasing fill factor (most notable for small periods), remains the same also for other t_g and t_{ox} combinations. For thinner substrates Eq. (3) gives a smaller $\bar{\lambda}$, and the locations of the maxima in Fig. 5 will shift towards shorter periods.

#119649 - $15.00 USD Received 6 Nov 2009; revised 24 Feb 2010; accepted 24 Feb 2010; published 3 Mar 2010

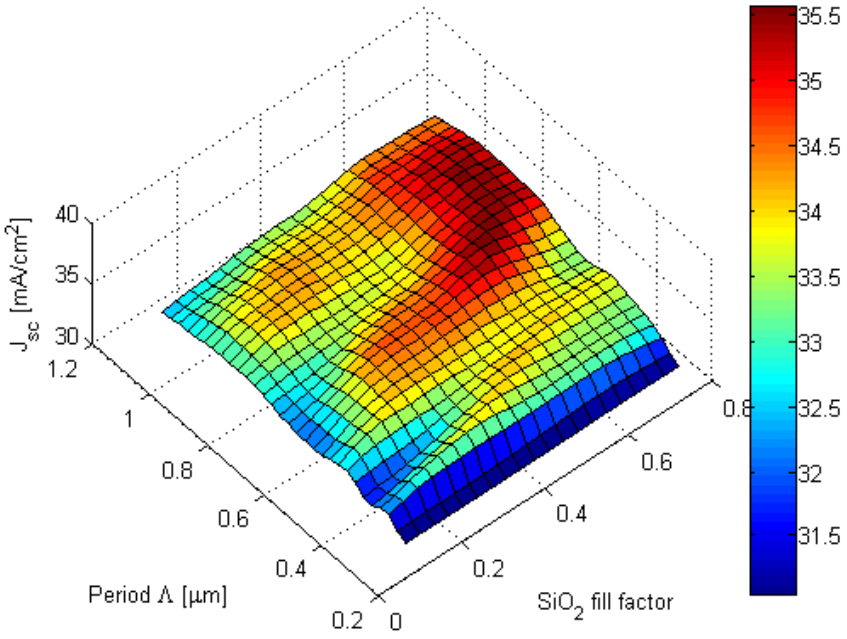

Fig. 5. The figure shows J_{sc} for different combinations of grating period Λ and fill factor for a grating thickness t_g = 0.23 μm and a spacing layer thickness t_{ox} = 0.2 μm.

For Λ outside the interval $\Lambda \in (\lambda / n_{Si}, \lambda)$ described earlier, J_{sc} drops significantly. For smaller periods J_{sc} drops because only the zeroth diffraction order remains and D_{OH} = 0. For periods larger than 1 μm there are still higher orders that may be diffracted at large angles, so the cut-off is not as sudden as the cut-off for small periods.

In Fig. 6 the spectral absorbance in the light-trapping structure from Fig. 1 is compared with the spectral absorbance in a reference cell having equal thickness and AR-coating, but a planar back side Al reflector. The figure shows a significant improvement in the wavelength range from 0.8 to 1.1 μm. At wavelengths below 0.7 μm there is no discernable difference in the absorption, and the front side reflectance is the limiting factor. Figure 6(a) shows the rapid Fabry-Perot oscillations resulting from interference in the 20 μm thick Si slab. A time-consuming dense wavelength sampling is required to resolve the oscillations. Analysis of the D_{HO} is therefore an efficient way to do a faster analysis of the structure. In Fig. 6(b) one can see remnants of these oscillations, after they have been reduced with the help of a digital low-pass filter (a moving average), for easier comparison of the curves.

#119649 - $15.00 USD Received 6 Nov 2009; revised 24 Feb 2010; accepted 24 Feb 2010; published 3 Mar 2010

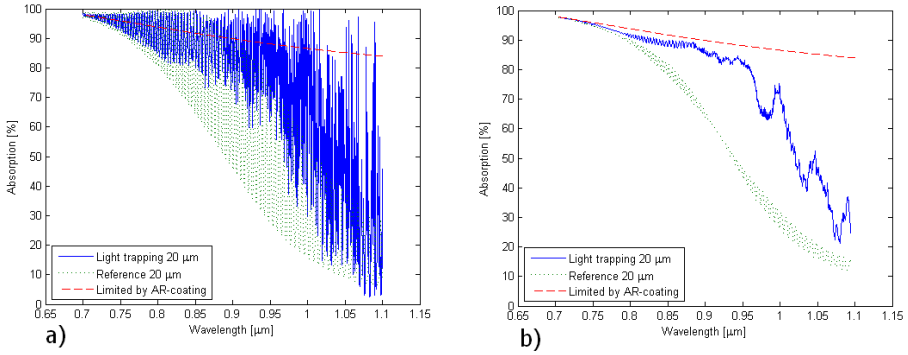

Fig. 6. The figure shows absorption as a function of wavelength for the light-trapping design (solid line) and the reference (dotted line), compared to the limitation imposed by the front-side reflectance from a single layer AR-coating on top of an infinite Si slab (dashed line). (a) shows the simulated spectral response, and (b) shows a moving average of the same data. A Λ of 0.7 µm, fill factor of 0.6, t_g of 0.23 µm and t_{ox} of 0.2 µm are used for the light trapping structure.

In Table 1 the absorbance in Fig. 6 is inserted in Eq. (1) to calculate the J_{sc}. We see that the light-trapping structure with Al reflector holds the potential to improve J_{sc} by 5.1 mA/cm^2, or 17% relative, compared to a 20 µm thick reference cell.

Table 1. Comparison of J_{sc} for different model structures assuming all excited charge carriers reach the contacts. The spectral response of the 20 µm reference and the light-trapping structure with Al-reflector is shown in Fig. 6. The same parameters are used for all light trapping three cells, varying only the back side reflector. The AM 1.5 absorbance is the percentage of the photons in the wavelength interval 300-1100 nm which are absorbed in the Si.

Structure	J_{sc} [mA/cm^2]	AM 1.5 absorbance
Light trapping 20 µm – ideal reflector	36.1	83.0%
Light trapping 20 µm – Ag reflector	35.9	82.5%
Light trapping 20 µm – Al reflector	35.5	81.6%
Reference 20 µm	30.4	69.9%
Reference 160 µm	36.6	84.1%

The reflectance of Ag is in general significantly better than for Al. Table 1 show us that we will gain 0.4 mA/cm^2 by replacing the Al reflector in Fig. 1 with Ag. Actually, the parasitic J_{sc} is reduced by 0.7 mA/cm^2 for the Ag reflector (not shown), but only a bit more than half of this is contributing to the J_{sc}. For a perfect reflector the J_{sc} reaches 36.1 mA/cm^2. The light-trapping cell with Al reflector from Table 1 actually achieves the same J_{sc} as a 5 times thicker planar reference cell with the same AR coating and an Al reflector. This is equivalent to an average absorption length of 180 µm in silicon, or an increase in optical thickness by a factor of 9. In other words, the number of photons absorbed in the light-trapping cell with an Al reflector is the same as what would be absorbed in the first 180 µm of an infinitely thick Si-slab with the same AR-coating as the light-trapping cell. The light-trapping structure with Ag reflector increases optical thickness by a factor of 11.

4.4 Comparison with literature

Comparison with different light-trapping concepts is not straight forward due to the differences in cell design, thickness, surface structures, and material and cell materials. To further complicate the picture, different authors use different parameters to describe the effect of their light-trapping design. Quantitative comparison of back-side light-trapping structures with AR-structures is unsuitable since the back-side structures address only the part of the solar spectrum that reaches the back side, while AR-structures address the whole solar spectrum. The predicted light-trapping effect in solar cells for periodic structures have been confirmed experimentally by other authors for 1D gratings [13,18]. No such comparison has

#119649 - $15.00 USD Received 6 Nov 2009; revised 24 Feb 2010; accepted 24 Feb 2010; published 3 Mar 2010

been found for 2D gratings. However, a 2D Al dimple pattern was recently compared to one of the best random structures available, and showed good results [9].

Most of the relevant data from literature focus on thinner cells. For comparison purposes we have modeled the light trapping response of our periodic structure on thinner cells. However, a separate optimization of AR-coating or grating parameters for the given thickness has not been performed. Therefore, a further improvement of light trapping could be expected from our structure by performing the optimization for the given thickness.

Mutitu et al. [17] found a J_{sc} of 30.3 mA/cm^2 for a 5 µm thick c-Si cell including both a 1D triangular shaped back-side grating with a dielectric Bragg reflector, and a front side binary grating with a double layer AR-coating. A J_{sc} of 27.4 mA/cm^2 was obtained with no front-side grating, and a binary grating together with the Bragg reflector on the back side. We obtain an equivalent J_{sc} (30.3 mA/cm^2) with a planer front-side AR-coating and our back-side structure. We observe that parasitic absorption in the Al-reflector has more than doubled at this thickness compared to the 20 µm cell. The use of Ag back reflector would be more advantageous at this thickness than for the 20 µm thick cell.

Bermel et al. [15] modeled a 2 µm c-Si cell with a dielectric Bragg back-reflector in combination with different types of periodic light scattering structures. Bermel used Henry's model [32] for radiative recombination as a loss mechanism, to get efficiency from J_{sc}. Bermel's best result was obtained for a 2D triangular back-side cylinders pattern, and showed an efficiency of 16.32% corresponding to a J_{sc} of 23.9 mA/cm^2 for a lossless model like ours. With our structure and the Al back reflector applied to a 2 µm thick cell we obtain a J_{sc} of 26.4 mA/cm^2, or an improvement of 10% over Bermel's structure.

4.5 Angular dependence

For non-tracking solar panels the angle of the incident light (i.e. the sun) varies with time. Thus, it is of great interest to study the response of the light-trapping structure at different incidence angles. The angle of incidence is in general specified by the polar angle θ and the azimuth angle φ. We have studied the effect of θ on the J_{sc} while keeping φ fixed so that the incidence plane is along one of the directions of periodicity. Both s-polarization and p-polarization are considered. For s-polarization the E-field is transverse to the normal of the layer structure, while for p-polarization the E-field is in the plane of incidence. The solar irradiance is unpolarized, thus the light incident at the solar cell contains equal amounts of s- and p-polarization. In real life, the solid angle captured by the module (as seen from the sun) decreases with cos(θ). Small angles of incidence will therefore be relatively more important with respect to power generation than larger angles of incidence. In Fig. 7 a constant solid angle is assumed, so that each angle represents a solar panel with a different area.

Figure 7 shows the angular dependence of J_{sc} for both the light-trapping structure and the reference cell. Contrary to what one might assume, the average J_{sc} increases with incidence angle for both cell structures. For the light-trapping cell J_{sc} is notably higher at angles around 10 - 20 degrees than at normal incidence, before it starts to drop steadily cell for higher θ. The reference cell has a smaller J_{sc} increase at small θ, but it lasts all the way to 55 degrees.

#119649 - $15.00 USD Received 6 Nov 2009; revised 24 Feb 2010; accepted 24 Feb 2010; published 3 Mar 2010

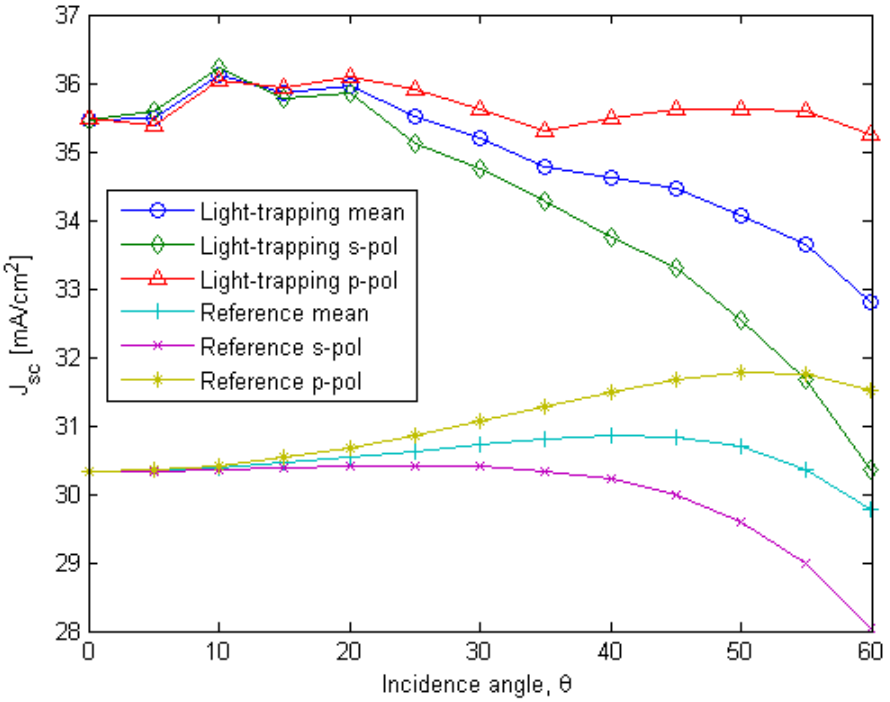

Fig. 7. The figure shows the effect of incidence angle on J_{sc} for the cell with light-trapping structure and for the reference cell. Both p-polarization and s-polarization and their mean are shown.

The increase in J_{sc} for the reference cell can be explained by the Brewster angle effect, where front-side reflectance will be reduced towards zero for p-polarization. The light-trapping cell will experience the same Brewster angle effect at the front surface. However, the improvement in J_{sc} is more than what would be expected from this effect at small θ while J_{sc} is significantly lower where the Brewster effect is at its strongest. An increase in J_{sc} at small θ was also reported in [17] for a 1D line grating. We believe this increase might be attributed to less out-coupling of light due to the reduced symmetry at oblique incidence. The problem of out-coupling is discussed in [6].

Varying the incidence angle θ_i in the grating equation (i.e. Eq. (2)) will also change the angles of the outgoing modes in the same plane. By inserting $\bar{\lambda}$ from Eq. (3) into Eq. (2) we find that at an incidence angle θ_i = 23.5 degrees, the m = –1 mode (in the same plane) will no longer be totally internally reflected at the front surface. This gradual escape of diffraction orders is an effect which may explain parts of the reduction in J_{sc} that we observe for the light-trapping structure.

5. Discussion

Due to the recent advances in crystalline Si substrate manufacture described above, we have chosen to focus our attention on Si cells with a thickness of 20 µm. This is considerably thinner than state of the art wafer-based cells today (around 160 µm), but also well above the common thin-film technologies with layer thickness of only a few microns. The relative gain by adding a light trapping structure will of course be larger the thinner the cell, and most of the earlier works focus on cells significantly thinner than 20 µm. However, an advantage of the semi-thin (e.g. 20 µm) cells investigated in this work is that the spectrum of the light that is transmitted to the back side is narrower than for thinner cells, due to significantly stronger

#119649 - $15.00 USD Received 6 Nov 2009; revised 24 Feb 2010; accepted 24 Feb 2010; published 3 Mar 2010

absorption at shorter wavelengths. It is therefore possible to optimize the light trapping effect for the narrow spectral range that reaches the back side of the 20 μm thick Si-slab. Periodic structures are particularly well suited for this purpose, since they can easily be exploited to make a narrowband trapping response.

In general, the parasitic absorption in a metal mirror is higher, the higher the index of refraction is in the adjacent dielectric where the light propagates. The SiO_2-Al boundary reduces parasitic absorption of light in the metal compared to a Si-Al boundary. Another vital effect of the SiO_2-layer is to move the metal away from the grating, so that the evanescent waves from the grating that reach the metal are weaker. As we saw in Table 1, Ag may help to further reduce the parasitic absorption. However, the improvement of 1.1% by replacing the Al mirror with Ag is not as large as one would expect by looking at the reflecting properties of the two materials. The reason for this we believe to be that our structure is optimized both for light scattering and for reduced absorption, thus maximizing J_{sc}. We should point out that we have just simulated the performance of an Ag mirror used with a grating structure optimized for an Al mirror; we have not optimized the grating structure for an Ag mirror. The advantages of using Al as a back reflector instead of Ag are not just the material costs, but also that Al is directly compatible with the laser fired contact process [33], which is one obvious way of making the electrical contact at the back side of the cell.

We have focused in this work on binary cylindrical geometries with oxide cylinders in silicon as shown in Fig. 1. Binary structures have the advantage of requiring relatively short computation times with RCWA compared to more complex geometries. In addition they may be fabricated using conventional silicon micro-fabrication technology. The simplicity of such a binary system is also favorable for analyzing the interactions between light and the grating structure. Other geometries may possibly hold the potential for even more efficient light trapping. For example, it has been shown that blazed gratings perform better than binary gratings for a 1D structure when the grating structure was applied to both the front and the back side [6,18].

We have investigated different cylinder configurations; triangular lattice instead of square, and silicon cylinders instead of oxide cylinders. We found no significant difference in the maximum J_{sc} between the different configurations. We have found that a SiO_2 fill-factor above 0.5 (i.e., oxide cylinders with radius above 0.4Λ or Si cylinder with radius below 0.4Λ) is favorable for silicon cylinders as well as for oxide cylinders. On the other hand, Fig. 5 shows that there is a wide range of different periods and fill factor combinations that have the potential of providing a high J_{sc}. This freedom in design with respect to period, fill factor and material may be an advantage with respect to fabrication.

To further increase the light trapping a better AR-coating is needed. A double layer AR-coating would add more than 1 mA/cm^2 to all the J_{sc}-values of Table 1. Encapsulating the cell would also help reduce the front side reflectance by making the change in refractive index more gradual. To reduce the reflectance further, a front-side texturing of some sort is usually applied. Configurations with a 1D front and back-side periodic grating have been shown to increase light trapping compared to configurations with only a 1D back-side grating [11,17]. The effect of a randomly structured front side, however, is difficult to assess. Simulation of random structures with the RCWA method are very slow, because they are typically done with the help of very large unit cells that are many wavelengths on the side, but with adequate resolution to resolve the periodic structures.

6. Conclusion

We have presented a light-trapping design for a solar cell, incorporating a back-side bi-periodic pattern of silica (SiO_2) cylinders combined with a layer of SiO_2 to detach the grating from the back-side Al mirror. The grating increases the coupling of light into the Si solar cell, while the layer of SiO_2 reduces the parasitic absorption in the Al mirror and ensures a good surface passivation. Simple design criteria for optimizing grating performance have been presented. In particular the interaction between the EM-waves in the grating layer and oxide layer has been investigated for two extreme cases (i.e. large periods and short periods),

#119649 - $15.00 USD Received 6 Nov 2009; revised 24 Feb 2010; accepted 24 Feb 2010; published 3 Mar 2010

showing good agreement between fully vectorial EM-field simulation results and simple scalar optical field models. The scalar models are very helpful in limiting the parameter space for the numerical simulations. We have performed numerical simulations to quantify the light trapping in terms of the short circuit current density. Our simulations show that for an optimized 20 μm thick Si solar cell, a short circuit current density of 35.5 mA/cm^2 would be obtained if all the charge carriers are collected at the contacts. This is an increase of more than 17% compared to a reference cell with the same thickness and a planar back-side Al mirror. Our design is also effective for thinner cells, and we see an improvement compared to two recently published papers for cell thicknesses of 2 and 5 μm, respectively. The light-trapping design presented shows promising behavior over a wide range of incidence angles. To further improve the light trapping, the front-side reflection should be reduced.

Acknowledgments

The author acknowledges the Nordic Center of Excellence in PV and the Norwegian Research Council through the Nanomat program for the financial support.

#119649 - $15.00 USD Received 6 Nov 2009; revised 24 Feb 2010; accepted 24 Feb 2010; published 3 Mar 2010

2D blazed grating for light trapping in thin silicon solar cells

Jo Gjessing[1,2,3], Aasmund Sudbø[4,2], Erik Stensrud Marstein[1,4]
[1] *Institute for Energy Technology, Pb 40, 2027 Kjeller, Norway*
[2] *University Graduate Center at Kjeller, Norway*
[3] *University of Oslo, Department of physics, Norway*
[4] *University of Oslo, Faculty of Mathematics and Sciences, Norway*
Corresponding author e-mail address: Jo.gjessing@ife.no

Abstract: We propose a novel sub-micron back-side grating for light trapping in thin silicon solar cells. The 2D-blazed grating has the potential to increase the optical thickness of the solar cell by a factor of 17.

OCIS codes: (050.1970) Diffractive optics; (350.6050) Solar energy.

1. Introduction

Decreasing the thickness of Si solar cells appears to be one of the most promising ways of reducing the cost of solar electricity. Methods for making crystalline Si substrates with a thickness below 20μm, well below the 150 -200 μm commonly used today, have recently been demonstrated, using lift-off techniques based on proton implantation [1]. However, due to the poor absorption of crystalline Si in the near-infrared spectrum, light trapping is essential to avoid optical losses in such thin substrates.

The surface textures commonly used in the relatively thick cells of today are in general not suitable for cell thicknesses below 20μm, because of the large feature size of these textures (2-10 μm). For thin-film cells, typically having thicknesses on the order of 1 μm, textures of front side oxides have been developed. All of these textures are of a random nature. Yablonovitch [2] showed that for an ideal randomizing structure, the maximum theoretical intensity increase for a weakly absorbing material with an index of refraction of n is $4n^2$ (~50 for Si). In actual fabricated cells, this factor is more in the range of 10 [3]. Periodic structures have the potential to exceed the limit of the randomizing textures [4], and seem promising for light trapping in thin Si solar cells, as verified through both theoretical [5] and experimental studies [6].

According to Heine and Morf [7], a blazed 1D grating (i.e., regular grating with straight parallel grooves) on the back side of a solar cell is beneficial for light trapping. This is attributed to a reduced out-coupling of light by avoiding mirror symmetries in the grating. Unfortunately, a 1D grating can trap only one of the two polarizations present in sunlight efficiently. We overcome this limitation by designing a novel 2D blazed back-side grating structure with excellent light-trapping properties. In addition to the 2D blazed grating, our light-trapping scheme consists of a back-side Al mirror separated from the grating by a thin layer of SiO_2, as shown in [8]. The purpose of the SiO_2 layer is to reduce the absorption in the back-side metal by reducing the electromagnetic coupling from the Si and the grating to the metal. SiO_2 is also excellent for passivation of Si, which is especially important in thin crystalline Si solar cells, where more of the generation of charge carriers will occur close to the back side.

2. Methodology

Figure 1 shows the total, optical model structure that we have investigated numerically. We performed the electromagnetic computation with Grating Diffraction Calculator (GDC) [9]. GDC uses rigorously coupled wave analysis (RCWA), wherein the Maxwell equations are solved independently in horizontal layers in the Fourier space, before the solutions are coupled with the specific boundary conditions. This method is especially effective for computations where there are large differences in the thicknesses of the individual layers. The oblique planes of the blazed grating are represented by a staircase structure consisting of 10 steps.

We have optimized the structure by varying the following three different parameters illustrated in Figure 1; the grating period Λ, the grating thickness t_g, and the thickness t_{ox} of the oxide layer separating the grating from the back side metal. To limit the necessary computational time, the three-dimensional parameter scan was performed for an infinitely thick Si slab for a single wavelength. From the parameter scan we analyzed the diffraction into higher orders D_{HO} given by Eq. (1).

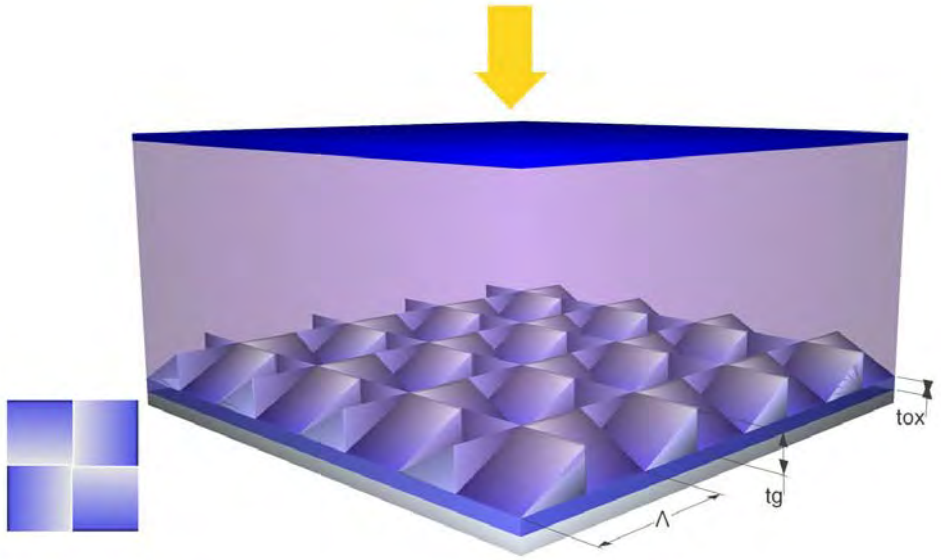

Figure 1: Model of the 2D blazed structure. Each unit cell consists of 4 quadrants with oblique planes sloping in different directions. The inset shows a false-color representation of one unit cell viewed from above, with color representing height. Beneath the grating is a layer of SiO_2, and an Al mirror. Above the grating is a 20 µm thick Si-slab with an anti-reflection coating. The model is not to scale.

$$D_{HO} = \sum_{m_x} \sum_{m_y} D_{m_x m_y} - D_{00} \quad (1)$$

The summation is performed over a finite number of diffraction orders (m_x, m_y). Evanescent (non-propagating) diffraction orders transfer no power in a lossless Si slab, so all the power is contained within the propagating diffraction orders. The zero order (specular) reflection D_{00} is subtracted to get the power diffracted into higher orders. This method is useful for locating potential maxima where in-coupling is high and back-side absorption low. However, D_{HO} does not reveal the angles of diffraction and internal distribution of power between the higher diffraction orders. Neither will effects such as out-coupling be identified in the process. The maxima must therefore be explored in further detail before running the full structure computations.

We use the maximum short circuit current density J_{sc} (assuming that all photo-generated charge carriers are collected at the contacts) to quantify the light-trapping effect. J_{sc} is found by weighting the spectral absorption calculated with GDC with the photon flux from the AM1.5 spectrum corresponding to 1000 W/m^2. The integration needed to obtain J_{sc} is performed from 300 nm to 1100 nm due to low solar irradiance or absorption values outside this interval.

To study the effect of back-side absorption and front side reflection, we have investigated both Al and Ag mirrors and single- and double-layer antireflection coatings (SLAR and DLAR). Wavelength dependent optical data is used for Si [10], Al and Ag [11]. For the SLAR we used Si_3N_4 with a refractive index of n=1.95 and a thickness of 78 nm. The DLAR consisted of 108 nm of magnesium fluoride (MgF_2, n=1.37) and 60 nm of zinc selenide (ZnS, n=2.35).

3. Results and discussion

The maximum J_{sc} for the 2D blazed grating was found for a period Λ=0.95 µm, t_g =0.4 µm and t_{ox}=0.1µm. The spectral absorption with these parameters is shown in Figure 2. The corresponding J_{sc} is 36.8 mA/cm^2, which is more than 20 % higher than for the reference cell also shown in Figure 2. It is interesting to note that the spectral absorption makes a leap at exactly 950 nm, which is also the period of the grating. For wavelengths larger than the period, only the zeroth order is allowed to propagate in air, which reduces the number of allowed escape modes for the light. The resulting J_{sc} for the different configurations are summed up in Table I.

From Table I we see that a 20 µm thin solar cell with the light trapping supplied by the 2D blazed grating structure can produce more current than the 8 times thicker 160 µm reference cell. This is found to correspond to an increase in optical thickness of a factor of 17. In other words, an absorbing Si-slab with the same AR-coating would need a thickness of 340 µm to absorb the same amount of photons as the 20 µm thick cell with 2D blazed grating and

Al-mirror. This increase in optical thickness also implies that the light will have several interactions with the back side, thus the reflectivity of the mirror will be of special importance. Changing to a higher reflectivity metal like Ag reduces the parasitic absorption from 1.3 mA/cm^2 to 0.5 mA/cm^2 (not shown) giving a J_{sc} of 37.3 mA/cm^2, or equivalent to an increase in optical thickness of 22.

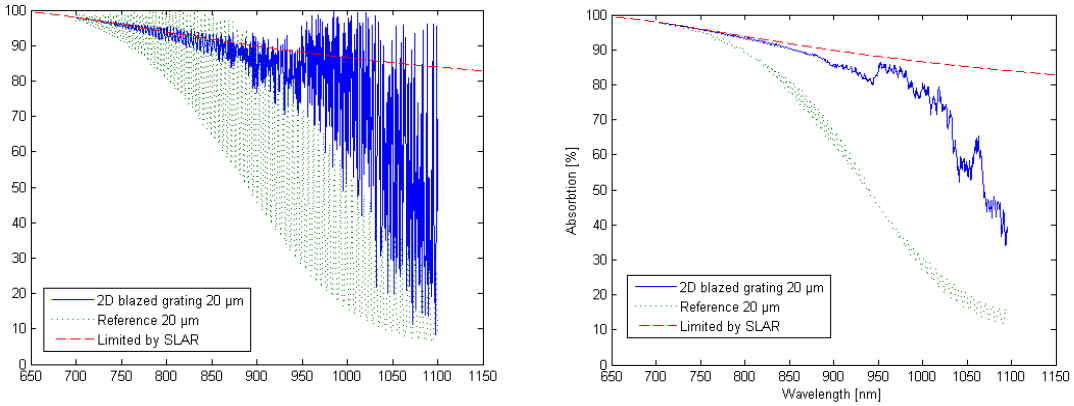

Figure 2: To the left is the spectral absorption in a 20 µm thick Si-cell with a 2D blazed grating with Al-mirror and SLAR (solid), the estimated absorption in a reference cell with equal thickness and a planar back side Al-mirror (dotted), and the limitation given by the front side reflection from a SLAR (dashed). The rapid oscillations in the figure to the left is caused by Fabry-Perot interference in the 20 µm thick Si-slab. To the right is a moving average of the values on the left.

Table I: Comparison of potential J_{sc} for different solar cell configurations.

Structure	J_{sc} with SLAR [mA/cm^2]	J_{sc} with DLAR [mA/cm^2]
2D Blazed 20 µm Al-mirror	36.8	38.7
2D Blazed 20 µm Ag-mirror	37.3	39.3
Reference 20 µm Al-mirror	30.4	31.8
Reference 160 µm Al-mirror	36.6	38.6

A comparison of the configurations from Table I reveals that the front-side reflection is a key to further improvement of light trapping. The change from SLAR to DLAR increases J_{sc} by 2 mA/cm^2. The best configuration with DLAR and Ag mirror gives a J_{sc} of 39.3 mA/cm^2, corresponding to absorption of more than 90 % of the photons in the solar spectrum in the interval 300-1100 nm. DLARs are not, however, commonly used in manufactured modules due to the cost of manufacture combined with the constraints imposed by the refractive index of the front-side cover glass. The encapsulated modules will have increased reflection losses compared to the DLAR, but compared to the SLAR reflection losses may actually be reduced due to a more gradual change in refractive index. However, absorption in the glass and the laminating polymer (EVA) must be accounted for in the case of an encapsulated cell.

We conclude that an extension of the blazed grating to two dimensions provides a successful light-trapping structure with an 8 times increase in optical thickness compared to a planar reference cell. Combined with a proper front-side anti-reflection coating this allows for high efficiency solar cells made of thin Si-wafers.

[1] F. Henley et al., “Direct film transfer (DFT) technology for kerf-free silicon wafering,” 23rd PVSEC, Valencia, Spain (2008).
[2] E. Yablonovitch, “Statistical ray optics,” J. Opt. Soc. Am., Vol.72, (1982).
[3] J. Nelson, “The Physics of Solar Cells,” 1.Ed., World Scientific Publishing, (2003).
[4] P. Sheng et al., “Wavelength-selective absorption enhancement in thin-film solar cells,” Appl. Phys. Lett. Vol. 43 (1983).
[5] D. Zhou and R. Biswas., “Harvesting photons in thin film solar cells with photonic crystals,” Mater. Res. Soc. Symp. Proc., Vol. 1101, (2008).
[6] H. Sai et al., “Enhancement of light trapping in thin-film hydrogenated microcrystalline Si solar cells using back reflectors with self-ordered dimple pattern,” Appl. Phys. Lett., Vol. 93, (2008).
[7] C. Heine and R.H. Morf, “Submicron gratings for solar energy applications,” Applied Optics, Vol. 34, pp 2476-2482, (1995).
[8] J. Gjessing, E.S. Marstein, A. Sudbø, "Modelling of light trapping in thin silicon solar cells with back side dielectric diffraction grating,”, presented at the 24th EU PVSEC, Hamburg, Germany, 21-25 Sept. (2009).
[9] http://software.kjinnovation.com/GD-Calc.html
[10] C.M. Herzinger et al., ” Ellipsometric determination of optical constants for silicon and thermally grown silicon dioxide via a multi-sample, multi-wavelength, multi-angle investigation,” J. Appl. Phys., Vol. 83, pp 3323–3336, (1998).
[11] E.D. Palik, “Handbook of Optical Constants of Solids,” Academic press (1985).

A novel broad-band back-side reflector for thin silicon solar cells

Jo Gjessing[1,2,3], Aasmund S. Sudbø[4,2], Erik S. Marstein[1,4]
[1]Institute for Energy Technology, Pb 40, 2027 Kjeller, Norway
[2]University Graduate Center at Kjeller, Norway
[3]University of Oslo, Department of Physics, Norway
[4]University of Oslo, Faculty of Mathematics and Sciences, Norway
e-mail: jo.gjessing@ife.no

Summary
Efficient light trapping is necessary if Si-wafer thickness is to be reduced without compromising efficiency. In this work we propose a back-side 2D periodic structure with exceptional light trapping properties. We find through numerical simulations that the efficiency of our design exceeds that of ideal Lambertian light trapping.

Introduction

Cost reduction schemes aim to reduce the thickness of wafer based silicon (Si) solar cells. Currently, light trapping in industrial solar cells results from alkaline anisotropic or acidic isotropic etches. These methods create structures with sizes that typically vary from 1 µm up to 10 µm depending on etch times, concentrations etc. Because of their large and random structure size, these structures may be difficult to implement if the thickness of solar cells is reduced to a few tens of µm. In addition, the textures are developed mainly for good anti-reflection behaviour, and more efficient light trapping is obtainable with other structures. Yablonovitch [1] showed that within geometrical optics, a limit on path length enhancement of $4n^2$ (~50 for Si) can be expected in a weakly absorbing material. A perfect Lambertian surface could provide such ideal light trapping.

In this work we discuss a novel light-trapping scheme consisting of a 2D periodic back-side structure. The design has shown in simulations to provide light trapping exceeding that of the ideal Lambertian reflector. We demonstrate its performance on Si slabs with thicknesses above 10 µm. This thickness is much larger than the thickness of conventional thin film cells which commonly use textured transparent conductive oxide materials to improve light trapping.

Methodology

The light-trapping structure investigated in this work is shown in Figure 1. The structure is slightly less symmetric than our earlier proposed structure in which the oblique plane of each quadrant slopes in a different direction [2]. In this structure the quadrants of the extended unit cell slopes in only two different directions. The thickness of the Si slab used in the calculations was 20 µm. The grating thickness t_g, period Λ and the thickness of the oxide layer t_{ox} was varied within a limited interval. This process is described in more detail in [3]. We have used the software Grating-Diffraction Calculator (GD-Calc) [4] to investigate the structure. GD-Calc uses rigorously coupled wave analysis (RCWA).

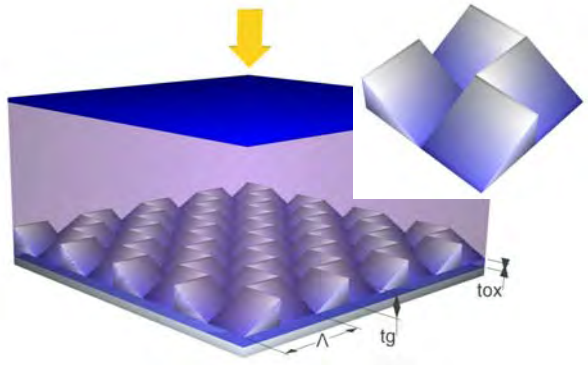

Figure 1: Optical model for simulations (left) consisting of a planar ARC, Si active material, and light trapping layer, back side oxide and metal mirror. The inset shows two unit cells of the structure.

To quantify the light trapping effect, the spectral absorption calculated with GD-Calc is weighted against the AM1.5 spectre and converted to an equivalent short circuit current density J_{sc} by assuming 100 % collection efficiency of the charge carriers.

Results and discussion

Figure 2 shows the spectral absorption of the light trapping structure with an Ag-reflector. Low absorption for shorter wavelengths is due to front side reflection, while above 800 nm it is the combined effect of front side reflection and incomplete light trapping. A moving average is used to smooth the fringes resulting from interference in the Si-slab for easier comparison. The spectral absorption for the Ag-mirror corresponds to a J_{sc} of 37.7 mA/cm^2. Replacing the Ag mirror with Al reduces J_{sc} to 37.25 (not shown), due to increased parasitic absorption in the back side metal. A maximum J_{sc} was found for a parameter combination of Λ=1.4 µm (for the extended unit cell), t_g=0.6 µm and t_{ox} of 0.1 µm.

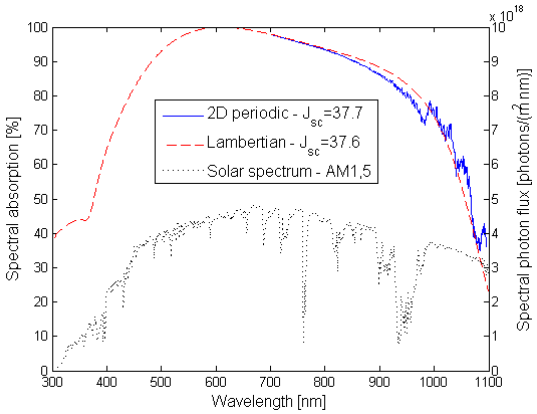

Figure 2: Spectral absorption plot of our light trapping structure (solid, blue curve) compared ideal Lambertian light trapping constrained by a single ARC in front (dashed, red curve). Also shown is the spectral photon flux (dotted, black curve).

Deckman et al. [5] derived an expression for absorption assuming an ideal Lambertian diffuser and no front side reflection. For comparison with our model we have adjusted the model by adding front side reflection corresponding to a planar ARC of Si_3N_4. The resulting absorption is shown in Figure 2. We see that the light trapping from our structure with Ag-reflector (37,7 mA/cm^2) actually exceeds the ideal Lambertian light trapping (37,6 mA/cm^2). However, this is not contradictory to theory, because the limit is derived for isotropic irradiance. Light trapping can exceed this limit for a narrower irradiance as in this case with normal incidence.

The improvement of our new light-trapping structure, when compared to the structure presented in [2] may be due to the symmetry of the structure that couples light more efficiently in some orders than others. This might reduce the leaking of orders due to out-coupling.

Conclusion

We have found a light trapping design with exceptional light trapping properties, matching that of the conventional theoretical limit for light trapping. This is a structure which can in principle be fabricated, despite its complexity. We believe that it is possible to design a 2D grating that has the same light trapping properties as the one we propose here, and lends itself to actual fabrication.

References

[1] E. Yablonovitch, J. Opt. Soc. Am. 72, 899-907 (1982).
[2] J. Gjessing, A. Sudbø, E.S. Marstein, Optics for Solar Energy, Tucson USA, (2010).
[3] J. Gjessing, E.S. Marstein, A. Sudbø, Opt. Express, Vol. 18, 5481-5495 (2010).
[4] http://software.kjinnovation.com/GD-Calc.html
[5] H. W. Deckman et al., Appl. Phys. Lett Vol. 42, 968-970 (1983).

A novel back-side light trapping structure for thin silicon solar cells

J. Gjessing
jo.gjessing@ife.no
Institute for Energy Technology, Department of Solar Energy, P.O. Box 40, 2027 Kjeller, Norway
University of Oslo, Department of Physics, P.O. Box 1048 Blindern, 0316 Oslo, Norway
University Graduate Center at Kjeller, P.O. Box 70, 2027 Kjeller, Norway

A. S. Sudbø
University of Oslo, Department of Physics, P.O. Box 1048 Blindern, 0316 Oslo, Norway
University Graduate Center at Kjeller, P.O. Box 70, 2027 Kjeller, Norway

E. S. Marstein
Institute for Energy Technology, Department of Solar Energy, P.O. Box 40, 2027 Kjeller, Norway
University of Oslo, Department of Physics, P.O. Box 1048 Blindern, 0316 Oslo, Norway

Decreasing silicon consumption is one of the most important ways of reducing the cost of solar cells. High-quality light trapping provides the possibility of making thinner silicon solar cells without sacrificing optical efficiency. In this work we introduce an advanced bi-periodic back-side structure with promising light trapping properties. The structure combines high coupling efficiency of light to oblique travelling modes with the ability of keeping the light within the solar cell for multiple reflections between the front and the rear side. We have done numerical simulations of light trapping for normal incidence in our structure, and we show that our structure with real materials holds the potential to exceed the light trapping of an ideal Lambertian surface. We also investigate the behaviour of our light trapping structure as a function of incidence angle and state of polarization, and compare it to the Lambertian behaviour. [DOI: 10.2971/jeos.2011.11020]

Keywords: solar cells, light trapping, diffraction grating

1 INTRODUCTION

Light trapping is essential in any silicon (Si) solar cell due to poor absorption in the infrared. Light trapping in industrial solar cells nowadays is commonly achieved by alkaline anisotropic etching for monocrystalline Si or by acidic isotropic etching for multicrystalline Si. These methods create structures with sizes that typically vary from 1 μm up to 10 μm depending on etch times, concentrations, temperatures etc. Because of their large and random size, these structures may be difficult to implement if the thickness of solar cells is reduced to a few tens of microns as new production methods may allow [1]. Conventional textures have been developed mainly for good anti-reflection behaviour and are not optimized for light trapping. In thinner cells, light trapping will be even more important. For thin-film solar cells light trapping is usually achieved through texturing of transparent conductive oxides (TCOs) before depositing the active solar cell material.

A benchmark for light trapping is the geometrical optics limit on path length enhancement for isotropic irradiance of $4n^2$ (~50 for Si) in the limit of weak absorption [2]. A perfect Lambertian surface could provide such ideal light trapping. In practice, conventional light trapping structures show path length enhancements closer to 10 [3]due to lack of total randomization and absorbing surfaces. Recently it has been shown that light trapping in periodic structures can exceed the geometrical optics limit considerably at normal incidence [4]. 2D skewed pyramids [5] and more complex 3D structures [6] have already through modelling been shown to result in an increase beyond the geometric light trapping limit at normal incidence. There is experimental evidence of light trapping from periodic plasmonic structures exceeding that of the Asahi U-type glass, a state-of-the-art textured TCO glass, in thin-film solar cells [7, 8].

In this work we discuss a novel light trapping scheme consisting of a 2D periodic back-side structure as shown in Figure 1. The design has been shown through simulations to provide light trapping exceeding that of the ideal Lambertian surface at normal incidence [9]. Here we investigate the light trapping performance at nonzero angles of incidence. We also analyse the mechanisms behind the light trapping in greater detail.

2 NUMERICAL METHODS

The light trapping structure we have investigated and the unit cell of the grating is shown in Figure 1. The structure is based on a square lattice. The quadrants of the unit cell slopes in two different directions, so that the structure lacks the inversion of our earlier proposed structure in which the

Received December 17, 2010; published April 25, 2011 ISSN 1990-2573

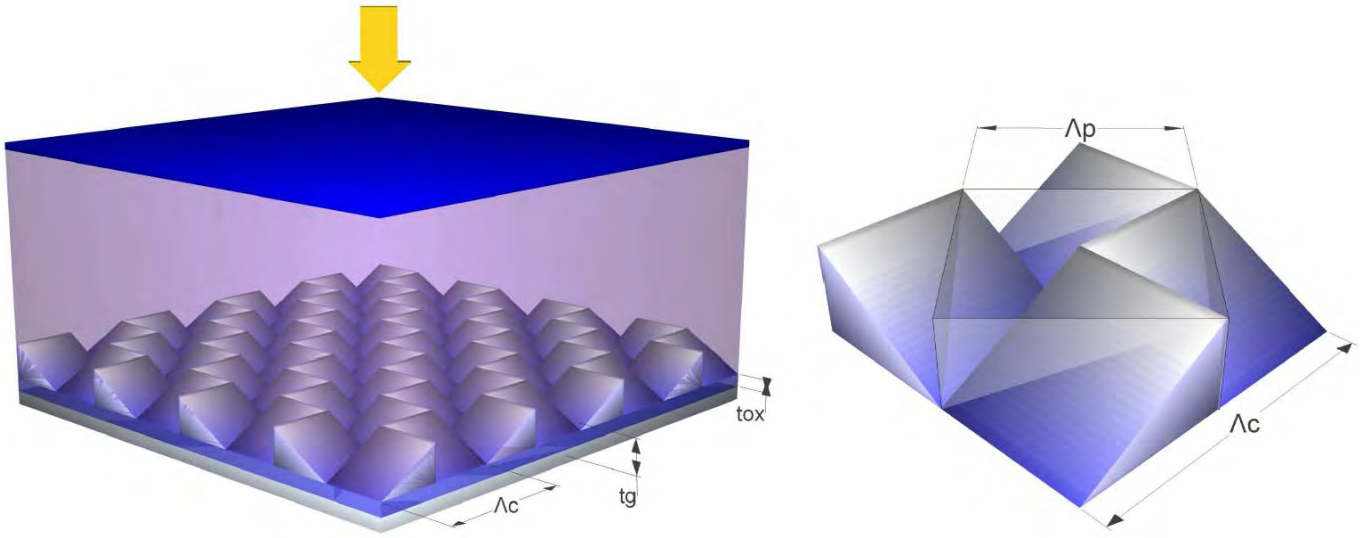

FIG. 1 Optical model for simulations (left) consisting of a planar anti-reflection coating (ARC), Si active material, light trapping layer, back-side oxide and metal mirror. The figure to the right shows the unit cell in false-colour representation. Also shown is the contour of the primitive unit cell of our structure.

oblique plane of each quadrant slopes in different directions [10]. The unit cell in false colour representation to the right also shows the contour of the primitive unit cell, which has half the area of the unit cell used in the actual calculations. The relation between the width of the primitive unit cell Λ_p and the computational unit cell Λ_c, is given by $\Lambda_p = \Lambda_c/\sqrt{2}$.

Light trapping is investigated numerically by means of rigorously coupled wave analysis with the commercial software GD-Calc [11]. In GD-calc the geometrical shapes are made out of rectangular prisms. The inclined planes are thus represented numerically by the stair-case approximation using 10 steps.

A unit cell which is larger than the primitive unit cell will have a larger density of reciprocal lattice vectors than the primitive unit cell. However, only the reciprocal lattice vectors of the larger unit cell with a corresponding reciprocal lattice vector of the primitive unit cell will contribute to diffraction. Because the computational unit cell is twice the size of the primitive unit cell, we expect the diffraction efficiency of half the diffraction orders to be equal to zero. This was also what we observed in our simulations. For computations with unit cells composed of more than one primitive unit cell, our simulation software allows us to include only the non-vanishing diffraction orders in the calculations to reduce the time taken by the computations. The reduction is significant: a reduction of the unit cell area by a factor of two decreases the computation time by a factor of eight.

We have varied period Λ, grating thickness t_g and oxide thickness t_{ox} shown in Figure 1 in search of the optimal parameter combination. We calculated absorption with experimentally determined optical constants for Si [12] and for Ag and Al [13]. As a metric for comparing the different parameter combination we used the maximum achievable short circuit current density J_{sc}. A limit for the J_{sc} is found by

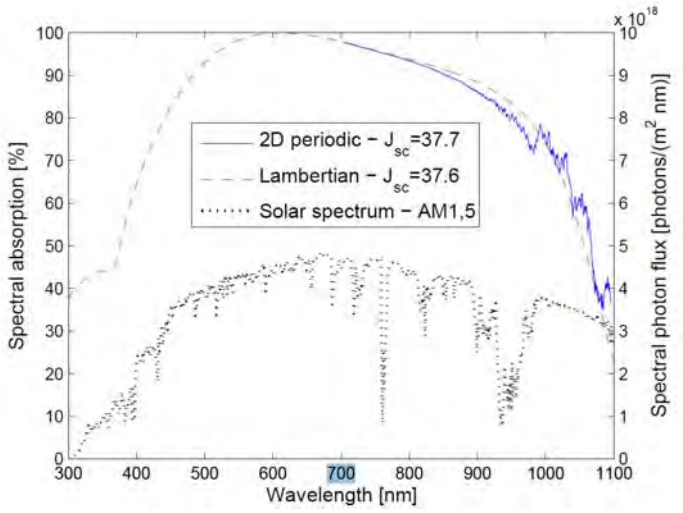

FIG. 2 Spectral absorption plot of our light trapping structure (solid, blue curve) compared to ideal Lambertian light trapping constrained by a single layer ARC (dashed, red curve). Also shown is the spectral photon irradiance (dotted, black curve).

weighting the Si absorption with the AM 1.5 global solar spectrum [14] and assuming that one electron-hole pair is generated for each photon absorbed in the Si. We integrate over the spectral distribution from 300 to 1100 nm.

3 RESULTS AND DISCUSSION

A maximum J_{sc} of 37.7 mA/cm^2 was found for the 20 μm thick Si slab with Ag reflector and the parameters Λ_c = 1.4 μm (i.e. $\Lambda_p = \Lambda_c/\sqrt{2}$), t_g = 0.55 μm and t_{ox} = 0.1 μm. Figure 2 shows the spectral absorption from such a structure. Al is more commonly used as reflector material than Ag in the PV industry due to lower price and more attractive electrical properties. If we substitute the Ag reflector with Al we find a

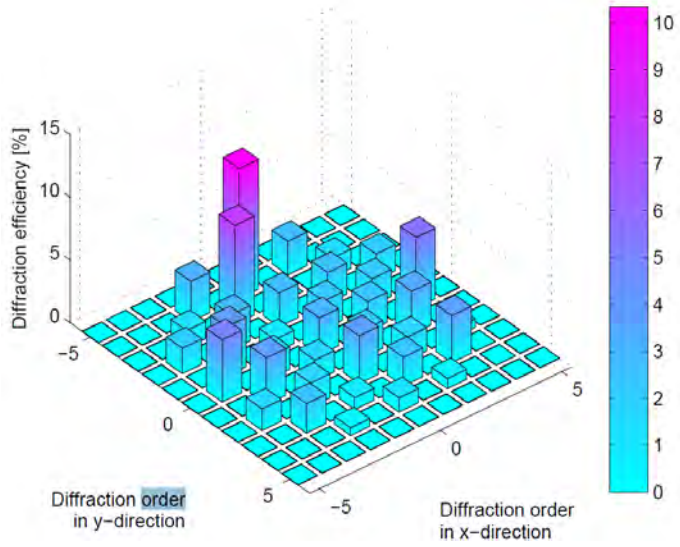

FIG. 3 Power distribution in the different diffraction orders. Every other diffraction order are zero due to the choice of unit cell.

J_{sc} of 37.25 mA/cm^2. The decreased performance when compared to Ag is due to a parasitic absorption of about 1 mA/cm^2 in Al compared to only 0.4 mA/cm^2 in an Ag reflector. As a comparison it can be mentioned that the corresponding J_{sc} in a planar slab without the grating structure would be 31.4 mA/cm^2 and 30.6 mA/cm^2 with an Ag and Al reflector respectively.

The low absorption observed in Figure 2 for wavelengths below 600 nm is due to front-side reflection from the ARC, while the absorption above ~800 nm is limited by the combined effect of front-side reflection and incomplete light trapping. Our simulated spectral absorption curves exhibit strong and rapid oscillations resulting from interference between the front and back-side reflections in the Si slab. To make our main results evident from Figure 2, we have removed these oscillations from the curve with the help of a digital filter (a moving average).

Deckman et al. [15] derived an expression for absorption in a dielectric assuming a perfect Lambertian diffuser and no front-side reflection. To compare the light confinement in our model with Lambertian light confinement, we have made a simple adjustment to the Lambertian diffuser model. We have modified the absorption calculated with the model of [15] by adding a nonzero front-side reflection corresponding to the reflection of a 78 nm Si_3N_4 ARC, which is the same as we used in our structure. The resulting spectral absorption is shown in Figure 2 (red dashed line). It shows that the light trapping from our structure with Ag-reflector (37.7 mA/cm^2) exceeds our simplified Lambertian light trapping model (37.6 mA/cm^2). For wavelengths below ~990 nm, the Lambertian model exhibits more effective light trapping than ours, while our structure performs better for large wavelengths. $\lambda = 990$ nm is the wavelength where $\lambda = \Lambda_p$. For wavelengths with $\lambda > \Lambda_p$ only the zeroth diffraction order (specular reflection) can propagate to the ambient while the higher diffraction orders are totally internally reflected. This corresponds well with the observed increase in light trapping in Figure 2 at $\lambda = \Lambda_p$ ~990 nm.

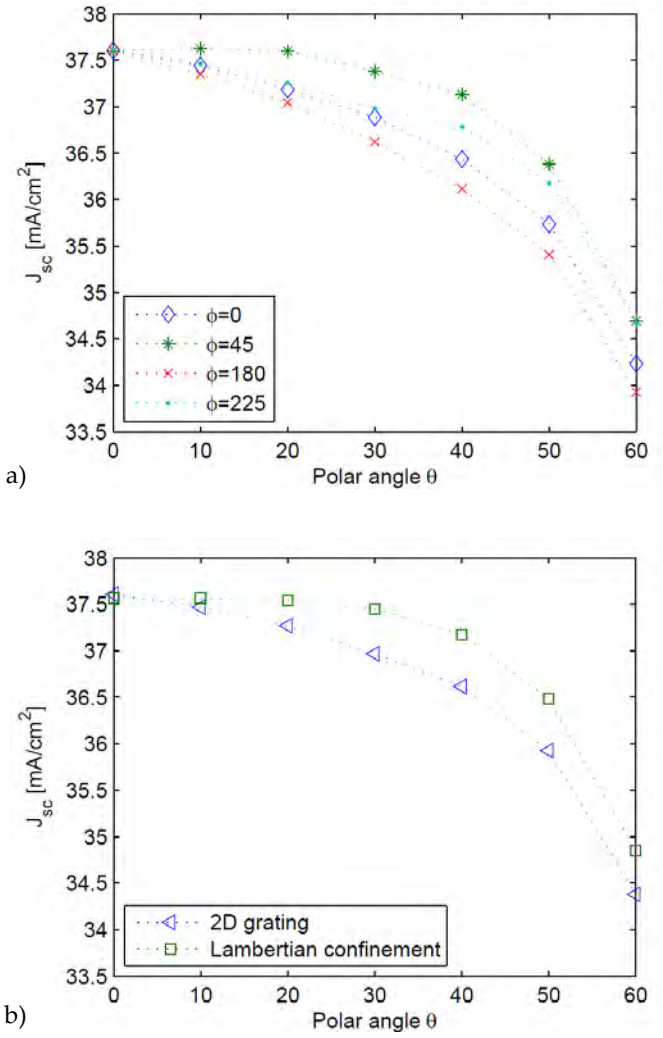

FIG. 4 Short circuit current density Jsc dependence on polar angle for four different azimuth angles a) representing the four main symmetry axes of the square lattice of the bi-periodic grating. Each point in the plot represents an average over the s- and the p-polarization. In b) and side each triangle in the graph represents an average over all four azimuth angles in a). The squares show Lambertian light trapping limited by the front-side reflectance expected from a Si_3N_4 ARC at the given incidence angle.

In Figure 3 we show the power distribution in the various diffraction orders for normally incident light at $\lambda = 1$ μm calculated with light incident from Si. Two important properties that we have seen earlier to give good light trapping [16] are both fulfilled here: firstly, the zeroth order reflection is low (around 3%) and secondly, light is distributed between several different diffraction orders. What is remarkable with this distribution compared to most other periodic structures is the lack of symmetry between the positive and negative diffraction orders. The reduced symmetry of this structure compared to other back-side grating structures with equivalent overall coupling to higher orders is believed to explain the success of this light trapping structure.

For higher angles of incidence the condition for total internal reflection may no longer be satisfied even if $\lambda > \Lambda_p$, and a reduction in J_{sc} is expected. In addition, reflection from the ARC will increase for higher angles of incidence. In Figure 4a)

we have plotted J_{sc} as a function of incidence angle up to a polar angle θ of 60 degrees for four different azimuth angles (0°, 45°, 180°, 225°). The different azimuth angles correspond to the four main symmetry axes of the square lattice of the bi-periodic grating. Azimuth angles of 0° an 180° represent alignment in the direction of periodicity of the computational unit cell, while 45° and 225° represent alignment in the direction of periodicity of the primitive unit cell, i.e. diagonally to the computational unit cell 1. Each curve is an average of s and p-polarization. The actual solar irradiance on the solar cell is reduced by $\cos(\theta)$ which for $\theta = 60$ degrees is equal to half of the irradiance at normal incidence. This geometric reduction factor is not included in Figure 4.

The advantage of Lambertian surfaces is their isotropic response. In Figure 4b) we try to differentiate the reduction in J_{sc} due to higher front-side reflection from that of reduced grating performance at higher angles of incidence. The green squares show the response of the Lambertian model, limited by the front-side reflectance at the given angle of incidence. The blue triangles represents the light trapping with our structure averaged over the four curves in Figure 4a). We see that light trapping is reduced below the Lambertian limit at non-normal incidence. Most of the degradation at higher angles of incidence is due to higher front-side reflectance of s-polarized light. In addition, there are considerable variations in light trapping between the different azimuth angles. While the best curve of Figure 4a) is almost identical to the Lambertian curve, the least good are up to 1 mA/cm^2 lower. We can see that light trapping is better for $\phi = 45$ and $\phi = 225$ than for $\phi = 0$ and $\phi = 180$. This can be explained by the fact that $\phi = 0$ and $\phi = 180$ couples to more escape channels than what is the case for $\phi = 45$ and $\phi = 225$. Light trapping is expected to be lower when fewer escape channels exists [4].

4 CONCLUSION

We introduce a novel bi-periodic structure with light trapping properties matching that of Lambertian light trapping at normal incidence. A study of the coupling efficiency in the various diffraction orders reveals a non-symmetric pattern. We believe the lack of symmetry in the structure is the reason for the good light trapping achieved. We find that light trapping is reduced below that of a Lambertian structure at higher angles of incidence. Most of this reduction is caused by increased front-side reflectance for s-polarized light. The reduction in light trapping caused by less optimal grating response at higher angles of incidence is below 0.5 mA/cm^2 for all angles of incidence up to at least 60 degrees. A structure with light trapping property as the one we present here would render possible the production of highly efficient solar cells with thicknesses of only 20 microns.

ACKNOWLEDGEMENTS

The authors would like to acknowledge the Norwegian Research Council and the Nordic Center of Excellence in Photovoltaic for funding this work.

References

[1] F. Henley, A. Lamm, S. Kang, Z. Liu, and L. Tian, ''Direct film transfer (DFT) technology for kerf-free silicon wafering'' in *Proceedings of the 23rd European Photovoltaic Solar Energy Conference*, 1090-1093 (Valencia, 2008).

[2] E. Yablonovitch and G. D. Cody, ''Intensity enhancement in textured optical sheets for solar cells'' IEEE Trans. Electron. Dev. **29**, 300–305 (1982).

[3] J. Nelson, *The Physics of Solar Cells* (First Edition, World Scientific Publishing, London 2003).

[4] Z. Yu, A. Raman, and S. Fan, ''Fundamental limit of light trapping in grating structures'' Opt. Express **18**, 366–380 (2010).

[5] S. E. Han and G. Chen, ''Toward the Lambertian limit of light trapping in thin nanostructured Silicon solar cells'' Nano Lett. **10**, 4692–4696 (2010).

[6] A. Chutinan, N. P. Kherani, and S. Zukotynski, ''High-efficiency photonic crystal solar cell architecture'' Opt. Express **17**, 8871–8878 (2009).

[7] V. E. Ferry, M. A. Verschuuren, H. B. T. Li, E. Verhagen, R. J. Walters, R. E. I. Schropp, H. A. Atwater, and A. Polman, ''Light trapping in ultrathin plasmonic solar cells'' Opt. Express **18**, 237–245 (2010).

[8] H. Sai, H. Fujiwara, M. Kondo, ''Back surface reflectors with periodic textures fabricated by self-ordering process for light trapping in thin-film microcrystalline silicon solar cells'' Sol. Energy Mater. Sol. Cells **93**, 1087–1090 (2009).

[9] J. Gjessing, A. S. Sudbø, and E. S. Marstein, *A novel broad-band back-side reflector for thin silicon solar cells* (EOS Annual Meeting, Paris, 26-28 October 2010).

[10] J. Gjessing, A. S. Sudbø, and E. S. Marstein, *2D blazed grating for light trapping in thin silicon solar cells* (Optics for SOLAR, Tucson, 7-9 June 2010).

[11] http://software.kjinnovation.com/GD-Calc.html

[12] C. M. Herzinger, B. Johs, W. A. McGahan, J. A. Woollam, and W. Paulson, ''Ellipsometric determination of optical constants for silicon and thermally grown silicon dioxide via a multi-sample, multi-wavelength, multi-angle investigation'' J. Appl. Phys. **83**, 3323–3336 (1998).

[13] E. D. Palik, *Handbook of optical constant of solids* (Academic Press, Orlando,1985).

[14] http://rredc.nrel.gov/solar/spectra/am1.5/

[15] H. W. Deckman, C. B. Roxlo, and E. Yablonovitch, ''Maximum statistical increase of optical absorption in textured semiconductor films'' Opt. Lett. **8**, 491–493 (1983).

[16] J. Gjessing, E. S. Marstein, and A. S. Sudbø, ''2D back-side diffraction grating for improved light trapping in thin silicon solar cells'' Opt. Express **18**, 5481–5495 (2010).

Available online at www.sciencedirect.com
ScienceDirect
Energy Procedia 00 (2011) 1–5
Energy Procedia
www.elsevier.com/locate/procedia

European Materials Research Society Conference
Symp. Advanced Inorganic Materials and Concepts for Photovoltaics

Colloidal Crystals as Templates for Light Harvesting Structures in Solar Cells

E. Haugan[a,*], H. Granlund[b], J. Gjessing[a], E.S. Marstein[a]

[a]*Department of Solar Energy, Institute for Energy Technology, Instituttveien 18, 2007 Kjeller, Norway*
[b]*Department of Physics, Norwegian University of Science and Technology, Høgskoleringen 5, 7491 Trondheim, Norway*

Abstract

Monolayer colloidal crystals are formed using silica- and polystyrene beads and used as etch masks for the formation of regular, μm period hexagonal arrays of indentations in a silicon wafer. Such patterns can be used as diffraction gratings or as seeds for further processing, for example by pit-catalysed electrochemical etching. In another experiment, multilayer colloidal crystals are infiltrated with titania before subsequent removal of the beads, forming inverse opals displaying tuneable reflectivities which are interesting for use as selective reflectors.

Keywords: light trapping, solar cells, nanosphere lithography, colloidal crystals, inverted opals, diffraction gratings

1. Introduction

The crystalline silicon solar cell industry is continuously moving towards thinner and thinner wafers as the production of solar cell grade silicon is a costly and energy intensive process. Thinner wafers are also beneficial because the collection efficiency of photogenerated free charges increases due to a shorter path way to the contacts. However, making a solar cell thinner allows more low-energy photons to pass through the entire structure without being absorbed, thus reducing efficiency. For this reason light harvesting (trapping) of low-energy photons is becoming an issue of increasing significance also for crystalline silicon solar cells. If the path length of photons inside the wafer can be increased by such light trapping structures, then the wafer can be made proportionally thinner without sacrificing efficiency. The most common light harvesting method in industry today is surface texturing by chemical etching, which scatters light into the solar cell due to refraction at the surface. This typically yields an average path length enhancement factor no greater than 10, which is only one fifth of the theoretical Lambertian limit for random scatterers in crystalline silicon [1].

*Corresponding author. Tel.: +47-95734413; fax: +47-63816356.
E-mail address: einar.haugan@ife.no

Periodic gratings with lattice periods close to photon wavelength may scatter light into non-zero diffraction orders, effectively increasing the path length of light inside the wafer. It has even been shown that the Lambertian limit can be exceeded by such geometries [2]. We have synthesised various periodic light harvesting structures for solar cell applications using colloidal crystal templates. 3D crystals are infiltrated with a dielectric material before the template is removed, leaving inverted opals displaying photonic band gaps giving sharp reflectivity peaks which make them interesting as selective reflectors. 2D crystals are used in nanosphere lithography for creating periodic patterns of pits, which may be used as diffraction gratings directly, or as initiation points or "seeds" for further processing into honeycomb-like structures by chemical or electrochemical etching.

2. Experimental

2.1. Substrate pre-treatment

Monocrystalline silicon wafers were used as substrates. Prior to template growth, the wafers were cleaned thoroughly using DI water and placed in a bath of DI water/NH_3(27%)/H_2O_2(30%), 515:85:100 volume ratio, at 70°C for 15 minutes. This was done to make the surface hydrophilic.

2.2. Colloidal crystal templates

In our experiments, 2D and 3D templates were grown from suspensions of microspheres purchased from Bangs Laboratories, Inc. Polystyrene (PS) beads gave the highest crystal quality and were therefore used when possible, while silica beads were used when high temperature processing was required. Bead diameters were selected for the optical properties of the final structures, determined by simulations [3, 4].

3D crystal synthesis. A 0.75 wt% solution of 490 nm diameter colloidal PS beads was prepared in a 25 ml glass beaker. The solution was thinned out to the desired concentration using DI water, before the glass beaker was placed in an ultrasonic bath for 15 minutes to break up any aggregates of colloidal spheres that may have formed.

Sphere self assembly was achieved using evaporation induced self assembly (EISA) [5]. Two cleaned substrates were inserted vertically into the beaker and placed in a heating cupboard for 24 hours at 63°C for the solvent to evaporate and the spheres to self-assemble on the substrate surface. According to Nagayama et al. [6] the growth rate v and hence the thickness of a multilayer colloidal crystal formed in this way depends on the volume fraction of solids in the solution, φ , as $v \propto \frac{\varphi}{1-\varphi}$. As the concentration of beads in the solution increases during deposition, it is therefore difficult to obtain homogeneous films by this method. Our samples typically showed a thickness variation from 10 layers (top) to 40 layers (bottom) of the substrate. For the optical properties, the thickness is not critical as long as it exceeds 5-8 layers [7]. Finally, the samples were sintered at the glass transition temperature of polystyrene (95°C) for 20 minutes.

2D crystal synthesis. Suspensions of 800 nm diameter silica beads were ultracentrifuged to increase the volume fraction of solids in water to approximately 30%. Solutions were sonicated for 5 hours at 24-27°C to break up aggregates, as suggested by Kumar [8] prior to spin-coating using a Bidtec SP100 spin coater. This was done by applying approximately 100 μl of solution onto a $1.5x1.5$ cm^2 substrate, rotating the substrate to achieve full wetting, and then spin coating at 300 RPM for 1 second before increasing to 5500 RPM for 30 seconds. The same method was used for 1 μm PS beads, except only 5 minutes ultrasonication was needed.

2.3. 3D photonic crystals. Infiltration and inversion

With the 3D colloidal crystals in place, the next step is to fill the voids in the opal with a dielectric to enhance the refractive index contrast and thus maximize the band gaps. Infiltration with titania (TiO_2) was done using a Beneq TFS-500 atomic layer deposition machine. The precursors used were $TiCl_4$ (Aldrich 98%) and DI water. The chamber was purged using nitrogen of purity > 99.9999% between precursor pulses. The pulse/purge routine was: 0.25/0.75/0.25/0.75 seconds $TiCl_4$/purge/H_2O/purge. The deposition temperature was set to 85°C.

After infiltration, the PS colloidal sphere template was removed by calcination, leaving an inverse opal. This was done by heating to 525°C for 2 hours in a furnace with a 2 hour ramp-up. Besides removing the polystyrene, heat treating at these temperatures is reported to initiate the phase transition from amorphous titania to anatase [3].

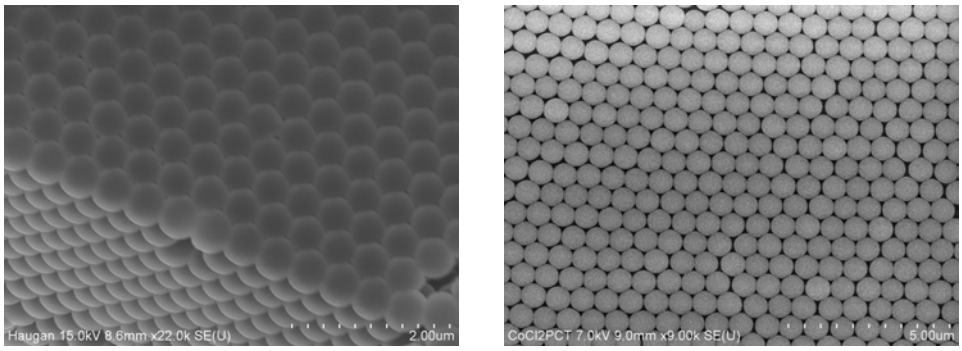

(a) Multilayer crystal (b) Single layer crystal

Figure 1: Scanning electron microscopy (SEM) images of the mono- and multilayer colloidal crystals synthesised

2.4. 2D photonic crystals by selective etching

In the first method, 50 nm of silicon nitride was deposited onto 2D colloidal crystals of silica beads to create an etch mask. The nitride was deposited using a Plasmalab System 133 PECVD at 400°C and 150 W RF power. After nitride deposition, the beads could be removed by sonication in ethanol for 2 minutes, leaving a silicon nitride etch mask. The substrates were then dipped in a 47% potassium hydroxide (KOH) solution for 30 seconds to etch pyramidic pits through the holes in the etch mask. At these conditions the etch rate along the {110} directions is approximately 700 nm/min [9, 10].

In the second method, monolayers of PS beads were covered by a 70 nm thick film of silver by thermal evaporation. The beads were removed by sonication, leaving behind triangular islands of silver. The samples were then submerged in a 4.6 M HF / 0.44 M H_2O_2 solution for 60 seconds. Silver is a catalyst for the etching of silicon by this solution.

3. Results

3.1. Colloidal crystal templates

3D crystal synthesis. The 3D crystals made were polycrystalline, with predominantly an hexagonal close packed ordering. This could be confirmed by laser diffraction experiments, looking at the reflection from the sample of a red laser beam of wavelength $\lambda = 650$ nm on a sand blasted plexiglass screen. The pattern of the reflected light showed clear hexagonal features, representing the Fourier transform of the structure. This would indicate that the real-space structure also has hexagonal symmetry [11]. Importantly, the laser spot size was so large that it would span across something in the order of 100 crystal domains, so the clear diffraction pattern indicates that adjacent domains maintained the same crystallographic orientation and packing conformation. Further corroboration of this comes from the fact that rotating the sample also caused the diffraction pattern to rotate accordingly. Thus, hexagonally close packed multilayer colloidal crystals could routinely be manufactured with thicknesses exceeding 10 layers.

2D crystal synthesis. The spin coating procedure produced a polycrystalline monolayer of spheres of predominantly hexagonal close-packed conformation, as seen in Figure 1 and confirmed by the presence of six-armed reflection patterns under white light. The monolayer quality was investigated in optical microscopy and scanning electron microscopy (SEM). Polycrystalline monolayers of PS beads covering typically 85% of the sample area were routinely manufactured, with the remaining area being mostly double layer. However for silica beads, agglomeration in solution prior to spin coating remained a problem even after several hours of ultrasonication at carefully controlled temperatures. Silica bead monolayers thus contained regions of poor quality in between crystal domains.

3.2. 3D photonic crystals. Infiltration and inversion

3D colloidal crystal templates were infiltrated with titania. Figure 2a shows the final structure after removal of the template. The refractive index of the relevant crystalline phases of titania have a refractive index in the range 2.3–3.0 in the wavelength range of interest. This contrast is too low to give rise to full photonic band gaps even after

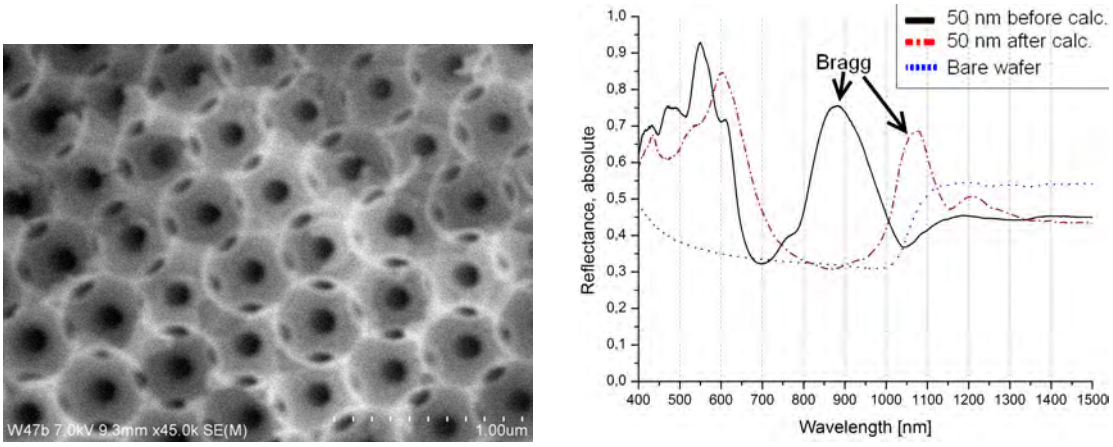

(a) SEM image of inverse titania opal

(b) Optical response of titania infiltrated opal before and after template removal by calcination. Interstices saturated with titania

Figure 2: Inverse titania opal. Template sphere diameter 490 nm

inversion of the opals. However, band structure simulations by King [12] predict several incomplete band gaps to arise following infiltration and inversion, detectable as peaks in the reflectivity spectrum.

Figure 2b shows the reflectivity of a titania infiltrated template. In addition to the Bragg peak, reflectivity peaks are also observed at high energies. After template removal (inversion) by calcination the refractive index contrast is increased, causing a blue shift of the reflectivity peaks. Also, some of the high-energy peaks get more pronounced. Templates with smaller diameter spheres gave similar reflectivity spectra, but with peaks at shorter wavelengths, demonstrating the size dependence of the band structure of these geometries.

We have achieved very good control and understanding of these structures, and we are able to tailor the reflectivity spectrum. However we also conclude that the band gaps, and thus the reflectivity peaks, are too narrow to be used as broad back reflectors in solar cells. We foresee that these structures are most relevant as spectral filters or selective reflectors in advanced solar cell applications.

3.3. 2D photonic crystals by selective etching

Method # 1. Silicon nitride etch masks, KOH etching. After nanosphere liftoff by sonication a thin layer of silicon nitride remained on the wafer, even in the "shadow regions" beneath the spheres. Atomic force microscopy (AFM) scans of these structures confirm the gradual thickness decrease of the nitride in the shadow region, forming a concave shape. Typical thickness variations from top to bottom of these concave shapes was 5 nm. At the bottom of each concave pit the bare silicon wafer was exposed in a 100 nm diameter patch, where the bead was touching the substrate.

Samples were then submerged in KOH, which etches crystalline silicon preferentially along the {110} directions. The etch does not attack silicon nitride, giving an essentially infinite etch selectivity [13]. Figure 3a shows a SEM image of a structure after KOH exposure and subsequent nitride stripping. This image reveals how the etching has indeed been confined to only the small exposed areas. Due to the high selectivity of the KOH etch on different crystallographic planes, etching is self-limiting.

Method # 2. Silver catalysed etching of silicon. AFM scans of the silver islands revealed that silver deposition was highly directional, as expected, with very little coverage in the shadow regions underneath the spheres. This is in sharp contrast to the nitride deposition in the previous section.

With the metal islands in place, samples were submerged in the HF / H_2O_2 etchant solution. As can be seen from Figures 3b and 3c, this method proved successful. From the top-down image, Figure 3b, we see that dark spots are formed where the silver islands used to be. The dark spots represent depressions in the wafer. The cross-sectional SEM image in Figure 3c demonstrates that the sidewall profile is indeed very straight, with no appreciable widening or narrowing of the groove. This is in line with the results by Huang et al [14]. Energy-dispersive X-ray spectroscopy (EDS) scans of the pits (Figure 3c, inset) show a high silver content at the bottom of the pits, as expected.

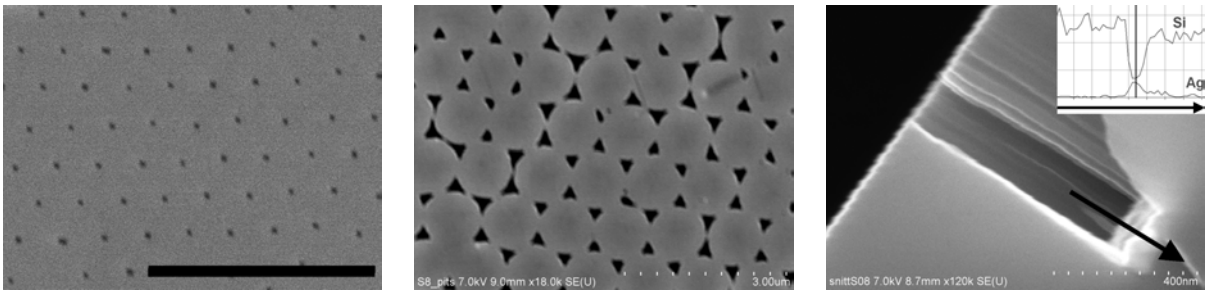

(a) Method # 1, after KOH etching and nitride stripping. Dark spots are pyramids etched out by the KOH. Scale bar 4 μm

(b) Method # 2, metal catalysed pits (dark) seen from above

(c) Method # 2, metal catalysed pit seen from the side. The inset shows an EDS line scan (elemental analysis) along the arrow. At the bottom of the pit the silver concentration is high. 60 second etch

Figure 3: SEM images of etch pits, formed by the two methods

4. Conclusion

In conclusion, we have successfully manufactured single- and multilayer colloidal crystals on silicon wafers and used them as templates for the production of various geometries intended for light harvesting in solar cells. Specifically, we have made titania inverse opals displaying multiple reflectivity peaks whose wavelength position can be tuned by altering the degree of infiltration and template bead size. These structures are intended for use as selective reflectors in advanced multilayer solar cells. Also, we have demonstrated two different techniques for the formation of hexagonal arrays of dents or dimples in a wafer. These methods can either be used to form 2D light harvesting structures directly, or to form initiation points ("seeds") for further processing into honeycomb structures by chemical- or electrochemical etching. Specifically, silicon nitride etch masks were made by nanosphere lithography, displaying 100 nm diameter holes with a sub-micron pitch. These masks were then used as etch masks for KOH etching, forming pyramidal dents in the exposed wafer. Silver catalysed etching was also used to form hexagonal arrays of pits.

References

[1] J. Nelson, The Physics of Solar Cells, Imperial College Press, London, 2003.
[2] Z. Yu, A. Raman, S. Fan, Fundamental limit of light trapping in grating structures, Optics Express 18 (103) (2010) A366–A380.
[3] J. King, D. Heineman, E. Graugnard, C. Summers, Atomic layer deposition in porous structures: 3D photonic crystals, Applied Surface Science 244 (1-4) (2005) 511–516.
[4] J. Gjessing, A. Sudbø, E. Marstein, Comparison of periodic light-trapping structures in thin solar cells, Journal xx (2011) xx, submitted for publication.
[5] P. Jiang, J. Bertone, K. Hwang, V. Colvin, Single-crystal colloidal multilayers of controlled thickness, Chem. Mater 11 (8) (1999) 2132–2140.
[6] A. Dimitrov, K. Nagayama, Continuous convective assembling of fine particles into two-dimensional arrays on solid surfaces, Langmuir 12 (5) (1996) 1303–1311.
[7] H. Granlund, Fabrication of a photonic crystal using self-assembly. a potentially new rear reflector in solar cells, Master's thesis, NTNU, Trondheim, Norway (2009).
[8] K. Kumar, Preparation and characterization of spin-coated colloidal templates and patterned electrodeposited cobalt, Ph.D. thesis, Memorial University of Newfoundland (2008).
[9] H. Seidel, L. Csepregi, A. Heuberger, H. Baumgartel, Anisotropic etching of crystalline silicon in alkaline solutions, J. Electrochem. Soc 137 (11) (1990) 3612–3626.
[10] K. Mangersnes, Back-contacted back-junction silicon solar cells, Ph.D. thesis, University of Oslo (2010).
[11] A. Sinitskii, V. Abramova, T. Laptinskaya, Y. Tretyakov, Domain mapping of inverse photonic crystals by laser diffraction, Physics Letters A 366 (4-5) (2007) 516–522.
[12] J. King, Fabrication of opal-based photonic crystals using atomic layer deposition, Ph.D. thesis, Georgia Institute of Technology (2004).
[13] K. Williams, K. Gupta, M. Wasilik, Etch rates for micromachining processing-Part II, Microelectromechanical Systems, Journal of 12 (6) (2003) 761–778.
[14] Z. Huang, H. Fang, J. Zhu, Fabrication of silicon nanowire arrays with controlled diameter, length, and density, Advanced Materials 19 (5) (2007) 744–748.

Comparison of periodic light-trapping structures in thin crystalline silicon solar cells

Jo Gjessing,[1,2,3,a)] Aasmund S. Sudbø,[3] and Erik S. Marstein[3]
[1]*Institute for Energy Technology, Department of Solar Energy, P.O. Box 40, Kjeller 2027, Norway*
[2]*University of Oslo, Department of Physics, P.O. Box 104 8 Blindern, Oslo 0316, Norway*
[3]*University Graduate Center at Kjeller, P. O. Box 70, Kjeller 2027, Norway*

(Received 6 April 2011; accepted 17 June 2011; published online 4 August 2011)

Material costs may be reduced and electrical properties improved by utilizing thinner solar cells. Light trapping makes it possible to reduce wafer thickness without compromising optical absorption in a silicon solar cell. In this work we present a comprehensive comparison of the light-trapping properties of various bi-periodic structures with a square lattice. The geometries that we have investigated are cylinders, cones, inverted pyramids, dimples (half-spheres), and three more advanced structures, which we have called the roof mosaic, rose, and zigzag structure. Through simulations performed with a 20 μm thick Si cell, we have optimized the geometry of each structure for light trapping, investigated the performance at oblique angles of incidence, and computed efficiencies for the different diffraction orders for the optimized structures. We find that the lattice periods that give optimal light trapping are comparable for all structures, but that the light-trapping ability varies considerably between the structures. A far-field analysis reveals that the superior light-trapping structures exhibit a lower symmetry in their diffraction patterns. The best result is obtained for the zigzag structure with a simulated photo-generated current J_{ph} of 37.3 mA/cm^2, a light-trapping efficiency comparable to that of Lambertian light-trapping. © *2011 American Institute of Physics*. [doi:10.1063/1.3611425]

I. INTRODUCTION

Light trapping increases current generation in solar cells and makes it possible to reduce material costs by utilizing thinner solar cells. In addition to the reduced material consumption, a thinner solar cell also relaxes the demand on material quality as the dependence of efficiency upon bulk recombination is reduced. Light trapping is, therefore, a key issue of reaching the ambitious cost reduction plans for the photovoltaic (PV) industry.

Nowadays, state-of-the-art silicon (Si) solar cells have a thickness of around 150-200 μm. Fabrication of significantly thinner sheets of high quality Si with a thickness below 20 μm has been demonstrated by various techniques.[1–3] Throughout this work, we use a Si thickness of 20 μm as a case of study when exploring the light-trapping ability of the various structures. This is thinner than today's wafer-based solar cells by a factor of 10 and at the same time thicker than ordinary thin-film solar cells by a factor of 10. With proper light trapping, a Si solar cell with such a thickness has the potential of reaching high conversion efficiencies. This is crucial, due to the high importance of efficiency in determining the cost of a PV system. Working with an optical solar cell model, we use the photo-generated current density instead of conversion efficiency as a measure of light-trapping quality, as this requires fewer assumptions about the specific cell configuration.

Conventional light trapping varies according to cell type and configuration. For monocrystalline Si, alkaline etching of a [100] oriented wafer is used to make a texture of square pyramids with the {111} planes revealed.[4] Alkaline etching may also be used for multicrystalline Si, but due to the random orientation of the crystal grains, isotropic acidic etching that results in a random dimple-like pattern is a more common approach.[5] Pyramidal structures have been demonstrated on crystalline Si solar cells with thickness in the 30 micron range[6] despite structure sizes with a depth of more than 10 μm. These structures have excellent anti-reflection properties, but better light confinement may be achieved with other structures. Moreover, pyramidal structures are not applicable to proton cleaved wafers, which is a method for making very thin kerf-free wafers.[3] These wafers have a [111] oriented surface, while the conventional pyramidal texture requires a [100] oriented surface.

In thin-film solar cells, texturing of transparent conductive oxides (TCOs) on glass substrates is the common approach for light trapping.[7] This creates a random submicron texture, which effectively scatters light, especially at shorter wavelengths.

II. BACKGROUND

Periodic structures with lattice periods in the range of the wavelength of light are compatible with thin solar cells, and they unlock a potential outside the conventional light-trapping based on random textures. Such structures have been thoroughly analyzed in the past,[8–10] but have attracted renewed attention lately.[11–14] Recently, it has been shown that periodic structures may increase light trapping beyond that of the Lambertian $4n^2$ limit,[15,16] but with a significant angular dependency. At the same time, it has also been shown that bi-periodic gratings, in general, are expected to

[a)]Author to whom correspondence should be addressed. Electronic mail: jo.gjessing@ife.no.

have a higher potential than uni-periodic gratings. Lately, we have seen simulation results that are comparable to the geometric light-trapping limit over a broad wavelength range for bi-periodic gratings.[16–19] Common for these structures is that the Lambertian light-trapping limit is exceeded at normal incidence, while the Lambertian limit, although theoretical, is independent of incidence angle.

Light trapping from periodic structures have also been verified in experimental work. It has been shown that there is good agreement between modeling and experimental results for a uni-periodic grating applied to a 5 μm thick Si cell.[20] Recently, light trapping obtained from a periodic plasmon structure has been shown to exceed that of the Asahi U-type glass,[21] which is the thin-film solar cell standard. A similar result is also presented in Ref. 22. They found that a self-assembled periodic dimple structure made by anodic oxidation of Al improved light trapping in the infrared part of the spectrum above that of the Asahi U-type glass.

In this work, we investigate, in simulations, the impact of the specific unit cell geometry on seven different bi-periodic diffractive structures with regard to light trapping. The structures comprise the binary cylinder structure;[14] common non-binary structures, such as inverted pyramids, cones, and dimples, or half spheres; and, finally, three more advanced structures, which we call the roof-mosaic structure, the rose structure,[23] and the zigzag structure.[24] Some of these structures have also been investigated before. Modeling of coexisting front- and back-side pyramids is presented in Ref. 25; modeling results of cylinders are presented in several works,[12,14,26,27] while modeling of cones is performed in Ref. 28.

It is of great interest to quantify and to compare the light-trapping potential inherent in periodic structures of different geometry. Unfortunately, the above-mentioned results are difficult to compare because they are applied to different cell configurations using various materials and methodologies. We present here a joint comparison of all the above mentioned structures, including three novel structures, applied to the same model. This allows for a reasonable comparison of the structures. Furthermore, the structures are compared both at normal and oblique angles of incidence, which is important for outdoor conditions of non-tracking solar cells. Finally, we present an analysis of the far-field diffraction pattern of the optimized structures at a wavelength of 1 μm. In contrast to standard thin-film solar cells, light trapping in a 20 μm thick Si cell involves primarily a narrow wavelength region around this wavelength. A crystalline Si slab with 20 μm thickness is used as a model in this work; however, the methodology and analysis may also hold for solar cells with other thicknesses and for other material types.

III. MODEL STRUCTURE

We have investigated numerically seven different bi-periodic structures with square lattices. The structures are cylinder, cone, dimple, inverted pyramid, roof-mosaic, rose, and zigzag structure. The unit cells of each structure are shown in Fig. 1. To simplify the representation of the zigzag and roof-mosaic structure, we have used a unit cell in the computations with twice the area of the primitive unit cell. Figure 1 shows both the computational and the primitive unit cell of these structures.

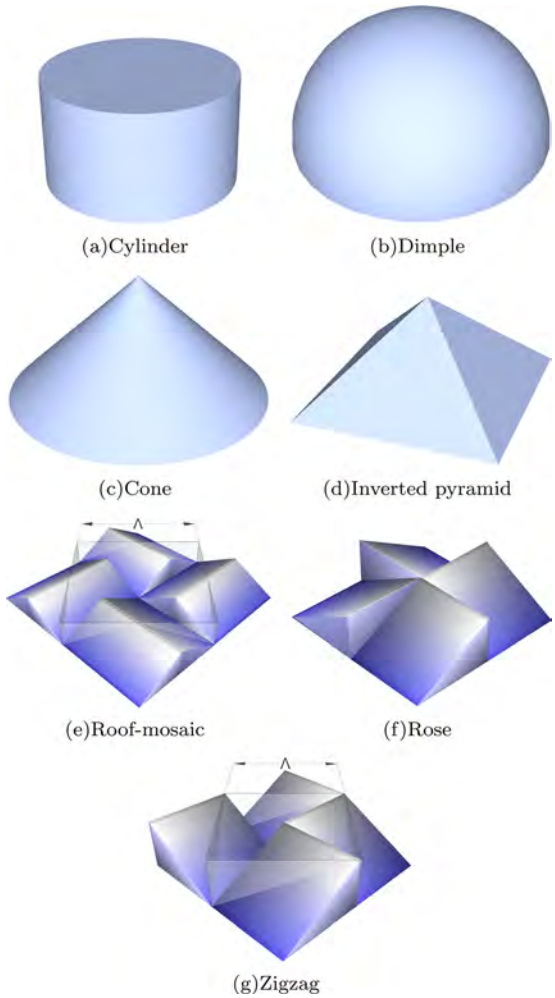

FIG. 1. (Color online) The geometry composing the unit cells of each of the investigated periodic light-trapping structures. For the roof-mosaic and the zigzag structure, Λ illustrates the lattice period of the primitive unit cell.

The full optical model of the solar cell used in the computations is depicted in Fig. 2. A 20 μm thick Si slab is covered with a planar front-side anti-reflection coating (ARC) consisting of 78 nm silicon nitride. A dielectric grating, a silicon oxide layer, and an aluminum (Al) reflector constitute

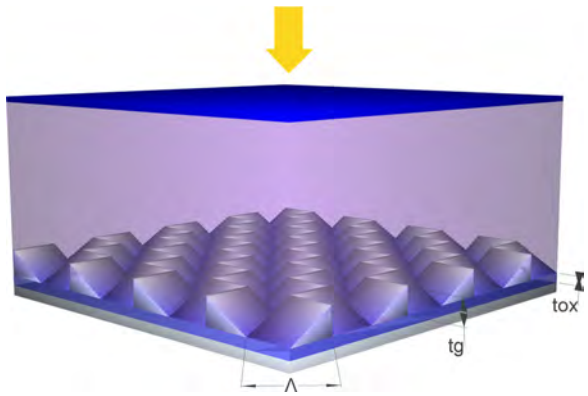

FIG. 2. (Color online) Schematic drawing of a typical optical solar cell model used in the simulations (not to scale). The Si slab has an anti-reflection coating on the front side; on the back side it has a dielectric bi-periodic grating filled with silicon oxide. The grating layer is separated from a back-side aluminum reflector by a layer of silicon oxide.

the rear side of the model. The grating is constructed from the geometries in Fig. 1, imprinted into the Si slab, and filled with silicon oxide. The purpose of the silicon oxide layer that separates the grating from the Al reflector is to reduce parasitic absorption losses in the Al. The oxide used in the separating layer and in the grating could, in principle, be replaced by another material with a low refractive index, such as air. However, silicon oxide has good passivation qualities, and there exists well known methods to make contacts through such a layer.[29] Both properties are important in a real solar cell configuration.

IV. METHODOLOGY

Modeling is performed using rigorously coupled wave analysis (RCWA).[30] With RCWA, the Maxwell equations are solved rigorously at each wavelength and the computation at each wavelength is performed independently. Experimental data for optical properties are, therefore, easily implemented and are used for Si[31] and for Al.[32] For convenience, both the ARC and the oxide layer are assumed to be non-absorbing with a refractive index of 1.95 and 1.5 representative for silicon nitride and silicon oxide, respectively.

The software package GD-Calc[33] is used as the modeling tool in this work. GD-Calc represents all types of geometries with rectangular blocks. This implies that circular structures, like the cylinder structure, are approximated by a finite number of blocks. The same holds for oblique structures, like the pyramids, which are also represented by a finite number of blocks. In the case of oblique structures, this is known as the staircase approximation.[34]

A. Grating design considerations

The most important property of the grating structure is its ability to scatter light efficiently into oblique angles, thereby extending the path length of the light inside the absorbing material. The angles of the diffracted orders can be found from the bi-periodic grating equation.[34] The polar angle of the diffracted orders θ_o can be found from Eq. (1).

$$sin^2(\theta_o) = \left(\frac{n_i}{n_o} sin(\theta_i) cos(\phi_i) + \frac{m_x \lambda}{n_o \Lambda_x}\right)^2 + \left(\frac{n_i}{n_o} sin(\theta_i) sin(\phi_i) + \frac{m_y \lambda}{n_o \Lambda_y}\right)^2. \quad (1)$$

The angles and lattice periods of Eq. (1) are defined in Fig. 3. θ_i and ϕ_i are the polar and azimuth angles of the incident beam respectively, Λ_x and Λ_y are the lattice periods in the x- and y-direction, λ is the wavelength of light in vacuum, while n_i and n_o are the refractive index of the medium of incidence and of the outgoing wave, respectively. For a reflection grating $n_o = n_i$. m_x and m_y are integers that denote the diffraction order in the x- and y-direction. The number of allowed diffraction orders is determined by the fact that the outgoing wave vector must lie on the same unit sphere, depicted in Fig. 3, as the incoming wave vector. Consequently, the expression on the right side of Eq. (1) needs to

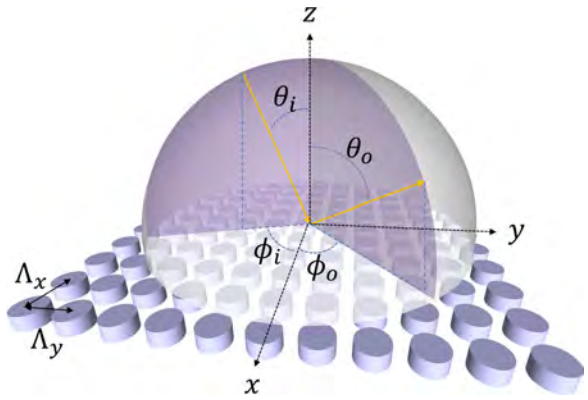

FIG. 3. (Color online) Definitions of the angles involved in diffraction from a bi-periodic grating.

be less than unity to provide a real solution (i.e., a propagating diffraction order).

For normal incidence with lattice period $\Lambda_x < \frac{\lambda}{n_o}$ and $\Lambda_y < \frac{\lambda}{n_o}$, there exists only one solution to the bi-periodic grating equation, namely the zero diffraction order $m_x = m_y = 0$. In this case, the grating will act as a specular reflector and will, therefore, not be suited for light trapping. Larger periods will allow for more diffraction orders; however, the angles of the diffracted orders will decrease with increasing period, thereby reducing the potential path-length enhancement of the lowest diffraction orders. When Λ exceeds the free-space wavelength λ, the lowest diffraction orders may also propagate in air. Therefore, these diffraction orders will not be totally internally reflected within a periodically patterned slab, regardless of the refractive index of the slab, and the light-trapping ability will be reduced.

The grating equation can only predict the angles of diffraction, while rigorous modeling must be performed to find the power distributed in each order. To optimize each structure for light trapping, we varied the lattice period Λ, grating thickness t_g, and oxide layer thickness t_{ox} (see Fig. 2). For the cylinder structure, we also varied the fill factor, i.e., the fraction of the cylinder base area to the total unit cell area, while for the rest of the geometries, the fill factor was set as large as possible without overlapping the neighboring unit cells. We chose not to confine the pyramid structure to the standard 54.7 degree angle, which is the side angle of the pyramids that are formed from alkaline etching of a [100] oriented Si wafer. Consequently, the pyramidal structure also has three independent variables. The dimple structure has, by definition, $t_g \equiv \Lambda/2$ when fill factor is maximum and, therefore, contains only two independent variables, i.e., Λ and t_{ox}.

Due to the huge number of different geometries and configurations that are investigated, a method is needed to quickly locate the grating dimensions that favor light trapping. The method that we used was to have light incident directly from an infinitely thick Si superstrate, allowing the analysis of the propagating diffraction orders. Optimal grating configurations have low specular reflection and low parasitic losses in the back-side Al reflector, and, consequently, efficient coupling into higher diffraction orders, denoted D_{HO}:

TABLE I. Maximum J_{ph} achieved with various light-trapping structures made from the structures in Fig. 1, modeled with the full structure shown in Fig. 2. The grating dimensions corresponding to the maxima are also shown.

Structure	Maximum J_{ph} [mA/cm^2]	Lattice period Λ[μm]	Grating thickness t_g [μm]	Oxide thickness t_{ox} [μm]	Fill factor
Cylinders	35.6	0.7	0.23	0.2	0.6
Roof mosaic	36.1	0.92	0.3	0.4	Max
Inverted pyramids	36.2	0.95	0.325	0.1	Max
Cones	36.3	0.98	0.38	0.1	Max
Dimples	36.4	0.975	$\Lambda/2$	0.14	Max
Rose	36.8	0.95	0.4	0.1	Max
Zigzag	37.3	0.988	0.55	0.1	Max
Reference cell	30.7	—	—	—	—

$$D_{HO} = 1 - D_{00} - A_{par}. \quad (2)$$

In this equation, D_{00} is the diffraction efficiency in the zero order, i.e., specular reflection, while A_{par} is parasitic loss in the form of absorption in the Al rear reflector. The result of Eq. (2) is mapped for the independent grating variables of each structure. As long as the diffraction modes are reasonably stable within the narrow wavelength region that is partially transmitted through the 20 μm thick Si slab, such computations may be performed with a low wavelength resolution.

We have used the resulting D_{HO} maps in the initial steps to locate the optimum grating dimensions in section V A. Previous experience has shown that the peaks in the D_{HO} maps correspond with peaks in light trapping with full-structure calculations, i.e., with the absorbing 20 μm thick Si-slab on top of the light-trapping structure and incidence from air. However, the D_{HO} maps do not include effects of secondary interactions with the grating, nor do they contain any information about the angles of the diffracted orders and the distribution of light between the orders. Consequently, the actual light-trapping efficiency may still vary greatly between the peaks, even though the size of their D_{HO} is identical. The various peaks from the D_{HO} maps are, therefore, further investigated with full-structure modeling. The absorption spectra resulting from such a full-structure modeling exhibit rapid Fabry-Perot interference fringes from interference in the 20 μm Si slab. To resolve these fringes, a high wavelength resolution is needed. This leads to significantly longer computational time for a full-structure calculation than for the computation of D_{HO}.

The absorbed photo-current density J_{ph} is used as a metric to compare the light-trapping ability of the different structures. J_{ph} is calculated by Eq. (3) and corresponds to the maximum potential short-circuit density assuming a carrier collection efficiency of 100%:

$$J_{ph} = q \int_0^{\infty} A(\lambda)\Phi(\lambda)d\lambda. \quad (3)$$

Here, q is the elementary charge, $\Phi(\lambda)$ the spectral density of the photon irradiance from the global AM 1.5 spectrum,[35] and $A(\lambda)$ is the spectral absorptance, a dimensionless wavelength-dependent factor between zero and one calculated by the full-structure modeling in GD-Calc. The integration in Eq. (3) is for wavelengths from zero to infinity, but, in practice, integration was performed from 300 nm to 1100 nm. Extension of the integral outside this range increased computational time with little effect on J_{ph}.

V. RESULTS

A. Light trapping at normal incidence

Each structure has been optimized for maximum J_{ph} using D_{HO} maps to locate favorable grating dimensions and full structure calculations to explore their corresponding light-trapping potential. The maximum J_{ph} values and the corresponding grating dimensions are summarized in Table I. A 20 μm thick reference cell with a front side ARC and a back-side planar Al reflector is also included for comparison. To better appreciate the difference in light-trapping between the structures, a plot of J_{ph} versus effective optical thickness is shown in Fig. 4. The figure illustrates the path length required through a Si slab, using the same ARC as in Fig. 2, to absorb an amount of photons corresponding to a given J_{ph}. In Fig. 4, we have also included the effective optical thickness corresponding to Lambertian light trapping, limited by the same ARC as the rest of the structures in Table I.

Not surprisingly, the light trapping from the periodic structures clearly exceeds the case of the reference cell with a planar reflector and an ARC. However, the light trapping

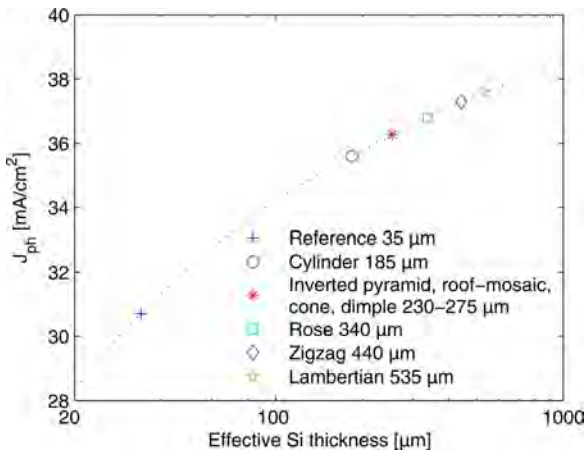

FIG. 4. (Color online) Optical thickness of Si required to provide a given photo-generated current density J_ph. The markers show the effective optical thickness corresponding to the J_ph values from Table I.

of the different periodic structures also varies significantly. We note that the best-performing structure in Table I is the zigzag structure with a J_{ph} of 37.3 mA/cm^2. This is only 0.3 mA/cm^2 below that of Lambertian light trapping. Replacing the Al reflector with an Ag reflector will further increase J_{ph} of the zigzag structure by 0.4 mA/cm^2, thereby exceeding the Lambertian light trapping at normal incidence.[24]

From Table I, we see that optimal light trapping is achieved with a lattice period of about 0.95 μm for all structures except the cylinder structure, where we found the highest J_{ph} for a period of 0.7 μm. However, as we show in Ref. 14, the cylinder structure has a broad maximum plateau extending from periods of 0.7 μm to about 1 μm, where there are only minor differences in J_{ph}.

B. Far-field analysis

To understand the differences in performance for the various light-trapping structures in Fig. 1, we explore their far-field properties. The far-field properties are shown in Fig. 5 in the form of diffraction efficiency D_{m_x,m_y} of the diffraction order m_x,m_y. The fractional power of all diffraction orders except for the zero order, i.e., $m_x = m_y = 0$, corresponds to the D_{HO} defined in Eq. (2). The allowed number of propagating diffraction orders and the corresponding diffraction angles can be found from Eq. (1).

To calculate the diffraction efficiencies in Fig. 5, we have used Si as an incidence medium. We found the diffraction efficiencies to be reasonably stable within the spectral region that is transmitted through a 20 μm thick Si slab, i.e., ~800–1100 nm. Consequently, the diffraction maps shown in Fig. 5 are representative for the entire spectral region. After verifying convergence with more diffraction orders, we included diffraction orders up to $|m_x| < 10$ and $|m_y| < 10$ in the computations. We still show only the diffraction orders up to $|m_x| < 3$ and $|m_y| < 3$, as all higher orders are evanescent, i.e., their diffraction orders hold zero power.

Figure 5 shows the diffraction efficiency for each structure in Fig. 1 when optimized for light trapping. The optimized structures each have low D_{00} and low parasitic absorption in the Al reflector, yielding D_{HO} in excess of 90% for all the structures. The distribution of power within the different diffraction orders, however, varies considerably.

The incident light in Fig. 5 is chosen to be circularly polarized, since this choice of polarization provides rotational symmetry. The diffraction efficiencies of all structures can be seen to have four-fold rotation symmetry. The exception is the diffraction pattern of the zigzag structure, which has no apparent symmetry. For the rose structure, we show the diffraction efficiencies for both left- and right-handed polarized light. Both diffraction patterns can be seen to exhibit a four-fold rotational symmetry, but the distribution of power within the diffracted orders are completely different for the two polarizations. For the rest of the structures, on the other hand, left- and right-hand polarizations yield equivalent diffraction patterns, but mirrored about the x- and y-axis (not shown). The exception is again the zigzag structure, where the diffraction pattern is mirrored only about one of the axes and not the other.

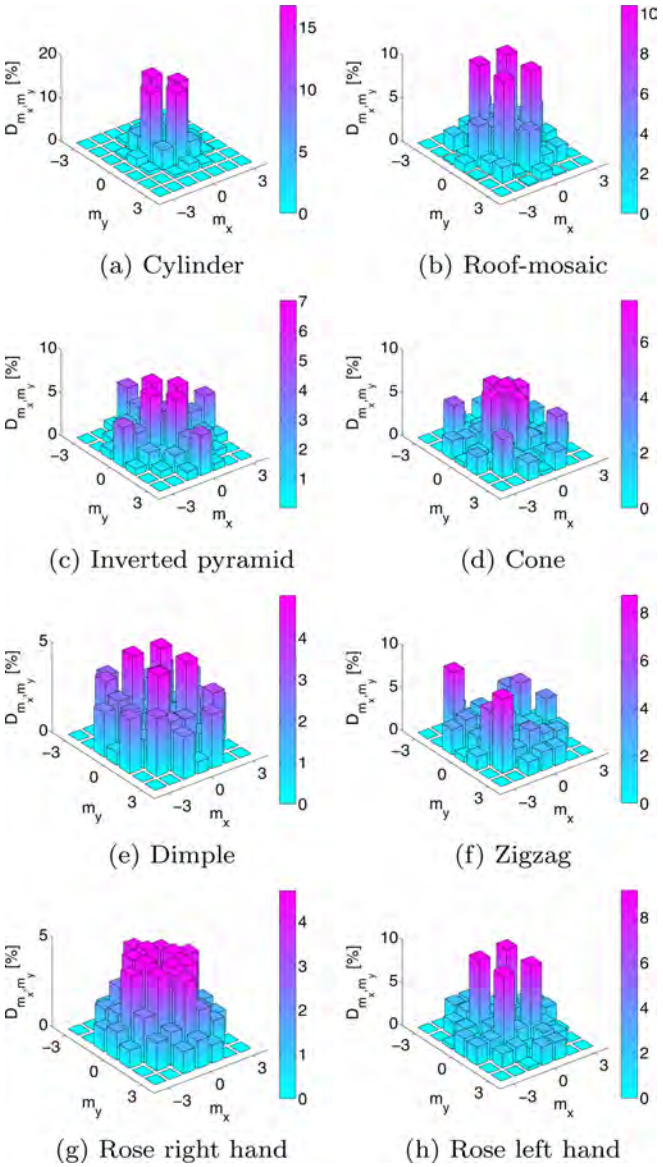

FIG. 5. (Color online) Diffraction efficiencies for circularly polarized light with $\lambda = 1$ μm at normal incidence. The diffraction efficiency of the rose structure is shown for both left- and right-handed polarization. Each structure is optimized for maximum J_{ph}, with the dimensions and corresponding J_{ph} shown in Table I. Note that the scale of the vertical axis varies between the figures.

C. Oblique incidence

The incidence angle of the solar illumination varies during the course of a day according to season and location. Moreover, diffuse radiation also makes a significant contribution to the global irradiance in several parts of the world. The properties of diffraction gratings are naturally dependent on incident angle. The behavior under oblique illumination conditions is, therefore, an important part of the performance investigation of such structures.

The light-trapping efficiency will, in general, depend on the azimuth angle ϕ in addition to the polar angle, here defined as the incidence angle from air θ_{air}. The energy that is actually captured by a solar module will, in reality, depend on the projected area of the solar module as $cos(\theta_{air})$. This

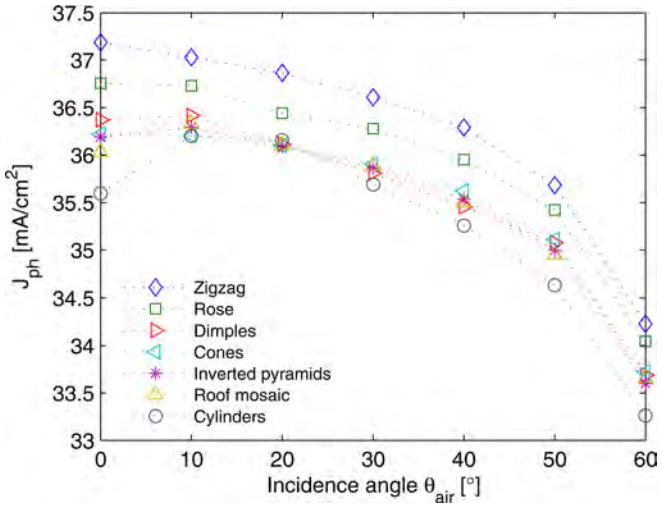

FIG. 6. (Color online) Performance of the different light-trapping structures from Fig. 1 under oblique incidence illumination. Each point represents an average of the photo-generated current density J_{ph} over two azimuth angles (four for the zigzag structure) and over s- and p-polarized light at each azimuth angle.

geometric factor is here omitted to better compare the actual light-trapping efficiency at the various angles of incidence.

All structures we investigated, except for the zigzag structure, have four-fold rotation symmetry. Dependence on θ_{air} is, therefore, studied at the two extreme azimuth angles: at $\phi = 0°$, along one of the directions of periodicity, and at $\phi = 45°$. Due to the lack of symmetry of the zigzag structure, it is characterized at four different azimuth angles: 0°, 45°, 180°, and 225°. Equivalent results were achieved for the zigzag structure at azimuth angles of 90°, 135°, 270° and 315°. In Fig. 6, the average J_{ph} of each structure is shown as a function of the angle of incidence in air above the solar cell.

The behavior of the structures in Fig. 6 may be divided into four classes by their performance. The zigzag structure is superior at all angles of incidence, while the rose structure is a clear number two. The third class consists of the dimple, cone, inverted-pyramid, and roof-mosaic structure, which are all quite similar in their performance. The fourth and last class, with the lowest performance at normal incidence, is the cylinder structure. The performance of this structure, however, increases significantly compared to the rest of the structures for non-normal angles of incidence. In general, the difference in light trapping between the structures is somewhat lower at higher angles of incidence than for normal incidence.

The reduction in J_{ph} at higher angles of incidence is primarily due to increased front-side reflection of s-polarized light. However, this does not explain the variation between the different light-trapping structures.

An important mechanism at oblique angles of incidence is the escape of diffraction orders that are no longer totally internally reflected within the Si slab. Consider the case of light with a wavelength of 1 μm incident from air on a Si slab with a back-side periodic structure having a lattice period of 0.95 μm. In this case, Eq. (1) may be used to find the allowed number of propagating diffraction orders in air by setting $n_i = n_o = 1$ and $\theta_i = \theta_{air}$. For incidence in the plane of periodicity ($\phi = 0°$), this will yield one escaping diffraction order in addition to the zero order for incidence angles $\theta_{air} > 5°$. For incidence in the $\phi = 45°$ plane, on the other hand, Eq. (1) yields up to three escaping diffraction orders in addition to the zero order. The angular response for incidence in the $\phi = 0°$ plane may, therefore, be expected to exceed the response at $\phi = 45°$. In fact, this trend is evident for all structures except for the cylinder structure. With a period of only 0.7 μm, Eq. (1) will show that incidence in the $\phi = 45°$ plane does not allow any escaping orders except the zero order as long as the wavelength is above 1 μm. Consequently, the cylinder structure has a better angular response for $\phi = 45°$ than for $\phi = 0°$ (not shown). Additionally, due to the smaller lattice period of the cylinder structure, an incidence angle $\theta_{air} > 20°$ is needed before any higher diffraction orders may escape.

The analysis above is a qualitative approximation, as we consider only a single wavelength of the extended spectrum that reach the back side and we neglect the fact that the diffraction efficiencies will also change with incidence angle. Nevertheless, the main difference that can be observed between the grating structures may, in large part, be explained by this simple analysis.

VI. DISCUSSION

A. Interpretation of results

In general, a low zero-order diffraction efficiency is a prerequisite for good light trapping, and, indeed, the zero-order diffraction efficiencies in Fig. 5 fulfill this requirement. Furthermore, high diffraction angles will increase path length more than low diffraction angles. For a grating with a given lattice period, this implies that coupling to higher diffraction orders is better for light trapping than coupling to lower orders (see Eq. (1)). Nevertheless, the photo-generated current density J_{ph} of the dimple structure is below that of the rose structure, even though the dimple structure seems to have larger part of its diffracted power in the highest diffraction orders. The reason for the success of the rose and the zigzag structure must, therefore, be caused by another effect.

Our first assumption for the success of the rose and the zigzag structure was that the number of sharp edges and corners in these structures increased scattering and, therefore, light trapping. However, the roof-mosaic structure also has several sharp corners, yet it has significantly lower J_{ph}. A further investigation of Fig. 5 reveals that the symmetry in the diffraction patterns of the two structures having the highest J_{ph} differs from the rest of the structures. The diffraction pattern of the zigzag structure has no symmetries, while the rest of the structures show a four-fold rotational symmetry. By reversing the direction of the circularly polarized light, we found that the diffraction patterns are reproduced, but mirrored about the x- and y-axis. The exceptions are for the zigzag and the rose structures. The diffraction pattern of the zigzag structure is only mirrored about one axis. The diffraction pattern from the rose structure is completely changed with polarization, although it still exhibits a four-fold rotational symmetry.

We believe that the reduced symmetry in the diffraction patterns of the rose and zigzag structure in Fig. 5 reduces the

chance of out-coupling on subsequent interactions with the diffraction grating. This argument is similar in nature to the one of Ref. 9. The results we see here also match well with what has been suggested recently by Refs. 16 and 18. They suggest that to break the symmetry of the unit cell will allow the coupling to more modes, thereby increasing light trapping.

B. Implementation in solar cells

To obtain success with a periodic light-trapping structure, it is important to avoid the excessive absorption that may arise in the metal reflector that is usually placed on the back side of a solar cell. We reduce the parasitic absorption with an oxide layer that separates the rear reflector from the grating. In this work, we use a planar metal reflector. Absorption is expected to be higher if the grating structure is transferred to the Al.[36,37] Other approaches with Bragg reflectors have also been proposed to avoid parasitic absorption.[12,13] We find that a separation of the grating and rear reflector is necessary, not only for Al, but also for a less absorbing Ag reflector.

A low back-surface recombination velocity is crucial to obtain high efficiency with thin solar cells, where diffusion length may be several times the thickness of the cell. Improper surface passivation has been shown to be a barrier for the successful implementation of back-side diffractive structures in solar cells.[36] The oxide layer used in this model may serve as a back-side passivation layer. In principle, a thin planar optically inactive oxide layer may be inserted between the grating layer and the bulk Si to further reduce surface recombination.

From Fig. 4, we see that the best structures are not far from a Lambertian surface when it comes to light confinement. However, for these structures, the largest loss mechanism is no longer incomplete absorption, but instead the front-side reflectance from the single layer ARC. The front-side reflectance is also mainly responsible for the reduced performance of all the structures at higher angles of incidence (see Fig. 6).

Front-side pyramidal textures are commonly used in today's solar cells. For short wavelengths that do not penetrate to the back side, a front-side texture will certainly increase light absorption by reducing front-side reflectance. The effect of a grating in combination with a textured front surface is, of course, much smaller than for a planar front surface. The exact effect on light confinement for long wavelengths are difficult to predict, since a front-side texture will change the incident angles and affect the light trapping from a back-side grating. Such macroscopic structures are difficult to model rigorously and are outside the scope of this work. Such computations could, in principle, be performed using a combination of ray-tracing and RCWA.[37]

In a solar module, the solar cells will be encapsulated with glass on the front side. Since the light reflected from a Si-glass interface is lower than from a Si-air interface, the advantage of a front-side texture over that of a planar cell will be somewhat reduced with encapsulation compared to the case without encapsulation. Nevertheless, to further increase absorption, a lower front-side reflectance is required. Multiple or graded ARCs are possible solutions that will conserve the light-trapping ability of the back-side periodic structures and, at the same time, reduce front-side reflectance.

Fabrication of sub-micron periodic structures on large areas is obviously not trivial. Some techniques that might have potential for large scale production include nano-imprint lithography or hot embossing[38,39] and interference (holographic) lithography.[38,40] Self-assembled structures are yet another possibility. One example of this is a periodic dimple structure with a triangular lattice that has been realized by anodic etching of Al.[22] The different geometries in this work may have various possibilities for fabrication. Nobody has fabricated structures like the rose and zigzag structure today, and large area fabrication of such structures will not be a simple task. Hopefully, low-symmetry light trapping structures that lend themselves to fabrication may be designed.

The structures presented in this work are all subject to the limitation that they require patterning of Si (or another high index material). The grating does not necessarily need to be filled with an oxide. A grating consisting of Si and air could, in principle, provide a more broad-banded response than a Si-oxide grating because of the larger refractive index contrast.

VII. CONCLUSION

We have optimized and compared the light-trapping potential of seven different periodic structures with essential differences in the geometry of their unit cells. The geometries comprise the cylinder, inverted pyramid, cone, dimple, roof-mosaic, rose, and zigzag structure. We found that the optimized structures had similar lattice periods despite their difference in geometry. The light-trapping potential of the structures range from a photo-generated current density J_{ph} of 35.6 mA/cm^2 for the cylinder structure, corresponding to an effective optical thickness increase of a factor of 9, to a J_{ph} of 37.3 mA/cm^2 for the zigzag structure, corresponding to an increase in optical thickness of a factor of 22.

Analysis of the diffraction patterns revealed that the two structures with the highest J_{ph} have less symmetry than the rest of the structures. The best light trapping is achieved for the least symmetric of the structures. This agrees well with literature, which suggests that non-symmetric structures are superior to symmetric ones. The light trapping achieved with the zigzag structure is close to that of the Lambertian limit, in spite of the fact that the zigzag structure makes use of the strongly absorbing Al as reflector material.

The investigation at oblique angles of incidence shows that the back-side gratings perform well at angles of incidence up to 60 degrees, also when considering an average over several azimuth angles and both polarizations. The reduced performance at higher angles of incidence is dominated by the increase in front-side reflectance of s-polarized light from the planar ARC.

The comparison we present in this work is applied to a 20 μm thick Si slab, but the light-trapping structures, as

such, are not constricted to a certain material or thickness. We have used Si as a case of study, since the poor absorption of Si makes light trapping specifically important. A different choice of thickness or material is expected to change the optimal grating dimensions. Particularly, the optimal lattice period is expected to be reduced for thinner solar cells, where a broader spectrum will reach the back side.

ACKNOWLEDGMENTS

The authors would like to acknowledge the Norwegian research council through the program Nordic Center of Excellence in Photovoltaics (NoCEPV).

[1]A. W. Blakers, K. J. Weber, M. F. Stuckings, S. Armand, G. Matlakowski, A. J. Carr, M. J. Stocks, A. Cuevas, and T. Brammer, Prog. Photovoltaics **3**, 193 (1995).
[2]K. Feldrapp, R. Horbelt, R. Auer, and R. Brendel, Prog. Photovoltaics **11**, 105 (2003).
[3]F. Henley, A. Lamm, S. Kang, Z. Liu, and L. Tian, in *Proceedings of the 23rd European Photovoltaic Solar Energy Conference*, Valencia, Spain, 1–5 September 2008.
[4]A. Luque and S. Hegedus, *Handbook of Photovoltaic Science and Engineering* (Wiley, New York, 2003).
[5]D. H. Macdonald, A. Cuevas, M. J. Kerr, C. Samundsett, D. Ruby, S. Winderbaum, and A. Leo, Sol. Energy **76**, 277 (2004).
[6]D. Kray and K. R. McIntosh, Phys. Status Solidi A **206**, 1647 (2009).
[7]J. Müller, B. Rech, J. Springer, and M. Vanecek, Sol. Energy **77**, 917 (2004).
[8]M. Gale, B. Curtis, H. Kiess, and R. Morf, Proc. SPIE **1272**, 60 (1990).
[9]C. Heine and R. H. Morf, Appl. Opt. **34**, 2476 (1995).
[10]P. Sheng, A. N. Bloch, and R. S. Stepleman, Appl. Phys. Lett. **43**, 579 (1983).
[11]C. Haase and H. Stiebig, Prog. Photovoltaics **14**, 629 (2006).
[12]P. Bermel, C. Luo, and J. D. Joannopoulos, Opt. Express **15**, 16986 (2007).
[13]J. G. Mutitu, S. Shi, C. Chen, T. Creazzo, A. Barnett, C. Honsberg, and D. W. Prather, Opt. Express **16**, 15238 (2008).
[14]J. Gjessing, E. S. Marstein, and A. S. Sudbø, Opt. Express **18**, 5481 (2010).
[15]E. Yablonovitch, J. Opt. Soc. Am. **72**, 899 (1982).
[16]Z. Yu, A. Raman, and S. Fan, Opt. Express **18**, 366 (2010).
[17]A. Chutinan, N. P. Kherani, and S. Zukotynski, Opt. Express **17**, 8871 (2009).
[18]S. E. Han and G. Chen, Nano Lett. **10**, 4692 (2010).
[19]J. Gjessing, A. S. Sudbø, and E. S. Marstein, paper presented at the EOS Annual Meeting, Paris, France, 26–28 October 2010.
[20]L. Zeng, P. Bermel, Y. Yi, A. Alamariu, K. A. Broderick, J. Liu, C. Hong, X. Duan, J. Joannopoulos, and L. C. Kimerling, Appl. Phys. Lett. **93**, 221105 (2008).
[21]V. E. Ferry, M. A. Verschuuren, H. B. T. Li, E. Verhagen, R. J. Walters, R. E. I. Schropp, H. A. Atwater, and A. Polman, Opt. Express **18**, 237 (2010).
[22]H. Sai and M. Kondo, J. Appl. Phys. **105**, 094511 (2009).
[23]J. Gjessing, A. S. Sudbø, and E. S. Marstein, paper presented at Optics for SOLAR, Tucson, AZ, USA, 7–9 June 2010.
[24]J. Gjessing, A. S. Sudbø, and E. S. Marstein, J. Eur. Opt. Soc. Rapid Publ. **6**, 11020 (2011).
[25]C. Haase and H. Stiebig, Appl. Phys. Lett. **91**, 061116 (2007).
[26]D. Zhou and R. Biswas, J. Appl. Phys. **103**, 093102 (2008).
[27]S. B. Mallick, M. Agrawal, and P. Peumans, Opt. Express **18**, 5691 (2010).
[28]R. Biswas, D. Zhou, and L. Garcia, Mater. Res. Soc. Symp. Proc. **1153**, 1153-A03-02 (2009).
[29]E. Schneiderlöchner, R. Preu, R. Lüdemann, and S. W. Glunz, Prog. Photovoltaics **10**, 29 (2002).
[30]L. Li, J. Opt. Soc. Am. A **13**, 1024 (1996).
[31]C. M. Herzinger, B. Johs, W. A. McGahan, J. A. Woollam, and W. Paulson, J. Appl. Phys. **83**, 3323 (1998).
[32]Handbook of Optical Constant of Solids, edited by E. D. Palik (Academic, New York, 1985).
[33]See http://software.kjinnovation.com/GD-Calc.html for more information about the grating diffraction calculator.
[34]K. C. Johnson, *Grating Diffraction Calculator (GD-Calc) - Coupled-Wave Theory for Biperiodic Diffraction Gratings* (2006).
[35]See http://rredc.nrel.gov/solar/spectra/am1.5/for more information about the AM 1.5 spectrum.
[36]P. Berger, H. Hauser, D. Suwito, S. Janz, M. Peters, B. Bläsi, and M. Hermle, Proc. SPIE **7725**, 772504 (2010).
[37]M. Peters, M. Rüdiger, D. Pelzer, H. Hauser, M. Hermle, and B. Bläsi, in *Proceedings of the 25th European Photovoltaic Solar Energy Conference*, Valencia, Spain, 6–10 September 2010.
[38]A. Gombert, K. Rose, A. Heinzel, W. Horbelt, C. Zanke, B. Bläsi, and V. Wittwer, Sol. Energy Mater. Sol. Cells **54**, 333 (1998).
[39]M. Heijna, J. Loffler, B. Van Aken, W. Soppe, H. Borg, and P. Peeters, Mater. Res. Soc. Symp. Proc. 1101 (2008).
[40]S. H. Zaidi, J. M. Gee, and D. Ruby, in *28th IEEE Photovoltaic Specialists Conference*, Anchorage, AK, 15–20 September 2000, pp. 395–398.

COMPARISON OF LIGHT TRAPPING IN DIFFRACTIVE AND RANDOM PYRAMIDAL STRUCTURES

J. Gjessing[1,2,3*], **E. S. Marstein**[1,2], **A. S. Sudbø**[2,3]
1. Institute for Energy Technology, Department of Solar Energy, P.O. Box 40, 2027 Kjeller, Norway
2. University of Oslo, Department of Physics, P.O. Box 1048 Blindern, 0316 Oslo, Norway
3. University Graduate Center at Kjeller, P.O. Box 70, 2027 Kjeller, Norway
*email: jo.gjessing@ife.no, Tel: (+47) 6380 6637

ABSTRACT: Good light trapping is essential to make high efficiency silicon solar cells. As silicon wafers are being made increasingly thinner, light trapping becomes even more important. In this work we compare in simulations light trapping from conventional random pyramid textures, with structure sizes of several microns, to that of light trapping from diffractive structures with lattice periods comparable to the wavelength of light. More specifically we compare light trapping in front-side and double-sided random pyramidal textures to that of two different back-side bi-periodic structures applied to a 20 µm thick Si slab. We find that a photogenerated current density of 40.0 mA/cm^2 is achieved for a double-sided pyramidal texture with a rear oxide layer and a silver reflector. This is slightly higher than the best diffractive structure with a planer front side and rear texture. The pyramidal textures show exceptional broad-band anti-reflection behavior, while the diffractive structures excel in the long-wavelength part of the solar spectrum.
Keywords: Light Trapping, Ray Tracing, Pyramidal Textures, Periodic Textures

1 INTRODUCTION

Light trapping is an area which has been given increasing attention in recent years. Light trapping is particularly important in Si solar cells due to the poor absorption of near-infrared light close to the absorption edge. Light trapping is an important part of today's solar cells which have typical thicknesses of around 150-200 µm. With the advance of fabrication methods for silicon (Si) wafers with a thickness of around 20 µm [1-4], light trapping will become one of the critical factors for improving the solar cell conversion efficiency.

Conventional texturing of monocrystalline Si wafers relies on an anisotropic alkaline etch of a [100] oriented crystal. This results in a random pattern of pyramids with 54.7º facet angles and with sizes in the order of a few to more than 10 microns. The texturing removes part of the Si material and a certain wafer thickness is therefore necessary to avoid penetration through the wafer, although pyramidal textures have been demonstrated on wafers with a thickness below 50 µm [5]. Methods for fabrication of thin wafers that involve cleaving will often result in wafers with other crystal orientations [1, 4]. Light trapping in such wafers must rely on other types of textures.

Periodic structures with lattice period comparable to the wavelength of light will, if dimensions are chosen correctly, diffract light into guided modes inside the slab waveguide represented by the silicon wafer. Such structures has been investigated as promising candidates to improve light trapping in solar cells ranging from thin-films [6] to thick wafer based cells [7]. Such structures are significantly smaller in size than conventional pyramidal Si textures. Although diffractive structures have yet to break through in commercial production, progress in fabrication techniques makes such structures increasingly interesting also for high-throughput large-area applications.

In this work we compare in simulations the light trapping properties of random pyramidal structures with the light trapping properties of diffractive structures, using a 20 µm thick Si slab as a case of study. Front-side (FS) and double-sided (DS) random pyramidal structures with different reflector materials are investigated together with two types of optimized back-side diffractive structures, a cylinder structure [8] and a structure we call the zigzag structure [9]. To our knowledge a comparison between diffractive structures and random pyramidal structures has not been shown before. Ordinarily such structures are applied to different cell types, i.e. pyramidal structures for thicker wafers [10] and diffractive structures in thin-film solar cells [11], but as Si wafer thickness is gradually reduced, we come to the point where a comparison is relevant.

2 APPROACH

2.1 Random pyramidal texture

Ray tracing, which is based on geometric optics, is a good approximation for light interaction with macroscopic structures, i.e. structures with size much larger than the wavelength of light. The pyramidal structures used in solar cells have typical structure sizes that are several times larger than the wavelengths of the solar radiation that are absorbed in the solar cell. A discussion of the validity of geometrical optics on pyramidal structures is found in Ref. [12].

We have used the ray-tracing software TracePro [13] to compute the light absorption in a silicon slab with a front side (FS) or double-sided (DS) random pyramidal structure. The different structures are compared by their photogenerated current density J_{ph}. This value is found by weighting the Si absorption with the AM1.5 global solar spectrum and converting it to an equivalent current assuming that every absorbed photon excites one electron-hole pair.

The model for the random pyramidal structure was created by first creating a regular pattern of partly overlapping pyramids and then randomly displacing the position of the pyramids. The apexes of the pyramids are held at the same height while the valleys between the pyramids will vary in depth as the pyramids overlap at random distances. We verified that displacement of the pyramids perpendicular to the wafer had a negligible effect on the simulated light trapping, as reported by [14, 15]. We found that a unit cell consisting of 10 by 10 randomly displaced pyramids provided a desired degree of randomness. An example of such a pattern is shown in Figure 1.

As a check of the randomness of our structure we compared the calculated reflectance with the reflectance from a random pyramidal structure calculated with the software OPAL [15]. OPAL calculates front-side reflection from random pyramids by weighting the probabilities of possible ray paths with the reflection from the corresponding ray path. The probabilities of the different ray paths are calculated in advance by ray tracing, using a different method to generate the pyramids than the one that is used in this work. The reflectance calculated with TracePro was within ± 1 % relative to that found from OPAL.

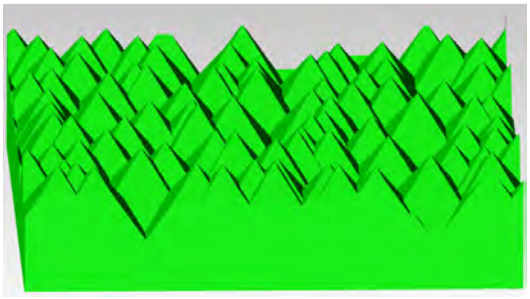

Figure 1: Random pyramidal pattern of 10 by 10 pyramids as created with TracePro. A different random pattern is created for each simulation.

In the ray-trace simulations we used wavelength dependent optical data for Si [16], and for the aluminum (Al) and silver (Ag) reflectors [17]. The ray-trace simulations ignore interference effects, but it is possible to specify thin-film interference effects as surface properties to an interface. We used this to incorporate an oxide layer of 100 nm and a refractive index of 1.5 between the Si material and the metal reflector. In this way parasitic absorption in the metal reflector, caused by evanescent waves from frustrated total internal reflection, is also included in the simulations. On the front side we added a thin film anti-reflection coating (ARC) of silicon nitride with a thickness of 78 nm and a wavelength independent refractive index of 1.95.

We have included the effects of polarization in our ray tracing simulations. This is important because a ray that is reflected or transmitted from a surface at non-normal incidence will in general be polarized. This will affect the reflection coefficient for the interaction with the next surface.

We used an effective thickness of the textured Si slab of 20 µm in our calculations. The effective thickness corresponds to the thickness of a coplanar material with the same volume and base area. Consequently, the distance from the top of the front to the top of the back surface is larger than the effective thickness.

2.2 Periodic structures

To compute the light trapping of the sub-micron periodic structures the full vectorial Maxwell equations needs to be solved. For this purpose we used the software package GD-Calc [18], which is based on rigorously coupled wave analysis (RCWA). A more detailed description of this method is found elsewhere [8].

Here we compare two types of bi-periodic structures, a cylinder array [8] and a structure which we have called the zigzag structure. The zigzag structure has a unit cell consisting of planes sloping in two perpendicular directions as shown in Figure 2. This configuration reduces the symmetry of the structure and has shown exceptional light-trapping properties [9]. The periodic structures are applied to the configuration shown in Figure 2 with a thin silicon oxide layer and a metal reflector behind the grating layer. The ARC at the front side is either a single silicon nitride layer or double layer stack with 108 nm magnesium fluoride ($n = 1.37$) and 60 nm of zinc sulfide ($n = 2.35$). The grating dimensions have been optimized for light trapping in a 20 µm thick Si slab.

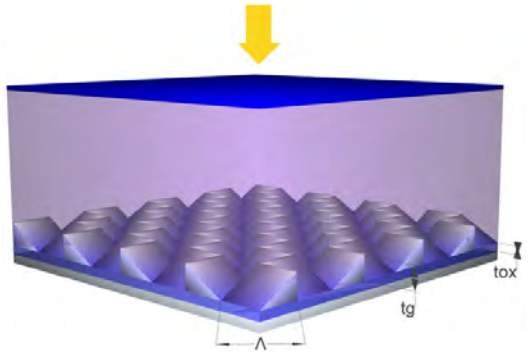

Figure 2: The bi-periodic structures are imprinted on the back side of a 20 µm slab of Si. They are filled with an oxide and covered by a planar metal reflector of either Al or Ag. The front side of the Si slab is planar and covered by a silicon nitride anti-reflection coating. The figure is not to scale.

3 RESULTS

The photogenerated current densities J_{ph} achieved for various combinations of pyramidal structures and periodic structures are shown in Table I. All structures have a metal reflector consisting of either Al or Ag, except for one structure which has an ideal metal reflector with a reflectance of 100 %. J_{ph} is also calculated for reflectors of Al and Ag separated from the Si bulk by an oxide layer.

Table I shows that J_{ph} is higher for Ag reflectors than for Al reflectors, which is expected due to the higher reflectivity of Ag. The oxide layer also increases J_{ph} by reducing metal absorption. The improvement is therefore particularly large for the Al reflectors. The DS pyramidal texture is better than the FS texture for all types of reflectors.

The best light trapping, with a J_{ph} of 40.4 mA/cm^2, is achieved for a DS pyramidal structure with an ideal metal reflector with unity reflectance. Replacing the rear pyramids with an ideal Lambertian reflector yields the same photogenerated current density, a fact that has also been reported by Campell et al. [10]. An ideal Lambertian reflector scatters light in all directions with a constant radiance and such a reflector is known to give the highest light trapping achievable in the geometric optics approximation [19].

Table I: Photogenerated current densities J_{ph} in 20 µm Si for different light-trapping configurations. The structures have reflectors made of aluminum (Al), silver (Ag) or ideal metal with unity reflectance, and an oxide layer is inserted between the Si and the metal for some of the structures. All structures have a single layer anti-reflection coating, except for the periodic structures which are also calculated with double-layer anti-reflection coatings.

Structure			J_{ph} [mA/cm^2]		
Front side	Back side	Oxide	Al	Ag	Ideal
Pyramids	Planar	No	35.7	37.3	
Pyramids	Planar	Yes	37.7	37.9	
Pyramids	Pyramids	No	36.1	38.9	
Pyramids	Pyramids	Yes	39.4	40.0	
Pyramids	Pyramids	-			40.4
Planar	Cylinder	Yes	35.6	36.0	
Planar*	Cylinder	Yes	37.6	38.0	
Planar	Zigzag	Yes	37.3	37.7	
Planar*	Zigzag	Yes	39.3	39.7	

*Double layer anti reflection coating

Figure 3 and Figure 4 shows the spectral absorption for some of the structures in Table I. Figure 3 compares FS and DS pyramids with the back-side periodic cylinder structures. All structures have Al reflectors and a single layer ARC, while the cylinder structure also has an oxide layer separating the cylinders from the Al reflector. For short wavelengths the pyramidal structure is superior to the back-side cylinder structure with its planar front side. In the long-wavelength part of the spectrum the light trapping of the back-side structure becomes notable and here the cylinder structure is superior.

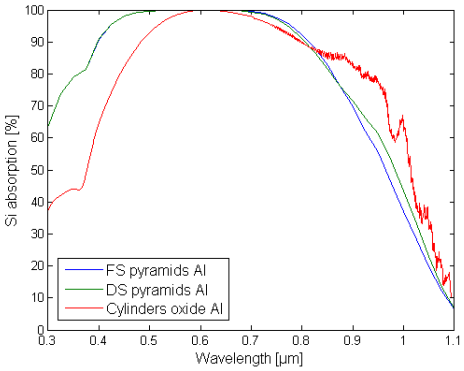

Figure 3: Spectral absorption in Si for front-side (FS) and double-sided (FS) pyramids, and for a back-side periodic cylinder structure. All structures have a single layer anti-reflection coating and an Al reflector. The cylinder structure also has a thin layer of oxide inserted between the cylinders and the Al reflector.

Figure 4 shows the spectral absorption for the FS and DS pyramids, with oxide layers, Ag reflectors and single layer anti-reflection coatings (SLAR). Also shown is the back-side periodic zigzag structure, with Ag reflector, oxide layer and double layer anti-reflection coating (DLAR). The pyramidal structures with SLAR still displays better short wavelength behavior than the planar DLAR, but the difference in front-side reflection is now considerably smaller, corresponding to a J_{ph} of about 0.7 mA/cm^2. In the long wavelength region the zigzag structure and the DS pyramidal structure is clearly superior to the FS pyramidal structure. The J_{ph} of the DS pyramids is 0.3 mA/cm^2 above that of the zigzag structure even though the zigzag structure is somewhat better at longer wavelengths.

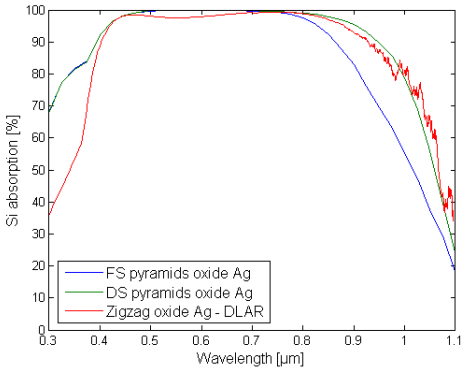

Figure 4: Spectral absorption for double-sided (DS) pyramids with Ag reflector, front-side (FS) pyramids with Lambertian reflector, and back-side periodic zigzag structure with Ag reflector and double-layer anti-reflection coating (DLAR). The other two structures have single layer anti reflection coatings (SLAR).

4 DISCUSSION

The DS pyramidal structure obviously increases the average path length more than the FS structure does, as can be seen from the increased J_{ph} in Table I. This is not surprising since the DS structure will randomize the light in fewer surface interactions than the FS structure. Yet the difference between the FS and DS structures is more pronounced for the Ag reflector than for the Al reflector. This is caused by the fact that a large part of the light will scatter twice off the rear reflector for each pass through the cell. This increases the probability of absorption in the rear reflector, particularly for the Al reflector which has the highest absorption.

The difference between the Al and Ag absorbers is less pronounced when an oxide layer is inserted between the Si and the reflector. The oxide layer reduces absorption losses in the rear reflector. Despite the superior optical properties of Ag, Al is the standard material for rear reflectors in industrial solar cells today due to lower costs and favorable electronic properties. In fact, the screen printed Al commonly used in industrial solar cells is expected to have even higher absorption due to the rougher surface compared to the planar surfaces that have been used in our simulations. On the other hand, such rough surfaces might also help to randomize the light and thereby improve light trapping [20], particularly for the FS pyramidal texture.

The back-side periodic structures will influence absorption only for wavelengths above about 800 nm where a significant part of the light is transmitted to the back side of the 20 µm slab. In this range the periodic structures perform well. Despite the good long wavelength absorption, the planar front side yields high reflection losses compared to the structures with pyramids on the front side. By utilizing a DLAR instead

of a SLAR the J_{ph} is improved by 2 mA/cm^2. The zigzag structure with DLAR and an Ag reflector has an overall absorption which is only 0.7 mA/cm^2 lower than the DS pyramidal structure with an ideal reflector. This difference corresponds to the front side loss of the zigzag structure due to the planar front side. Admittedly, a DLAR would also have reduced reflectance of the pyramidal structures, but this improvement is less than 0.5 mA/cm^2 and even lower in an encapsulated configuration.

In a solar cell module the solar cells will always be covered by a glass to improve their environmental stability. The glass encapsulation of the solar cell in general serves as an anti-reflective coating because the refractive index of the glass is between the indices of air and Si. Since the pyramids already provide a low reflectance, this structure will gain less from an encapsulation than a planar surface. In fact, for structures with a SLAR the difference in front-side reflectance between a planar surface and a surface textured with pyramids will be reduced by more than 1 mA/cm^2 for an encapsulated cell compared to an unencapsulated cell. The same argument also holds for a DLAR and for graded ARCs. Such ARCs will greatly reduce the handicap of a planar surface compared to a pyramidal surface, both for encapsulated and unencapsulated solar cells.

Although the DS pyramids and the zigzag structure use two very different approaches to light trapping, their photogenerated current density is actually fairly similar even though the DS pyramids have a slight advantage due to the lower front-side reflection. It should be noted that the zigzag structure achieves this light-trapping effect with only one side textured. This could be an advantage with respect to reducing surface recombination which is crucial for high efficiency thin solar cells.

5 CONCLUSION

We have investigated light trapping in FS and DS random pyramidal structures with different rear side reflectors, and in back-side periodic structures which are considerably smaller in size. The pyramidal structures provide a very low front-side reflectance. The DS pyramids have considerably better light confinement than the FS pyramids, but they are also particularly sensitive to absorption in the rear reflector. An oxide layer inserted between the Si and the metal will significantly reduce absorption in the metal reflector. Such a layer is crucial for light trapping, particularly if Al is used as reflector material. The maximum potential of the pyramids, using a reflector with unity reflectance, corresponds to that of Lambertian light trapping at normal incidence.

The periodic back-side structures confines light well in the long wavelength range, but suffer from high reflectance due to the planar front side. This handicap is greatly reduced for a double-layer anti-reflection coating (DLAR). Light trapping from the periodic cylinder structure with DLAR is about the same as for the FS pyramids with oxide layer. Light trapping from the zigzag structure is significantly higher and close to light trapping from the DS pyramids with oxide layer.

Encapsulation, double and graded anti-reflection coatings will reduce reflectance from both types of structures, but because planar surfaces suffer the highest losses these structures also have a higher potential for such improvements. Light trapping both from the DS pyramids and the zigzag structure is close to that of a structure with a pyramidal front side and a Lambertian reflector. The DS pyramids have a slightly higher J_{ph} due to lower reflectance, but the fact that the zigzag structure achieves this light trapping effect with only one side textured could be an advantage with respect to reducing surface recombination.

ACKNOWLEDGEMENTS

The authors would like to acknowledge the Norwegian research council through the program Nordic center of excellence in photovoltaic (NCoEPV).

REFERENCES

[1] Henley, F., Lamm, A., Kang, S., Liu, Z., Tian, L., Direct film transfer (DFT) technology for kerf-free silicon wafering, Proceedings of the 23rd European Photovoltaic Solar Energy Conference, Valencia, Spain, (2008).
[2] K. Feldrapp, R. Horbelt, R. Auer, R. Brendel, Thin-film (25.5 µm) solar cells from layer transfer using porous silicon with 32.7 mA/cm2 short-circuit current density, Progress in Photovoltaics: Research and Applications, 11 (2003) 105-112.
[3] M. Ernst, R. Brendel, Large area macroporous silicon layers for monocrystalline thin-film solar cells, in: Photovoltaic Specialists Conference (PVSC), 2010 35th IEEE, 2010, pp. 003122 -003124.
[4] R.A. Rao, L. Mathew, et al., A novel low-cost 25 µm thin exfoliated monocrystalline Si solar cell technology, in: Photovoltaic Specialists Conference (PVSC), 2011 37th IEEE, 2011.
[5] D. Kray, K.R. McIntosh, Analysis of ultrathin high-efficiency silicon solar cells, Phys. Status Solidi A, 206 (2009) 1647-1654.
[6] Zeng, L., Bermel, P., Yi, Y., Alamariu, A., Broderick, K. A., Liu, J., Hong, C., Duan, X., Joannopoulos, J, Kimerling, L. C., Demonstration of enhanced absorption in thin film Si solar cells with textured photonic crystal back reflector, Applied Physics Letters, 93 (2008) 221105.
[7] P. Berger, H. Hauser, D. Suwito, S. Janz, M. Peters, B. Bläsi, M. Hermle, Realization and evaluation of diffractive systems on the back side of silicon solar cells, Proc. of SPIE, 7725 (2010) 772504-772501.
[8] J. Gjessing, E.S. Marstein, A.S. Sudbø, 2D back-side diffraction grating for improved light trapping in thin silicon solar cells, Opt. Express, 18 (2010) 5481-5495.
[9] J. Gjessing, A.S. Sudbø, E.S. Marstein, A novel back-side light-trapping structure for thin silicon solar cells, J. Eur. Opt. Soc, Rapid Publ., 6 (2011) 11020.
[10] P. Campbell, M.A. Green, Light trapping properties of pyramidally textured surfaces, J. Appl. Phys., 62 (1987) 243-249.
[11] Bermel, Peter, Luo, Chiyan, Joannopoulos, John D., Improving thin-film crystalline silicon solar cell efficiencies with photonic crystals, Optics Express, 15 (2007) 16986-17000.
[12] F.Llopis, I. Tobias, Influence of Texture Feature Size on th eOptical Performance of Silicon Solar Cells, Prog. Photovolt: Res. Appl., 13 (2005) 27-36.
[13] TracePro, in, http://www.lambdares.com/

[14] J.M. Rodríguez, I. Tobías, A. Luque, Random pyramidal texture modelling, Solar Energy Materials and Solar Cells, 45 (1997) 241 - 253.
[15] S.C. Baker-Finch, K.R. McIntosh, A freeware program for precise optical analysis of the front surface of a solar cell, in: Photovoltaic Specialists Conference (PVSC), 2010 35th IEEE, 2010, pp. 002184 -002187.
[16] C.M. Herzinger, B. Johs, W.A. McGahan, J.A. Woollam, W. Paulson, Ellipsometric determination of optical constants for silicon and thermally grown silicon dioxide via a multi-sample, multi-wavelength, multi-angle investigation, J. Appl. Phys., 83 (1998) 3323-3336.
[17] Handbook of optical constant of solids, Academic Press, 1985.
[18] K.C. Johnson, Grating Diffraction Calculator (GD-Calc). http://software.kjinnovation.com/GD-Calc.html.
[19] E. Yablonovitch, G.D. Cody, Intensity Enhancement in Textured Optical Sheets for Solar Cells, IEEE Trans. Electron. Dev., 29 (1982) 300-305.
[20] D. Kray, M. Hermle, S.W. Glunz, Theory and Experiments on the Back Side Reflectance of Silicon Wafer Solar Cells, Prog. Photovolt: Res. Appl., 16 (2008) 1-15.